1-1-2000

The property and structure evolution with external stimuli in high performance fibers.

Yuanqiao, Rao
University of Massachusetts Amherst

THE PROPERTY AND STRUCTURE EVOLUTION WITH EXTERNAL STIMULI IN HIGH PERFORMANCE FIBERS

A Dissertation Presented

By

YUANQIAO RAO

Submitted to the Graduate School of the
University of Massachusetts Amherst in partial fulfillment
of the requirements for the degree of

DOCTOR OF PHILOSOPHY

May 2000

Polymer Science and Engineering Department

THE PROPERTY AND STRUCTURE EVOLUTION WITH EXTERNAL STIMULI IN HIGH PERFORMANCE FIBERS

A Dissertation Presented

By

YUANQIAO RAO

Approved as to style and content by:

Richard J. Farris, Chair

Alan J. Lesser, Member

Thomas J. Lardner, Member

Steven R. Allen, Member

Richard J. Farris, Department Head
Polymer Science and Engineering Department

DEDICATION

To my dear father,

from whom I inherit the intelligence and perseverance to achieve goals.

ACKNOWLEDGEMENTS

It is difficult to say goodbye to this memorable place. Life is a journey and I feel fortunate to set one of my milestones in this great place with loving people. I have truly enjoyed my precious five-year graduate school, thanks to many people…

I am very grateful to Prof. Richard J. Farris. As my advisor, he has given me everything needed for my growth, like sunshine, water and fertilizer to the growth of crops. His expertise in applied mathematics and continuous mechanics has helped me to develop a solid knowledge of them. His creativity in polymer experimentation has always inspired my desire of invention. His encouragement has built strong confidence in me. His support has enabled me to explore the scientific unknowns that truly interest me. He not only cares about my research but also be concerned about my development of personal skills. Prof. Farris has been a great example of being an advisor.

Dr. Steve Allen deserves special acknowledgement. He is the person who first introduced me into my research project. He has given me a great deal of advice, suggestion and comments through innumerous e-mails. He is a great resource whenever I have questions. His early dissertation work at UMass has also been a good reference. I am also thankful to Professor Alan J. Lesser and Professor Thomas J. Lardner for their support as committee members.

The writing of this disseration brings back many memories. I clearly remembered that I almost bumped into Prof. Porter when I stepped out of the elevator in the very early of my graduate school. He smiled back and asked me if I was on the right floor. Later we had quite communication and he had given me valuble suggestions on my research.

Polymer Science and Engineering Department has been a great place to study at. Past members in the Farris group such as Mike Chen, Naveen Agarwal, Shalabh Tandon and Jennifer Stewart have helped me to start up with my research. Arun Raman and Jeremy Morin have been

good friends to talk to on either scientific or personal issues. I always rely on them to help me moving heavy stuff. Ru Feng helped me in our synchrotron x-ray measurements. I was moved by her hard work. Lesser group members such as Bob Kody, Ed Kung and Terry Hobbs have also given me tremendous help. My appreciation is also extended to the PSE support staff: Alan Waddon, Eileen Besse, Sophia Michelson and Andre I'melcuk who have made my research smooth.

I have developed friendship within and outside our department. Bodan Ma was the person who hosted my interview with the department. As my college alumnus, his strong recognition of this department assured my decision to pursue my Ph.D. in this department. Weiguo Hu, also my college alumnus, and his wife Zhaohui Fan have been close friends. Zhaohui Su and his wife, Danhong Zhu, Chunping Xie and his wife, Ni Gao are also good friends. We have had many happy times together in the past five years. Heather Hays, my classmate, gave me a ride to our first-year party. She has been very helpful to me to accustom to American culture. Gregory and Susan Schueneman, as friends, have also offered many good suggestions.

Finally, I would like to recognize the love and support from my family. My father first inspired my interests in natural science and gave me all the financial and spiritual support. My mother dedicated all her spare time to educate and take care of her children. My brother and sister always believe in my ability even when I was doubtful myself. I could not thank enough my husband, Xin Jin. His love integrates my happiness beyond personal achievement.

ABSTRACT

THE PROPERTY AND STRUCTURE EVOLUTION WITH EXTERNAL STIMULI IN HIGH PERFORMANCE FIBERS

MAY 2000

YUANQIAO RAO, B.S., TSINGHUA UNIVERSITY, CHINA

M.S., TSINGHUA UNIVERSITY, CHINA

Ph.D., UNIVERSITY OF MASSACHUSETTS AMHERST

Directed by: Professor Richard J. Farris

This dissertation presents an investigation on the long-term behavior and the structure-property relation in high performance polymeric fibers. These fibers have wide applications in structural cable and ropes and reinforced composites. Therefore, the understanding of their structure-property relation and their behavior under external mechanical stress is very important.

The fatigue and creep behavior were studied. A general lifetime equation was derived to correlate the material lifetime with the applied stress level. The failure criterion of "*critical strain*" was identified. The failure mechanism was shown to be a deformation route. The fatigue lifetime was predicted from known material constants. Several material parameters were defined to characterize the fatigue and creep properties. The fatigue property is characterized by the fatigue strength and fatigue strength index; while the creep property is characterized by the creep strength and creep strength index. The fatigue strength index was used to show that fiber with a rigid chain structure, such as Kevlar®, Techanora® and Vectran®, generally have better fatigue resistance than a flexible chain fiber, such as Spectra®.

Twisting was found to influence yarn properties. A model based on composite theory was developed to predict the change in the yarn modulus with the degree of twist.

The desire for nondestructive prediction of the residual lifetime of a used material initiated the efforts to find a signature of the stress and thermal history in Kevlar® fibers. To achieve this, a new testing methodology has been developed. An iso-strain force-temperature test (IFTT) was shown to yield quantitative information on the stress and thermal history as well as the information of relaxation and transitions in many materials. The IFTT behavior of a Kevlar® fiber maps well with its structure examined by X-ray diffraction. The IFTT was also used to screen the processing for property enhancement via post-treatment.

Different post-treatment routes have been investigated for Kevlar® fiber. Tension, heat, hydrostatic pressure, and different media of water, mercury and silicon oil have been utilized to alter the materials. The evolution of its property and structure have been carefully examined. It is shown that the modulus of PPTA is determined by two structure parameters: misorientation and a paracrystalline parameter.

TABLE OF CONTENTS

LIST OF TABLES

Table **Page**

LIST OF FIGURES

Figure **Page**

CHAPTER 1

INTRODUCTION

1.1 High Performance Organic Fibers

Naturally-occuring fiber is probably the oldest polymer that humans have used. Natural fibers woven into textile cloth are very important in every day use. It was also known that different fibers have different properties that meet different needs. The first man-made fiber was drawn from dissolved cellulose at the end of the 19th century. The objective of industry was to mimic natural fibers. Along with other advancements in polymer science, the use of fiber has progressed from textiles and cables into fiber reinforced composites, separation membranes, and widened from textiles into industrial, military and aerospace usage. High performance polymeric fibers are replacing conventional structural materials such as metals, because polymer fiber composites provide superior specific properties. Here, the term "high performance" refers to high strength, high modulus, thermal stability, dimensional stability, light weight and good solvent and chemical resistance.

Since the 1950s, significant advancements have been achieved in high performance fibers. Notably, the discovery of the poly(p-phenylene terephthalamide) (PPTA) fiber in 1972 brought much excitement to the polymer community. Polymers are composed of aggregates of long chain molecules. Each chain has the characteristic of high strength anisotropy, with strong atomic bonds along the chain and weak interchain bonds, such as the hydrogen bond and van der Waals' interaction. A fully extended chain structure is needed to eliminate chain deformation by bond bending and rotation so as to form a high modulus and high strength fiber. There are usually two approaches. One approach is to utilize a flexible chemical structure and adopt special processing techniques to eliminate entanglements, form fully extended chains and then to freeze them in place through crystallization. Ultra high molecular weight polyethylene fiber

(UHMWPE) is such an example.[1] Other possible systems in the category of flexible chain high performance fibers are poly(vinyl alcohol) (PVA), poly(acrylonitrile) (PAN) and poly(propylene) (PP). The other approach is to synthesize a rigid-rod chemical structure that can form a fully extended structure through self organization. PPTA is the first good example of this process.[2] The tensile properties of Kevlar® 29 are shown better than steel or glass fibers, compared on a specific weight basis.[3]

There are now many aromatic high performance fibers in the category of rigid-rod chain structure fibers. Their thermal stability was first recognized in the 1950s. The main types include aromatic polyamide, aromatic polyhydrazide, aromatic polyester, aromatic polyazomethine, aromatic polyimide and aromatic heterocyclic polymers. Commercially available aromatic fibers and other high performance fibers are listed in Table 1.1.[3] Most commercial rigid-rod chain high performance fibers exhibit liquid crystal either in solution, which is called lytropic liquid crystal, or upon heating, which is called thermotropic liquid crystal. There are two ways to process aromatic fibers: solution spinning and melt spinning. Most aromatic fibers show no glass transition or melting temperatures and can only be processed through solution spinning (lytropic). From the list above, aromatic liquid crystalline polyester is the only class that can be processed by melt spinning (thermotropic). The existence of a liquid crystalline state, either in solution or a high temperature melt, is believed to help the polymer to self-organize into a highly oriented morphology, which is critical for high performance. Compared with polyolefins, studies of the thermal behavior, structure and chain dynamics of aromatic polymers are far from complete. Solution spun aromatic polymers tend to decompose before melting and this makes it difficult to evaluate their thermal transitions. Although aromatic fibers have a very rigid structure, chain motion is still possible. These chain motions are very important for optimizing spinning conditions and understanding mechanical properties. The

study of chain motion for the fibers investigated in this dissertation will be summarized in the next section.

Table 1.1 High performance fibers produced in the United States

Fiber type	Producer	Trademark	End uses
Aromatic fibers			
Aramid	Du Pont	Nomex®	Thermal protective apparal, electrical insulation, filter
Aramid	Du Pont	Kevlar®	Protective apparel, armor, composites, rubber goods, ropes and cables, asbestos replacement
Aramid	Teijin	Technora®	Ropes, composites
Polyester	Hoechst Celanese	Vectran®	Thermoplastic composites, sailcloth
Polybenzimiidazole			Protective apparel
Heterocyclic polymers	Toyobo	Zylon®(PBO)	Composites, ropes, Protective apparel
Polyolefin fibers			
Polyethylene	Allied-Signal	Spectra®	Armor, ropes,
	Toyobo	Dyneema®	composites
Bicomponent	Avtex	ES	Nonwoven fabrics
Carbon fiber			
PAN based			Composites
Pitch based	BP Amoco	Thornel®	Composites
	Ashland	Carboflex®	Composites
Inorganic fibers			
Boron			Aerospace structures
SiC			Metal matrices
Al2O3-B2O3-SiO2	3M	Nextel®	Ceramic reinforcement
Glass	Owens-Corning	Fiberglass	Composites, armor
Poly(phenylene sulfide)			Chemical-resistant filtration
Steel	Bekaert		Tire cord, textiles, cables

1.1.1 Processing

Regardless of their chemical structure, processing is crucial to all aromatic fibers to achieve high performance properties. Typical processing of high performance fibers includes spinning, drawing, and annealing. Melt spinning usually can not yield the orientation required for the high performance because the operational time is longer than the corresponding relaxation time. The main goal in a melting spinning process is to achieve high speed spinning. Preheating temperatures and final spinning temperatures are key parameters in melt spinning. The preheating temperature should be higher than the clearing temperature, and the spinning temperature should be near the crystal-to-nematic transition to spin thermotropic liquid crystal materials. Although spinning from the liquid crystal state is generally used to achieve high orientation in as-spun fibers, Cheng's group argued that spinning from a liquid crystalline state largely limits the potential for post treatment. They showed that polyimide fibers spun from isotropic solution have superior mechanical properties after being post treated.[4-6] In solution spinning, dry-spinning is a process where the solvent is volatile and removed by evaporation; while wet-spinning is when the solvent is carried out by using a coagulant. Dry-jet wet spinning is an ingenious way to achieve high orientation from a solution spinning process.[7] Polyethylene is the most utilized polymer in the world. However, due to limitations in the properties, it had never been used in high performance applications until the discovery of UHMEPE fiber. The emergence of high performance polyethylene fiber has been a big success. Different processes such as solid state extrusion[8], gel spinning[1], zone-drawing-zone-annealing[9,10] or special drawing[11] are adopted to achieve high orientation and high crystallinity of ultra high molecular weight polyethylene.

As spun fibers often possess low orientation and low crystallinity. The properties of as-spun fibers usually can be further improved with post drawing. The draw ratio is defined as the ratio of final to initial length and is often measured as the ratio of initial to final cross-section

area. The properties of PPTA fibers are very sensitive to the temperature and tension in post treatment, and different types of Kevlar® fibers are produced from different post treatments. Annealing is used as the final step to stabilize the structure after post-treatment. Annealing is carried out with the fiber being kept at constant length or relaxed. Thermal annealing of aromatic polyester fiber can increase the tenacity by 50%.[12,13]

New processes of making high performance fibers are under development. Komatsu showed that pressurized melt drawing of poly(oxymethylene) (POM) fibers gives rise to higher draw ratio, a 30% increase in fiber modulus and a 40% increase in strength.[14,15] A vibrating hot drawing process was developed by Kunugi and coworkers.[16,17] An eletrospinning process has been invented recently, where an electric field is used to create a charged jet of polymer solution. As this jet travels through the air, the solvent evaporates leaving behind a charged fiber that can be electrically deflected or collected on a metal screen. The diameter of these fibers can be in the range of 0.05 to 5 microns, which is very small when compared to conventional fibers. The process has the potential to produce nanofibers, which may exhibit different properties.[18,19]

Many attempts have been made to modify and improve the properties of existing high performance fibers. The compaction and fusion of PE fibers without the addition of a matirx strives to create a composite with very high performance properties.[20-22] Extended-chain polymeric fibers usually have poor compressive strength. Efforts have been made to incorporate crosslinkable side groups into these polymers to improve the compressive properties.[23,24]

1.1.2 Structure-Property Relationships

There are different models that researchers assume for the structure of fibers. The most common is the two-phase model for semicrystalline fibers. An amorphous phase and a crystalline phase arranged in a serial manner for fibers. The structure quantities include the degree of crystallinity, the size and shape of the crystals, the orientation of the crystal phase and

amorphous phase, and the interconnectivity between the amorphous and the crystalline phases. Many fiber studies are based on this structure model: Hearle and Peters[25], Spruiell and White[26], and Ziabicki and Kawai[27], just to name a few.

Network theory for fiber was proposed and developed by Ward.[28] They have shown that a network is superimposed on the crystalline phase and amorphous phase.

1.2 PPTA Fiber and Other High Performance Fibers Investigated

1.2.1 PPTA Fiber

1.2.1.1 Structure

A great deal of research has been done to determine the structure of PPTA. It is generally agreed that there are three layers of structure for a PPTA fiber.

First, PPTA is a highly crystalline polymer. There is still debate about the crystallinity of PPTA, since no salient amorphous halo is observable from x-ray diffraction. Two models are taken: a single phase structure with crystalline imperfection and a two phase structure with amorphous and crystalline regions. The crystallinity of Kevlar® 29 fiber, based on Hindeleh's measurement, is 68%.[29] The crystal structure of PPTA shown by Northolt and Aartsen is a pseudo-orthorhombic.[30,31] The crystallographic density is 1.48 g/cm^3.[32] The orientation angles between the phenylene planes and the amide planes is 38° for the p-phenylene diamine segment and -30° for the terephthalic segment.[31] For Kevlar® 29 fibers, the crystal size is 50 nm along the *c*-axis, 3.6 nm along the *a*-axis and 2.5 nm along the *b*-axis, and the average crystalline orientation angle is 12°.[29] Panar and coworkers suggested a paracryatlline structure of the crystal with a second order distortion $g_{//}$ of 2.5 % along the *c*-axis.[33] It is believed that bond rotation is hindered by steric effects.

Secondly, the crystals are packed to form pleated sheets. A 35 nm periodicity was observed in fiber by transmission electron microscopy and small-angle x-ray scattering.[33] This periodicity is comparable to the polymer chain length and is designated to be the defect zone period. Using wide angle x-ray diffraction, different research groups have reported different crystal sizes in the *c*-axis direction. Panar and Barton [33,34] reported a correlation length of about 90 nm while Wu reported a number of 30 nm[35]. This number is important to the understanding of the structure. If the crystal size, which is the same as the correlation length, is bigger than the defect zone period, there must be a good bridging in the defect zone. It is believed that some chains extend through the defect zone. Transmission electron microscopy and micro x-ray diffraction measurements supported a radial lateral arrangement of the crystals along *b*-axis.[36,37] Pleats were observed using polarized optical microscopy. It is believed that pleated sheets are formed in the hydrogen-bond direction and are arranged radially. The pleats have 300-500 nm periodicity.[38] There are modified structural models based on the radial pleated structure proposed for PPTA fiber.[39] The existence of a pleat structure will decrease the stiffness of the fiber. The origin of the pleats is not clear.

Finally, a rich fibrillar structure is formed. A skin-core morphology is common due to processing.[40] The structure is shown schematically in Figure 1.1.

Little information exists on the amorphous region of PPTA fiber. Actually, the existence of an amorphous phase is under debate. The x-ray diffraction pattern, with the beam perpendicular to the fiber axis, shows no meridional amorphous trace. Orientation measurements by x-ray and acoustic pulse methods show that the overall orientation and crystalline orientation are comparable.[33] All these suggest that the amorphous phase, if there is one, is also highly oriented. This is quite different from conventional polymers, which usually have better crystalline orientation.

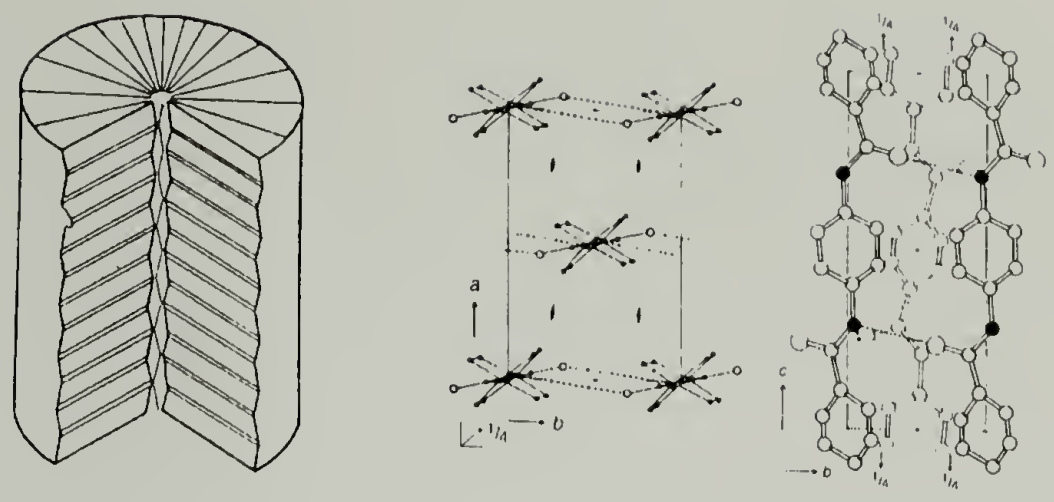

Pleat structure Crystal unit cell

Figure 1.1 Schematic structure of Kevlar® fiber[30,31,38]

1.2.1.2 Structure-Property Relationship

Since PPTA fiber has a highly crystalline structure and superior mechanical properties, it is a good material for structure-property relationship studeies. It is generally accepted that better orientation results in higher modulus. On the basis of a single-phase structural model, the following equation can be used to correlate the fiber compliance with the disorientation angle:[41]

$$S_{33} = e_3^{-1} + A\langle \sin^2 \phi \rangle + B\langle \sin^4 \phi \rangle$$

in which, S_{33} is the fiber compliance along the fiber axis, e_3 is the crystal modulus along the c-direction and ϕ is the orientation angle of the crystals

Barton tried to develop a correlation between the modulus and the paracrystalline parameter.[34] Hindeleh and Abdo, after a thermal annealing and aging study, believed that the fiber modulus increases but the strength and elongation decrease with increasing crystallinity.[29] Lee post-treated Kevlar® fibers under different temperatures and tensions and carried out mechanical testing and x-ray measurements. From his experimental results, a relation between the modulus and the orientation function and the removal of pleats was observed. Meanwhile, other structural features-- paracrystalline parameter, axial and transverse crystallite size-- do not

dominate the material stiffness.[42] The fiber inventors at Dupont believed that the perfection of the radial arrangement gives improved tenacity.[43] X-ray diffraction study has been carried out to correlate the macroscopic thermal expansion with the microscopic thermal expansion.[44] A shrinkage in *c*-axis dimension upon heating follows the macroscopic thermal shrinkage, while *a*-, *b*- dimensions expand upon heating.

1.2.1.3 Thermal Transitions and Chain Dynamics

Although the crystalline structure of PPTA is commonly accepted, there is considerate controversy regarding the chain motion. Solid-state NMR investigations have been made on the chain dynamics of PPTA.[45-50] Their results showed a fraction of the terephthalamide rings are able to flip and there is large degree of dynamic heterogeneity. A bimodal model was taken in the temperature range of 23 to 121°C. It is believed that the low temperature regime corresponds to the dynamics of the crystalline surface, while the high temperature regime is dominated by the dynamics of the crystallite interior. Different thermal analysis tools were also used to detect possible transitions and relaxations. The evaporation of absorbed water was seen by both DSC and TGA measurements.[51] A change in the slope of the linear thermal expansion versus temperature at 115°C was revealed by TMA measurements and assigned to the release of water.[51] Jaffe and Jones reported a T_g of 360°C and T_m of 560°C from DSC measurements.[52] DMTA measurements were attempted for low-crystallinity and low-orientation PPTA fibers.[53] Two main tanδ peaks were recorded: an α relaxation at 460°C and a β relaxation at 60°C. The 60°C peak was assigned to the motion of amide groups in the amorphous regions, because of the strong effect of the moisture content in the fiber. The activation energy for the α relaxation is 766 kJ/mol. There are two additional peaks for annealed samples at 270 and 170°C, and their origin is not clear.

1.2.1.4 Thermal Treatment

The thermal treatment of coagulated fibres is of particular interest because more desirable properties can be developed through post treatment. There are several different types of Kevlar® fibers, and their treatment conditions are well kept secrets. Wu et al. [54] has studied the crystal structure change of PPTA fiber under different annealing conditions. The annealing temperature ranged from 380°C to 480°C at either no-tension or constant-tension modes. X-ray diffraction of the treated fibers was measured and all the analysis was based on the diffraction of (006) plane. They proposed a residual-stress free *c*-dimension. Then, an increase in the *c*-axis dimension was observed for all modes. The higher the tension, the bigger the increment is; and the higher the annealing temperature, the smaller the increment. The apparent crystal size along *c*-axis increases with the annealing temperature under no-tension annealing and decreases with the applied tension under constant-tension annealing. The degree of orientation decreases with the annealing temperature under no-tension annealing and increases with applied tension under constant-tension annealing.

It was reported that the fiber tenacity does not change much at low and intermediate temperatures for short time annealing but drops when the temperature exceeds 450°C and degradation occurs.[32] Several hours of exposure to high temperatures deteriorates the strength but does not significantly affect the modulus.[55] The crystallites grow laterally along the *b*-axis upon thermal annealing.[56]

1.2.1.5 The Influence of Water

Another important structural aspect of PPTA is its water sensitivity. Kevlar® 29 fiber has a moisture content of 7%. Knoff showed the effect of water on lateral compressive properties.[57] It is believed that two types of moisture exist: a loosely bound water and a tightly bound water within the crystal lattice. The activation energy for desorption of the loosely bound

water is 6 kcal/mol and for the tightly bound water is 40 kcal/mol. The tightly bound water desorbs at a temperature above 350°C.[3] The presence of water may affect the local symmetry of the terephthalamide rings.[58] Fukuda and Kawai evaluated the structure change with moisture sorption at ambient temperature using wide-angle x-ray diffraction.[59] Dehydration and readsorption were done on the as-spun wet PPTA yarn and x-ray measurements were performed for different conditioned samples. The unit cell dimensions do not change with the moisture content. However, the intensity of (110) diffraction peak changes with the water sorption. Their results suggested the growth of the crystallite via hydrogen bonds in the *b*-axis direction and also *c*-axis direction during desorption. (Figure 1.2)

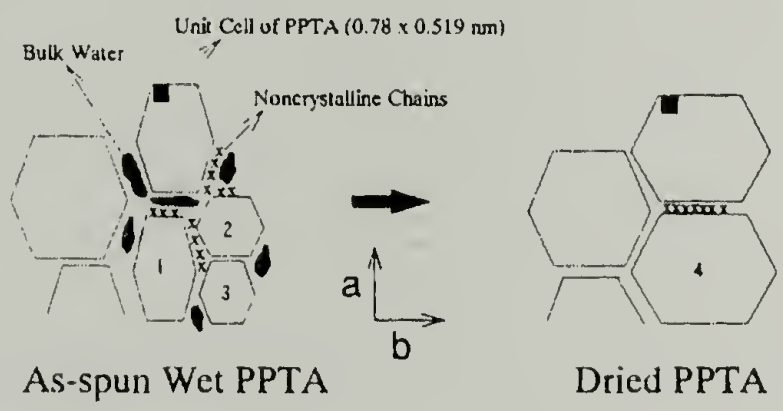

Figure 1.2 Crystal growth under thermal annealing and/or water desorption[59]

1.2.1.6 Deformation and Mechanics

PPTA fiber, as a high performance material, possesses high strength, high modulus and low failure strain. As a structural material, its deformation is of particular significance. Many studies have been done on creep[60-64], relaxation[65], fatigue[63,66-71], tensile deformation and failure[72-78] of the fiber.

Upon stretching, the deformation response of Kevlar® fiber is roughly linear. There is no yielding before fracture. By differentiating the stress strain curve, Allen showed a subtle nonlinearity.[73] Its nonlinear viscoelasticity can be described by a shape-invariant relaxation function.[65] The fiber shows almost no irreversible deformation when the maximum strain is

smaller than 0.5%. Further straining induces irreversible deformation.[60,62,79] The modulus increases with the strain and a reorientation process is observed during deformation.[60,62,79] Allen attributed the modulus change to the shear coupling effect from opening the pleat structure. An asymptotic modulus obtained from perturbation tests is believed to be more characteristic than the initial modulus. The asymptotic modulus can be correlated well with the tensile strength of the fibers using a shear failure criterion. The strength of the fiber is then determined by the inherent strength anisotropy of polymer chains and orientation of the fibers.[73,74] The deformation of PPTA was also extensively studied using Raman Spectroscopy.[75,77,78,80-83] A band position shift and band width change were observed when stress was applied to the fiber. The band position shifts are due to the stretching of the chain. The bandwidth is believed to reflect the stress distribution in the fiber and may be related to the fiber strength. The result supports the one-phase paracrystalline model.

Two fatigue modes, tension and compressive, have been studied. The compressive fatigue tests were carried out through filament flex life tests. The Kevlar® fibers does not exhibit strength loss in the first few cycles and then gradually decline afterwards. The modulus was reduced and fiber kinking was observed after the fiber was compressed beyond 0.57% strain.[66,67] Under tension fatigue condition, Lafitte and Bunsell found that both the maximum applied load and the load amplitude adversely affect the lifetime of a fiber.[84] The time to rupture under cyclic loading may be longer or shorter than the time to rupture under steady load at the cyclic maximum load level. The longer lifetime indicates a failure mechanism of creep and the shorter lifetime indicates a failure mechanism of accelerating fatigue. The fracture morphologies under tensile, creep and fatigue conditions are indistinguishable due to the splitting of the structure.[63,84] Considerable scatter in the mechanical behavior of single filaments prohibited a clear lifetime rule to be deduced.

1.2.2 Other Fibers Investigated

1.2.2.1 Vectran® Fiber

Vectran® is the only commercial fiber made from thermotropic liquid crystal polymer. Vectran® was first introduced by Hoechst-Celanese in 1988. It is a copolyester containing HBA/HNA 73/27. Kurary in Japan developed a heat-strengtheded form of Vectran® called Vectran® HT and Vectran® UM. It is said that Vectran® HT has superior abrasion and creep resistance, chemical resistance and low moisture absorption, but the cost of production is very expensive and its high temperature properties are inferior to Kevlar®. It has been used in fishing nets, industrial rope, cord, heating elements and optical fibers, protective clothing and sports goods.

Although there have been extensive studies on the thermal behavior and structure of Vectran® fiber, controversy appears in the results from different researchers. Thermal studies of Vectran® show three relaxations, with a α relaxation in the temperature range of 110-125°C.[85] Since Vectran® is a copolymer, its sequence has been studied using NMR and X-ray. While random distribution was observed for the material made from melt acetolysis, there is less disagreement about the sequence change upon heat treatment. The DSC spectrum of Vectran® shows a glass transition at100 °C and two melting peaks in the range of 200-280 °C.[86] The reason for two melting peaks is not clear. X-ray study did not show two different crystal forms, which may correspond to the two melting peaks. Upon heat treatment, a new DSC melting peak appears at 345 °C, which was attributed by Schmach and Vogel as evidence of transesterification. However, X-ray analysis indicates no change in comonomer sequencing but a hexagonal-to-orthorhombic lattice transition on heat treatment. X-ray indicates that heat strengthening only improve the lateral ordering but no major effect on longitudinal order. Erdemir et al.[87] proposed to use paracrystallinity to describe the quasi-three-dimensional order.

1.2.2.2 Technora® Fiber

Technora®, manufactured by Teijin, is a different kind of high performance fiber in term of processing. This fiber is made from a copolymer of para-phenylenediamine and 3,4-oxydianiline with terephthaloyl chloride. The synthesis, properties and structure were discussed by Ozawa and Matsuda.[88] The polymer is spun from isotropic solution in NMP, which is different from other rigid rod polymer chain fibers that are made from liquid crystal states. The copolymer structure with enhanced chain flexibility enables the fiber to be ''super-drawn'' at very high temperatures (greater than 495 °C). This super-drawing yields a well-oriented but less crystalline fiber than PPTA. Tensile properties are very good. Technora® is believed to have higher abrasion resistance and substantially higher hydrolytic stability than PPTA fibers. This stability is ascribed to the structure. The Technora® fiber less porous or permeable to water than PPTA. The fiber has a non-fibrous type of structure, which is different from PPTA fiber. Paracrystalline structure is also reported for Technora®.[35]

1.2.2.3 Spectra® Fiber

The tensile properties of this polyethylene fiber are comparable to those of PPTA. Its impact strength is reported to be higher than PPTA fiber.[89]

Smith and Lemstra showed that the Young's modulus of UHMPE fiber increases linearly with the draw ratio.[90] A structure model was developed from entanglement concepts by Grubb[91]. It is shown that the fiber with a draw ratio of 6 has a shish-kebab morphology and the fiber with a draw ratio of 80 has a fibrillar structure. The fully drawn fiber has a crystallinity of 93%. DSC of a low draw ratio (less than 36) shows three peaks.[92] A peak at 130 °C was assigned to the melting of folded chains. This peak disappears at higher draw ratio. A peak at 140 °C was attributed to the orthohomic-to-hexagonal phase transition, and the peak at ~ 150 °C was due to

melting of the hexagonal crystals. The DSC of unconstrained and constrained fibers was discussed.

Although the low cost of polyethylene is one of the main advantages for this development, the special processing of the fiber is very costly. In addition, the application of polyethylene fiber is ultimately limited by a low use temperature. The melting point of PE is around 150 °C. Thermal analysis shows a α relaxation around 90 °C, where the fiber starts to lose integrity. In addition, the creep of UHMPE fibers is more severe than rigid structure fibers. Its fatigue properties are even worse.[93,94] Its modulus decreases with time, which may be due to relaxation. The dynamics of the polyethylene chain has been extensively studied using DMTA[95] and solid state NMR[96]. The creep of PE is believed to undergo a α relaxation mechanism, which is a chain jumping and chain-chain slippage within the crystalline region.[95] Therefore, short branches are introduced into the main chain to increase the interchain interaction, which prevents chain slippage and improve the fiber creep resistance.[97]

1.3 Objectives and Motivation

In the use of a material, many times the material fails although the applied load is lower than the material strength. High performance polymeric fibers are newly developed materials and finds use as structural components. Thus, it is important to understand the fracture of these fibers. This dissertation aims to address questions regarding the failure criteria, deformation and failure mechanisms, the factors governing material lifetime, and the role of anisotropy and chain motions in high performance fibers. One objective of this research is to non-destructively examine a used fiber yarn, whose history of loading and temperature is unknown, and to predict the fiber's remaining lifetime. The research results should help to design and produce better materials.

Controlled and tailored properties are always desired for material. This can only be achieved through better understanding of the structure-property relationship. As for high performance fibers, this kind of research is limited. There is considerable controversy in the literature regarding deformation mechanisms, thermal properties, chain motions and structure-property correlation of high performance fibers. This is the starting point for this research.

One goal of this research is to create a better understanding of structure-property relationship of high performance fibers. The way to conduct the research is to stimulate the fibers with different external fields. These stimulations include exposing the fibers to long time oscillating load, long time constant load, twisting, different temperatures, high hydrostatic pressure, pressurized water and steam. The property and structural evolution with these stimulations were investigated. The experimental results helped to correlate the macroscopic properties with the microscopic structure of fibers. The information generated shall be conducive to the development of new materials.

1.4 Dissertation Overview

This dissertation is mainly about the long-term mechanical behavior and the structure-property relation of high performance polymeric fibers. The research work includes; 1- cyclic controlled stress fatigue and creep studies, 2- the mechanics of twisted yarns, 3- determining measures that would indicate the thermal and stress history of Kevlar® fibers, 4- characterizing the evolution of properties and structure resulting from external post-treatment stimulations, e.g. heat, tension and pressure, and 5- the overall structure-property relations in Kevlar® fibers. This research demonstrates the important influence of the anisotropic nature of the polymer chain on properties not normally considered to be sensitive to anisotropy. This research also provides an understanding of the difference between the fatigue behavior of high performance fibers and

conventional materials, as well as the processing-structure-property relation in Kevlar® fibers to control and achieve better performance.

A general overview of high performance fibers is given in Chapter 1. General information about high performance fibers is provided. The background related to the fibers investigated in this dissertation, such as Kevlar®, Vectran®, Technora® and Spectra®, is discussed.

Chapter 2 presents the general characterization of the studied high performance polymeric fibers. It includes the mechanical, thermal and structure characterization. The information was used in the subsequent studies on specific topics.

The study of fatigue and creep of high performance polymeric fibers is discussed in Chapter 3. This research has for the first time led to a systematic study of the creep and fatigue behavior of various high performance fibers. In this study, repeatable lifetimes for various fibers have led to a general lifetime equation to correlate the material lifetime with the applied stress level. The failure criterion of "*critical strain*" was identified. The failure and creep mechanism was also studied. The deformation of fatigue and creep were investigated. The fatigue lifetime was predicted from known material constants. Several material parameters were defined to characterize the fatigue and creep properties and the fatigue resistance of different fibers is compared.

During the fatigue study, it was found that twisting in yarns has a tremendous influence on their fatigue properties. As a result, the research was extended to include the mechanics of twist yarn and is the subject of Chapter 4. The influence of twisting on different yarn properties was studied and a model based on composite theory was used to predict the change in the yarn modulus with the degree of twist. This model gives much better prediction than previous models and includes for the first time the anisotropic nature of the fiber on the mechanics of twist yarn.

The desire for nondestructive predictions of the residual lifetime of a used material initiated our efforts to find a signature of the stress and thermal history in Kevlar® fibers. To achieve this, a new testing methodology has been developed, an iso-strain force-temperature test (IFTT), which yields quantitative information on the stress and thermal history exposure. Chapter 5 describes the results of our IFTT study of polymeric materials. The IFTT behavior of a Kevlar® fiber maps well with the structure examined by X-ray diffraction. The IFTT also provides abundant information about the relaxations and thermal transitions. It is shown that this is a general thermal mechanical method that helps to gain detail understanding of material properties. The IFTT was also used to screen the processing for property enhancement via post-treatment. This research has succeeded in increasing the modulus of Kevlar® 29 by 1.8 times.

Chapter 6 presents the results of post-treatment of PPTA fiber. Different post-treatment routes have been investigated. These post-treatments were not only designed to make better material but also to obtain materials with various properties to investigate their structure-property relation. Tension, heat, hydrostatic pressure, and different media of water, mercury and silicon oil have been utilized to alter the materials properties.

The PPTA fibers with a wide range of properties and structure produced through post-treatment as discussed in Chapter 6 facilitated the study of structure-property relation. A new structure property relation is presented in Chapter 7 between the unit cell dimension and the paracrystalline parameter. A new structure model of PPTA is also described.

CHAPTER 2

GENERAL CHARACTERIZATION OF HIGH PERFORMANCE FIBERS

2.1 Abstract

This chapter summarizes the general structure and properties of the high performance fibers investigated. The information forms a basis to study other specific topics in the following chapters. The mechanical and thermal properties and the crystal structure of these fibers were studied. For mechanical properties, the torsion shear modulus, the bulk modulus, and the volumetric thermal expansion coefficient and Poisson's ratio, which are rarely reported for these fibers, were investigated. For the first time, the DMTA study of single filaments of Technora® and Kevlar® was conducted. Our DSC study of Kevlar® fiber indicates different thermal properties from that reported.

2.2 Experimental

2.2.1 Materials

Commercial fiber yarns of Kevlar®29, Kevlar®119, Kevlar®49, Kevlar®149(DuPont, USA), Vectran® HS (Hoechst Celanese, USA), Technora® (Teijin, Japan), Spectra® 900 (Allied Signal, USA) were used in the studies of this dissertation. All of these samples possess typical properties of high performance fibers with high stiffness, high tenacity and a low elongation to break.

Kevlar® (DuPont)

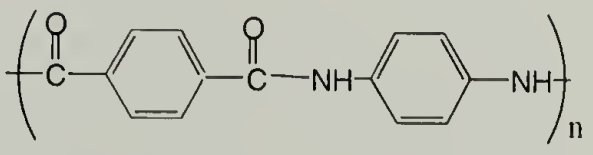

Vectran® (Hoechst Calanese)

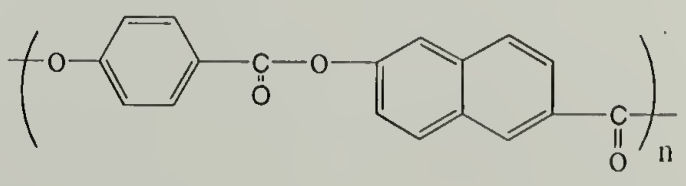

Technora® (Teijin)

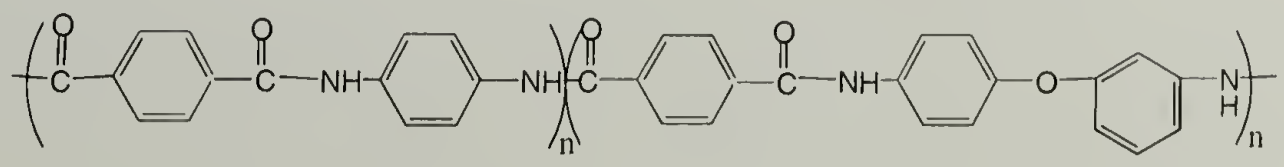

Nomex® (DuPont)

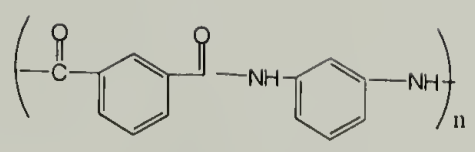

Spectra® (Allied Signal)

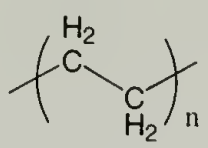

Different fibers were supplied in the form of yarns. The characterization of fibers was done either using single filaments or yarns. Except for mechanical tests, where as-received fibers were used, yarns were first rinsed with acetone to remove the finish and then dried at room temperature under vacuum before other measurements.

2.2.2 General Characterization

2.2.2.1 Diameter of fibers

Two methods were used to measure the diameter of fibers. One is to calculate the fiber diameter from the linear density and volumetric density. The linear density of single filaments was measured using a vibroscope. Usually two units are used for linear density. A denier is the mass of a fiber in grams with a length of 9000 m and a dtex is the mass of a fiber with a length of 10000 m. Volumetric density was measured by a density gradient column using the solvent system of n-heptane-carbon tetrachloride, whose density was calibrated by density standards. The second method was to measure the diameter using an Olympus BH-2 optical microscope.

2.2.2.2 Tensile Properties

Tensile testing of single filaments and yarns was performed using an Instron model 5564 testing machine. All of the tests were performed at standard conditions of 21 °C (± 1 °C) and 65% (± 2%) relative humidity. Pneumatic yarn/cord grips were used for the tests, with the effective gauge length set at 150 mm and a strain rate of 10%/min.

2.2.2.3 Bulk Modulus

Bulk Modulus was measured using a Gnomix® P-V-T apparatus. The compressibility was measured by the change in volume with the pressure at constant temperature,

$$\kappa = -\frac{1}{V_0}\left(\frac{\partial V}{\partial P}\right)_T$$

Equation 2.1

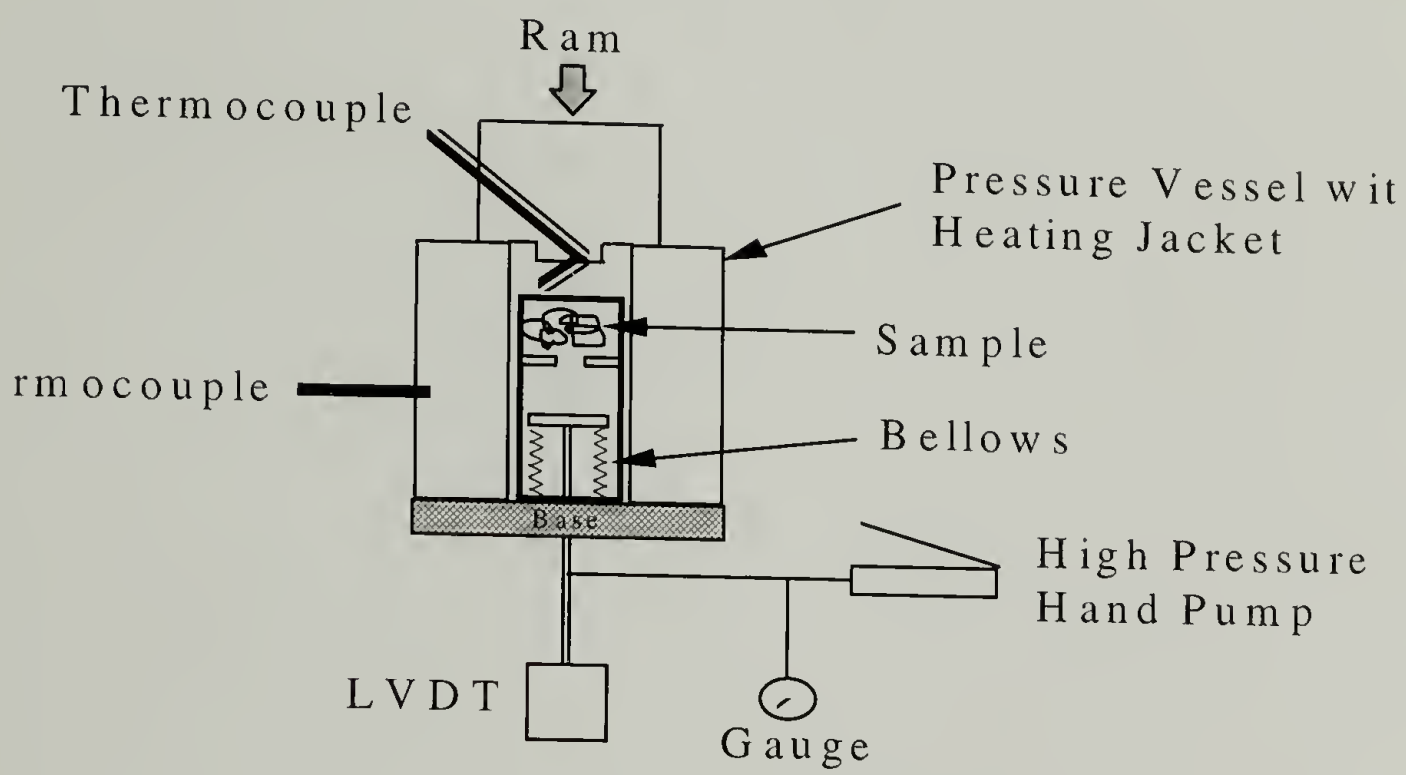

Figure 2.1 The schematic description of the P-V-T apparatus.[98]

This Gnomix P-V-T setup can also be used to measure the volumetric thermal expansion coefficient and density at a specific temperature (reference density must be known). The hardware parameters are as follows:

temperature range: 30 °C – 350 °C with the precision of 0.5 °C;

pressure range: atmosphere – 200 MPa (29 kpsi), with the precision of 0.25 MPa; and

specific volume change: 0.0001-0.6 cm^3/g with the precision of 0.0001 cm^3/g

It requires a minimum weight of 0.5 g, but a sample size of 1-2 g is preferred. The cell dimension is a cylindrical shape with ~ 2 cm in length and 1 cm in diameter.

2.2.2.4 Shear Modulus

Shear modulus was measured by torsion pendulum:

$$G = \frac{8\pi I_d l}{r^4 \tau^2}$$

Equation 2.2

Where I_d is the moment of inertia of the pendulum disc, which is 50.3 g.mm^2 in our measurement, l is the fiber length, r is the radius of the fiber and τ is the period of oscillation.

2.2.2.5 Poisson's Ratio

Pressure dilatometry was used for the measurement of Poisson's ratio of film.[99] It can also be used to measure the Poisson's ratio of fibers. When only the axial tension and hydrostatic tension are applied, the constitutive equation, Equation 2.8, can be simply expressed as:

$$\begin{pmatrix} \varepsilon_1 \\ \varepsilon_2 \\ \varepsilon_3 \end{pmatrix} = \begin{pmatrix} \frac{1}{E_1} & -\frac{\nu_{12}}{E_1} & -\frac{\nu_{13}}{E_1} \\ -\frac{\nu_{12}}{E_1} & \frac{1}{E_2} & -\frac{\nu_{23}}{E_2} \\ -\frac{\nu_{13}}{E_1} & -\frac{\nu_{23}}{E_2} & \frac{1}{E_3} \end{pmatrix} \begin{pmatrix} \sigma - P \\ -P \\ -P \end{pmatrix}$$

Equation 2.3

where, *1* is the axial direction and *2,3* are the transverse directions of fiber.

From which, the following is derived:

$$\varepsilon_1 \cdot E_1 = \sigma + P(\nu_{12} + \nu_{13} - 1)$$

Equation 2.4

When transverse isotropy is assumed for fiber,

$$\nu_{12} = \frac{1}{2} \cdot (1 - \frac{\partial \sigma}{\partial P}\Big|_{\varepsilon_1})$$

Equation 2.5

2.2.2.6 X-ray Diffraction

Wide-angle X-ray diffraction is the main tool used to study the structure of high performance fibers in this dissertation. This part of the experimental description only covers what is related to the results in this chapter. More detailed descriptions of methods and calculation will be described in Chapter 7.

X-ray diffractometry (Simens D-500) and Simens 2D area detector were used. Two kinds of specimens were tested: single filaments and bundled samples. The bundled sample was prepared by aligning 1000 filaments under slight tension and then confining them between two polyimide films. The average bundle thickness is 68 micron and the width is 2 mm.

WAXD measurements were carried out using filtered Cu-K_α radiation of 1.5418 Å wavelength beam generated at 40 KV and 30 mA. The diffracted intensity distribution as a function of Bragg angle 2θ was first corrected for background, polarization, Lorentz and adsorption factors, and then the contribution of the background was subtracted.

Polarization factor P is $P = 1/2(1+\cos^2 2\theta)$

Lorentz factor L is $L = \dfrac{1}{\sin\theta\cos\theta}$

Adsorption factor is $A = \dfrac{\exp(\mu t(1-\sec 2\theta) - 1}{\mu t(1-\sec 2\theta)}$ (normal-beam transmission)

$$A = \frac{\sec\theta}{\exp(-\mu t(1-\sec\theta))} \text{ (symmetrical transmission)}$$

where t is thickness, μ is linear absorption coefficient.

The linear absorption coefficient of PPTA for CuK_α can be calculated as follows:

Mass absorption coefficient:

$$\frac{\mu}{\rho} = \sum_i \omega_i (\frac{\mu}{\rho})_i$$

The chemical composition of PPTA: $C_{14}H_{10}N_2O_2$

Molecular weight: $\Sigma n_i A_i = 238$

Density (g/cm^3): 1.48 (crystalline)

Atom	n	A	μ/ρ (cm^2/g)	n_iA_i	ω_i	$\omega_i(\mu/\rho)_i$
Carbon	14.000	12.011	4.600	168.154	0.706	3.247
Hydrogen	10.000	1.008	0.435	10.080	0.042	0.018
Nitrogen	2.000	14.008	7.520	28.016	0.118	0.884
Oxygen	2.000	16.000	11.500	32.000	0.134	1.545
				238.250	1.000	5.694

Mass absorption coefficient (cm^2/g): 5.694

Linear absorption coefficient (cm^{-1}): 5.694*1.48=8.43

Therefore, the linear absorption coefficient of PPTA is 8.43.

The angle and the instrumental broadening were calibrated using a standard Corundum sample of 1μm for the diffractometer. A diffraction scan of Al_2O_3 crystal is shown in Figure 2.2, where a slit of 0.1° was used. The scan was first curve fitted using Voigt's function and then the width at half intensity maximum was calculated.

In most diffractometer measurements in our study, the slit width of 0.3° was chosen for intensity and resolution reason. The full width at half maximum (FWHM) of the instrument is then 0.33°.

Equatorial scan was performed at a normal-beam transmission mode and meridional scan was done at a $\theta/2\theta$, symmetrical transmission mode.

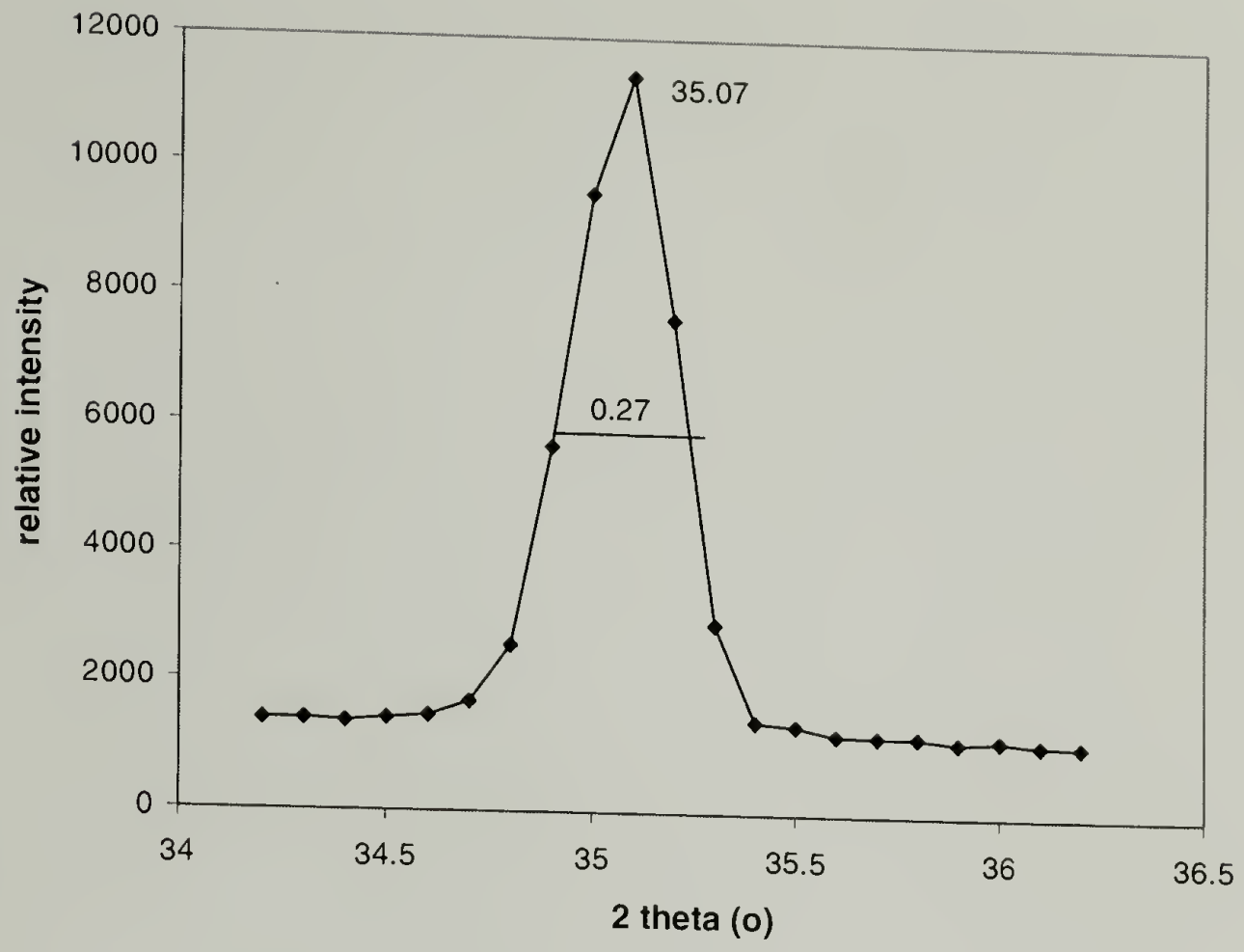

Figure 2.2 Diffraction scan of a standard Corundum sample (Al_2O_3), with particle size of 1 μm.

An important indication of the perfection of crystals—apparent crystal size—was calculated using the Scherrer Equation:

$$L_{hkl} = \frac{K\lambda}{\beta_0 \cos\theta}$$

Equation 2.6

Where L_{hkl} is the mean dimension of the crystallites perpendicular to the planes (hkl), β_0 is the breadth at half intensity maximum, and K is a constant. K was chosen as unity in our calculation. β_0 was corrected by the instrumental broadening using the following expression:

$$\beta_0 = \sqrt{(\beta^2 - d^2)}$$

Equation 2.7

Where β is the measured FWHM and d is the instrumental broadening.

2.2.2.7 DMTA

Dynamic Mechanical Thermal Analysis helps to identify the relaxations in the material, which is often related to the processing and end-use properties of the material.

Rheometric Mark IV was used in our study. Tensional modes were adopted to study single filaments. An oscillating strain of 0.3% and heating rate of 5 °C/min were used unless otherwise specified.

2.2.2.8 DSC

Differential Scanning Calorimeter was used to study the thermal transitions in the material. A TA Instruments DSC 2910 with a sample size of around 10 mg and heating rate of 10 °C/min was used.

2.2.2.9 TGA

Thermalgravimetry Analysis (TGA) was used to analyze the residual solvent and thermal stability of the material. A TA Instrument TGA 2950 with a sample size of about 10 mg and heating rate of 20 °C/min was used.

2.2.2.10 Morphology Characterization

Fracture topography was studied using an optical microscope (Olympus BH-2) and a scanning electron microscope (Jeol JSM- 35CF). For the SEM studies, the fracture surfaces were coated with gold while the sample was rotated in vacuum.

2.3 Results and Discussions

Figures and tables in this chapter summarize the general properties of high performance fibers studied in this dissertation. This general characterization provides a basis for the study of specific topics related to high performance fibers, which will be discussed in the following chapters in detail.

One characteristic of these high performance fibers is their high anisotropy. Different from isotropic materials, the following constitutive equation (Equation 2.8) is needed to represent the relation between the strain and stress. Therefore, nine constants are needed to characterize the elasticity of the material and three constants for the thermal expansion. If transverse isotropy is assumed, the nine constants for elasticity can be reduced to five and two constants are needed for thermal expansion.

$$\begin{bmatrix} \varepsilon_1 - \alpha_1 \Delta T \\ \varepsilon_2 - \alpha_2 \Delta T \\ \varepsilon_3 - \alpha_3 \Delta T \\ 2\varepsilon_4 \\ 2\varepsilon_5 \\ 2\varepsilon_6 \end{bmatrix} = \begin{bmatrix} C_{11} & C_{12} & C_{13} & 0 & 0 & 0 \\ C_{21} & C_{22} & C_{23} & 0 & 0 & 0 \\ C_{31} & C_{32} & C_{33} & 0 & 0 & 0 \\ 0 & 0 & 0 & C_{44} & 0 & 0 \\ 0 & 0 & 0 & 0 & C_{55} & 0 \\ 0 & 0 & 0 & 0 & 0 & C_{66} \end{bmatrix} \begin{bmatrix} \sigma_1 \\ \sigma_2 \\ \sigma_3 \\ \sigma_4 \\ \sigma_5 \\ \sigma_6 \end{bmatrix}$$

Equation 2.8

Where, ε is the strain, σ is the stress and ΔT is the temperature difference, C is the compliance and α is the thermal expansion coefficient. The fiber axis is direction of 1 and the transverse isotropy of directions of 2 and 3 is assumed. The relation between Cs and conventional defined moduli, E and G, and the possion's ratio, ν, is listed as follows.

$$C_{11} = 1/E_{11} \qquad C_{44} = 1/G_{12} \qquad C_{12} = C_{21} = -\nu_{12}/E_{11} = -\nu_{21}/E_{22}$$
$$C_{22} = C_{33} = 1/E_{22} \qquad C_{55} = 1/G_{13} \qquad C_{13} = C_{31} = -\nu_{13}/E_{11} = -\nu_{31}/E_{33}$$

2.3.1 Mechanical Properties

Table 2.1 and Table 2.2 list the mechanical properties of yarns and single filaments of several high performance fibers. All these materials show a high Young's modulus in the tens of GPa and high tensile strength of several GPa. The strain to break is lower for these materials compared to conventional fibers such as Nylon and Polyester. The comparative in values of one property for different fibers is the same for yarn or single filaments; however, the absolute values

of Young's modulus, tenacity, and elongation to break of single filaments are usually higher than those of yarns. In addition, the variation of the properties is much narrower in yarn than in single

Table 2.1 Mechanical properties of different fiber yarns

Sample		VECTRAN	TECHNORA	SPECTRA	KELVAR	KEVLAR	KEVLAR	KEVLAR	Nomex
	Type	Heat Stretched		900	29	119	49	149	
	Manufacturer	Hoechet Caleanese	Teijin	Allied Signal	DuPont	DuPont	DuPont	DuPont	DuPont
Linear Density (dtex)	mean	1717	1663	1330	1670	1630	1582	1570	1774
	σ	6	11	10	5	2	1	3	11
	CV%	0.3	0.7	0.8	0.3	0.1	0.1	0.2	0.7
	min.	1710.2	1643.8	1322.2	1660	1627.4	1581.1	1566	1756
	max.	1724.1	1672.9	1346.9	1677	1632.3	1583.8	1574.1	1784
	median	1718	1665.4	1328.33	1670	1629	1581.9	1570	1779
Modulus (GPa)	mean	80.0	79.5	68.0	82.8	63.6	125.1	164.3	15.8
	σ	0.9	1.1	0.7	1.4	0.8	1.0	1.9	0.17
	CV%	1.1	1.3	1.1	1.6	1.2	0.7	1.2	1.1
	min.	78.7	77.1	0.5	80.7	62.4	123.6	159.9	15.4
	max.	81.6	81.1	66.4	84.9	65.3	127.3	167.2	16
	median	80.0	79.7	69.1	83.4	63.5	124.9	164.5	15.8
Tenacity (GPa)	mean	2.98	3.22	2.34	2.48	2.96	2.40	2.15	0.75
	σ	0.06	0.10	0.07	0.05	0.05	0.08	0.05	0.004
	CV%	1.9	3	2.8	1.8	1.7	3.5	2.5	0.5
	min.	2.89	3.05	2.22	2.40	2.87	2.25	2.00	0.74
	max.	3.11	3.42	2.42	2.56	3.05	2.54	2.22	0.75
	median	3.00	3.20	2.35	2.49	2.98	2.4	2.15	0.75
Elongation at break (%)	mean	3.23	4.51	4.55	3.13	4.09	2.00	1.46	19
	σ	0.04	0.12	0.11	0.09	0.05	0.06	0.03	0.7
	CV%	1.2	2.7	2.3	2.7	1.3	3.1	2.1	3.4
	min.	3.13	4.26	4.33	3.00	4.01	1.87	1.39	18
	max.	3.25	4.78	4.71	3.30	4.20	2.10	1.51	20.5
	median	3.23	4.52	4.53	3.13	4.11	1.99	1.46	18.8
Energy to brk. point (J)	mean	1.17	1.76	1.59	0.95	1.27	0.51	0.36	2.94
	σ	0.02	0.09	0.08	0.03	0.04	0.03	0.01	0.08
	CV%	1.70	5.20	5.30	3.20	2.90	6.70	4.10	2.6
	min.	1.14	1.61	1.46	0.89	1.20	0.45	0.32	2.8
	max.	1.21	1.96	1.71	1.01	1.33	0.56	0.38	3.1
	median	1.17	1.75	1.58	0.95	1.27	0.51	0.36	2.9
Fiber	Density(g/cc)	1.40	1.39	0.98	1.44	1.44	1.45	1.47	
Number of specimens		20	20	20	20	20	20	20	20

CV%=(STDEV/mean)*100

filaments. The transformation of the filament property to a yarn property is a research topic that has interested many researchers. Our results in high performance fibers are consistent with a well accepted "Weak-link theory" in conventional fibers.[100,101] Several properties less reported for fibers are listed in Table 2.2, such as torsion shear modulus, bulk modulus and volumetric thermal expansion coefficient, and will be used in later studies. The diameter of the single filament is difficult to test and the error in the measurement of diameter contributes partly to the property differences between yarns and single filaments. The shape of the cross-section of these

high performance fibers is round except that of Spectra® and Nomex® when observed using optical microscope.

Table 2.2 Mechanical properties of single filaments

Sample	Type	KELVAR 29	KEVLAR 119	KEVLAR 49	KEVLAR 149	Nomex	VECTRAN Heat Stretched	TECHNORA	SPECTRA 900
	Manufacturer	DuPont	DuPont	DuPont	DuPont	DuPont	Hoechet Caleanese	Teijin	Allied Signal
Linear density (dtex)	mean	1.7	1.7	1.7	1.5	3.1	5.6	1.7	9.5
	CV%	3	3	3	4	5	5	3	2
Fiber Diameter (μm)	mean	13	13	13	13	14–24	22	13	33-38
	CV%	3	3	3	3		5	3	
Young's Modulus (GPa)	mean	88	72	118	153		81	80	48
	CV%	5	5	5	4		5	5	10
Torsional Shear Modulus(GPa)	**mean**	**1.82**	**1.55**	**1.48**	**1.30**	**0.91**	**0.65**		**0.73**
	CV%	**10**	**10**	**10**	**10**	**20**	**3**		**20**
Bulk Modulus(GPa)	**mean**	**9.6**		**9.45**	**10.50**				
	CV%	**2**		**3**	**2**				
Tenacity (GPa)	mean	2.92	3.21	3.04	2.27		3.60	3.38	2.93
	CV%	8	7	7	8		9	7	8
Elongation at break(%)	mean	3.38	4.14	2.64	1.48		3.66	4.34	4.55
	CV%	7	6	11	8		7	3	2
Volumetric Thermal Expansion Coefficient (ppm/°C)		**202**							
Fiber Density(g/cc)		1.44	1.44	1.45	1.47		1.40	1.39	0.98
Number of specimens*		50	50	50	50	50	50	50	50

* specimen number does not apply to the measurements of torsional shear modulus, bulk modulus and volumetric thermal expansion coefficient.

2.3.2 Thermal Properties

As expected, DSC of high performance fibers does not yield much information about their glass transitions because of the high orientation or crystalline nature of these fibers. (Figure 2.3) Two peaks appear in the DSC trace of Vectran® HS, which involve only a small amount of heat. The appearance of these two peaks might be due to crystal-crystal transformation. These two temperatures are much higher than those reported for Vectra®, which is not a fiber form. [86] The oriented chain and its tendency for deorientation upon heating in fibers might cause the increase in transition temperatures and also explain the small amount of heat associated.

Spectra® 900 appears to be highly crystalline and the crystallinity is about 94% according to the enthalpy of melting measured by DSC. (Figure 2.3) A melting temperature at 149 °C limits the use temperature of this fiber. Sometimes a shoulder appears after the

preliminary melting peak, which indicates an orthohombic-to-hexangonal transition in PE. The melting of Kevlar® and Technora® is higher than the maximum test temperature and is believed to be higher than their decomposition temperature. The peak appearing in the DSC diagrams of Kevlar® and Technora® around 100 °C ties to the residual water in these fibers. These peaks disappear in a second heating. Because of the existence of hydrophilic groups along the chain, the water used during fiber spinning can not be totally removed. Even after the fiber has been dried in vacuum, it regains the water upon atmosphere exposure.

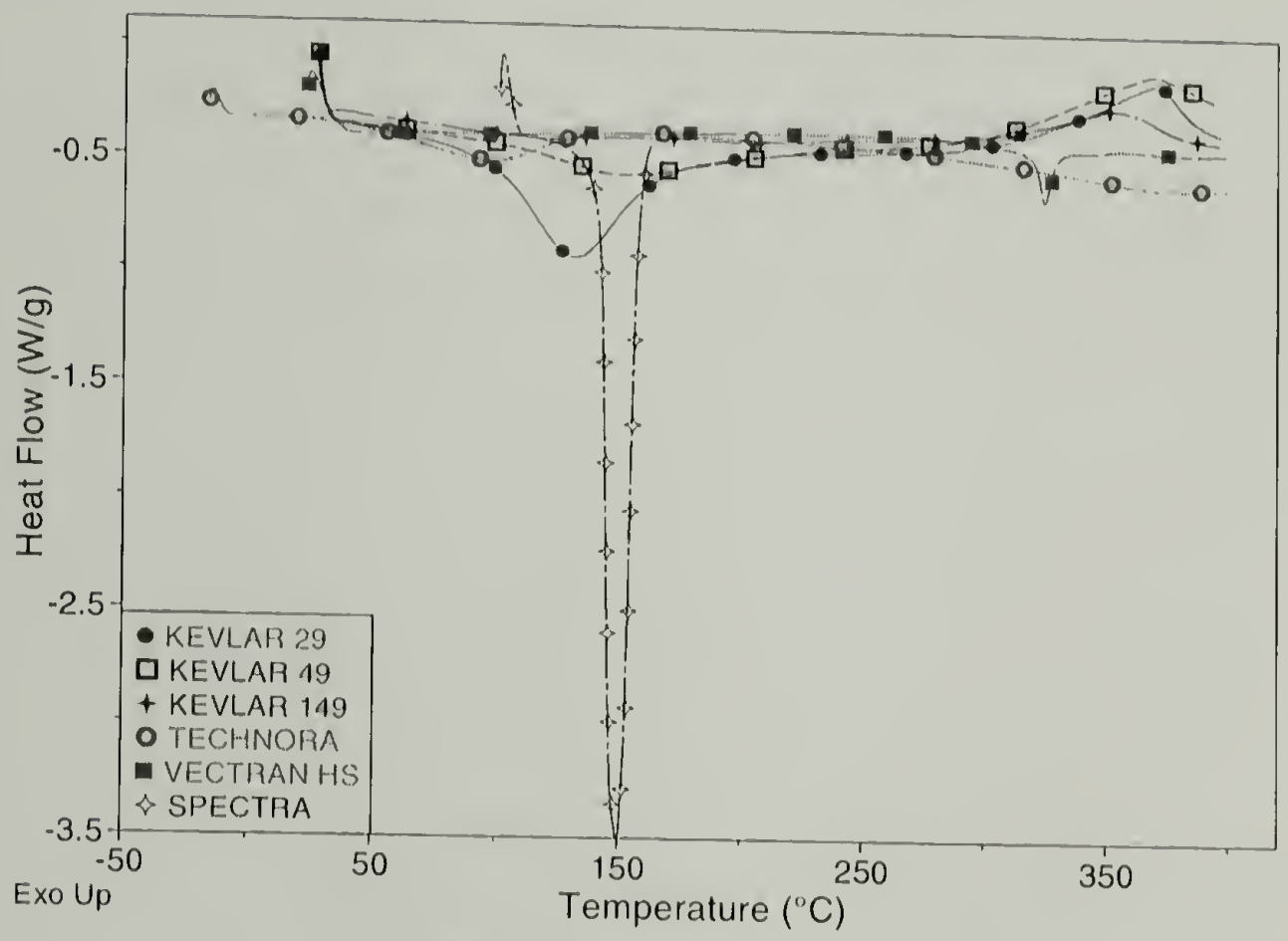

material	peak temperature (°C)	heat (J/g)
spectra®900	149	-254
Vectran® HS	317	-7
Vectran® HS	335	-0.5
Kevlar® 29	131	-90
Technora®	96	-52

Figure 2.3 DSC Spectra® of different fibers; the table lists peak temperature and corresponding heat

The peak temperature for water evaporation in Technora® is lower than that in Kevlar®. It is well know that Technora® lacks the three-dimensional order, which is found in Kevlar®.[35] Therefore, the water in Technora® appears more loosely connected with the structure than with Kevlar®. The amount of water in the material can be calculated based on the heat released. It varies slightly from sample to sample. There is about 8% water in Kevlar® 29 and 5% water in Technora®. No other thermal transitions in Technora® were detected by DCS other than the evaporation of water.

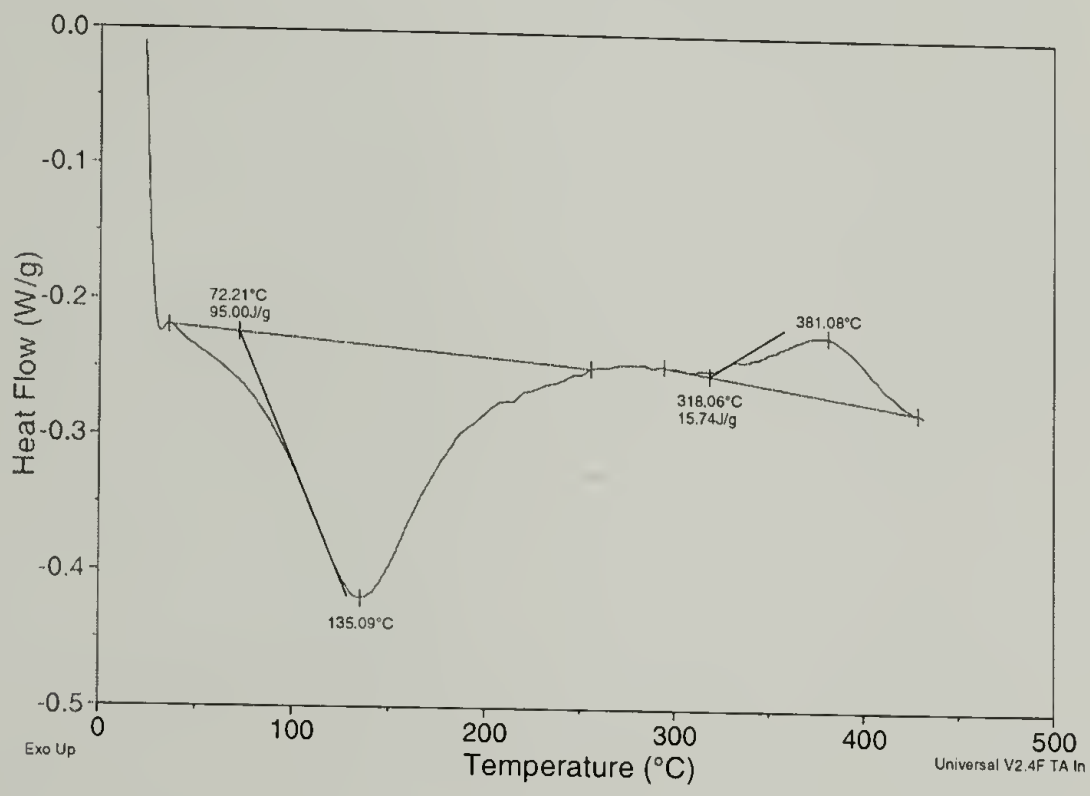

Figure 2.4 DSC trace of Kevlar® 29 fiber

A careful DSC study of Kevlar® 29 fiber yields a somewhat different results from that reported by Jaffe and Jones.[52] In their thermal study, they identified a glass transition of Kevlar® at 360 °C. As shown clearly in Figure 2.4, there is an exothermic peak at about 380 °C and the DSC trace of a second heating after first cooling does not show any shift in thermal capacity or other peaks. This suggests that the exothermic peak around 360 °C be due to the recrystallization in the structure. The evidence found in the thermal treatment of PPTA fibers further supports this hypothesis.

Figure 2.5 shows the TGA trace of different fibers. The thermal stability of Kevlar® is clearly better than Technora® and Vectran®. To study the decomposition behavior, the weight loss associated with the corresponding heat in Kevlar® is recorded by simultaneous TGA-DSC. Figure 2.6 indicates that the decomposition of Kevlar® is an endothermic process.

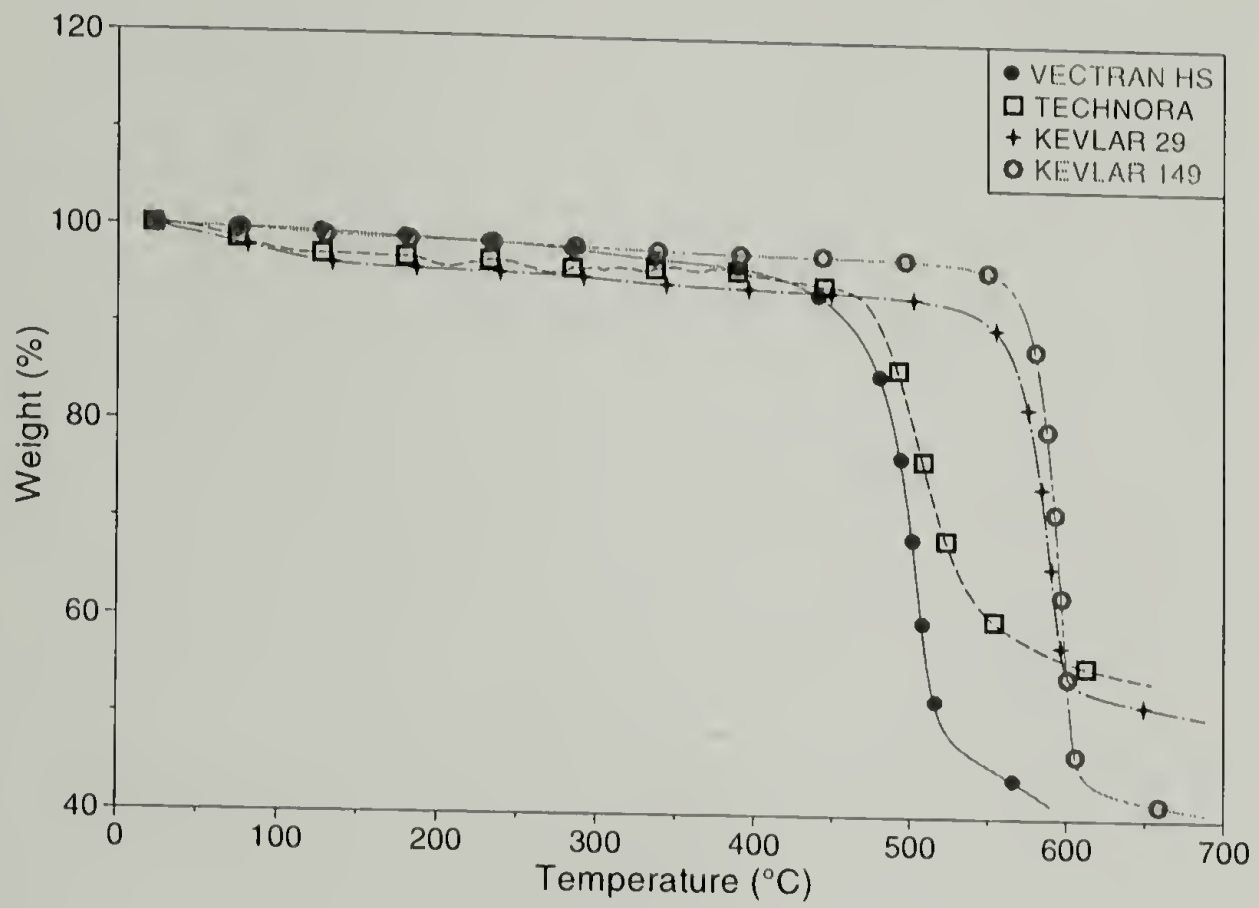

Figure 2.5 TGA of different fibers

DMTA of single filaments were conducted to gain more knowledge of the relaxations. The properties of high performance fibers often are achieved through post-treatments that usually need to utilize certain transitions to improve the structure. Therefore, the study of DMTA could be very helpful to the processing and use of fibers. The DMTA Spectra of Technora® and Kevlar® (Figure 2.7 and Figure 2.8) show the influence of residual water on the material's relaxation behavior. The tanδ peak of Technora® is high at first because the removal of the residual water dissipates energy and then it starts to increase again after 200 °C. It likely has another relaxation peak at higher temperature but could not be detected due to the temperature

limitation of the instrument. Commecial Technora® is post-stretched at very high temperature, about 490 °C, to give the desired properties.

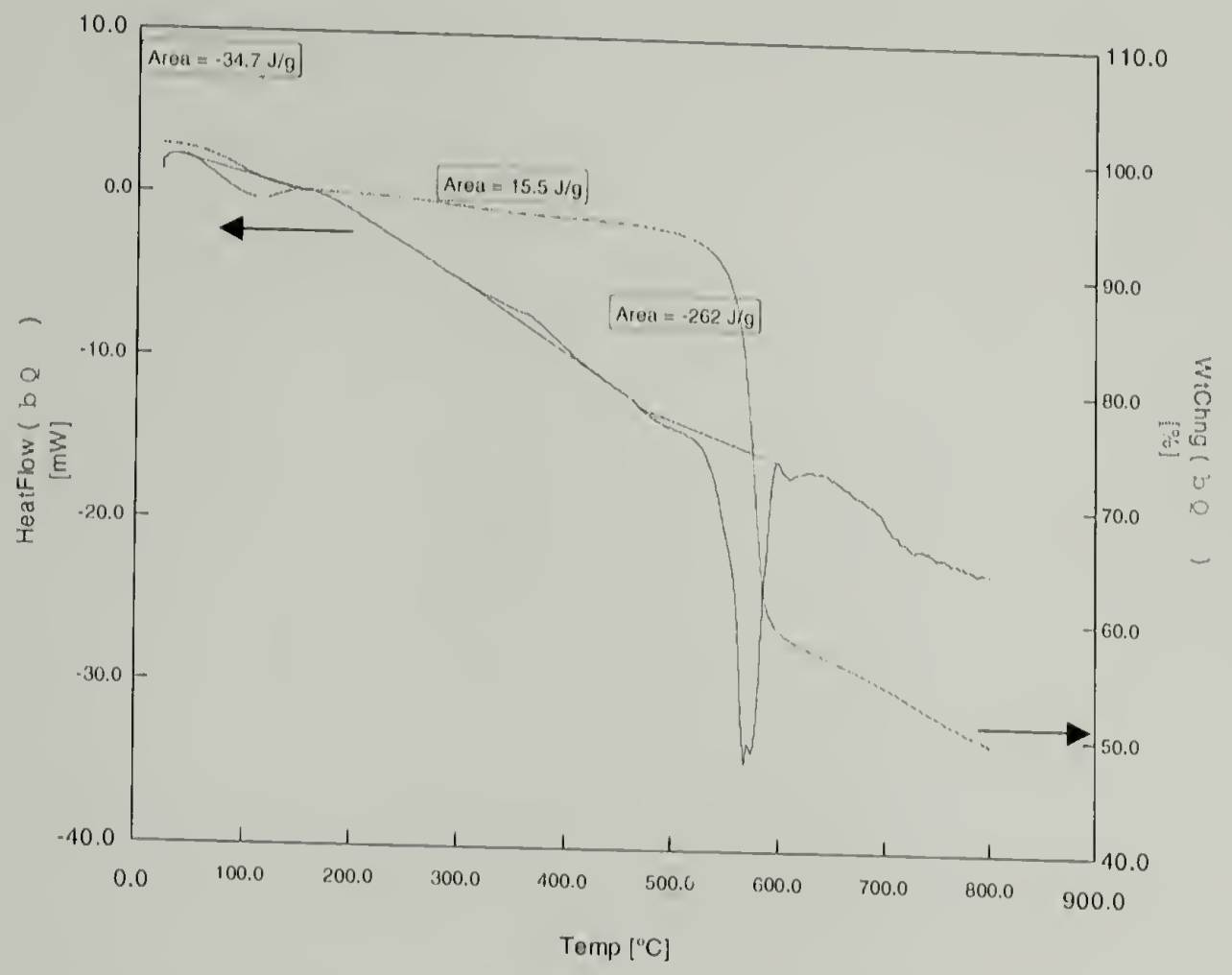

Figure 2.6 Simultaneous TGA-DSC of Kevlar® 29

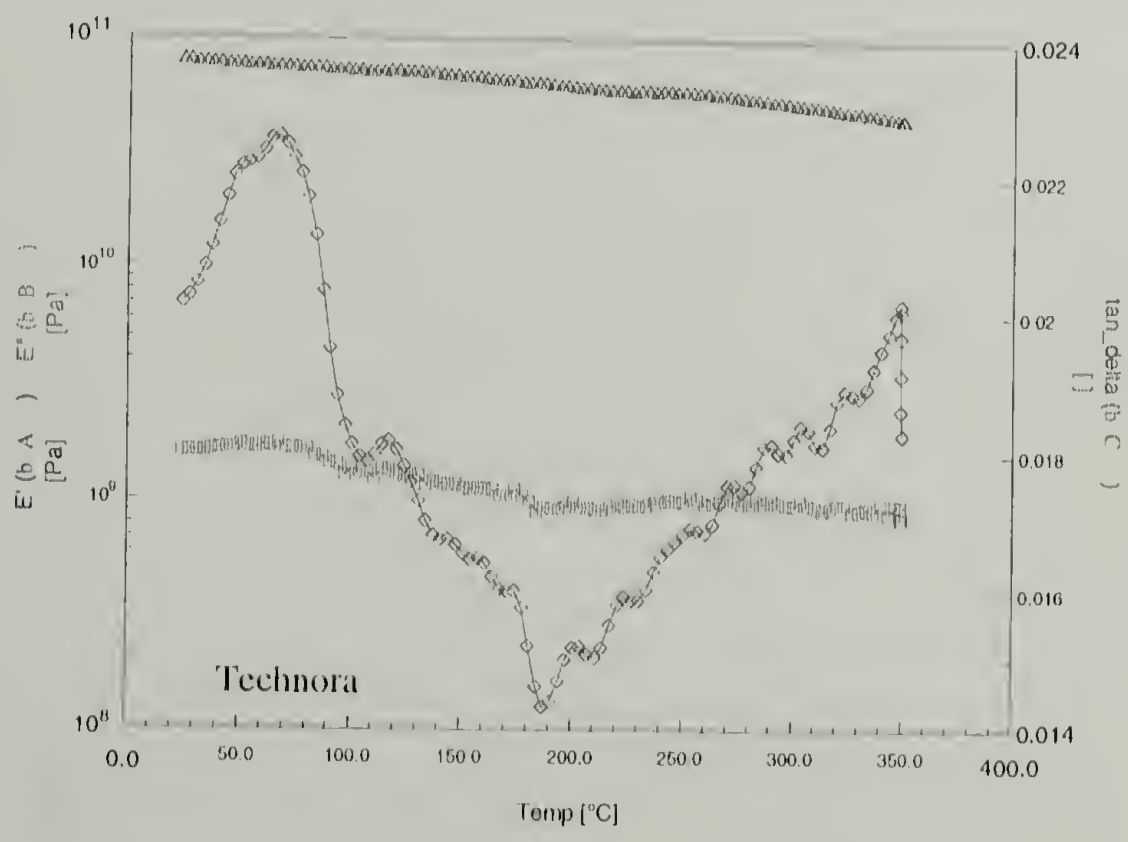

Figure 2.7 DMTA of a single filament of Technora®

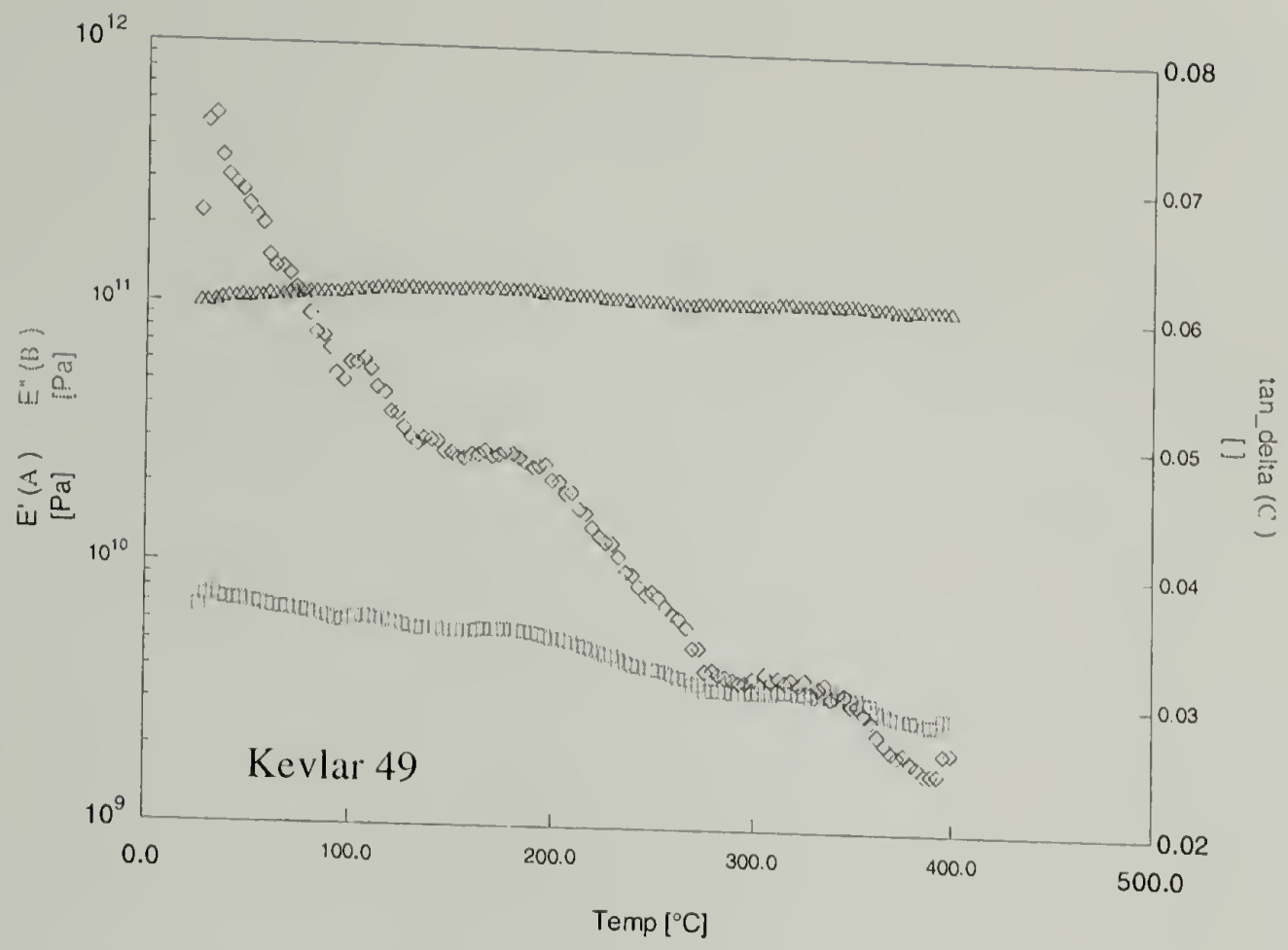

Figure 2.8 DMTA of a single filament of Kevlar® 49

2.3.3 Structure

Since most high performance fibers are highly crystalline, X-ray diffraction is very helpful to understand the structure and possible correlations between structure and property. Wide-angle X-ray diffraction patterns of different fibers show similar fiber patterns indicating high orientation in their structure. Figure 2.9 displays the wide-angle diffraction patters for different types of Kevlar® fibers. It is clear that the orientation and the perfection of crystal structure differ among different Kevlar® fibers. Kevlar® 149 has the highest orientation and most perfect crystal structure. Figure 2.10 indicates that while all of them are highly oriented, the crystal structure of Technora® and Vectran® HS are far from perfection. Nomex has well-oriented structure, but its nonlinear nature of the chain inhibits a high modulus of this material. The X-ray diffraction pattern of Spectra® shows that Spectra® is highly crystalline and highly oriented.

Figure 2.11 shows detailed equatorial scans of different fibers. It clearly indicates that the transverse crystal size in Spectra®, which is in the order of 800Å, is much larger than for Kevlar®, which is about 50 Å for Kevlar® 29. The fact that Spectra® is processed using special spinning technology to eliminate the chain entanglement might explain the difference. Figure 2.11 also shows that there is difference in peak position, peak width and intensity ratio between peaks among different Kevlar® fibers. Technora® lacks transverse order.

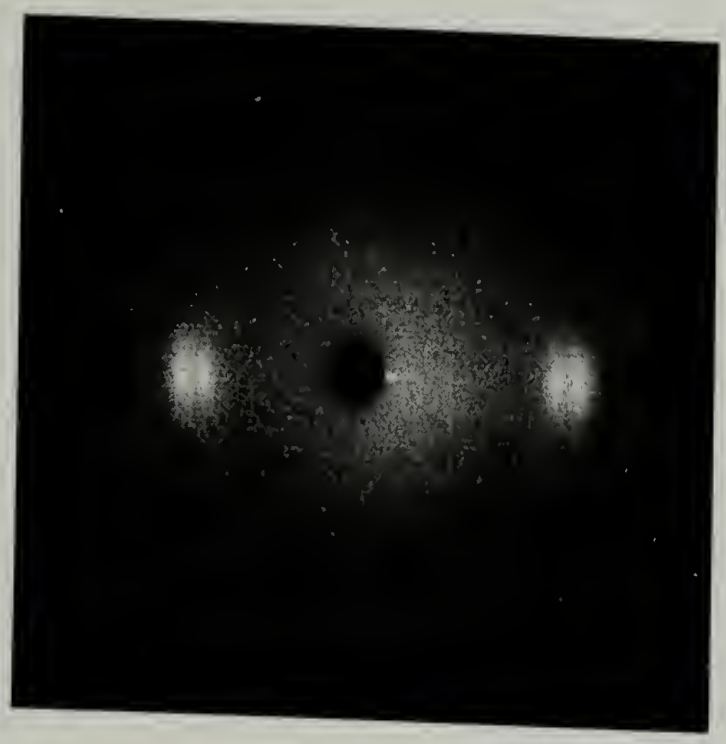

Kevlar 119

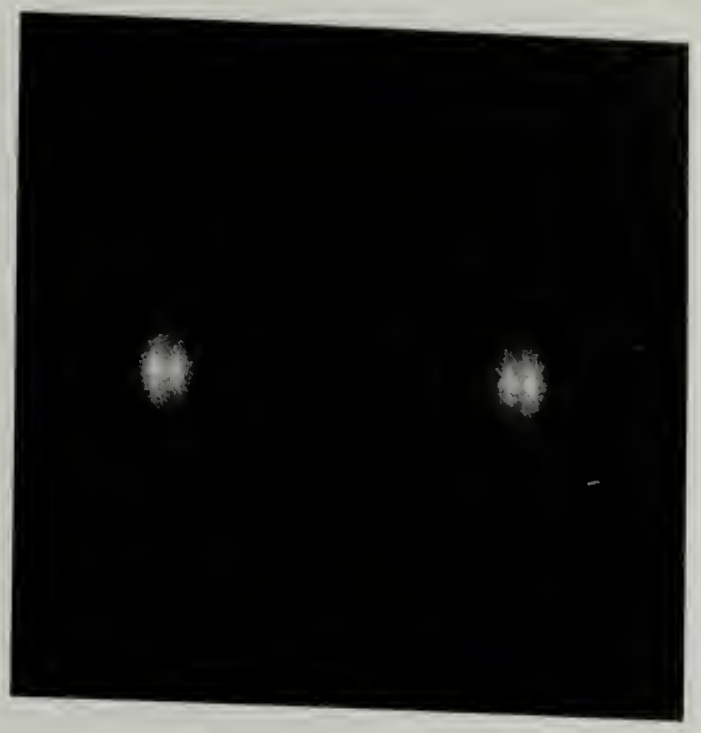

Kevlar 29

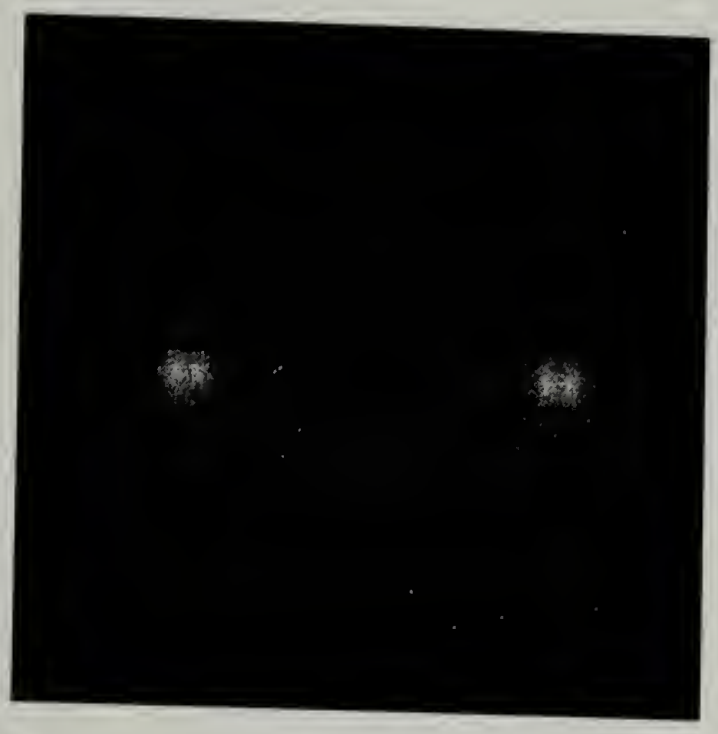

Kevlar 49

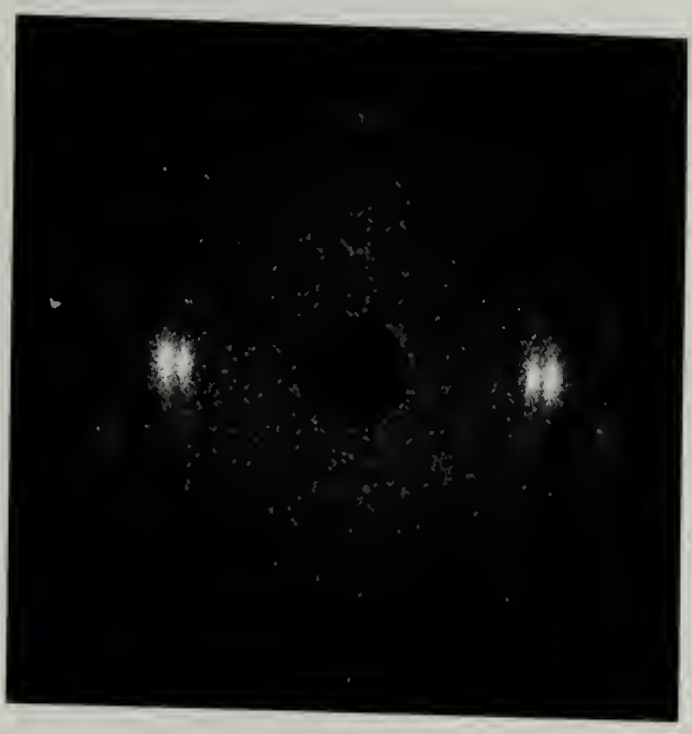

Kevlar 149

Figure 2.9 X-ray diffraction patterns of different Kevlar® fibers

Spectra 900

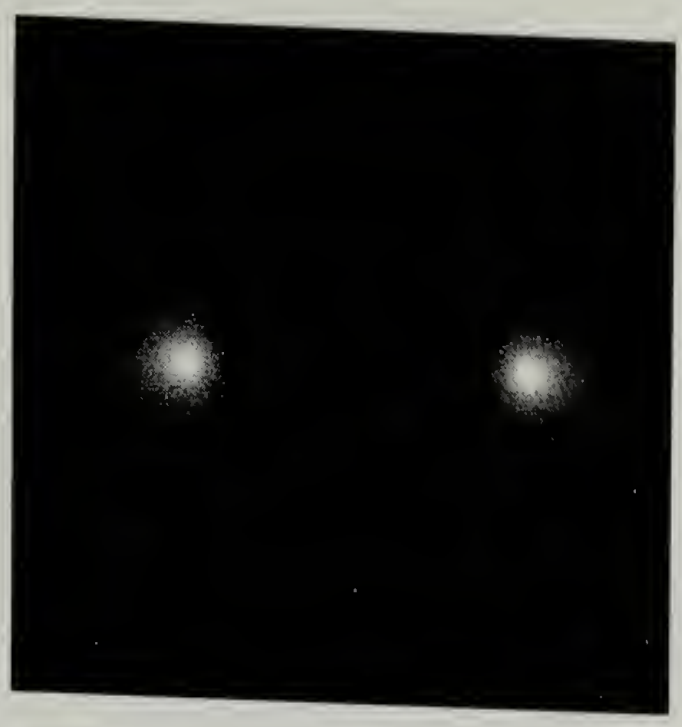

Technora

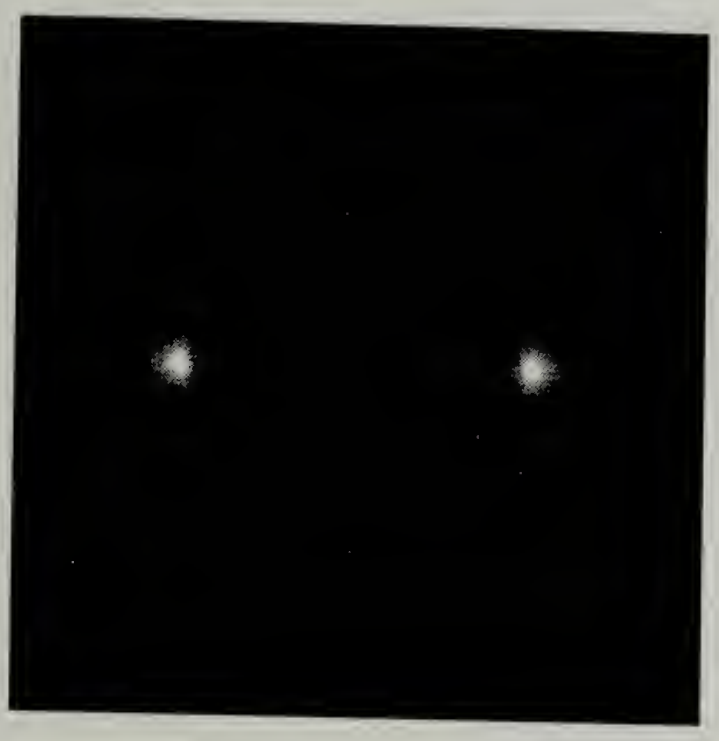

Vectran HS

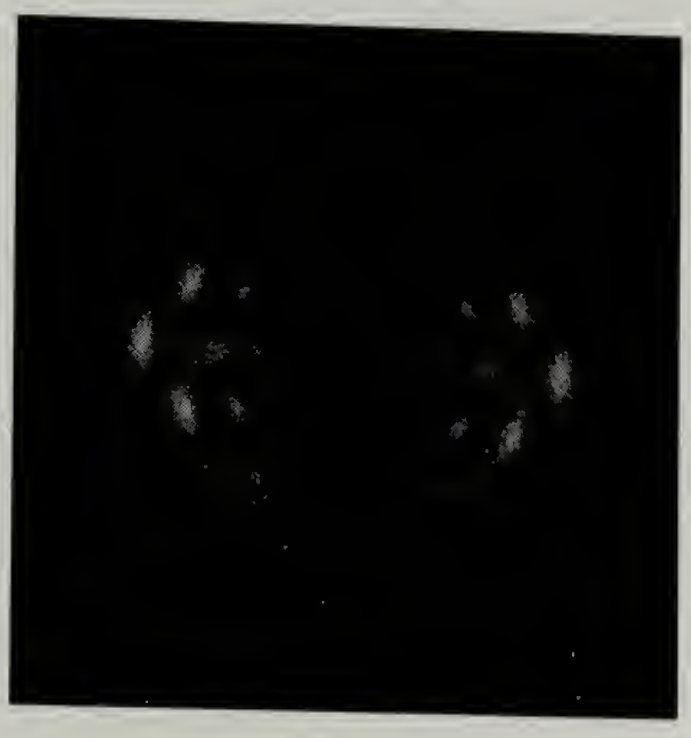

Nomex

Figure 2.10 X-ray Diffraction patterns of different fibers

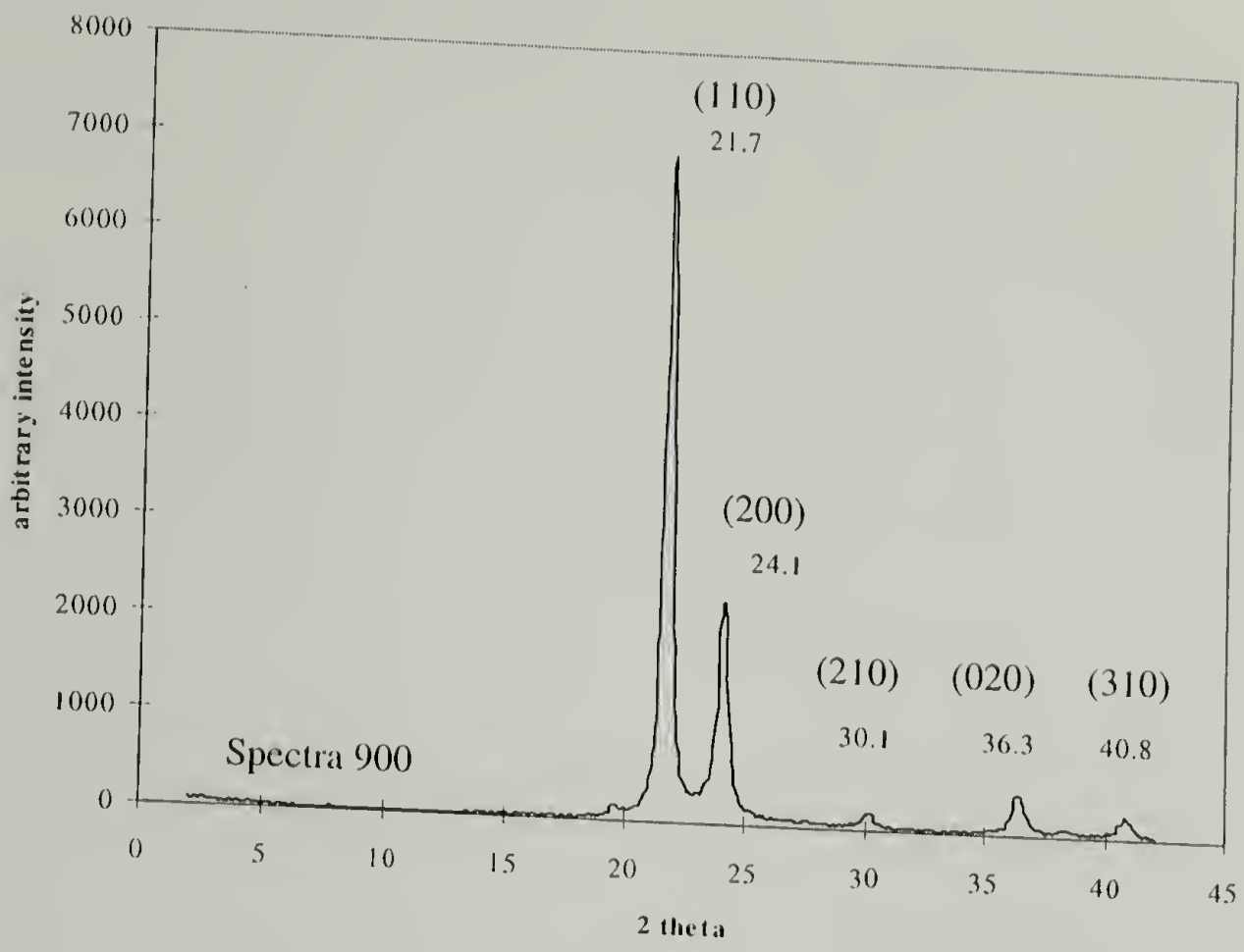

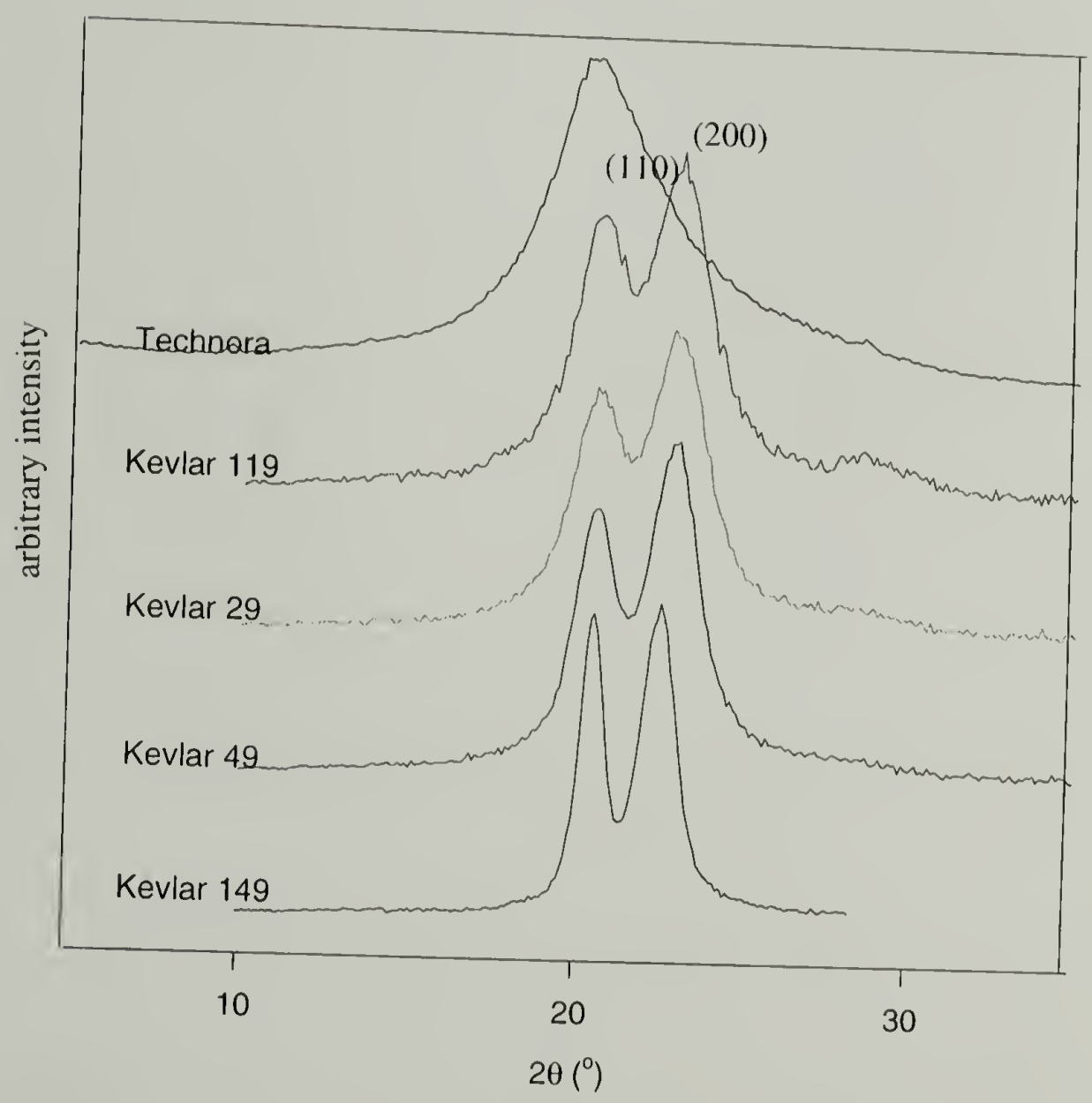

Figure 2.11 X-ray equatorial scans of different fibers

2.3.4 Comments on the Measurement of Possion's Ratio from the Dilatometric Measurement

As introduced in the experimental part, the Poisson's ratios of fibers can be derived using high pressure dilatometry if transverse isotropy is assumed. Attempts have been made to derive the Poisson's ratio of Kevlar® fibers, which is needed for later modeling on twist yarns.

Figure 2.12 shows that the change in the axial stress with the applied hydrostatic pressure at constant strain. According to Equation 2.5, the Poisson's ratio, υ_{12}, is –1.7.

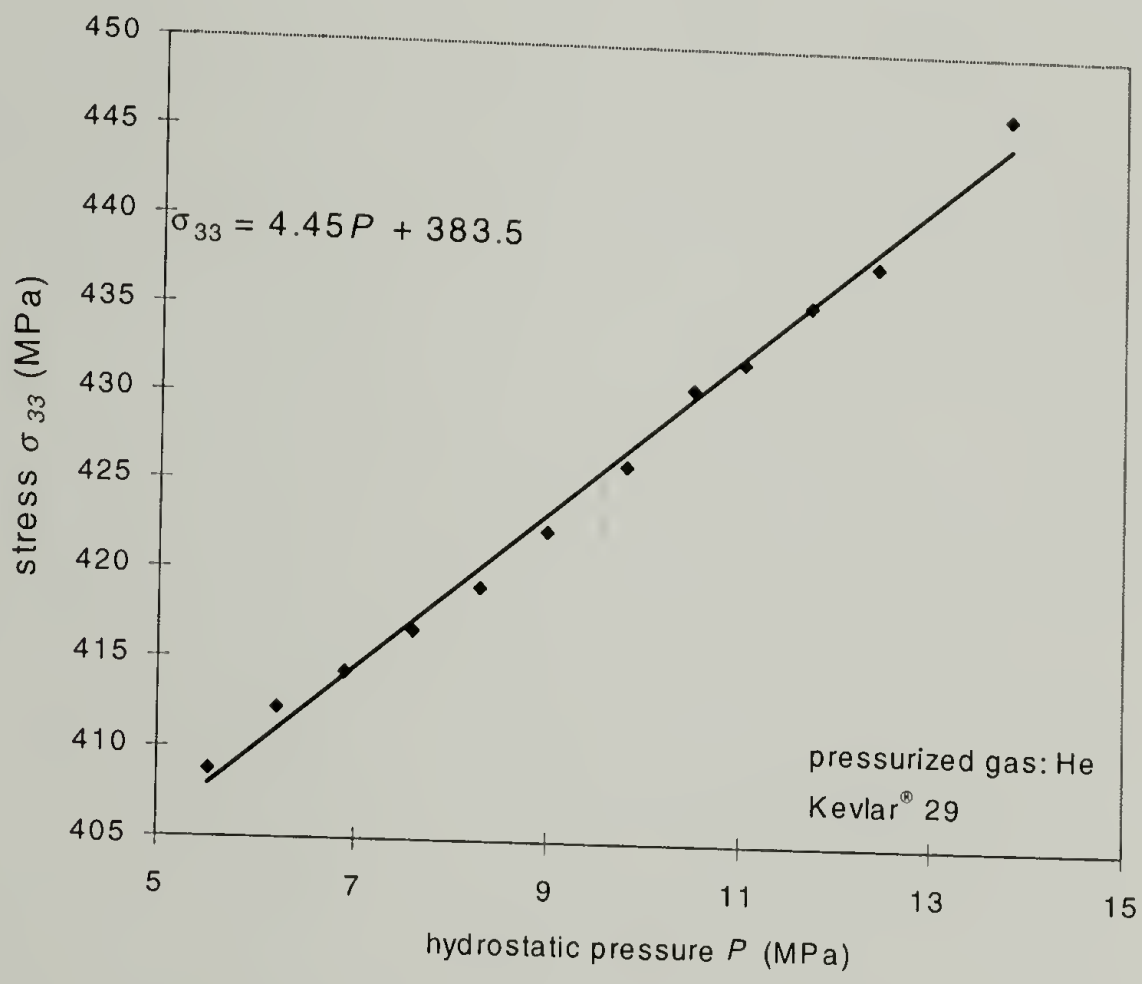

Figure 2.12 Axial stress vs. hydrostatic pressure in high pressure gas dilatometry

For an isotropic material, the Poisson's ratio must be in the range of $-1<\upsilon<0.5$, which is required for a positive strain energy. For an anisotropic material, the requirement leads to a different possible range of Possion's ratio. This requirement can be restated as a positive definite compliance matrix. Considering the constitutive equation of transversely isotropic fiber as Equation 2.8, the requirement of a positive definite matrix yields the following three relations:

$$1-\upsilon_{23}{}^{2}>0$$

$$\upsilon_{12}{}^{2}<\frac{E_1}{E_2}$$

$$-\sqrt{\frac{(1-\upsilon_{23})E_1}{2E_2}}<\upsilon_{12}<\sqrt{\frac{(1-\upsilon_{23})E_1}{2E_2}}$$

Equation 2.9

At reasonable approximation, take E_1/E_2 =10, and υ_{23}=0.3, (for high performance fibers), then

$$-1.87<\upsilon_{12}<1.87$$

Therefore, a υ_{12} of –1.7 is possible. However, the derivation of Equation 2.5 is based on the assumption that the studied material is elastic and the modulus is pressure independent. Further measurement (Figure 2.13) illustrates that the modulus of the fiber increases with the applied hydrostatic pressure, which may invalidate the derivation of Poisson ratio from the slope of the stress pressure relation at constatnt strain.

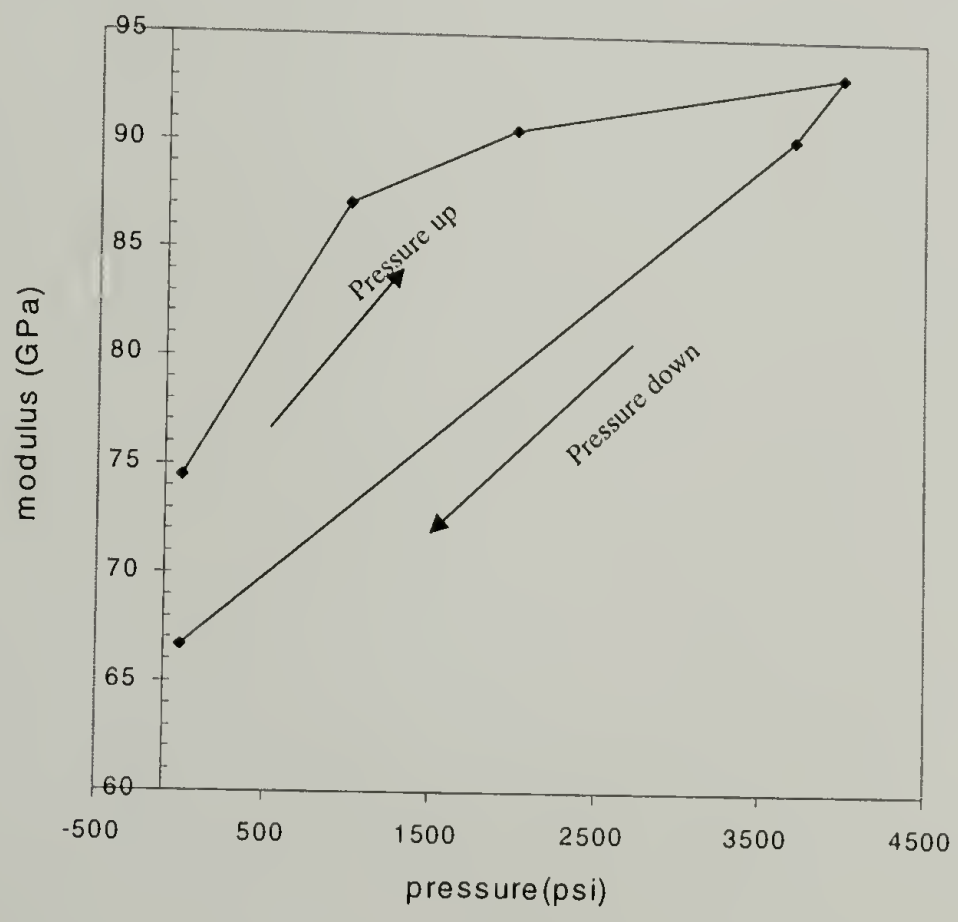

Figure 2.13 The apparent Young's modulus of Kevlar® fiber vs. hydrostatic pressure in high pressure gas dilatometor

CHAPTER 3

FATIGUE AND CREEP OF HIGH PERFORMANCE ORGANIC FIBER YARNS

3.1 Abstract

In this chapter, results of a systematic study of fatigue and creep behavior of a series of high performance fiber yarns are presented. Previous studies involving fatigue and creep were carried out on single filaments and tend to have large data variability. Our studies have focused on fiber yarns due to their obvious practical significance, and the data has shown better statistics. A competition between perfection and damage upon fatiguing was studied. The influence of factors such as stress range, mean stress, twisting, frequency, loading sequence and temperature on the fatigue of fibers was investigated. Empirical semilogrithmic lifetime principles for fatigue and creep were observed. A critical strain failure criterion was identified for different fibers under tensile, creep and fatigue loading. The correlation between deformation and damage in the fatigue and creep of fibers was established. This correlation allows a derivation of the lifetime principle of fatigue and creep from the deformation behavior of fibers. The derived lifetime principles agree with the empirical ones. Several material constants such as fatigue strength and fatigue strength index, creep strength and creep strength index were defined to characterize the fatigue and creep properties of these high performance fibers. This allows a comparison of fatigue and creep resistance among different fibers. The fracture morphology under different loading modes was examined. The fatigue-damaged fibers were examined by mechanical, thermal mechanical and structure measurements. In addition, two routes: thermal-mechanical measurements and structure characterization were proposed and validated to be used in the detection of the damage and prediction of the remaining lifetime in these fibers.

Keywords: fatigue, creep, high performance fibers, Kevlar®, Vectran®, Technora®, Spectra®, Nomex®, structure characterization, thermal-mechanical analysis, mechanical property, deformation

3.2 Background

High performance polymeric fibers have received a great deal of attention recently because of their high tensile properties, such as modulus, strength and dimensional stability. On a per unit weight basis, their specific properties are even superior to that of steel or glass fiber[3]. During their application as load bearing structural elements such as in marine ropes, industrial belts, and fiber-reinforced composites, complicated loading conditions usually shorten their service life dramatically. Some studies have been done on the study of creep[62,102,103], fatigue[40,63,84] and deformation under humidity[104] of these materials.

Two different strategies have been adopted to produce high performance fibers. In the case of flexible chain polymers, such as polyethylene, highly oriented and extended chain structures are obtained by specialized processing techniques[104]. Another approach[105] involves incorporating aromatic species in the polymer backbone to yield rigid rod-like extended chain structures; Kevlar®, Vectran® and Technora® are some examples. The relationship of such an extended chain morphology to material properties has been the focus of several studies[2,33-35,41,48,72,79,80,82,106]. Different techniques such as X-ray diffraction[34,35,41,72,79], Electron microscopy[106], Raman spectroscopy[33,80] and solid state nuclear magnetic resonance (NMR)[48] have been utilized to obtain a general understanding of the structure property relationship.

However, not enough effort has been made to relate the long-term properties, especially when in use, of these fibers to their structure. Our study provides some understanding of their long-term properties and possible correlation with the structure.

To study the fatigue and creep of high performance fibers, let us first discuss some results in the earlier studies.

3.2.1 Fatigue of Polymers

There are usually two modes of failure: creep failure, which is deformation driven, and fatigue failure, which is crack driven. Fatigue failure of a material refers to a failure that does not occur when the component is loaded initially, but after a number of similar load fluctuations. Under this loading fluctuation, the material undergoes a crack initiation, crack propagation and final failure. Two theories are used to characterize the material's behavior under fatigue: fracture mechanics theory focusing on crack propagation, and damage accumulation rules.

Table 3.1 lists the main theories proposed for material lifetime under fatigue conditions. These theories were used mainly to study the fatigue of metals.

Table 3.1 Summary of Fatigue Life Time Theory

	Governing Equation	Physical Meaning	Usage	Points of improvements
Palmgren-Miner's Law[121]	$\sum_{i=1}^{k}\frac{t_i}{T_i}=1$ (1) $\sum_{i=1}^{k}\frac{n_i}{N_i}=1$ (2)	Linear damage cumulating with (1) time (2) number of cycles	stress fluctuation or different stress sequence	Instead of using (1) as the failure criteria, statistically evaluating the possibility of the failure
Fracture Mechanics [111]	$\frac{da}{dn}\propto \sigma_f{}^m a^n$ $\propto A\Delta k^m$	Fatigue crack propagation rate depends on stress intensity factor (Δk)	Relate the measurable crack length to $\Delta k \Rightarrow$ material life $N_f=\frac{2}{(m-2)AY^m\Delta\sigma^m}\left[\frac{1}{a_0^{(m-2)/2}}-\frac{1}{a_f^{(m-2)/2}}\right]$	Including mean stress effect Goodman: $\sigma_a=\sigma_f(1-\sigma_m/\sigma_{ys})$ Gerber: $\sigma_a=\sigma_f(1-(\sigma_m/\sigma_{fs})^2)$ Sdoerberg: $\sigma_a=\sigma_f(1-(\sigma_m/\sigma_{fs}))$
Coffin-Manson's Law[175]	$N^k\Delta\varepsilon_p=C$ $\frac{\Delta\varepsilon}{2}=(\sigma_f/E)(2N_f)^b$ $+\varepsilon_f(2N_f)^c$	Deformation theory Elastic strain, Plastic strain combination	Life time prediction by strain amplitude	Including frequency factor, environmental fatigue
Robinson's Approach [175]	$\phi_{fatigue}+\phi_{creep}=1$	Damage cumulated by fatigue and creep		strain range partitioning can be used to separate creep and fatigue

where in the table,
t is the time under fatigue, T is the time under fatigue till failure,
n is the number of cycles under fatigue, N is the number of cycles till failure,
a is one-half of the fatigue crack length
σ_f is the fatigue stress, σ_m is the mean stress, σ_a is the fatigue stress amplitude, σ_{ys} is the yielding strength of the material, and σ_{fs} is the fatigue strength of the material
ε is the fatigue strain and ϕ is the fraction of time under different loading.

Fatigue is general viewed as a three-stage process as shown in Figure 3.1. The lifetime of the material is determined by the initiation, propagation and final failure. The initiation is rarely understood. Pre-cracking normally shortens the initiation process dramatically.

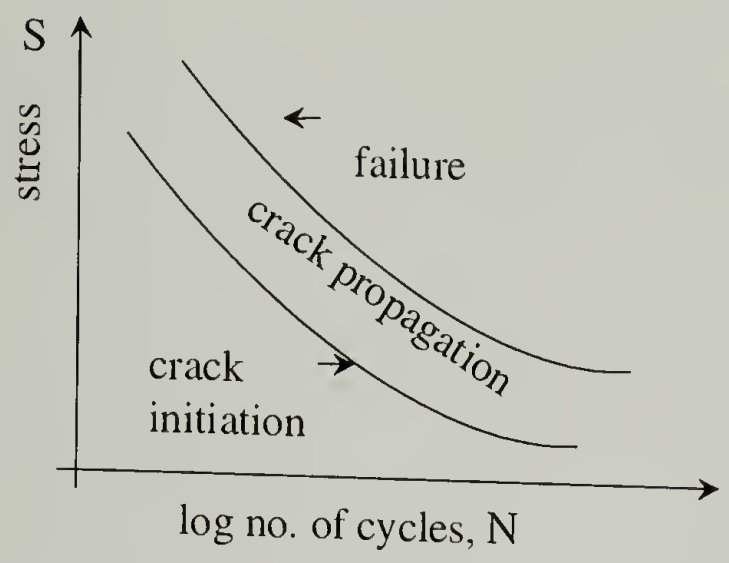

Figure 3.1 Phenomenological S-N Plot in fatigue of materials

Most fatigue studies focus on how the crack propagates. Based on fracture mechanics, many researchers have proposed lifetime laws that have the form

$$\frac{da}{dn} \propto f(\sigma, a)$$

Equation 3.1

where a is the fatigue crack length, n is the number of loading cycles and σ is the fatigue loading range. $\frac{da}{dn}$ is therefore called fatigue crack propagation (FCP) rate. More studies suggested Equation 3.1 truly is

$$\frac{da}{dn} = A\Delta K^m$$

Equation 3.2

where A, m are material constants and ΔK is stress intensity factor range, which is equal to K_{max}-K_{min}.[108-110]

In the study of metal fatigue, mean stress is found to have an influence on the fatigue lifetime. The effect of mean stress has been incorporated in different ways as shown in the following equations using the concept of apparent stress amplitude σ_a:[111]

Goodman: $\sigma_a = \sigma_{sa}(1-\sigma_m/\sigma_{ys})$

Equation 3.3

Gerber: $\sigma_a = \sigma_{sa}\ (1-(\sigma_m/\sigma_{fs})^2)$

Equation 3.4

Soderberg: $\sigma_a = \sigma_{sa}(1-(\sigma_m/\sigma_{fs}))$

Equation 3.5

in which, σ_{sa} is the applied stress range in a fatigue, σ_m is the applied mean stress, σ_{ys} is the yielding stress, σ_{fs} is the fatigue strength and σ_a is the applied stress amplitude in an *S-N* plot.

As for polymers, fatigue failure may be induced by large-scale hysteretic heating, resulting in actual melting of polymers, or by fatigue crack initiation and propagation. The fatigue behavior of some engineering plastics such as polycarbonate (PC), polymethyl methacrylate (PMMA), polystyrene (PS), Nylon and poly(vinylene chloride) (PVC) have been studied. The studies have concentrated on fatigue crack propagation (FCP). Figure 3.2[112] shows the relation between FCP rate and the applied stress intensity factor range in the fatigue of polymeric materials. Among these materials, PC and Nylon exhibit a low crack propagation rate, which is believed to be due to the ease of energy dissipation through main chain segmental motions. A crystalline phase in a polymer helps to improve the fatigue resistance. Frequency sensitivity of FCP is correlated to polymer chain motions.

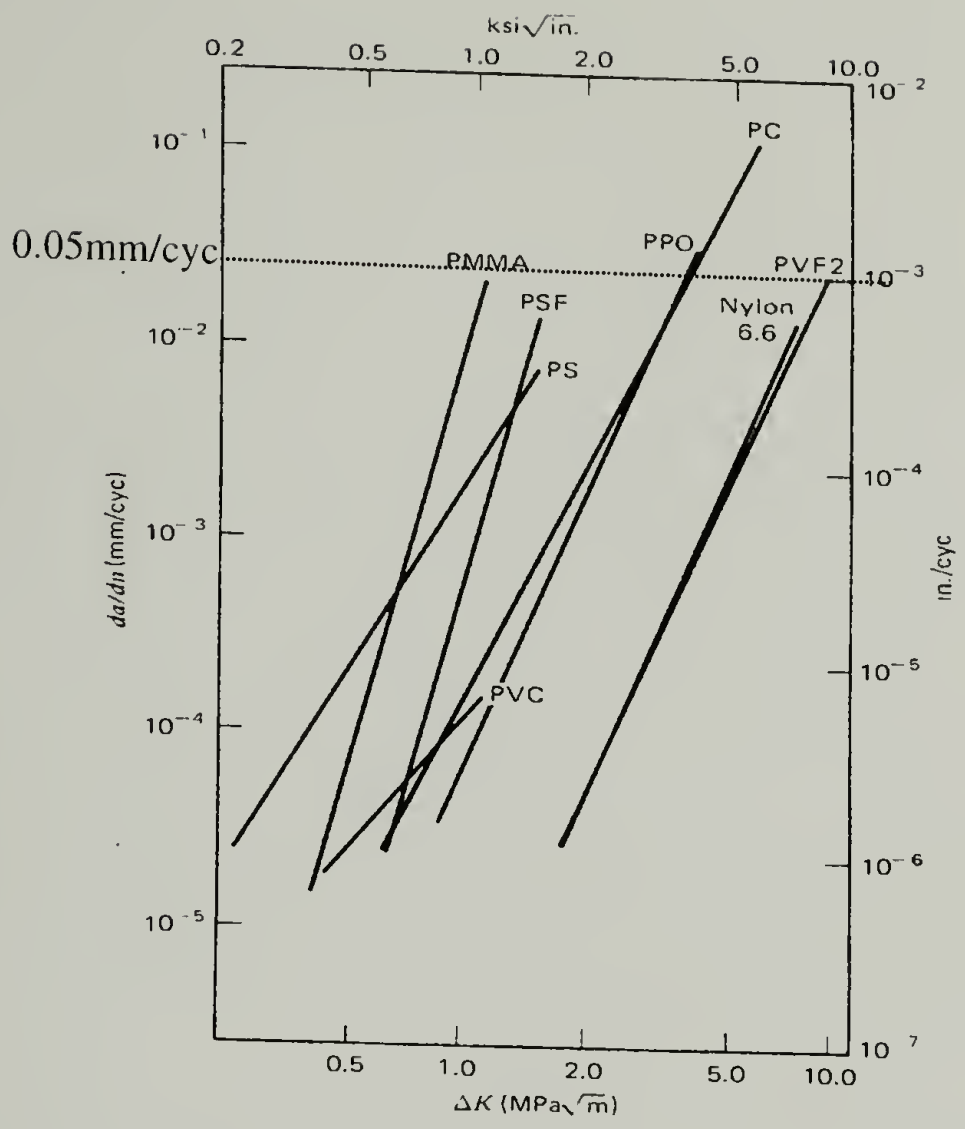

Figure 3.2 Fatigue crack propagating rate of several common plastics

There are very few studies on fatigue of fibers, although load fluctuation is unavoidable in real applications of fibers. One million cycles is usually used as the maximum test cycles and the material surviving after one million cycles is treated as non-failure. It was found that Nylon 66 fibers would fail in fatigue only if the maximum load was above about 60% of the nominal fiber breaking strength and that the minimum load was zero.[113] Similar results were found for Nomex® and polyester fibers by the same group. Kevlar® 49 was found not to fail unless the maximum applied load was greater than 80% of the tensile strength. The fatigue fracture morphology of Nylon 66 fiber is very different from those failed under tensile or creep loading. However, other fibers will show fibril fracture ends after fatigue failure, which is similar to those failed in tensile tests.

Although FCP is commonly used in the study of fatigue of metal and polymers, it is not suitable to describe the fatigue behavior of fibers. Fatigue cracks are never found inside fibers. A typical dimension of a bulk sample can be in the millimeter range, while the diameter of the fibers that we studied is only about 10 μm. We need to therefore approach the fatigue of fibers differently.

3.2.2 Creep in High Performance Fibers

When a constant stress is applied to the material, deformation can occur with time. This creep strain can result in the fracture of the material. The creep behavior of Kevlar® fibers has been studied since the appearance of Kevlar® commercial products.[61,62,64,103,104,114,115] Although some general observations have been made, the creep mechanism remains unclear.

By applying a high stress level, usually higher than 70 % of the nominal tensile strength, the fiber can fail within a finite time. A general empirical semi-logarithmic relation has been adopted to describe the correlation between the applied stress and time to rupture in creep.[103,115] Lafitte and Bunsell[103] reported the time to failure of Kevlar® 29 single filaments follows

$$\frac{\sigma_c}{\sigma_{ts}} = -0.08(\log t_r) + 1.1$$

Equation 3.6

Since there is a larger variation in the lifetime of single filaments under creep, some statistic treatment is reported. Wu and co-authors showed that the lifetime of single Kevlar®49 filament follows Weibull distribution.[115]

Two mechanisms have been proposed for creep-rupture: chain slippage and chain scission. Wilfong and Zimmerman[116] used chain slippage to explain the creep-rupture in Kevlar® fibres. Rather, Wu and co-authors[115] attributed the creep rupture to the chain scission because the activation energy of failure events they calculated, 80 kcal/mol, is close to the C-N

bond energy. Their calculation is based on a model that fiber failure undergoes an exponential kinetic breakdown.[117]

Studies of creep deformation and its mechanism for Kevlar® fiber are more extensive than lifetime studies.[62,64,103,104] Kevlar® fiber exhibits small creep under high stress. There are different correlations between the creep strain and the time under load. Lafitte and Bunsell adopted the following equation:[103]

$$\varepsilon_c(t) = \tau M_i \log(\frac{t+\tau}{\tau}) + M_s t$$

Equation 3.7

where τ is a time constant, t is time, M_i is the initial rate of strain and M_s is the final rate of strain. Ericksen took a slightly different form: [62,64,104,118]

$$\varepsilon_c(t)_{t>t_0} = \varepsilon'(\sigma_c, \tau) + \alpha(\sigma_c, \tau)\log_{10} t$$

Equation 3.8

$\alpha = \frac{d\varepsilon_c}{d\log_{10} t}$ is called creep rate parameter that is related to the creep rate $\dot{\varepsilon}$ by $\dot{\varepsilon} = \frac{\alpha}{2.3t}$.

The creep rate parameter was shown to increase with the applied stress by Ericksen and Guimaraes [62,64,104] but not to change with the applied stress by Lafitte and Lam. [103,118]

The molecular mechanism of creep is believed to be crystallite rotation through either lattice shear or boundary slip. (Figure 3.3) The maximum transient creep strain is about 0.07% for Kevlar® 49 and 0.16% for Kevlar® 29. A strain calculated by crystallite rotation is consistent with the observed creep strain. The apparent activation energy calculated using the creep rate parameter is about 8 kJ/mol.[62,104] This number indicates that the creep process may involve breaking of hydrogen bonds at the surface of crystallites. Ericksen further argued that the

existence of creep excludes recovery of the creep mechanism of grain boundary sliding, thus the creep is probably due to delayed elasticity.[62] Additional possible creep mechanisms include internal stress relaxation, molecular rearrangement, pleat structure, void and crack formation or growth, and increase in crystallinity.

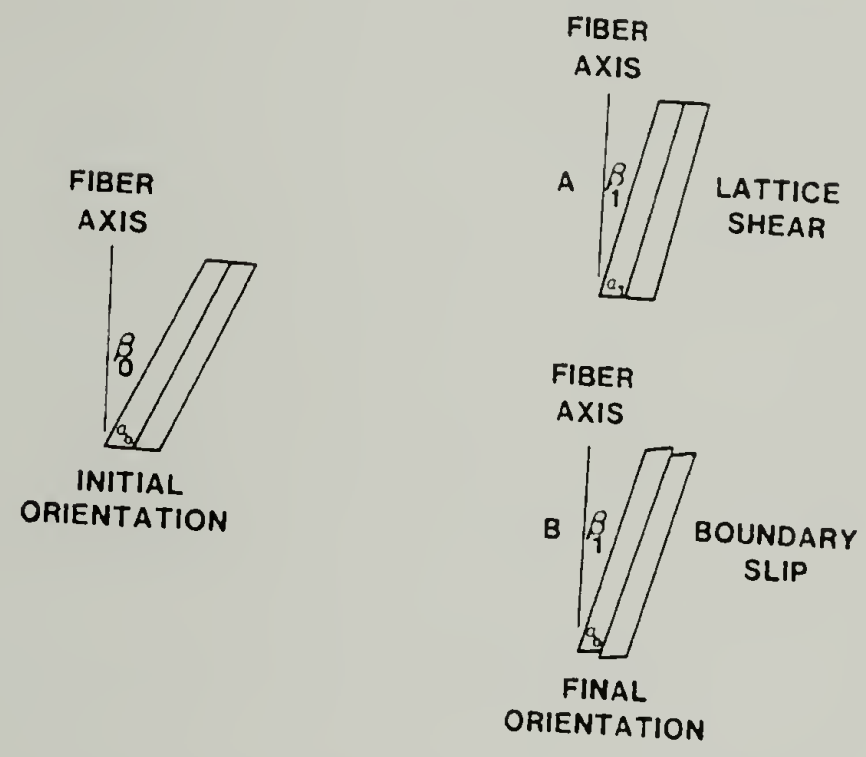

Figure 3.3 Creep deformation through crystal rotation

The effect of moisture on the creep behavior was studied by Wang et al.[104] Changes in moisture content changes the creep rate at different temperatures and stresses. The Creep activation energies calculated support the creep mechanism of hydrogen bond breakage.

In previous studies, there has been large scatter associated with the creep measurements of single filaments. There also lacks a bridge connecting creep deformation and creep rupture. In our study, we used yarn samples instead of single filaments to gain better statistics. A creep failure criterion for high performance fibers was proposed that makes the correlation between creep deformation and creep rupture possible.

3.3 Experimental

3.3.1 Fatigue experiments

Fatigue testing of the yarns was performed using an Instron model 8511 hydraulic dynamic tester. Yarns of the different fibers tested all had a similar linear density of about 1500 denier. Samples of gauge length around 150 mm were glued to special tabs held between two sets of grips. The load was programmed to be of a sinusoidal waveform under the load control mode. A minimum load of about 2N was applied to keep the samples under tension at all times. The cyclic maximum load, cyclic minimum load and frequency were varied to create different fatigue conditions over a fixed 10 million cycles. The stress amplitude varied between 50-98% of the tensile strength and the frequency was 5 Hz unless otherwise specified. During the cyclic loading, temperature, time, load, displacement and total number of cycles were tracked and transferred to the computer for storage. The data were analyzed after the experiment was completed. Figure 3.4 shows the experimental setup for the fatigue of fiber yarns.

There are four stress parameters in a fatigue test: cyclic minimum stress σ_{min}, cyclic maximum stress σ_{max}, stress amplitude σ_a or σ_{sa}, which is $(\sigma_{max} - \sigma_{min})$ and mean stress σ_m, which is $((\sigma_{max} + \sigma_{min})/2)$. The terms of stress amplitude and stress range have the same meaning in this dissertation.

Besides the constant load profile used in most fatigue experiments, a changing load profile was also applied in some fatigue experiments. The purpose of a changing load profile was to study the effect of loading sequence on fatigue behavior. Figure 3.5 illustrates the loading profile in a sequential loading experiment.

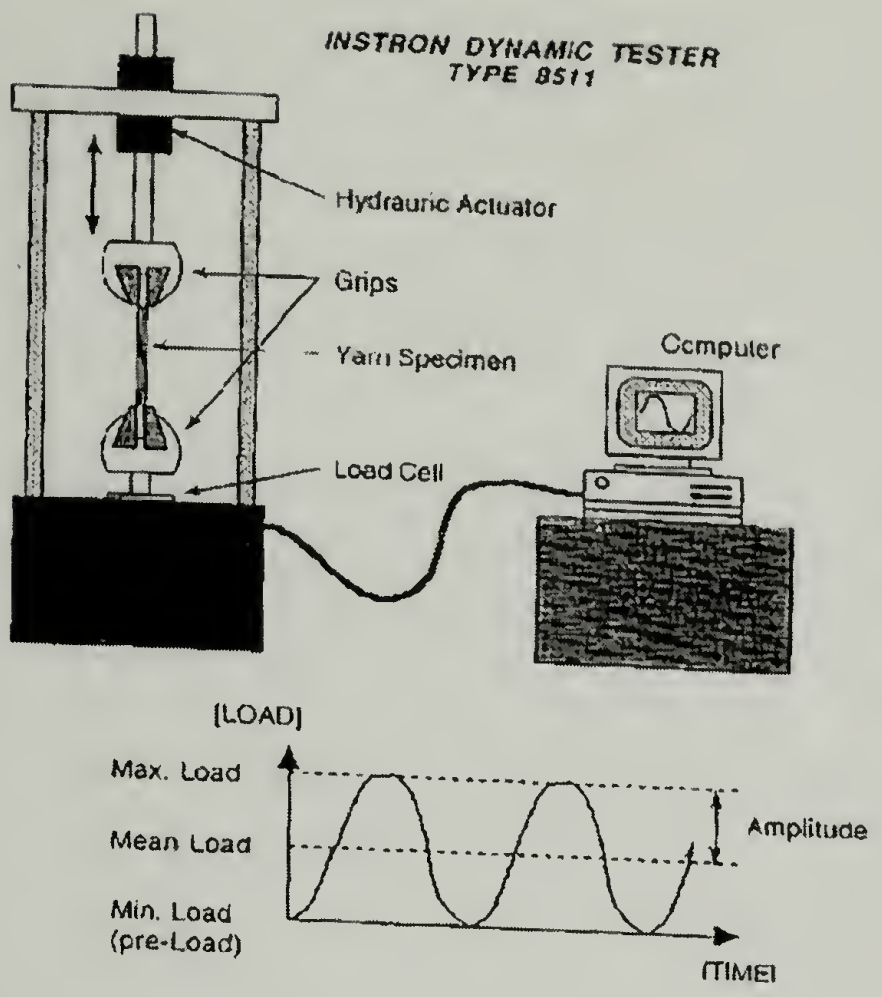

stress range: $\sigma_{sa} = \sigma_{\max} - \sigma_{\min}$

mean stress: $\sigma_m = (\sigma_{\max} + \sigma_{\min}) / 2$

room temperature, 5Hz, yarn sample

Figure 3.4 Experimental setup of fatigue of high performance fibers

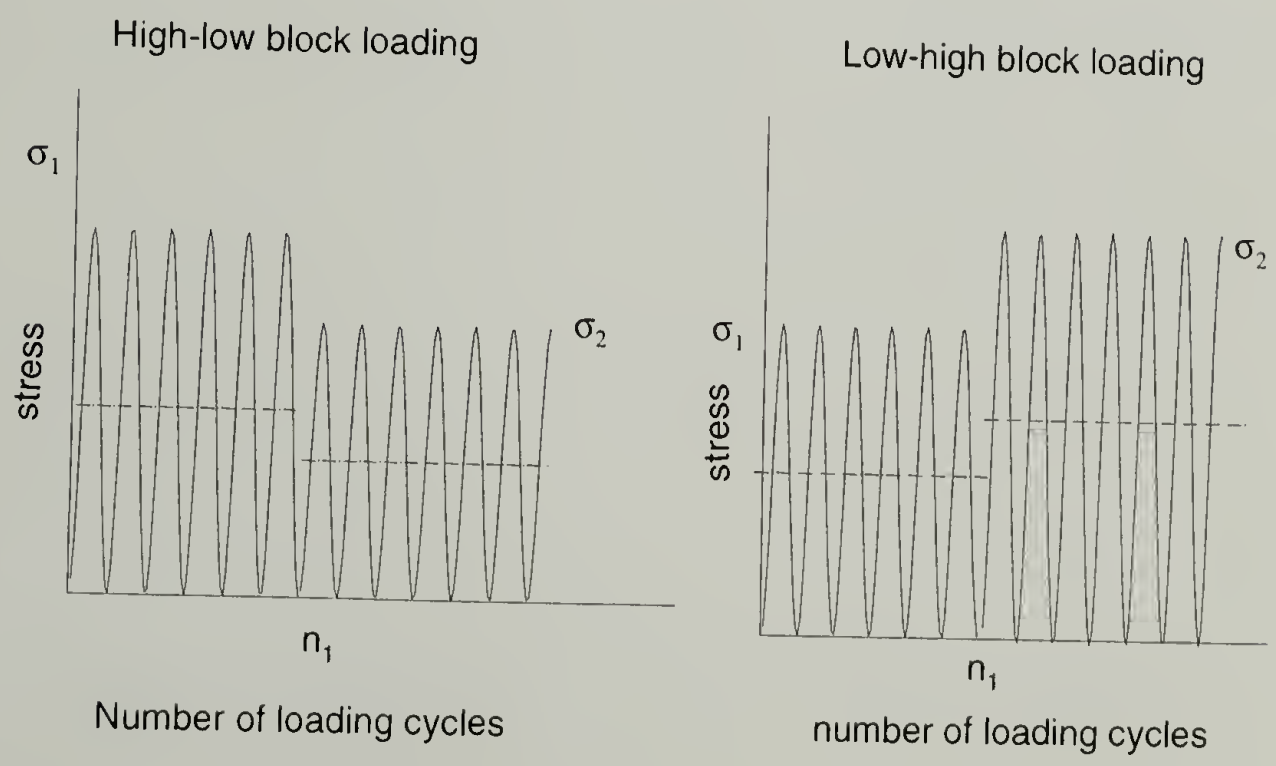

Figure 3.5 Stress profiles of block loading fatigue experiments

Before conducting fatigue experiments, an ideal steel wire sample was used to check the reliability of the system. Figure 3.6 shows that there is no energy dissipation in one cycle of loading for a steel wire indicating the pure elasticity of steel. Hysteresis between stress and strain indicates energy dissipated and is a common observation with polymer.

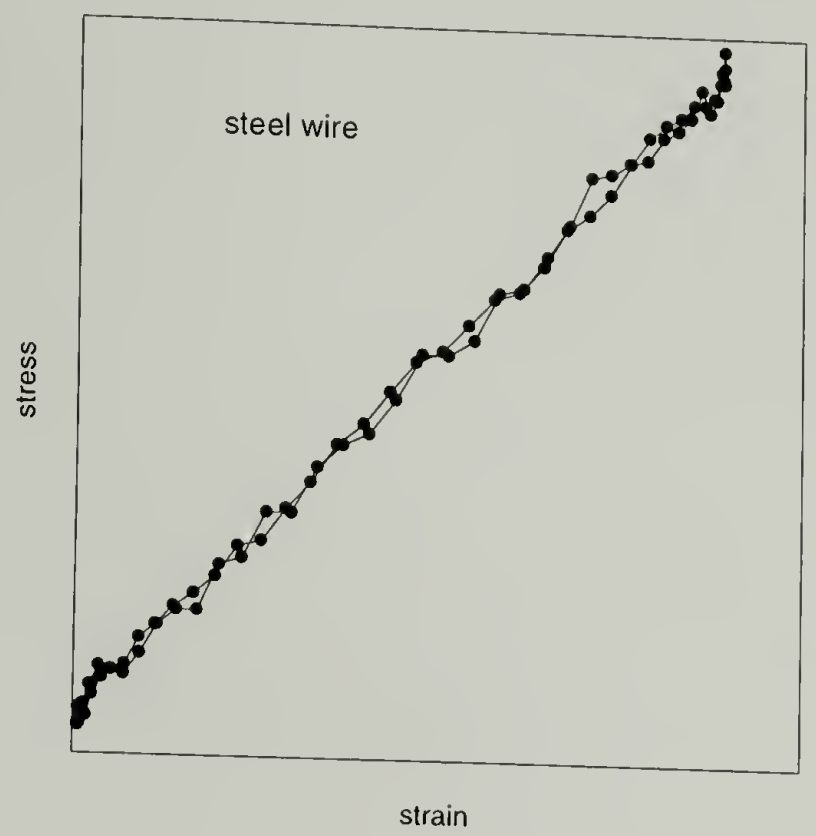

Figure 3.6 Instrumental check. Dynamic tester 8511

3.3.2 Creep Experiment

Two different specimens, single filaments and yarns, were used in the creep study. Most yarns have a linear density of about 1500 denier. Occasionally, 200 denier Kevlar® 29 yarn was used.

Two instruments were used to conduct creep experiments. For creep experiments of single filaments and yarns at ambient temperature, an Instron tester 5564 was used. DuPont TMA 2940 was used to test the creep of single filaments at elevated temperatures. In spite of a strain control mechanism for both instruments, a feedback loop controls the stress fluctuation within 2 %. The applied stress level ranged from a factor of 0.7 to 0.95 of the static strength.

In fatigue and most creep studies, yarn samples were used instead of single filaments. One reason for this is that the measurements of yarns have better statistics than that of single filaments, which is clearly shown in Table 3.2.

Table 3.2 Statistics of the properties of yarn and single filament of Kevlar® fibers

Sample	sample type	number of specimen	Load at Max.Load (N)		Modulus (AutYoung) (GPa)		Stress at Max.Load (MPa)		Strain at Max.Load (%)	
			mean	cv%	mean	cv%	mean	cv%	mean	cv%
Kevlar29 as spun	single	50	0.389	10.3	93	5.5	2900	6.9	3.38	7.7
	yarn	10	287	1.8	93	1.2	2600	1.73	3.14	2.7

*The AutYoung modulus is calculated using the steepest slope in a stress-strain curve and is higher than the initial modulus for Kevlar® fiber.

At least five samples were tested under one loading condition: either fatigue or creep. The logarithmic average of the lifetime in cycles for fatigue and in seconds for creep was used to generate the empirical lifetime equation. The variation of the logarithmical lifetimes is small (~ 5%) and could be used to derive useful lifetime equation. (See Figure 3.7)

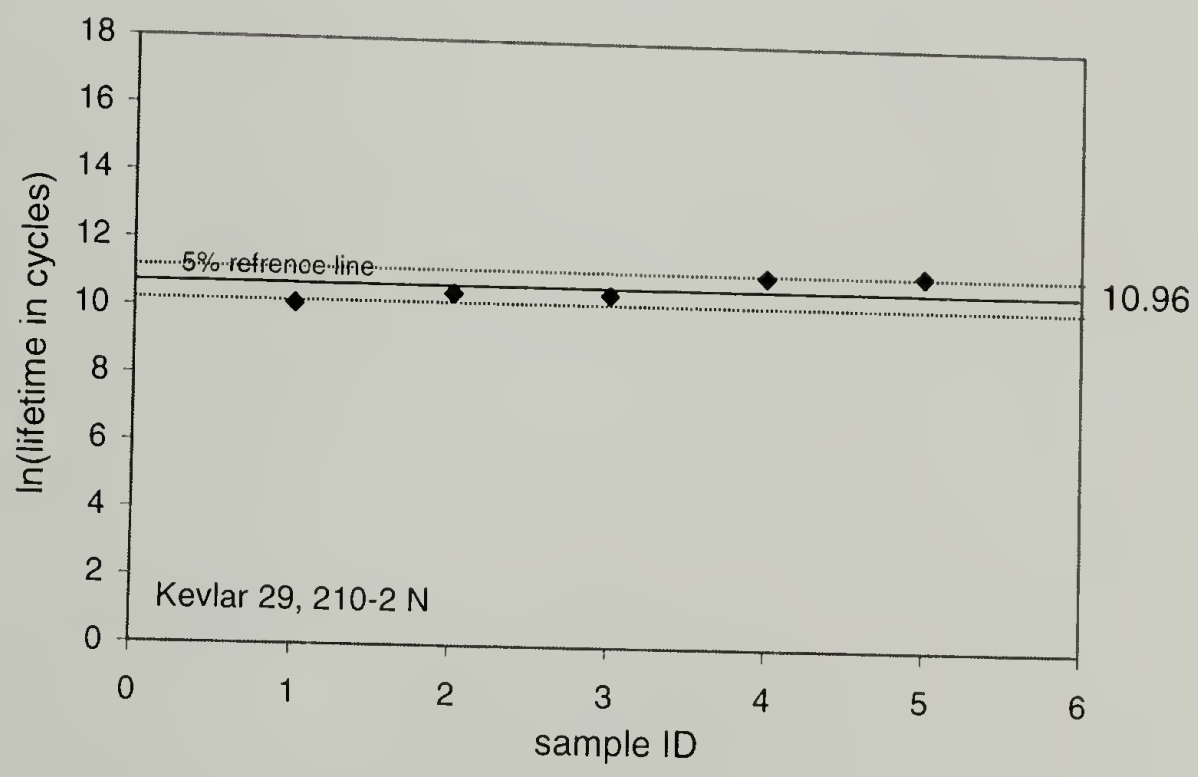

Figure 3.7 Variation in the lifetime measurements of fiber yarns under fatigue

3.4 Results and Discussion

3.4.1 General Fatigue Behavior

Figure 3.8 shows a general picture of the stress-strain curve during a fatigue experiment. The fatigue behavior of high performance fibers can be divided into the initiation, propagation and acceleration stages. In the initial stage, there is a relatively large hysteresis within one loading cycle. All fibers exhibit strain-hardening in the initial stage. Then in the propagation stage, the minimum strain in one cycle increases steadily with the number of loading cycles. Finally, the fiber yarn displays strain softening and soon fails. This strain softening is mostly due to the fact that the individual fibers start to fail in the third stage.

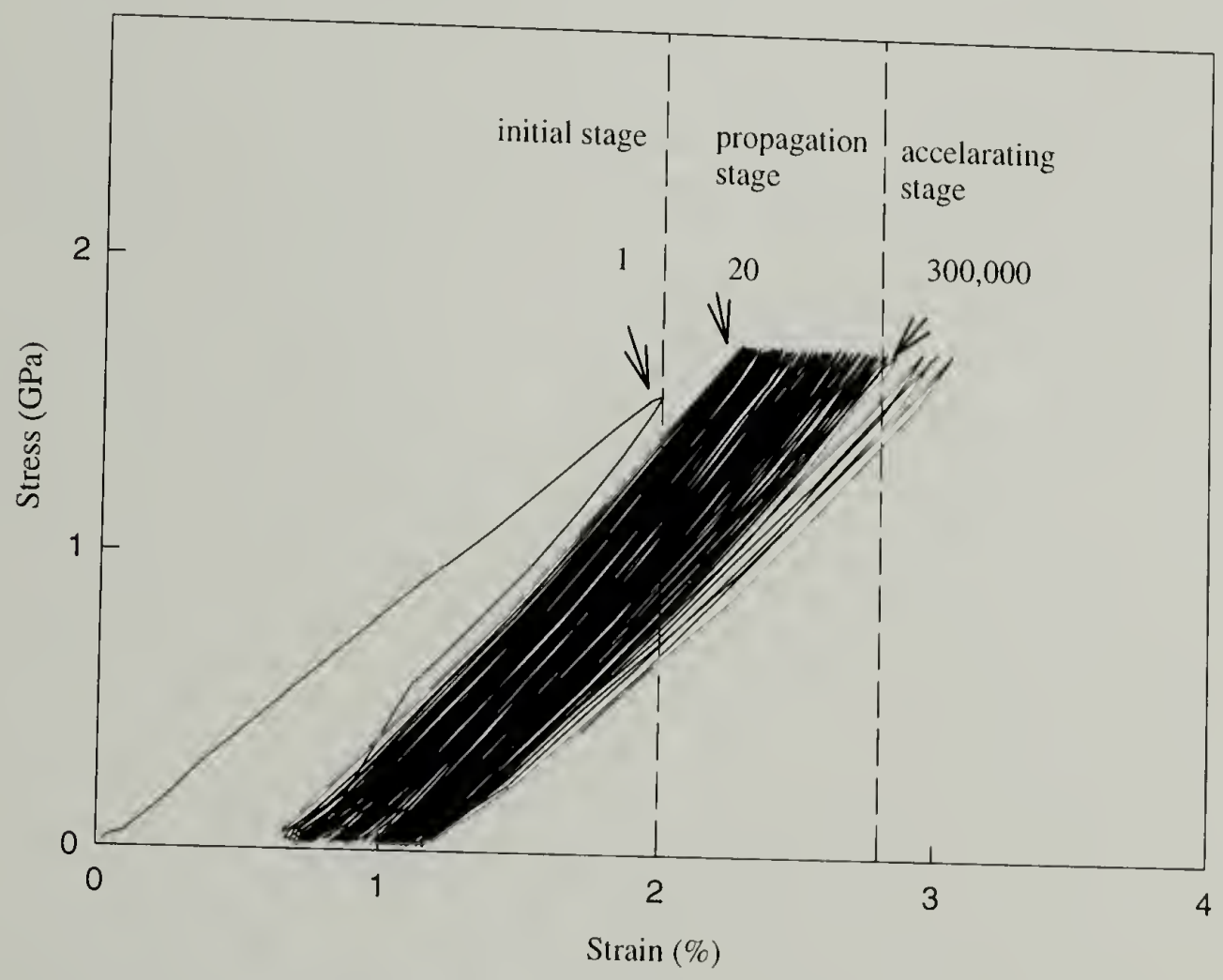

Figure 3.8 A general picture of stress-strain behavior of Kevlar® fiber during a fatigue test

We first studied the factors that influence the material lifetime under fatigue. The influencing factors that we investigated include applied stress range, mean stress, frequency, loading sequence and temperature.

3.4.1.1 Effect of Fatigue Stress Amplitude, and Effect of Mean Stress and the Concept of Apparent Stress Amplitude

A typical fatigue lifetime plot compares the applied stress amplitude and the number of lifetime in cycles, the S-N plot. The influence of stress amplitude was the first factor studied. Figure 3.9 shows the lifetime as a function of the applied stress amplitude for Kevlar® fiber yarns. The number of cycles to failure in material is seen to decrease dramatically upon increasing the applied stress amplitude. A linear regression of the data yields a good fit. The study of fatigue of

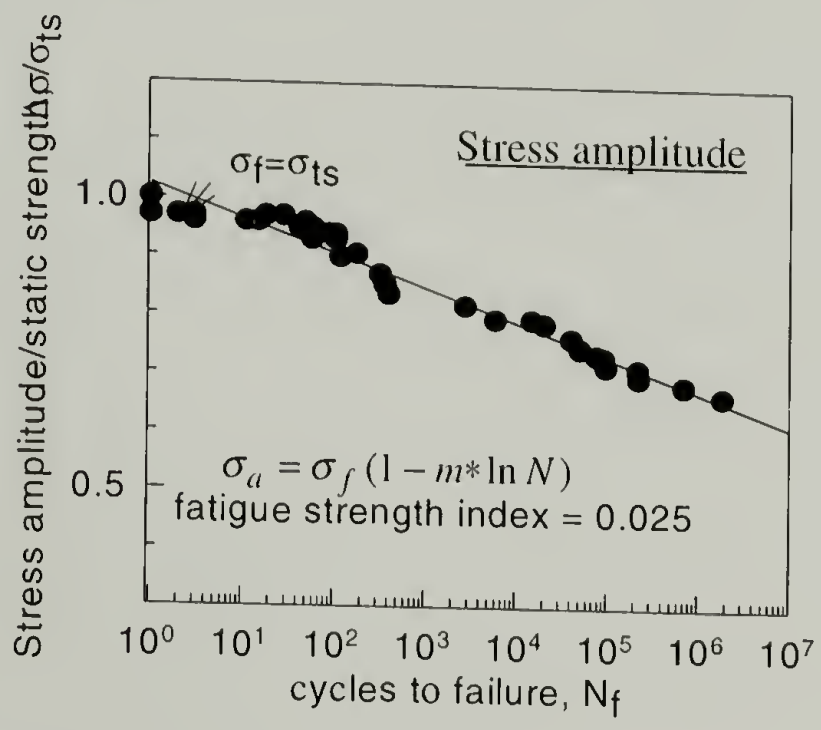

Figure 3.9 Fatigue lifetime of Kevlar® 29 under different applied stress amplitudes

other high performance fibers yields similar results. Therefore, the lifetime principle of high performance fibers can be described as

$$\sigma_{ma} = \sigma_{ts}(1 - m * \ln N_f)$$

Equation 3.9

where σ_a is the applied cyclic stress amplitude (σ_{max}-σ_{min}) and N_f is the number of cycles to failure. Equation 3.9 is an empirical lifetime equation. The intercept σ_{ts} is defined as the fatigue strength and the slope m is called the fatigue strength index. These two parameters are used throughout this study to compare the fatigue properties of all the test materials. For better fatigue performance, a high fatigue strength and small fatigue strength index is desirable.

During fatigue experiments, it is seen that both the stress amplitude and the mean stress in one cycle affect the material lifetime. It is observed that at a fixed σ_{max}, the material lifetime increases initially upon increasing σ_{min} due to a decrease in the stress amplitude. However, a decrease in the lifetime is observed when σ_{min} is increased beyond half of σ_{max}. Several empirical relationships have been developed to account for the effect of mean stress in fatigue of metals, such as Goodman's relation, Gerber's and Soderberg's relation[11](See background, earlier in this Chapter). All these equations fail to explain our results. A careful analysis of the data gives an apparent stress amplitude in the form of $\sigma_a = \sqrt{(\sigma_{max}^2 - \sigma_{min}^2)}$.

Figure 3.10 shows that the logarithm of material life cycles correlates linearly with the apparent stress amplitude. However, when σ_{min} is greater than half of the σ_{max}, fatigue lifetime is shorter than that predicted. This could be due to the combination of creep and fatigue effects under these loading conditions. In a simple creep experiment at a constant stress less than 90% of tensile strength, the lifetime of the material is longer than that under fatigue with σ_{max} the same as the creep stress. On the other hand, the material lifetime is longer under fatigue than creep when the applied stress exceeds 90% of the tensile strength. These experimental observations lead to the hypothesis that there are two competing deformation mechanisms in the material and the combination of these two effects governs the material service life. We will detail the results of the creep study in a later section.

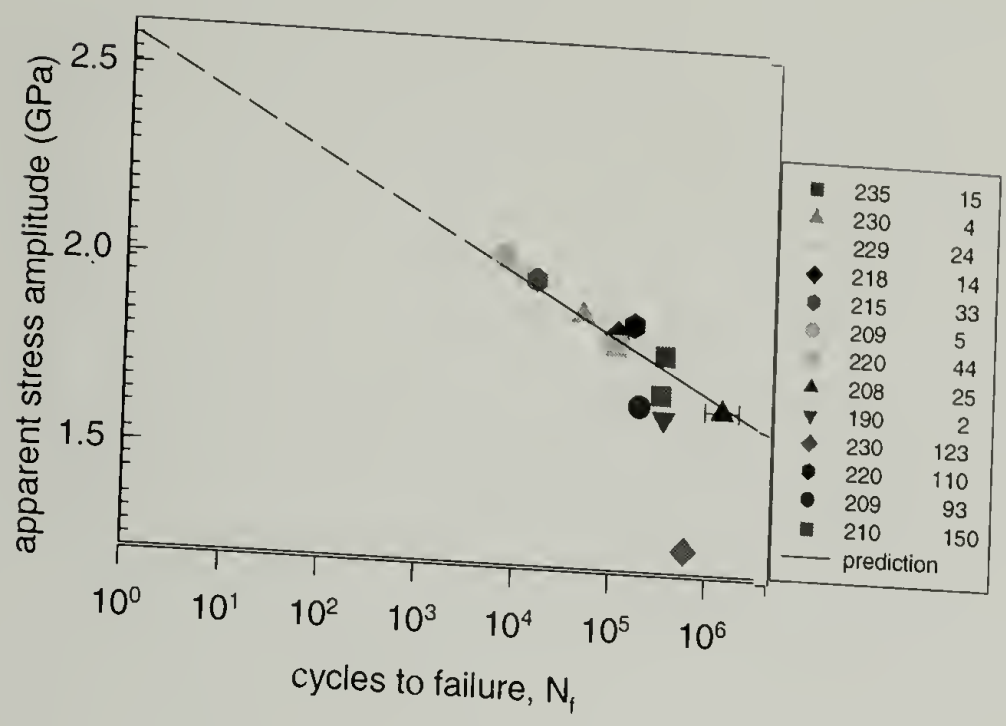

Figure 3.10 Fatigue lifetime of Kevlar® 29 under different mean stresses

3.4.1.2 Effect of Frequency, Effect of Stress Fluctuation and Cumulative Damage

The effect of frequency on the fatigue behavior of the fiber yarns was of interest initially because of the potential relation between mechanisms of creep and fatigue. A time-determined fatigue lifetime may indicate that the fatigue phenomena can be treated as cumulative creep. In addition, the fatigue of many polymers exhibit frequency dependence. This frequency sensitivity can be due to the hysteretic heat generated within the polymer that alters the structure. On the other hand, it may be due to the viscoelastic relaxation in the material. However, our studied high performance fibers demonstrate a frequency insensitivity. The experimental results on Kevlar® 29 and Vectran® HS (Figure 3.11. (a)) show that the number of loading cycles rather than the loading time determines the fatigue lifetime for the frequencies investigated. This result suggests a different mechanism for fatigue and creep in these materials.

This has been an interesting area of study, and some polymers such as PMMA, PS, PPO, etc., have been found to be frequency sensitive; while some others such as PC, Nylon 66, etc. behave independently of the frequency[119]. Efforts have been made to correlate the relative frequency sensitivity in polymers and the frequency of movement of main chain segments

responsible for generating the β transition peak in a dynamic mechanical test. Hertberg[120] pointed out that a material that revealed a β peak has the greatest frequency sensitivity at a fatigue test frequency comparable to that β transition frequency. Our results agree with this conclusion in that no β transition is observed at room temperature for these two materials according to our DMTA study.

In the early days of the study of fatigue, Miner[121] proposed the concept of cumulative damage leading to failure. He hypothesized that the number of loading cycles applied expressed as a percentage of the number to failure at a given stress level would be the proportion of useful life expended. When the total damage reaches 100 %, the specimen should fail. It can be expressed as the following equation,

$$\sum \frac{n_i}{N_i} = 1$$

Equation 3.10

where, i = ith stress level, n_i=number of cycles applied at σ_i, N_i=fatigue life at σ_i.

This concept will be applicable if the depletion of lifetime because of the damage caused by each independent loading linearly accumulates independently over the entire life of the material.

A block loading experiment was designed to verify the validity of the cumulative damage argument in the fatigue of fiber yarns. Two different loading conditions involving a high-low block and a low-high block were used. In the first case, a relatively high stress amplitude was applied for a certain number of cycles, which was then lowered to a reduced level until ultimate failure; the reverse being the case for the latter. (See Experimental Figure 3.5)

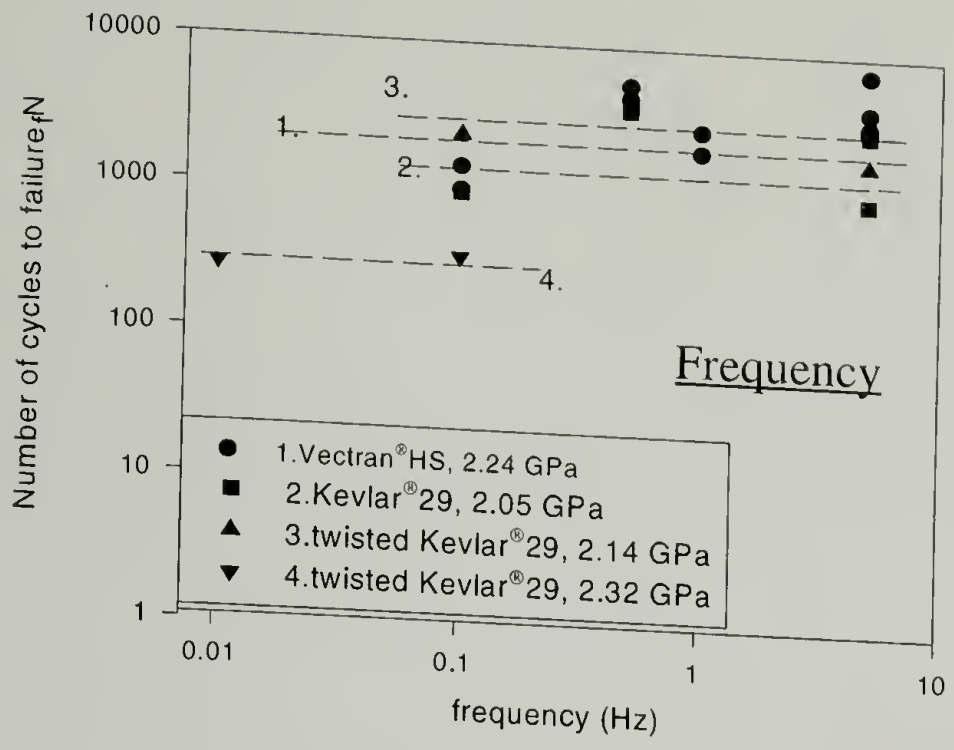

(a)

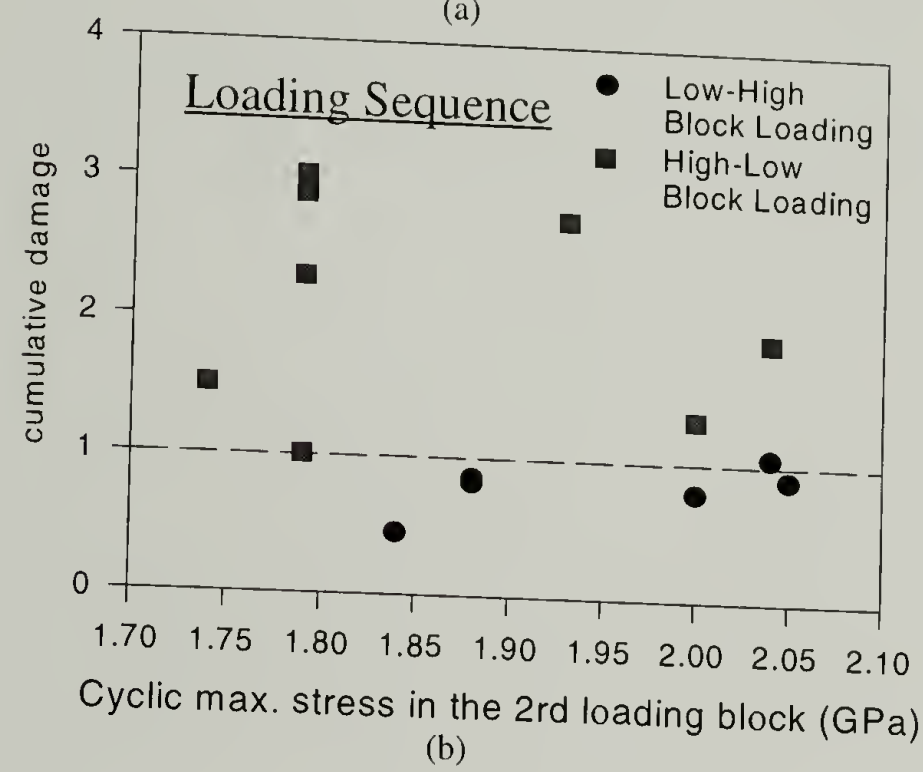

(b)

Figure 3.11 The fatigue lifetime of Kevlar® 29 at different frequencies (a) and loading sequence (b); numbers in the plot (a) are the applied stress amplitude

Figure 3.11.(b) summaries the results of these experiments. $\sum n_i / N_i > 1$ for high-low blocking loading fatigue illustrates that fibers under a high-low block loading fatigue have longer lifetime than low-high block-loading, where $\sum n_i / N_i < 1$.

An explanation of the effects of frequency and loading sequence will be given in 3.4.3.3.

3.4.1.3 Effect of Twist

A study and model development of twist effect on yarn properties was conducted in this dissertation and is discussed in Chapter 4. Related terminology is also listed in Chapter 4. To integrate our study of the influence of different factors on the fatigue behavior of high performance fibers, some results related to the effect of twist on the fatigue behavior are presented in this chapter.

Kevlar® 29 was chosen as a model material to study the effect of twist on the fatigue properties. Figure 3.12 shows that a slight twisting, a twist degree of 2 tpi, which means 2 turns for a length of 1 inch, increases the fatigue strength while the fatigue strength index remains relatively unchanged. Therefore, under the same loading condition, twist yarns have nearly a

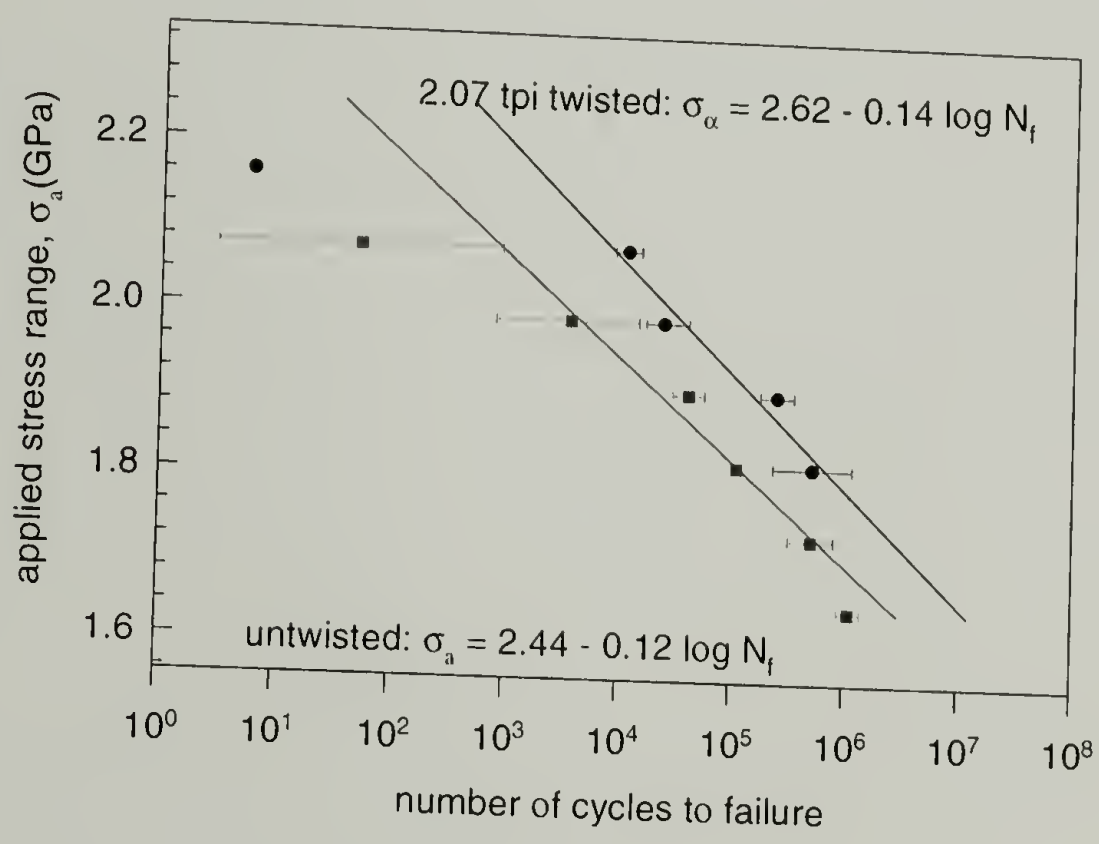

Figure 3.12 Difference in lifetime for untwisted and twisted yarns under fatigue loading

decade longer lifetime. Figure 3.13 summarizes the change in different properties with the degree of twist. It shows that the tenacity and the fatigue property change in a similar manner. It can be postulated that an interlocking mechanism may give rise to the higher tenacity and good

fatigue performance at small degrees of twist, whereas transverse crushing failure will destroy the material at high twist. This aspect is addressed in more detail in the section on the morphological characterization of twisted yarns. (See 4.4.6)

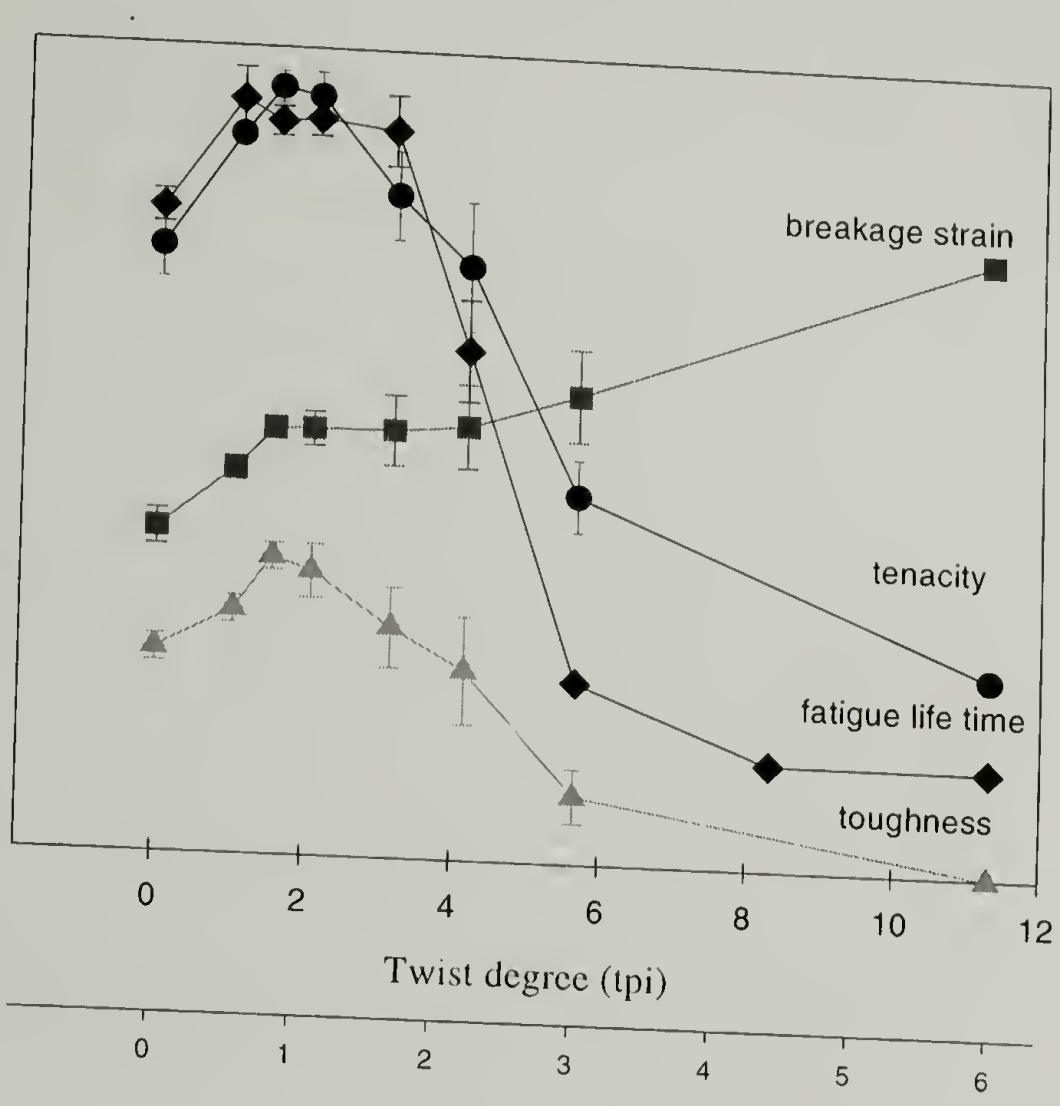

Figure 3.13 Fiber properties as a function of the degree of twist for Kevlar® 29 yarn

3.4.1.4 Effect of Temperature

Fatigue of Kevlar® 29 fiber yarns under elevated temperatures was studied. Figure 3.14 shows that temperature has a strong influence on the fatigue lifetime of the material. The lifetime of Kevlar® 29 fiber at 60 °C is only 1% of that at ambient temperature.

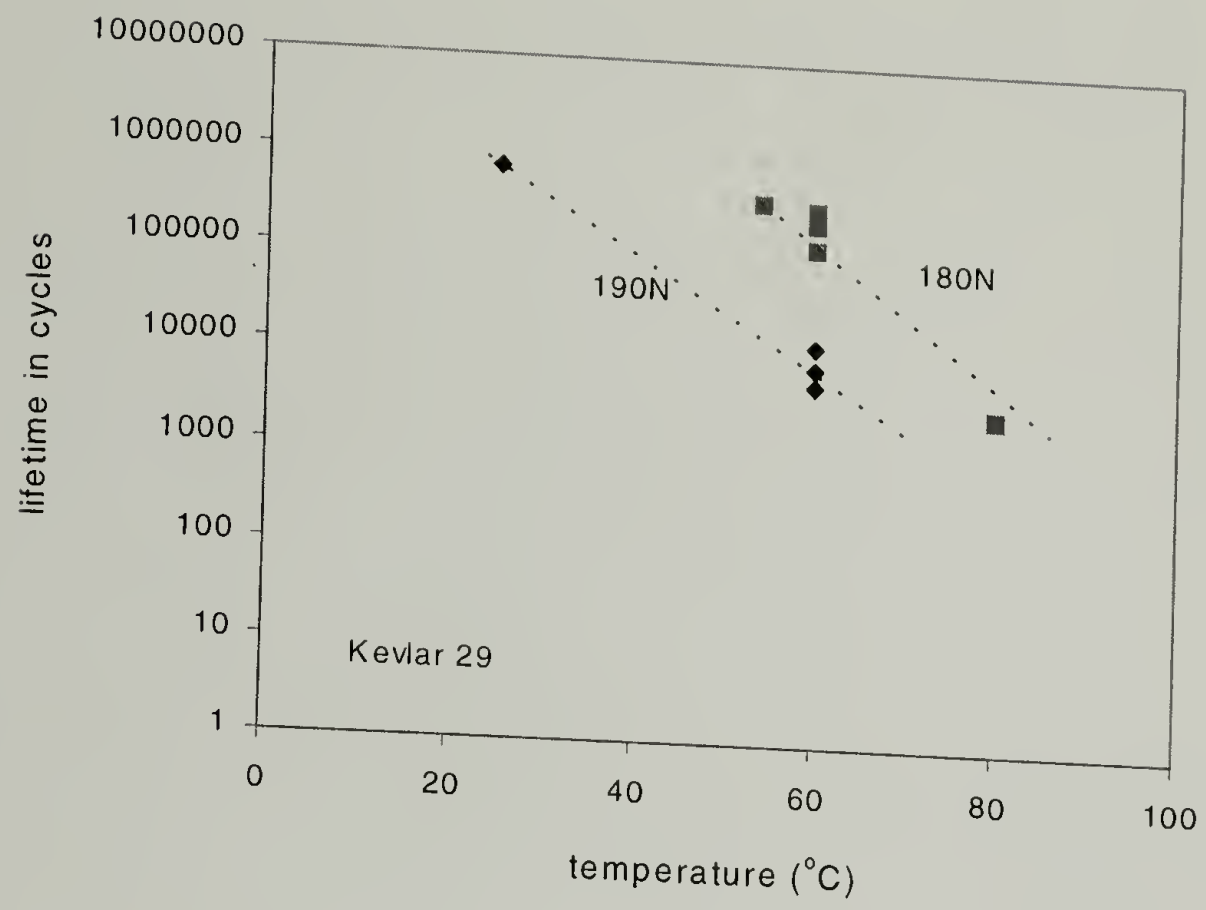

Figure 3.14 Fatigue lifetime at different temperatures.

3.4.1.5 Comparison among Different Fibers

The fatigue of different high performance fibers, different Kevlar® fibers, Technora®, Spectra® and Vectran®, was studied. There are two purposes for the study. One is to generate a general lifetime principle for these fibers; and the other is to compare the fatigue properties of different fibers. In our study, different high performance fibers exhibit the similar linear relation between the applied stress level and the logrithmic lifetime in cycles. Figure 3.15 displays a summary of the fatigue properties of different fiber yarns.

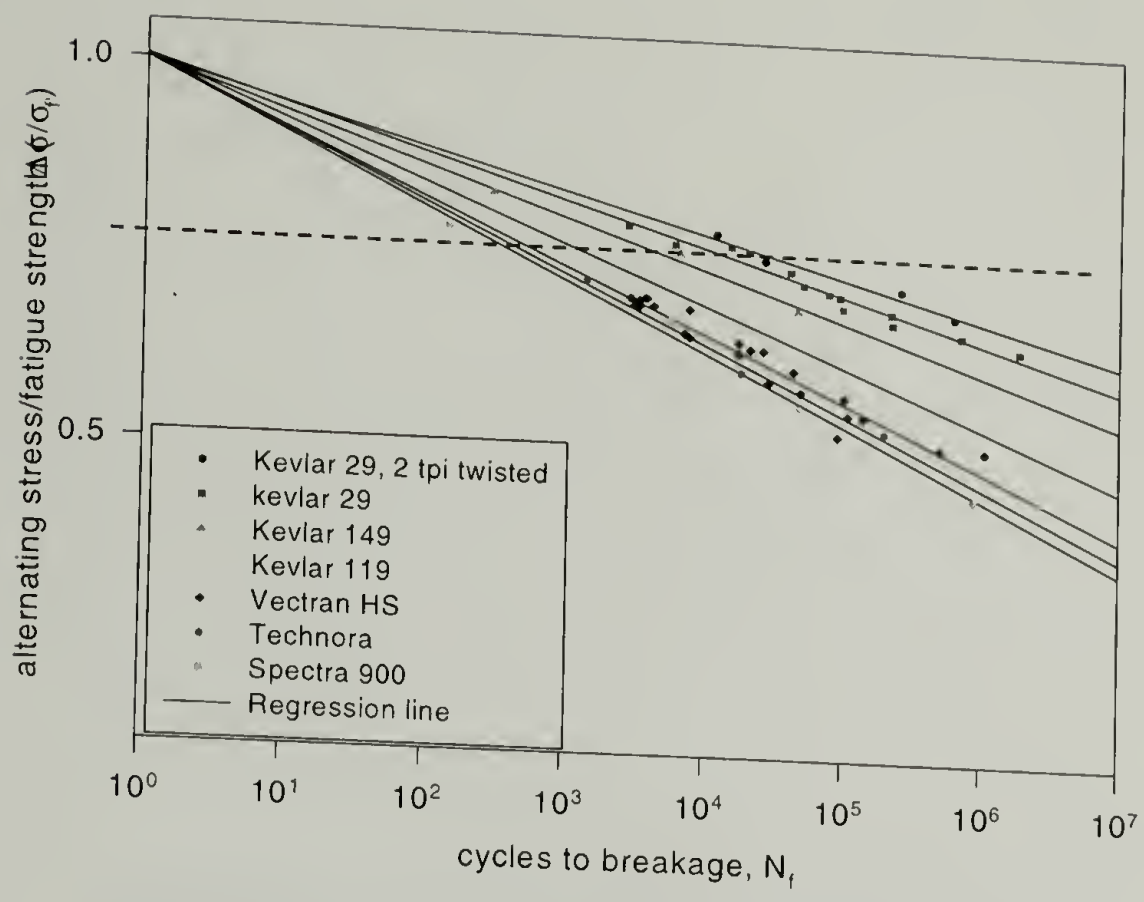

material	strength ratio $\sigma f/\sigma ts$	fatigue strength index, m
Kevlar 29, twisted	0.95	0.023
Kevlar 29	1	0.025
Kevlar 149	1.12	0.028
Kevlar 119	1.16	0.032
Vectran HS	1.06	0.039
Spectra 900	0.94	0.038
Technora	0.92	0.039

Figure 3.15 Fatigue lifetime of different fiber yarns

The ordinate is normalized by the respective fatigue strengths for direct comparison. The various fiber yarns can be ranked in the order of decreasing fatigue resistance as Kevlar® 29, Kevlar 149®, Kevlar 119®, Vectran HS®, Spectra 900® and Technora® according to the fatigue strength index shown in the table in Figure 3.15. The fatigue strength, obtained by linear regression of data in each case, is found to correlate directly to the tensile strength because the tensile stretching corresponds to a special case of fatigue where the material lifetime is only one half cycle.

It is worthwhile to point out that the fatigue strength indices for these fiber yarns are comparable to those obtained by Landgraf [122] who studied the fatigue of hardened steel for small strains. One difference is that a power law instead of a semilogarithmic law is found in the fatigue of metals:

$$\frac{\Delta\varepsilon_e E}{2} = \sigma_a = \sigma_f'(2N_f)^b$$

Equation 3.11

where $\Delta\varepsilon_e$ is the elastic strain amplitude, E is the modulus, σ_a is the fatigue stress amplitude (1/2 of the stress range in this particular case), σ_f' is the fatigue strength coefficient, N_f is the number of cycles to failure and b is called the fatigue strength exponent. Indeed, if a narrow range of stresses is used, these two types of relation are essentially equivalent.

The b value for steel at small strain is –0.06, which is comparable to the m value of the fibers, about –0.03. Although these values are similar, the metals exhibit a higher fatigue strength index when subjected to a high strain range[111], whereas the polymeric fibers do not show such a transition. For example, when Kevlar® is subjected to a large stress amplitude range (50 - 95% of tensile strength), as in Figure 3.9, the data falls on a single curve without any transitions. The transition in metals appears because the plastic strain at higher stress range is much larger than the elastic strain at low stress. The low hysteresis in one cycle of the fatigue of fibers at all stress levels indicates that there is no such transition.

3.4.2 Fatigue of High Performance Fibers—Competition between Perfection and Damage

To elucidate the mechanism of fiber fatigue, retrieved dynamic data at various stages of fatigue were analyzed and different mechanical and structure characterizations have been performed.

It is found that fatigue does not always mean damage to the material. Early stage of fatiguing is seen to improve the mechanical properties of high performance fibers. The structure analysis explains that the enhancement of the properties is due to the perfection in the structure.

A preliminary study of the property enhancement by cyclic mechanical conditioning was conducted. After subjecting the Kevlar® 29 yarn to high amplitude fast oscillating stress (1.99 GPa) for 10 cycles, the sample was removed from the tester and allowed to recover at ambient temperature for a day before further measurement. Table 3.3 shows an increase in the initial modulus by 23 percent and a small increase of 5 percent in strength for short-period fatigued fibers.

Table 3.3 Mechanical properties of as spun yarns and yarns being short-term fatigued

Material	Tensile Modulus (GPa)	Tensile strength (GPa)	Strain to break(%)	Diameter (μm)
as spun fiber	70.0(0.4)	2.79(.27)	3.0(.3)	13.2(1)
conditioned fiber*	**86.0(1.0)**	**2.93(.51)**	**2.0(.3)**	13.2(1)

*Treatment Condition:
Cyclic loading with triangular waveform applied to Kevlar 29 fiber yarn
Maximum cyclic load=230N/1.99 GPa, 10 cycles totally. Ambient storage: 1 week

The x-ray diffraction patterns (Figure 3.16) show improved orientation of the crystals after this mechanical conditioning treatment, while the transverse crystal sizes does not change. This indicates that reorientation occurs when the fiber is subjected to the external stress. This leads to a possible new route for post-treatment of fiber by oscillating stress at elevated temperature. The change in modulus upon deformation has been discussed by many researchers [62]. Erickson [62] has compared the modulus of fibers at the earlier stage and later stage of creep and the modulus of later creep is about 6 percent higher than that at the beginning. It is seen that the increase in modulus by cyclic loading is larger than that by static loading. This suggests that

cyclic loading facilitates the internal structure alternation and supports a model of boundary slip induced chain axis rotation instead of a lattice deformation model.

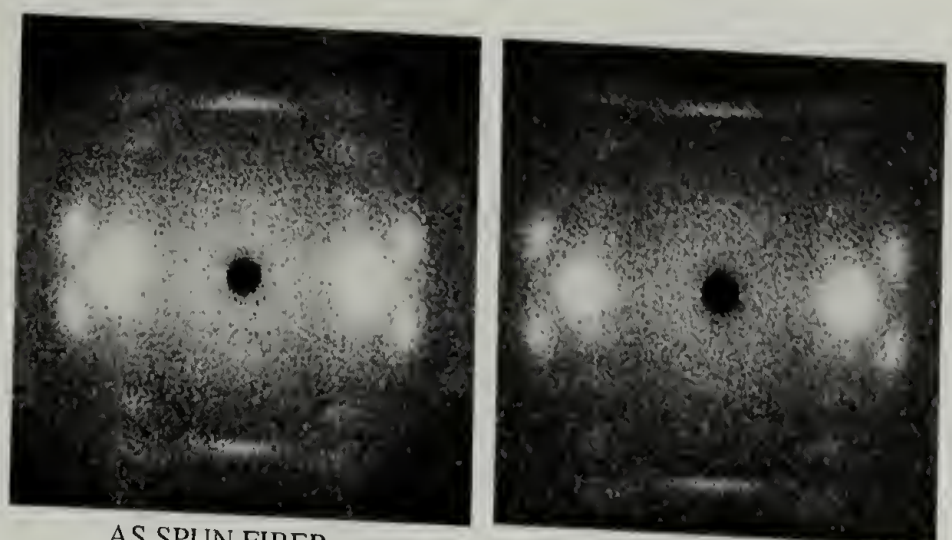

AS SPUN FIBER CONDITIONED FIBER

Type of Fiber	Kevlar 29 as spun	Kevlar 29 conditioned
$\langle\cos^2\Psi_{X,200}\rangle$	0.955	0.965
order parameter S	0.93	0.95
$\Psi_{X,200}$	12.2 (0.5)	10.8 (0.5)
Apparent crystalline size,Å		
plane (002)	656	———
plane (110)	52	57
plane (200)	46	51

Figure 3.16 X-ray diffraction pattern and some structure parameters of crystals in as spun fiber and those being short-term fatigued

Based on the above discussion, it is important to distinguish the perfection of the structure from the damage when the material is being subjected to cyclic loading. Figure 3.17 compares the stress-strain curves at the initial stage and later stage of fatigue for Kevlar® 29 fiber. The hysteresis always decreases with the number of cycles during structure perfection.

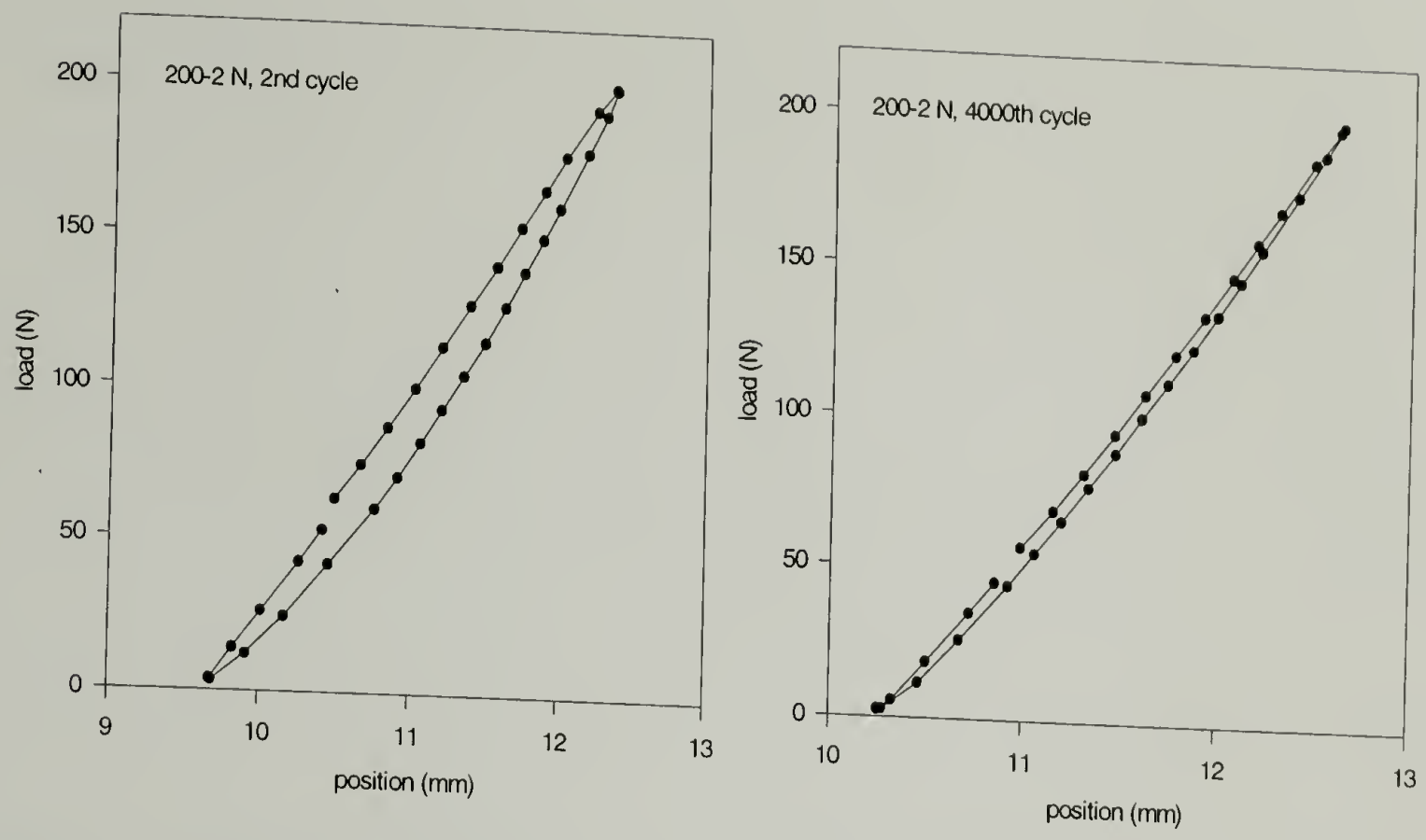

Figure 3.17 Load-displacement curves of one cycle in different stages of fatigue

An energy dissipation calculation has been carried to quantify the hysteresis. Instead of trying to integrate the stress-strain curve, an easy way was adopted by fitting the stress-time data and strain-time data into a sinusoidal function and using the phase lag to characterize the energy dissipation. Figure 3.18 shows that phase lag tan δ initially decreases rapidly with the number of loading cycles and then reach a constant of 0.033 around 10^3 to 10^4 cycles for a cyclic loading of a stress amplitude of 1.64 GPa. Also, the increase in modulus stops when tanδ plateaus. Considering the modulus change as the indicator of property change, this transition in tanδ and modulus can be viewed as a perfection-damage transition. The energy dissipation diagrams under different stress amplitudes were analyzed. It is found that the observed number of loading cycles at the transition corresponds to 0.1 to 1 percent of the lifetime of the material and is found independent of stress amplitudes. Additionally, for higher stress amplitude, the plateau tanδ is higher, which indicates higher energy dissipation.

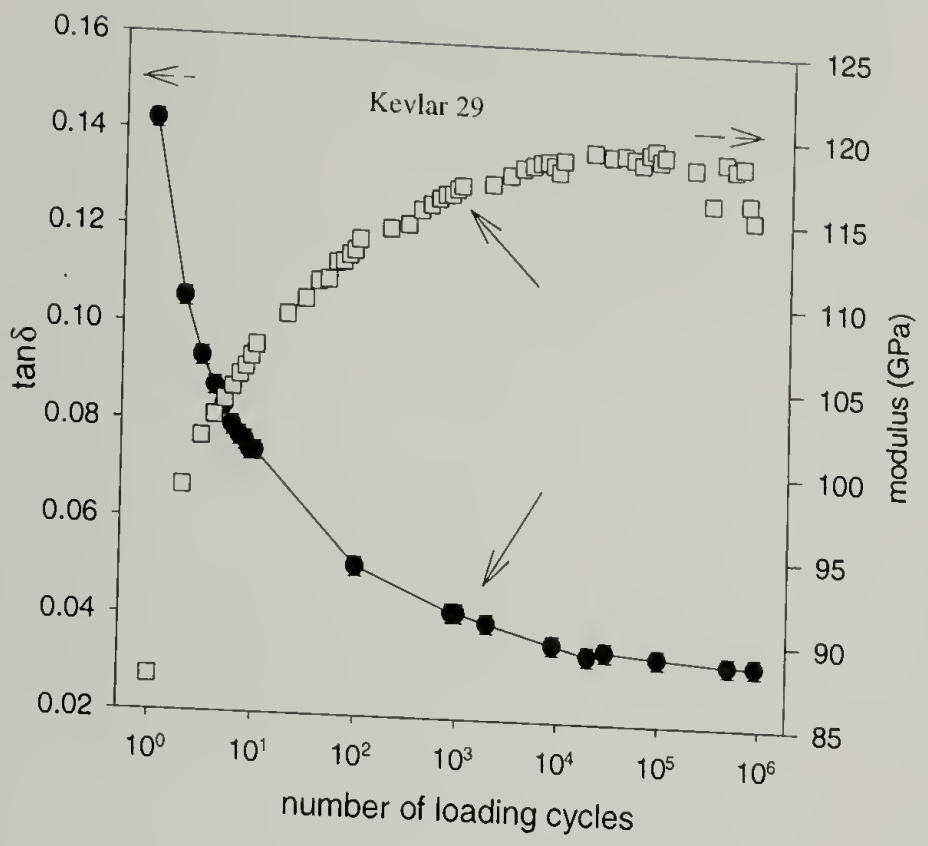

Figure 3.18 Structure perfection to fatigue damage transition indicated by energy dissipation; fatigue stress range is 1.7 GPa (stress level of 0.7)

The same analysis was also applied to the fatigue of Vectran® HS fiber. Figure 3.19 indicates that the energy dissipation of Vectran® HS fiber during fatigue undergoes a similar

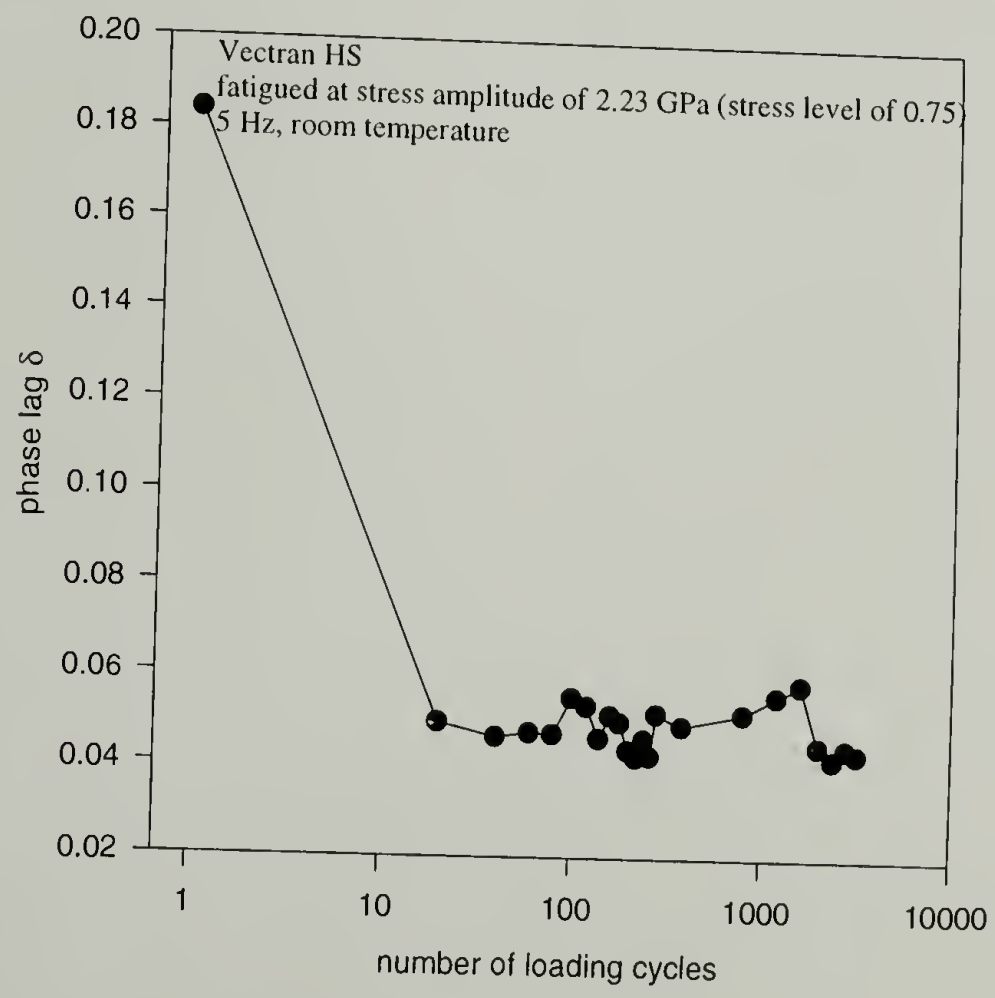

Figure 3.19 Energy dissipation along fatigue in Vectran® HS fiber yarn

transition to Kevlar®. We also observed that the plateau tanδ in Vectran® HS fiber is higher than that of Kevlar® 29 fiber under the same relative stress level. This might explain why Kevlar® 29 fiber has longer lifetime than Vectran® HS at the same stress level if a constant energy dissipation is assumed to destroy the material.

This enhancement of properties after short-term fatiguing was observed for all the high performance fibers investigated. Figure 3.20 shows the modulus change with the loading cycles for different fibers. All show modulus increases during the initial stage of fatigue while the ratio of enhancement is different for different fibers. Kevlar® 29 exhibits the highest increment in modulus upon cyclic loading and Kevlar® 149 exhibits the least increment.

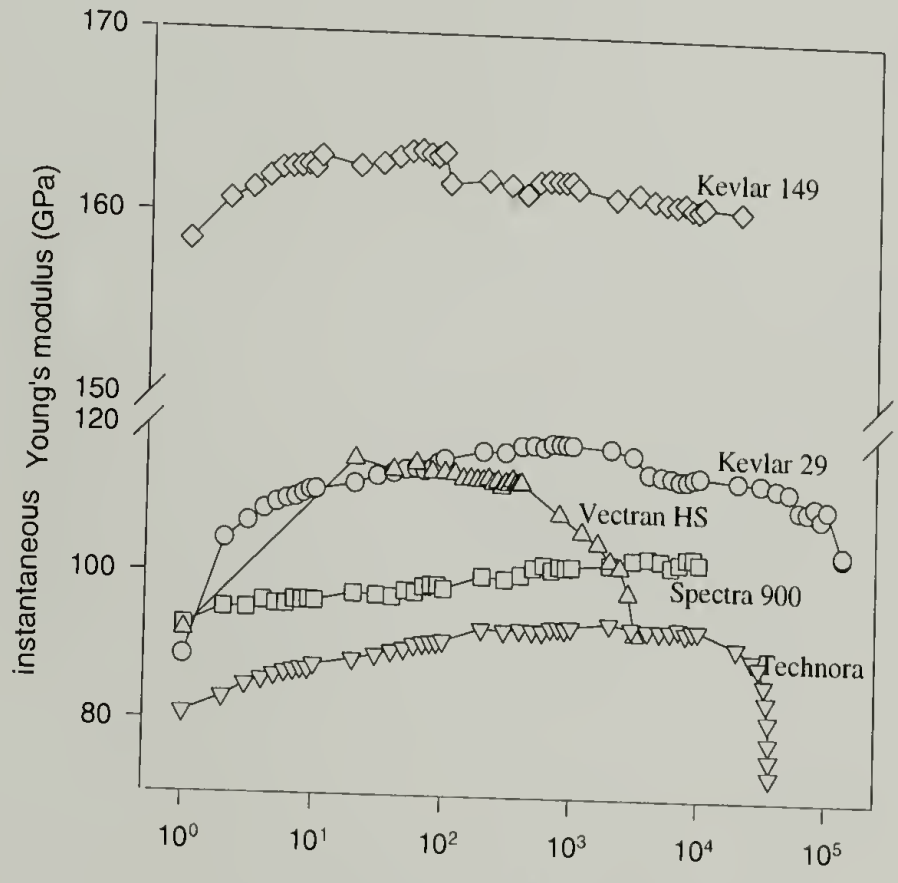

material	Eo (GPa)	Ep (GPa)	Ep/Eo
Kevlar29	88.6	117	1.32
Kevlar149	158	160	1.01
Spectra900	92.8	105	1.13
VectranHS	92	113	1.23
Tcchnora	80.9	93	1.15

Figure 3.20 Change of Young's modulus with the number of loading cycles for different fibers. E_0 is the initial modulus and E_p is the plateau modulus.

It is interesting to notice that for Spectra® 900 fiber the modulus almost increases linearly with the number of loading cycles as shown in Figure 3.21. The applied loading stress range is low for this experiment (0.3 of the static strength) and the material is far from failure.

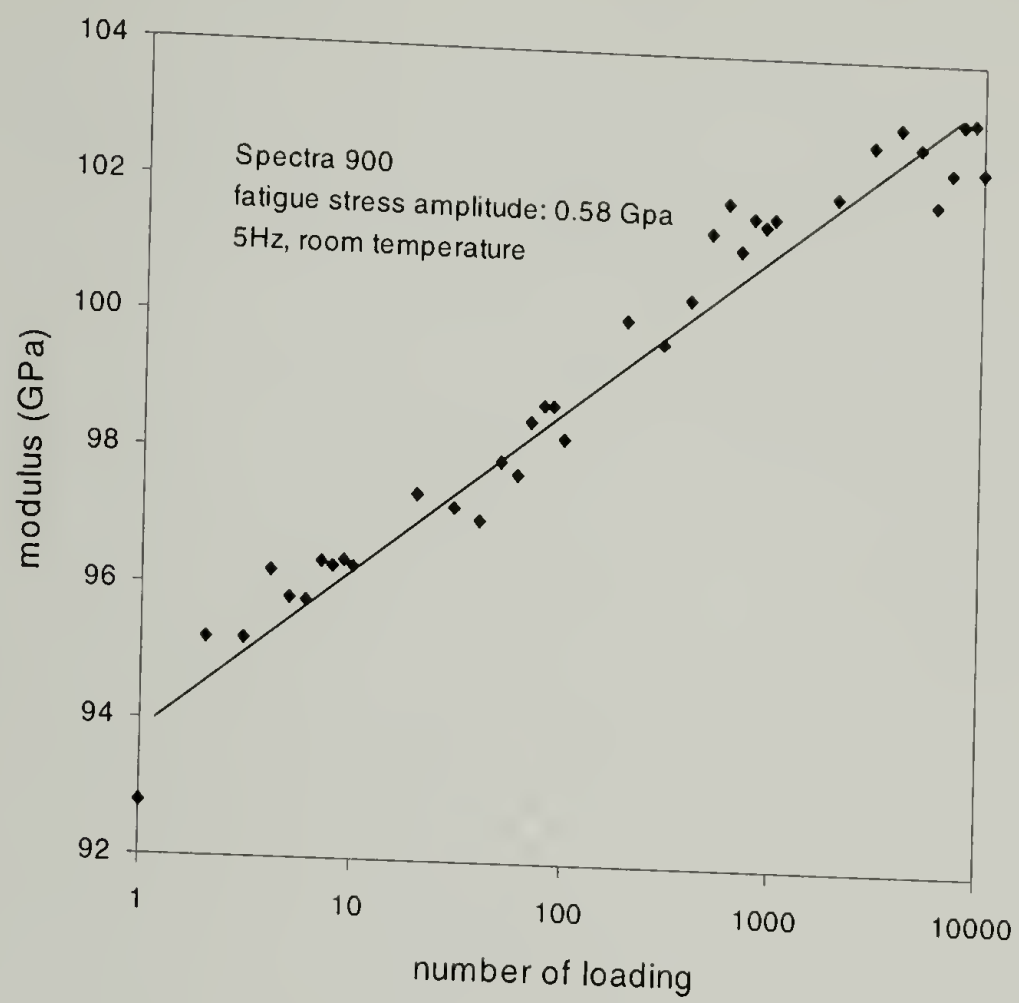

Figure 3.21 Modulus change with the loading cycles in a Spectra® fiber

The listed initial moduli in Figure 3.20 are higher than those in tensile testing reported in Chapter 2. These two moduli are different in that the moduli in Chapter 2 refer to the initial modulus, which was evaluated in a strain range lower than 1%, while here the moduli are the average moduli along loading in the initial cycle. For fibers such as Kevlar®, Vectran® and Technora®, this explains the discrepancy and if we calculate the modulus using a higher stress range in a tensile test, the obtained modulus is close to what we listed in Figure 3.20. However, for Spectra® 900, this does not explain the data. Strain rate is another factor that attributes to the difference in the moduli of Spectra® 900. The strain rate in our tensile test is 10%/min, while a fatigue experiment is done at 5 Hz. The strain rate in a fatigue experiment is therefore 5 times

faster than that in a tensile test. This higher strain rate in a fatigue experiment results in a higher value for the initial modulus.

3.4.3 Deformation and Failure Criteria in Fatigue and Creep

To better understand the fatigue mechanism, the fatigue deformation was carefully examined. The simultaneous stress-strain data recorded along fatigue allows us to study the fatigue deformation with the number of loading cycles. There are two variables characterizing the fatigue strain: cyclical minimum strain and cyclical maximum strain. A cyclical minimum strain is the instantaneous strain in the material when the applied stress reaches minimum (close to zero stress) and a cyclical maximum strain is the instantaneous strain in the material when the applied stress reaches the maximum. A cyclical minimum strain therefore represents the instantaneous permanent deformation in the material.

It was found that the deformation in the fiber yarns during fatigue is very well represented by certain equations. This dissertation also discloses a criterion for a series of high performance fibers to fail under different loading modes.

3.4.3.1 Fatigue Deformation

The development of the cyclical minimum strain in fatigue under different stress amplitudes in Kevlar® 29 yarns is shown in Figure 3.22. This permanent deformation was found to increase with the number of loading cycles in a semilogrithmical manner until the failure point. The higher the stress range, the higher the cyclical minimum strain at the end of first cycle and the faster this strain increases with the number of loading cycles.

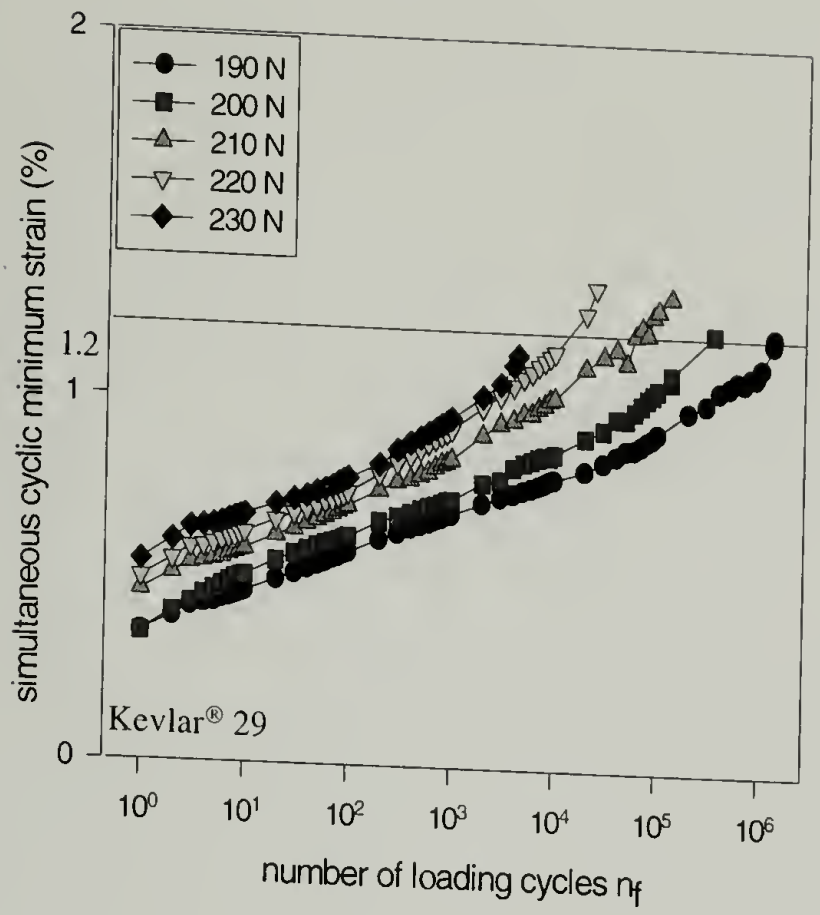

Figure 3.22 Permanent deformation during fatigue in Kevlar® 29 fiber yarns; legends are the applied stress amplitudes

More precisely, an equation of the following form describes the deformation in fiber as shown in Figure 3.23:

$$\varepsilon_{\min} = a + b \cdot \ln n_f + c \cdot n_f$$

Equation 3.12

where ε_{min} is the simultaneous strain at minimum stress in one cycle; n_f is the number of loading cycles; a, b and c are regression parameters. c is found very small and the contribution of the third term is negligible. Equation 3.12 can be simplified as

$$\varepsilon_{\min} = a + b \cdot \ln n_f$$

Equation 3.13

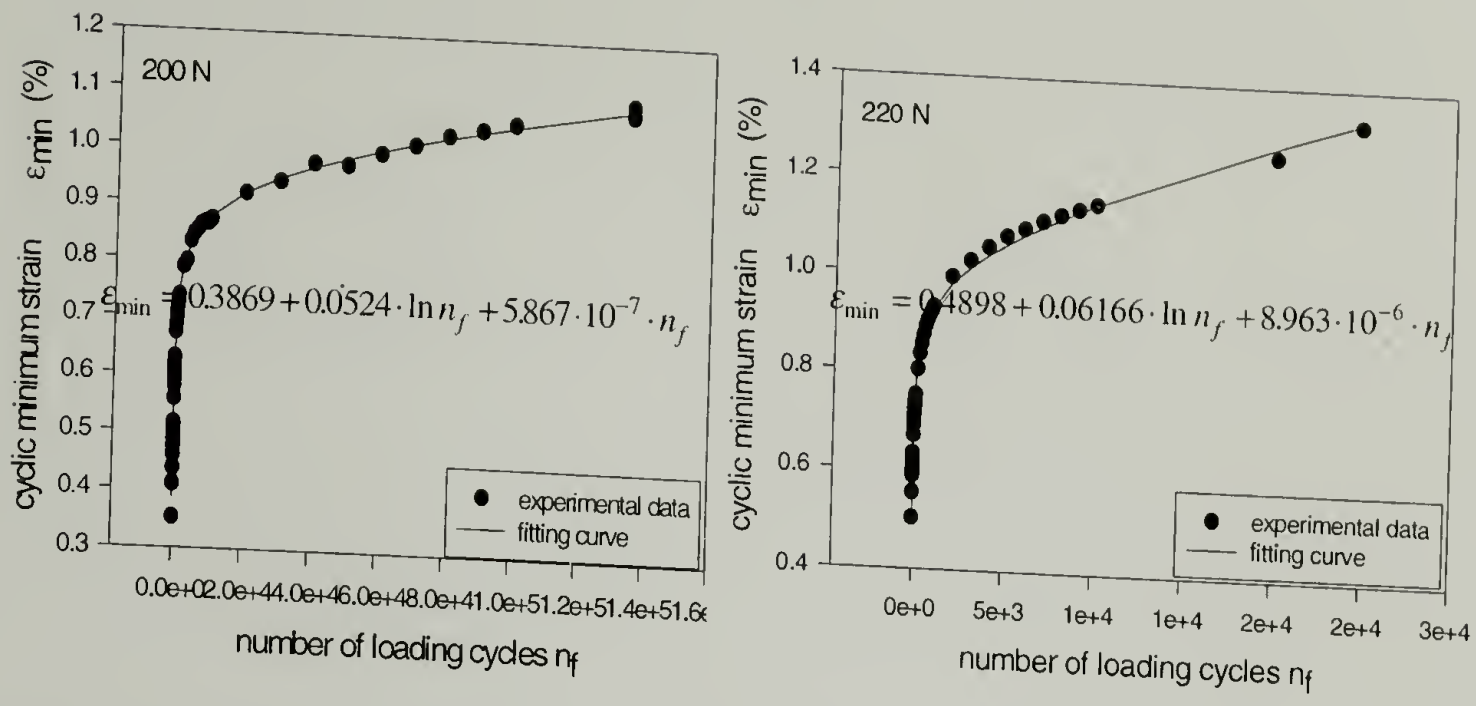

Figure 3.23 Fitting results of the development of cyclic minimum strain with number of loading cycles in fatigue-till-rupture experiments. In the plots, numbers are the applied load amplitudes. Equations are fitting functions.

Figure 3.23 clearly shows that there is a relative large deformation in the first cycle, 0.3 to 0.5 % depending on the applied stress range. This initial deformation is caused by the reorientation of the crystals that improves the modulus. Using the structure parameters listed in Figure 3.16, the orientation angles before and after short time fatiguing, a 0.5% deformation is calculated for the perfection period, which is consistent with the observation of the fatigue deformation.

Equation 3.13 also describes the fatigue deformation of other fibers: Vectran® HS (Figure 3.24) and Spectra® 900 (Figure 3.25). Figure 3.24 shows the cyclical maximum strain change till rupture in Vectran® HS fiber yarns and Figure 3.25 shows the cyclical maximum strain change in Spectra® 900 (not to failure). We generalize that cyclical minimum strain in a high performance fiber under fatigue follows a semilogrithmical principle.

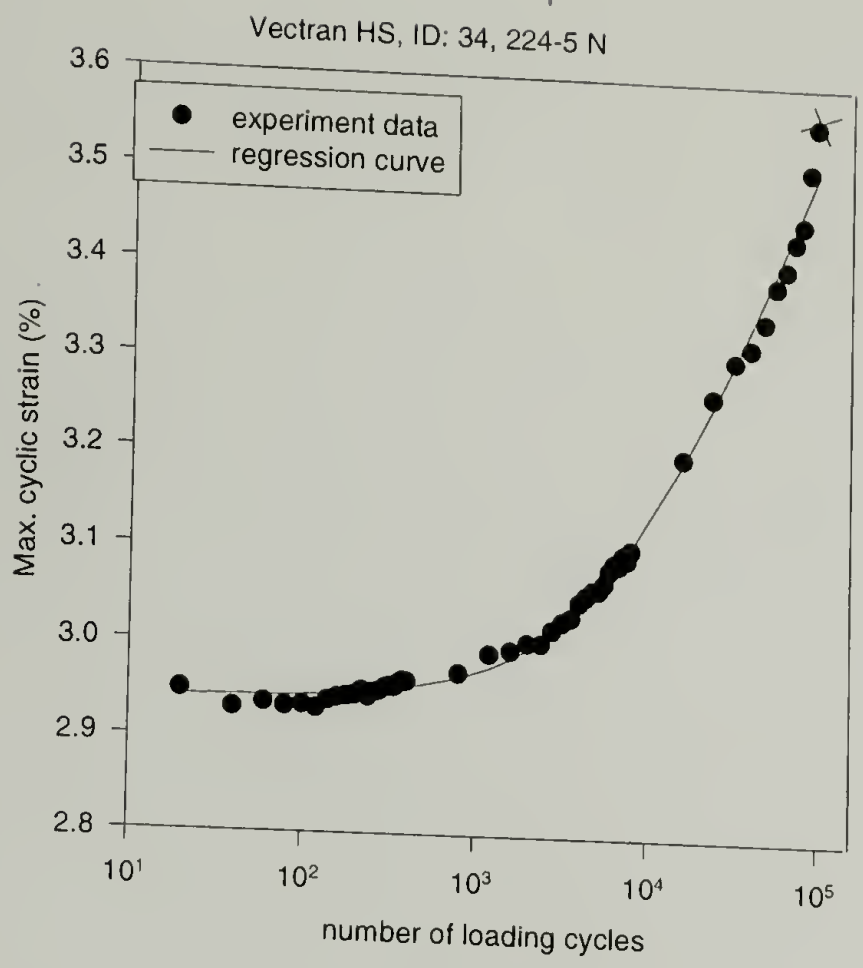

Figure 3.24 Fatigue-strain development in Vectran® HS.

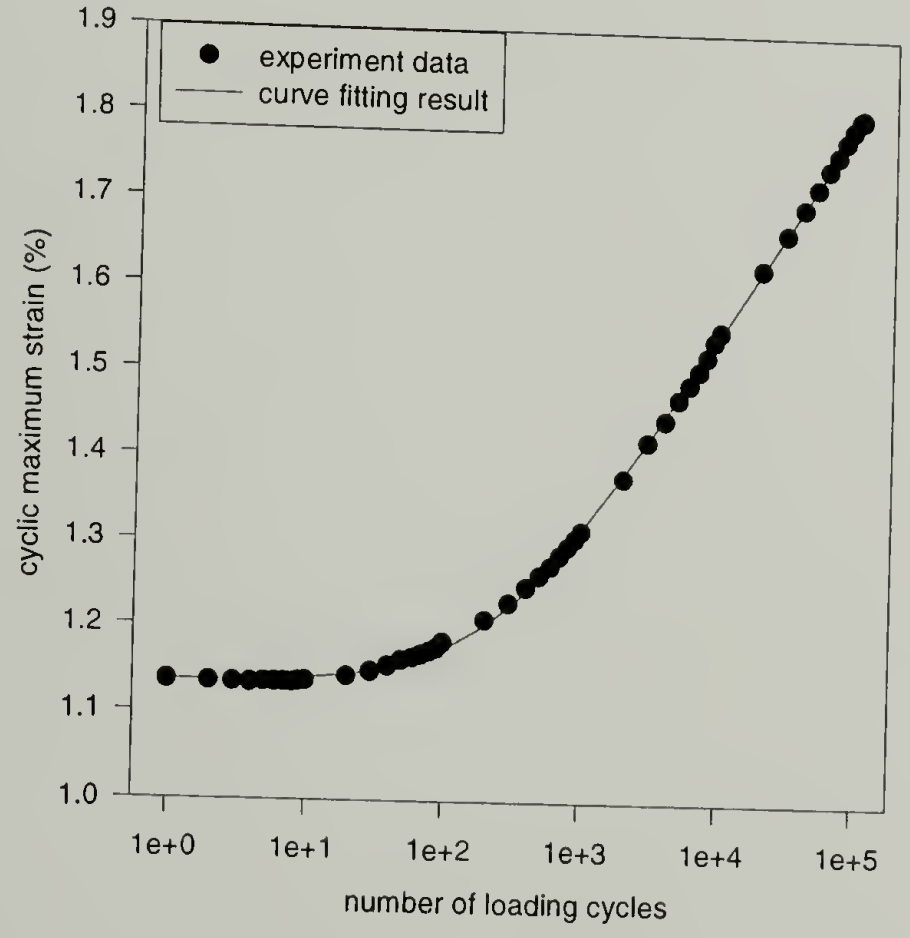

Figure 3.25 Strain development in a fatigue of Spectra® 900 fiber yarn

3.4.3.2 Failure Criteria for Different Failure Modes in High Performance Fibers—Fatigue, Creep and Tensile

It was found that high performance fibers fail under fatigue when the instantaneous strain reaches a critical value regardless of the stress amplitude. This is illustrated in Figure 3.26 for Kevlar® 29 fiber. This failure criterion of ***constant strain at break*** is also observed in the creep of high performance fibers shown in Figure 3.27. The value of the strain at break under fatigue or creep is the same as that in a tensile test (Table 2.1). This result is also observed in Vectran® HS and presumably extends to other high performance fibers. This illustrates that the failure is strain determined and might be derived through a shear failure mechanism. A correlation between damage and permanent deformation is then proposed for studied high performance fibers. An application of this is that a strain gauge can be embedded in a fiber yarn to indicate the useful material lifetime.

The failure criterion for high performance fibers can then be stated as: ***There is a critical strain at which the fiber fails independent of the stress history.***

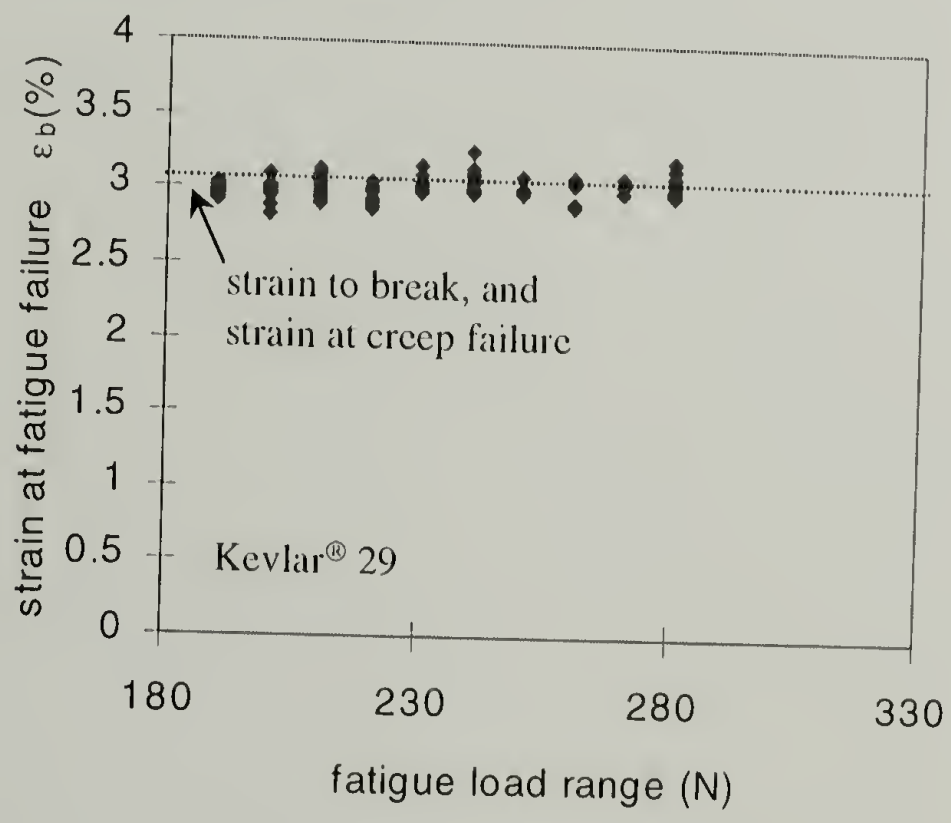

Figure 3.26 Strain at fatigue break under different applied stress amplitudes in Kevlar® 29 fiber yarns

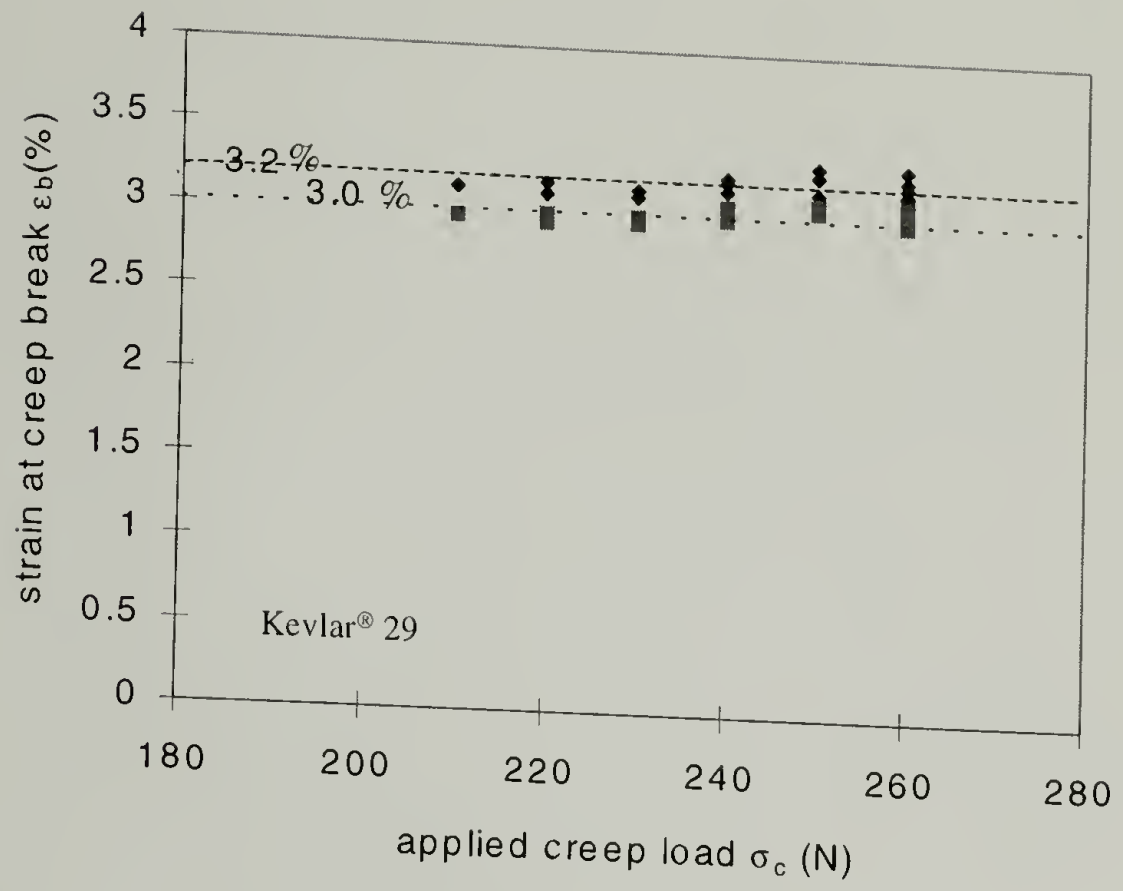

Figure 3.27 The strain at break under creep for different applied loads; the upper line of "3.2%" is the ultimate strain at break, and the lower line of "3.0%" is the onset strain for tertiary creep

3.4.3.3 Application of the Deformation-damage Correlation in Explaining General Fatigue Behavior

Since the deformation reflects the damage in a fatigued fiber, the simultaneous record of deformation helps to understand the influence of several factors on fatigue behavior discussed in 3.4.1.

3.4.3.3.1 Frequency Effect

Figure 3.28 illustrates that the fatigue deformation follows similar paths under different test frequencies. Therefore, the fatigue lifetime of Kevlar® shows a characteristic of number-of-cycle determination instead of a loading-time determination.

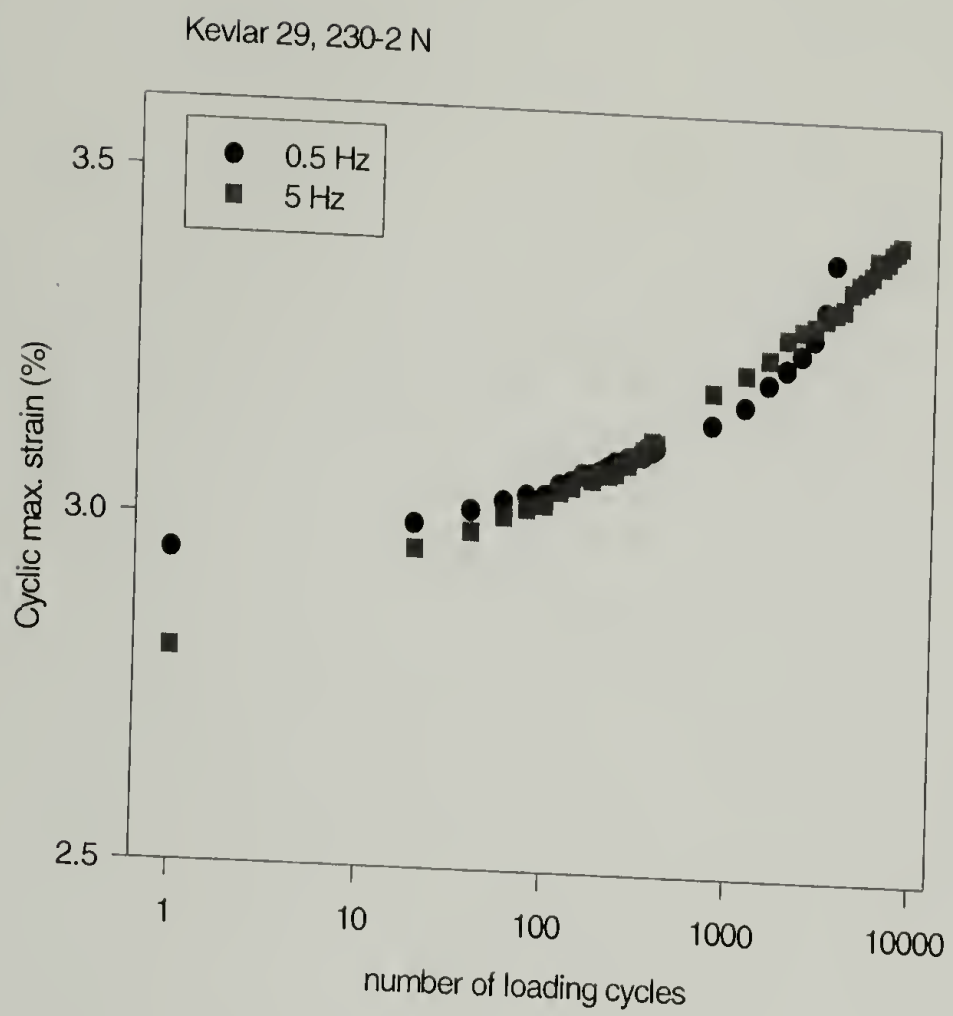

Figure 3.28 Fatigue deformation under different frequencies

3.4.3.3.2 Stress Sequence Effect

It was observed that a high-low block loading gives a longer lifetime than that predicted by the cumulative damage model. It might be due to the fact that recovery competes with the deterioration process when the second block loading is applied. This hypothesis is supported by the observation of deformation development in a stress sequence experiment. When the cyclic maximum strain development was used to monitor the damage along a fatigue experiment, a delay in the propagation of damage was observed after applying the low loading block in a high-low loading experiment. However, no such behavior occurs in a low-high block experiment. Figure 3.29 illustrates such a "healing effect".

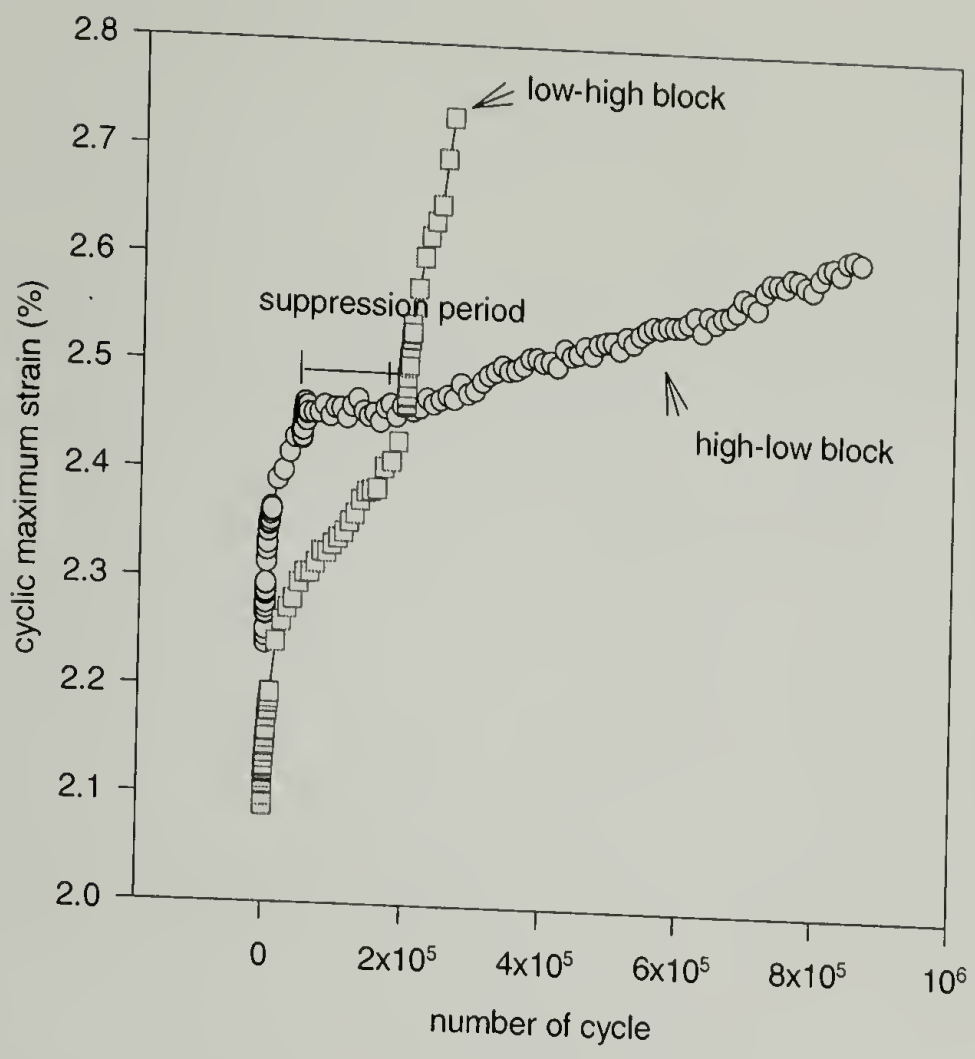

Figure 3.29 Strain behavior in an experiment of fatigue loading sequence

These results can be interpreted using a linear superposition law to calculate the cumulative damage, after two different blocks of loading are applied.

It was found from the results of fatigue behavior study that the increase in the cyclic maximum strain during the cyclic loading reflects the overall damage, and develops linearly with the logarithm of the number of loading cycles.

Considering that, the strain profile, which is shown correct in Equation 3.13, is the following:

$$\varepsilon_{\max} = \sigma_a (a' + b' \ln n_f)$$

where ε_{max} is the cyclic maximum strain; σ_a is the applied stress amplitude; a', b' are two regression parameters and n_f is the number of loading cycles. Considering a fixed number of high loading block n_1 and a fixed number of low loading block n_2-n_1 in a block loading

experiment, a comparison of final damage is made in terms of final permanent deformation after a high-low block and low-high block.

For a high-low block loading,

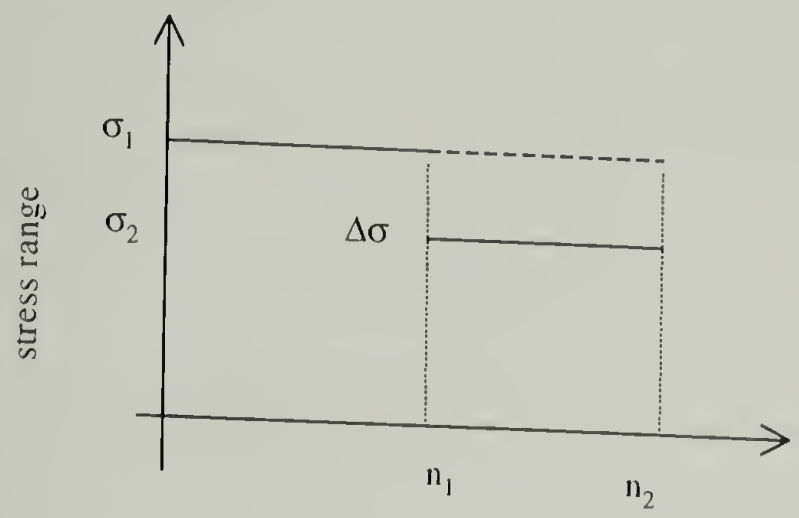

the deformation at the loading cycles of n_2 is

$$\varepsilon_{hl}(n_2) = \sigma_1(a' + b' \ln n_2) - \Delta\sigma(b' \ln(n_2 - n_1) + a')$$

while for a low-high block loading,

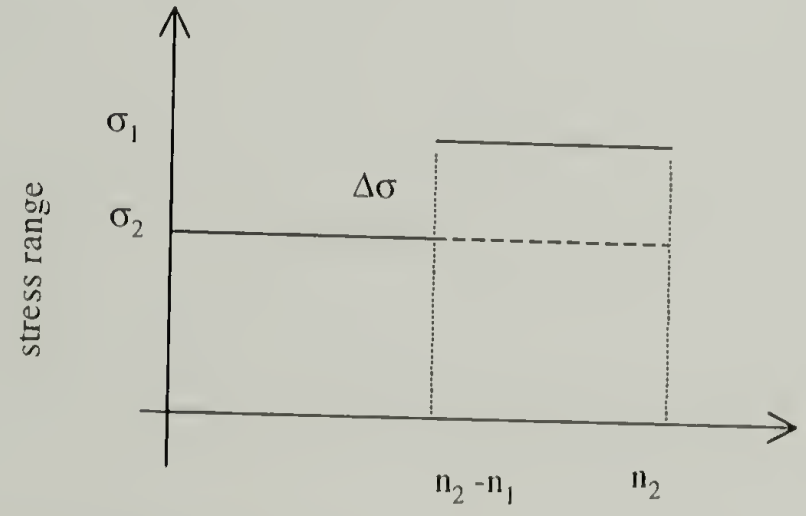

the deformation at the loading cycles of n_2 is

$$\varepsilon_{lh}(n_2) = \sigma_2(a' + b' \ln n_2) + \Delta\sigma(a' + b' \ln n_1)$$
$$= \sigma_1(a' + b' \ln n_2) - \Delta\sigma a \ln(n_2 / n_1)$$

Therefore,

$$\varepsilon_{hl}(n_2) - \varepsilon_{lh}(n_2) = -\Delta\sigma b' \ln((n_2 - n_1)n_1 / n_2) - \Delta\sigma a'$$
$$\therefore \varepsilon_{hl}(n_2) < \varepsilon_{lh}(n_2) \qquad \text{at } 1 < n_1 \leq n_2 - 1$$

In these equations, ε is the cyclic maximum strain; and the subscripts *lh* and *hl* denote a low-high loading block and a high-low block respectively. All parameters are positive. Since the deformation, the cyclical maximum strain, at the end of the loading profile is smaller in a high-low block loading experiment than that in a low-high block loading experiment, it is concluded that the damage caused by the low-high loading is bigger than that by high-low loading.

What this derivation means is that the cumulative principle is generally correct. However, the effective linear cumulative quantity varies with the system. In high performance fibers, the relation between damage and lifetime is not linear. Therefore, Miner's law is invalid. However, the damage, or the permanent deformation, is linearly additive.

3.4.3.3.3 Temperature Effect

In 3.4.1.4, it was shown that Kevlar® 29 fiber has a shorter fatigue lifetime at elevated temperatures. Its fatigue deformation at elevated temperatures was studied to investigate the origin of this phenomenon. It was observed that the critical strain at failure for Kevlar® fiber

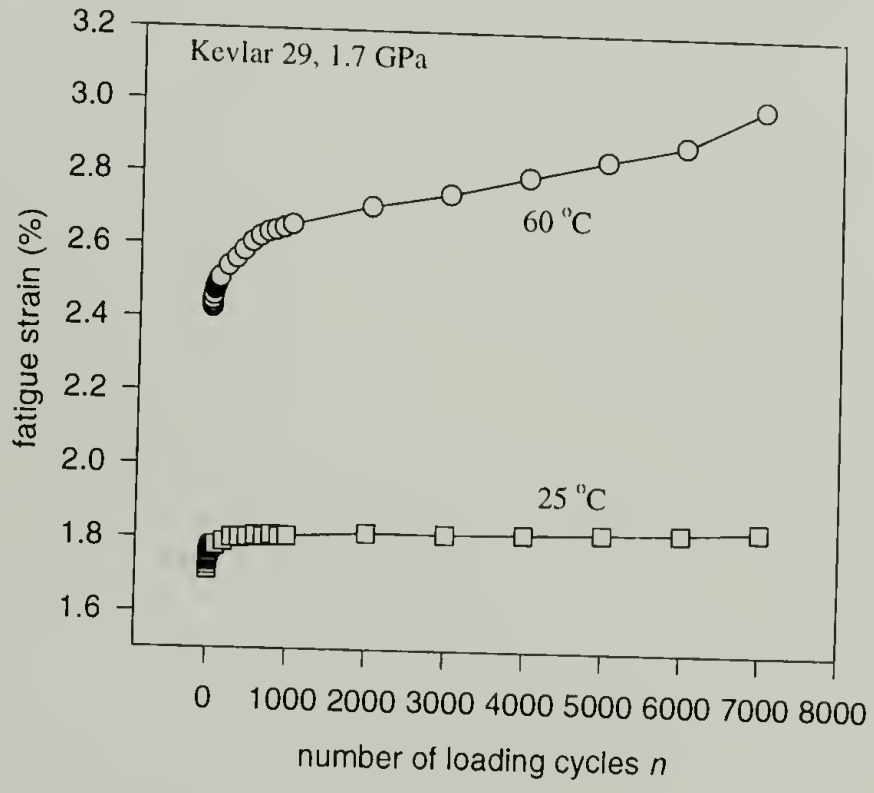

Figure 3.30 Fatigue strain in Kevlar® 29 increases with number of loading cycles at different temperatures

fatigued at elevated temperature is the same as that at ambient temperature. Figure 3.30 compares the fatigue strain of Kevlar® fiber at different temperatures. It shows that under the same loading condition, the fiber fatigued at higher temperature has a higher initial permanent deformation and faster fatigue strain rate.

The apparent activation energy for fatigue strain was calculated using the fatigue strain rate at different temperatures. From the slope in Figure 3.31, the activation energy for fatigue deformation is 10 kJ/mol. This number is very close to the activation energy reported for creep deformation[62,104]. It suggests that the deformation involves the breaking of hydrogen bonds.

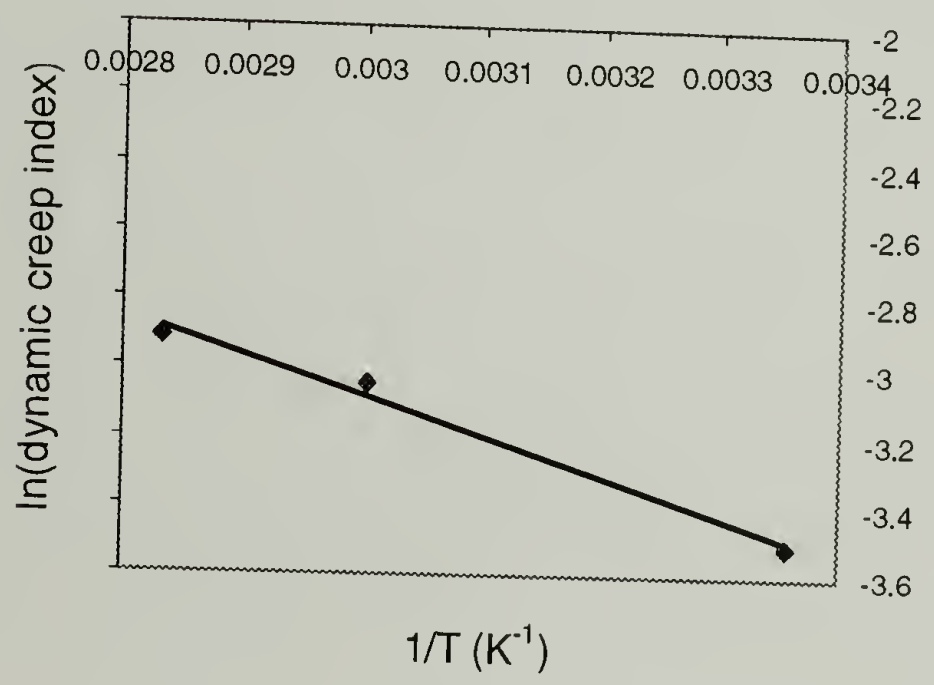

Figure 3.31 Arrhenius plot of Kevlar® 29 fatigue experiments

3.4.4 Fatigue Mechanism and Fatigue Resistance

In conventional bulk material, fatigue crack propagation is the focus in the fatigue mechanism study. Our studies show a distinctive difference of the fatigue behavior of high performance fibers from that of bulk materials reported. Although phenomenally the fatigue of high performance fibers also shows the three stages of initiation, propagation and acceleration

(Figure 3.1) as those in bulk materials, they are fundamentally different. The initiation stage in high performance fibers is actually a perfection stage. The propagation stage is a real damage stage. Therefore, our study of fatigue mechanism in high performance fibers concentrates on the understanding of the damage phase and its correlation with strain. Based on the understanding of fatigue mechanism, we will discuss the fatigue resistance in high performance fibers and what can be done to improve their fatigue properties. Figure 3.32 illustrates how we approached the damage related fatigue mechanism.

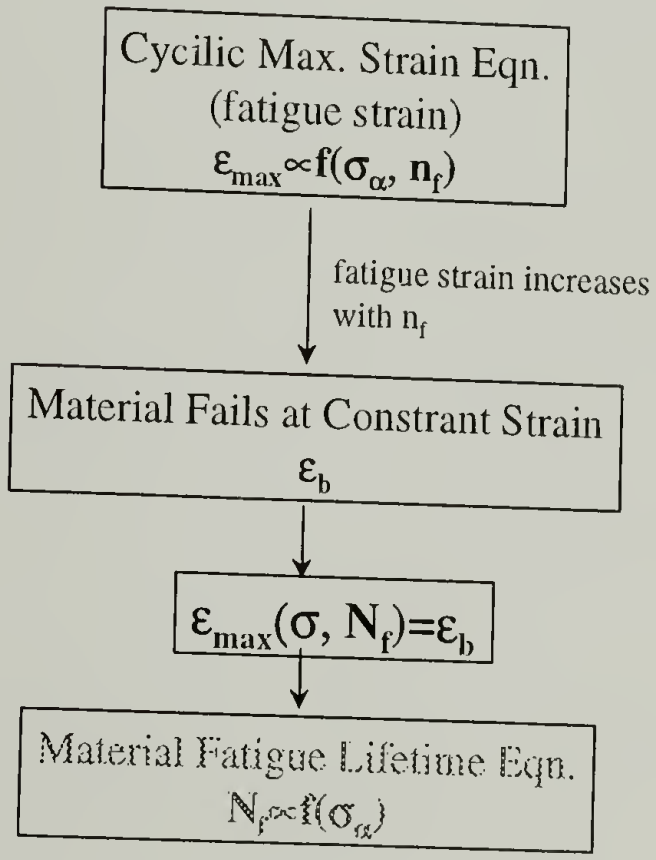

Figure 3.32 Flow diagram correlating deformation with fatigue failure in high performance fibers

The fatigue strain behavior of the fibers was discussed in 3.4.3.1 and is a function of the applied stress range and number of loading cycles. The fatigue strain is shown to increase with the number of loading cycles. The fatigue failure criterion has been identified as a **critical strain.** Therefore, at the failure cycle N_f, the fatigue strain is equal to a constant. If the function, $\varepsilon_{max}(\sigma,N_f)$, is known, a relation between the number of cycles to failure, N_f, and the applied stress range, the fatigue lifetime principle, can be derived according to Figure 3.32. If the derived fatigue

lifetime principle agrees with the empirical equation (Equation 3.9), the correlation between fatigue strain and damage is consequently proven.

3.4.4.1 The Applicability of the Concept of Dynamic Creep in Fatigue

In 3.4.3.1, the fatigue strain was shown to be affected by the applied stress range.(Figure 3.22) However, the true relation is not clear. To establish the function for fatigue strain in terms of fatigue stress range, a new concept was adopted. There are numerous studies on creep behavior concerning the relation between the creep strain and the applied load. A function of fatigue strain as the fatigue stress range was proposed based on the parallelism between creep and fatigue. In the following, it is shown that a creep deformation behavior can be derived by utilizing the viscoelasticity and deformation kinetics. This derived creep deformation behavior help to construct the fatigue deformation equation. However, it should be recognized that the following derivation is only a reference; while the real mechanism of the creep or fatigue needs further investigation.

Let us first examine the function form for a creep strain. The creep deformation behavior for Kevlar® 29 fiber can be approximated using Voigt's model and its relaxation spectrum. It is assumed that there is a flow probability for any part of the polymer chain. The activation energy spectrum of this flow is shown as the solid line in Figure 3.33.(a). The applied stress lowers the activation energy of flowing by $\sigma\upsilon$, where σ is the applied stress and υ is the activation volume of the flow, when the flow direction is at the same direction as the applied stress. (dash-line in Figure 3.33.(b))

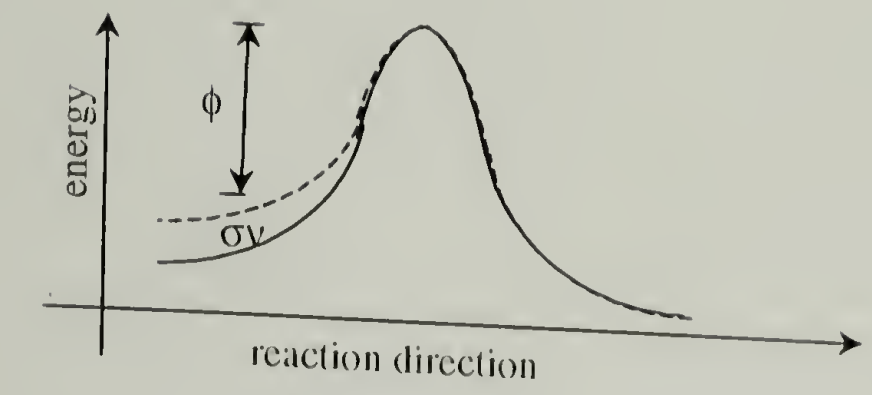

(a)

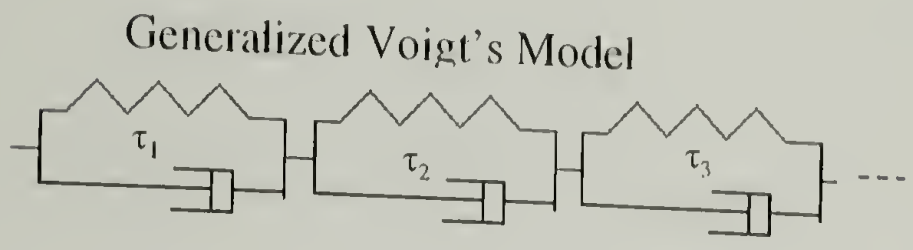

(b)

Figure 3.33 (a) Energy diagram of a material under steady load of σ; (b) Model of the system

Based on the illustration in Figure 3.33, the creep strain for a single Voigt element is:

$$\varepsilon_i = \varepsilon_o(1-\exp(-t/\tau))$$

Equation 3.14

in which, ε_i: creep strain for one Voigt element

τ_i: corresponding relaxation time

t: time under loading

Under stress field and utilizing deformation kinetics[123],

$$\varepsilon_0 = p_+ v - p_- v = v\exp(\sigma_c v/2kT) - v\exp(-\sigma_c v/2kT)$$
$$= v\sinh(\sigma_c v/2kT)$$

in which, υ: activation volume, p: possibility, and σ_c: applied stress

$$\therefore \varepsilon_i = v\sinh(\sigma_c v/2kT)(1-\exp(-t/\tau_i))$$

Equation 3.15

For a generalized Voigt's model, if the active energy spectrum is $f(\phi)$ then

$$\varepsilon_c = \sum_i \varepsilon_i = \int_0^\infty f(\phi)\varepsilon_i d\phi$$

$$= v \sinh(\sigma_c v / 2kT) \int_0^\infty f(\phi)(1 - \exp(-t/\tau)) d\phi$$

Equation 3.16

in which, ε_c is the creep strain of the material.

The activation energy spectrum $f(\phi)$ can be approximated from the compliance spectrum through the following equation:

$$f(\phi) = L(\tau) = -\left[dj'/d\log\omega + 1/2 d^2 j'/d(\ln\omega)^2 \right]_{1/\omega=\sqrt{2\tau}}$$
$$= B \qquad \text{at a wide range of } \tau \text{ or } \phi$$

Equation 3.17

in which, j' is the storage compliance and ω is the frequency.

Figure 3.34 shows the master curve of the compliance spectrum of Kevlar® fiber tested using DMTA. The slope, $dJ/d\tau$, is a constant in a large range of relaxation time indicating that $f(\phi)$ is constant.

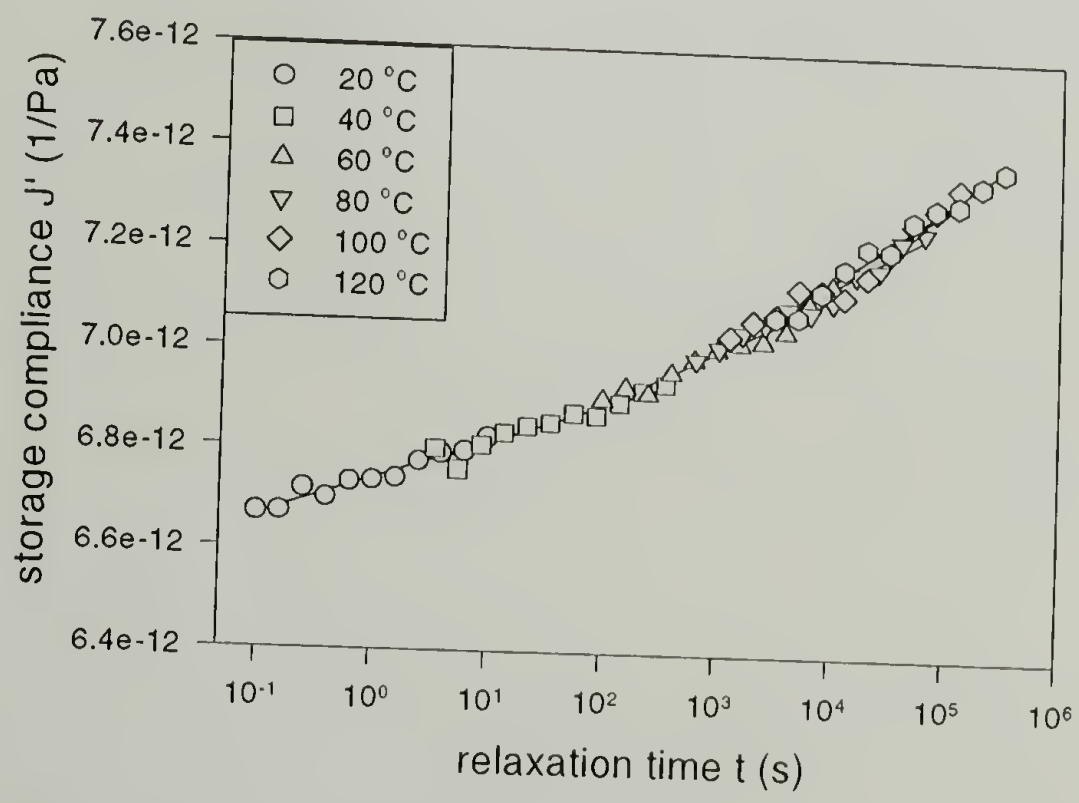

Figure 3.34 Master Curve constructed using DMTA for PPTA fiber

Then, Equation 3.16 becomes

$$\varepsilon_c = a_0 v^2 \sigma_c \ln(2At) + a_1$$

Equation 3.18

in which, a_0, a_1 and A are constants.

Equation 3.18 has the same form as Equation 3.13 if we replace time t in Equation 3.18 by number of loading cycles n_f. This inspired a concept of *dynamic creep*. Fatigue of fibers can be viewed as a *dynamic creep*. The difference between fatigue and creep is like that between dynamic friction and static friction. We are seeking the correlation between the fatigue deformation and the applied stress amplitude. In Equation 3.18, $a_0 v^2 \sigma$ dictates the creep rate and so does b for the fatigue rate in Equation 3.13. b is then called the fatigue rate. The similarity between fatigue deformation and creep deformation is shown as follows,

Fatigue		Creep
$\varepsilon_{\max} = \varepsilon_a + b \cdot \ln n_f$	$\longleftrightarrow$	$\varepsilon_c = a_0 v^2 \sigma \ln(2At) + a_1$

This similarity between deformation equations of fatigue and that of creep suggests a linear relation between the fatigue rate b and the applied stress amplitude σ_a, accordingly. A dynamic creep index is defined as follows:

$$\underline{\text{Dynamic Creep Index}}: \; d = \frac{\partial \varepsilon_{\max} / \partial \ln n_f}{\sigma_a} = \frac{b}{\sigma_a}$$

Equation 3.19

in which σ_a is the applied stress amplitude.

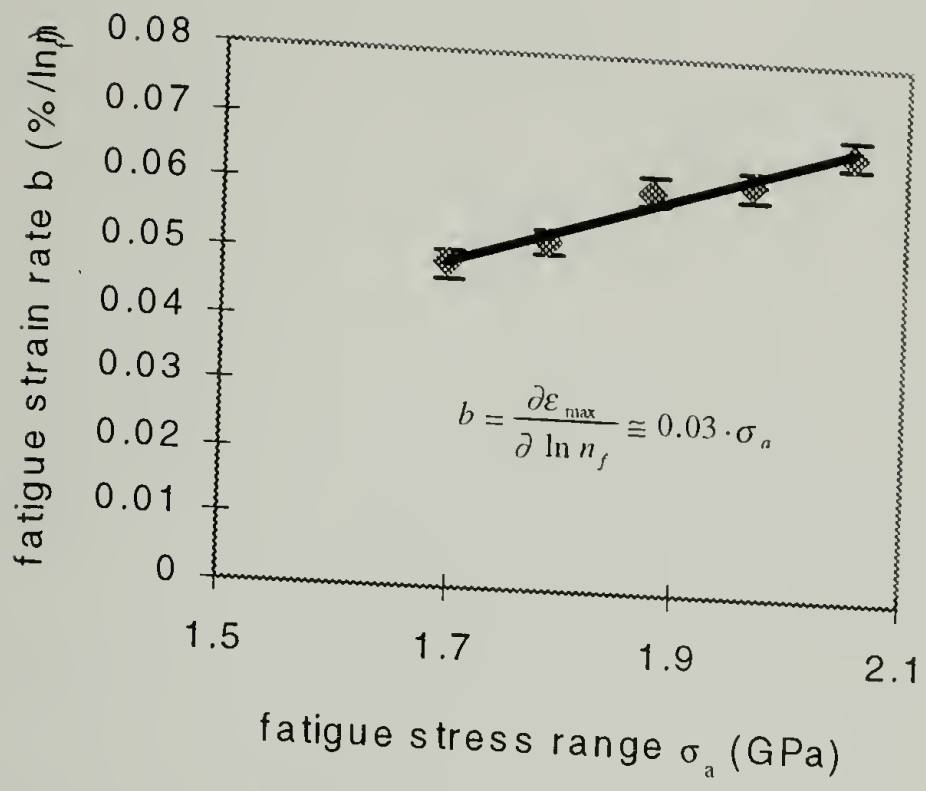

Figure 3.35 Establishment of the correlation between fatigue strain rate and fatigue stress range--Concept of Dynamic Creep

Figure 3.35 shows that indeed, there is a linear relation between the dynamic creep rate and the applied stress amplitude. Therefore, d is a material constant independent of stress condition and it is related to the material response to fatiguing.

3.4.4.2 The Derivation of Fatigue Lifetime Principle

After the fatigue strain as a function of stress range was established, the fatigue lifetime equation was derived based on the deformation-damage correlation.

Assuming:

1. Fatigue strain:

$$\varepsilon_{max} = \varepsilon_o + \sigma_a / E_s + \sigma_a \cdot d \cdot \ln n_f$$

Equation 3.20

where ε_0, d are constants, σ_a is the fatigue stress range and E_s is the stablized modulus.

2. Strain at break = ε_b

3. Dynamic creep index = d

Then, at the failure cycle N_f:

$$\varepsilon_b = \varepsilon_o + \sigma(1/E_s + d\ln N_f)$$

Equation 3.21

Figure 3.28 can be rewritten as:

$$1/\sigma_a = 1/(\varepsilon_b - \varepsilon_o)(1/E_s + d\ln N_f)$$
$$\sigma_f/\sigma_a = \sigma_f/(\varepsilon_b - \varepsilon_o)(1/E_s + d\ln N_f)$$

Equation 3.22

$$rewrite: \sigma_f/\sigma_a = 1/(\sigma_a/\sigma_f) = 1/(1+(\frac{\sigma_a - \sigma_f}{\sigma_f}))$$
$$\because \frac{1}{1+x} \approx 1 - x \quad \text{when } x < 1$$

Then Equation 3.22 becomes $(1 - \frac{\sigma_a - \sigma_{ts}}{\sigma_{ts}}) = \frac{\sigma_{ts}}{(\varepsilon_b - \varepsilon_o)}(1/E_s + d\ln N_f)$

Therefore, the Fatigue Lifetime Equation is:

$$\sigma_a = (2\sigma_{ts} - \frac{\sigma_{ts}^2}{(\varepsilon_b - \varepsilon_o)E_s}) - (\frac{\sigma_{ts}^2 d}{\varepsilon_b - \varepsilon_o})\ln N_f$$
$$= \sigma_{ts} \cdot (1 - m\ln N_f)$$

Equation 3.23

The functional form of Equation 3.23 is the same as the empirical lifetime equation (Equation 3.9). This validates the derivation. Therefore, two new parameters, fatigue strength and fatigue strength index, were defined for the material.

Fatigue Strength:

$$\sigma_f = \sigma_{ts}(2 - \frac{\sigma_{ts}}{(\varepsilon_b - \varepsilon_o)E_s}) \approx \sigma_{ts}$$

Fatigue Strength Index:

$$m = \frac{\sigma_{ts}^{\ 2} d}{(\varepsilon_b - \varepsilon_o)\sigma_f} \approx \frac{\sigma_{ts} d}{(\varepsilon_b - \varepsilon_o)}$$

The fatigue strength is close to the static strength and is reasonable. The static stretching is like a fatigue experiment with the lifetime cycle of 0.5. From the expression, the fatigue strength is determined by the static properties. On the other hand, the fatigue strength index, m, is proportional to a combination of some static properties and the dynamic property: fatigue creep rate *b*. Therefore, the *m* is the material constant that characterizes the fatigue resistance of the material.

Since all the static properties can be obtained from static measurements and the dynamic creep index *d* can be calculated from fatigue experiments, the fatigue strength and fatigue strength index of different fibers can be calculated. Table 3.4 shows the results of the calculation for Kevlar® 29 and Vectran® HS fibers. It indicates that the calculation gives rise to values of fatigue strengths and fatigue strength indices that are comparable to the experimental data.

This derivation confirms the fatigue mechanism of high performance fibers through a deformation route, and it also facilitates the prediction of fatigue lifetime of a new fiber from a few simple experiments. Imagining that a new fiber is designed and produced, and its fatigue properties are required for its use, normally, long time fatigue studies at multiple stress level need to be conducted to be able to summarize the lifetime principle or determine its fatigue strength and fatigue strength index. According to our derivation, to obtain these two parameters, only one short time fatigue experiment and static measurement are needed. From the short-time fatigue experiment, the dynamic creep index d can be calculated and the two parameters can be calculated as a result.

Table 3.4 Comparison of derived and experimental fatigue parameters for different fibers

material	Kevlar® 29	Vectran® HS	Twisted Kevlar® 29
dynamic creep index $d=a/\sigma$	0.03	0.057	0.038
stablized modulus E (Gpa)	110	103.5	110
static strength (Gpa)	2.48	2.9	2.9
static strain to break $\varepsilon_b(\%)$	3.1	3.7	4.1
instant permanent strain ε_o (%)	0.3	0.4	0.8
predicted fatigue strength	2.95	3.3	3.48
experimental fatigue strength	2.5	3.2	2.61
predicted fatigue strength index	0.023	0.045	0.028
experimental fatigue strength index	0.025	0.039	0.023

3.4.4.3 Scaling Relationship between Fatigue Resistance and Material Parameters

Efforts have been made to explore what material parameters determine the fatigue resistance of a fiber. A scaling argument helps to establish the possible correlation between the fatigue resistance and several material parameters. This can be used to guide the design to improve the fatigue resistance of materials.

Assuming that fatigue or dynamic creep is flow dominant, the scaling principle yields:

$$a_0 'v^2 \propto \frac{1}{G} \Rightarrow d \propto \frac{1}{G}$$

in which, G is the shear modulus

Therefore,

$$m \propto \frac{\sigma_f}{G * \varepsilon_b}$$

Table 3.5 shows that this hypothesis yields satisfactory rankings for the fatigue resistance among different fibers except for Kevlar® 149.

Table 3.5 Comparison of a combination of material parameters that dominates the fatigue resistance and the fatigue strength index *m*

Fiber	Kevlar 29	Kevlar 119	Spectra 900	Kevlar 49	Kevlar 149	Vectran HS	Technora
Shear modulus G_t(GPa)	1.82	1.55	0.73	1.48	1.3	0.65	
Strength σ_s(GPa)	2.48	2.96	2.34	2.4	2.15	2.98	3.05
Elongation ε_b(%)	3.13	4.09	4.55	2	1.46	3.23	4.51
strength/ultimate elongation*shear modulus $\sigma_s/(\varepsilon_b * G_t)$	0.44	0.47	0.70	0.81	1.13	1.42	
Fatigue strength index m	0.025	0.032	0.038		0.028	0.039	0.039

Shear moduli of high performance fibers measured by torsional pendulum

3.4.5 General Creep Behavior

The creep behavior of these high performance fibers was also investigated to enable a comparison and achieve better understanding of the general failure behavior.

3.4.5.1 Creep Strain

In applications where the dimensional stability is important, creep strain is an important material property.

It was observed that the creep of high performance fibers has three stages. Figure 3.36 shows these three stages in Kevlar® fibers: primary creep, secondary creep and tertiary creep. The primary and tertiary creep together only consume 15% of the lifetime of the material. Most studies of creep behavior concentrate only on the primary creep. [62,64,103]

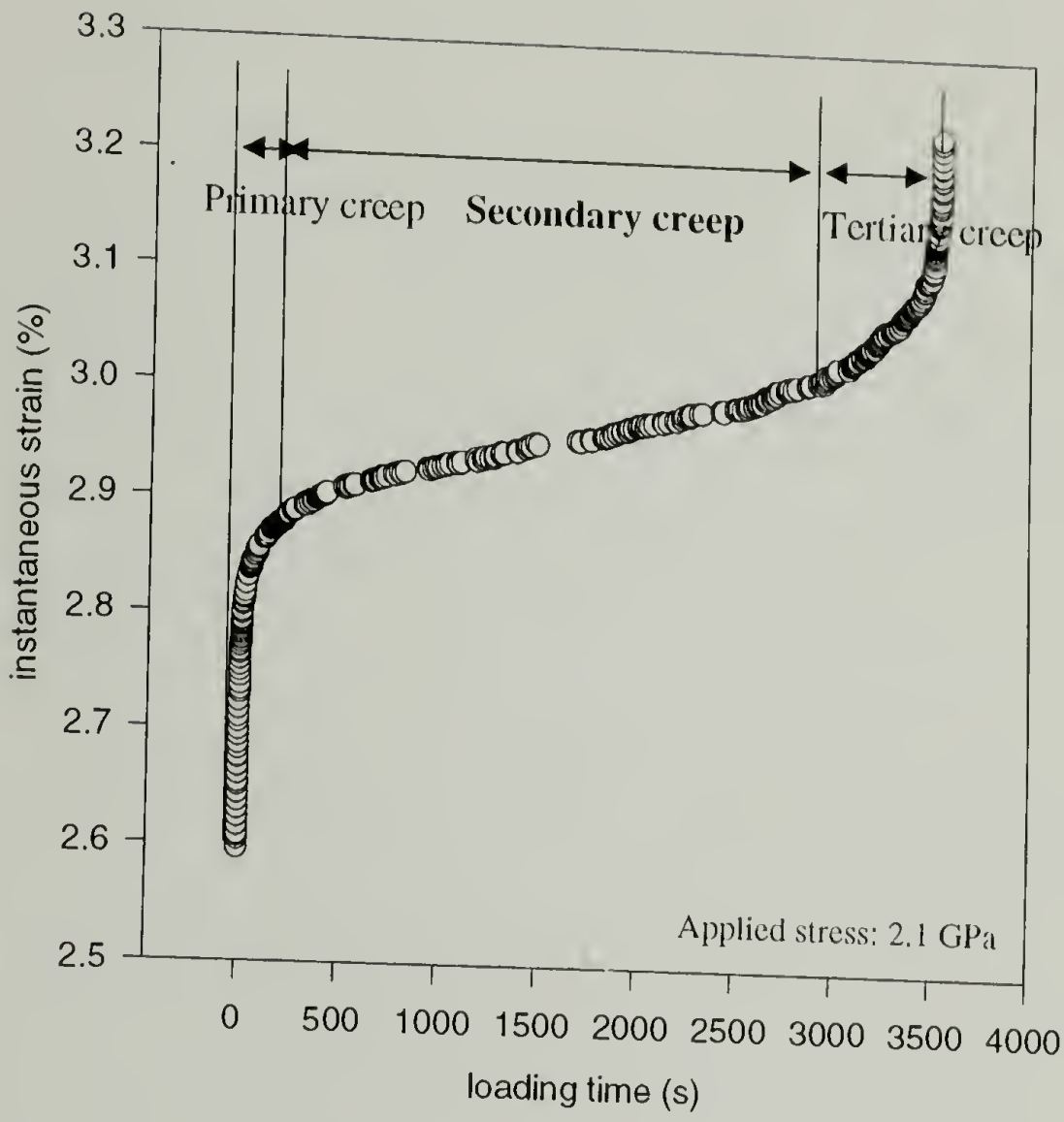

Figure 3.36 A typical creep-to-rupture curve for a Kevlar® 29 yarn

Figure 3.37, Figure 3.38 and Figure 3.39 illustrate that the individual creep stage can be represented by different equations. Good fits of the data using simple functions were achieved for the first and second stages of creep, but not for the third stage of creep. Figure 3.37 shows that the primary creep strain increases linearly with the logarithmic of the loading time. This observation is consistent with the results reported in the literature.[62,64,103] However, for the secondary creep, the creep strain increases linearly with the loading time. (Figure 3.38) This result has not been reported by others. The tertiary creep is complicated and could not be resolved easily.

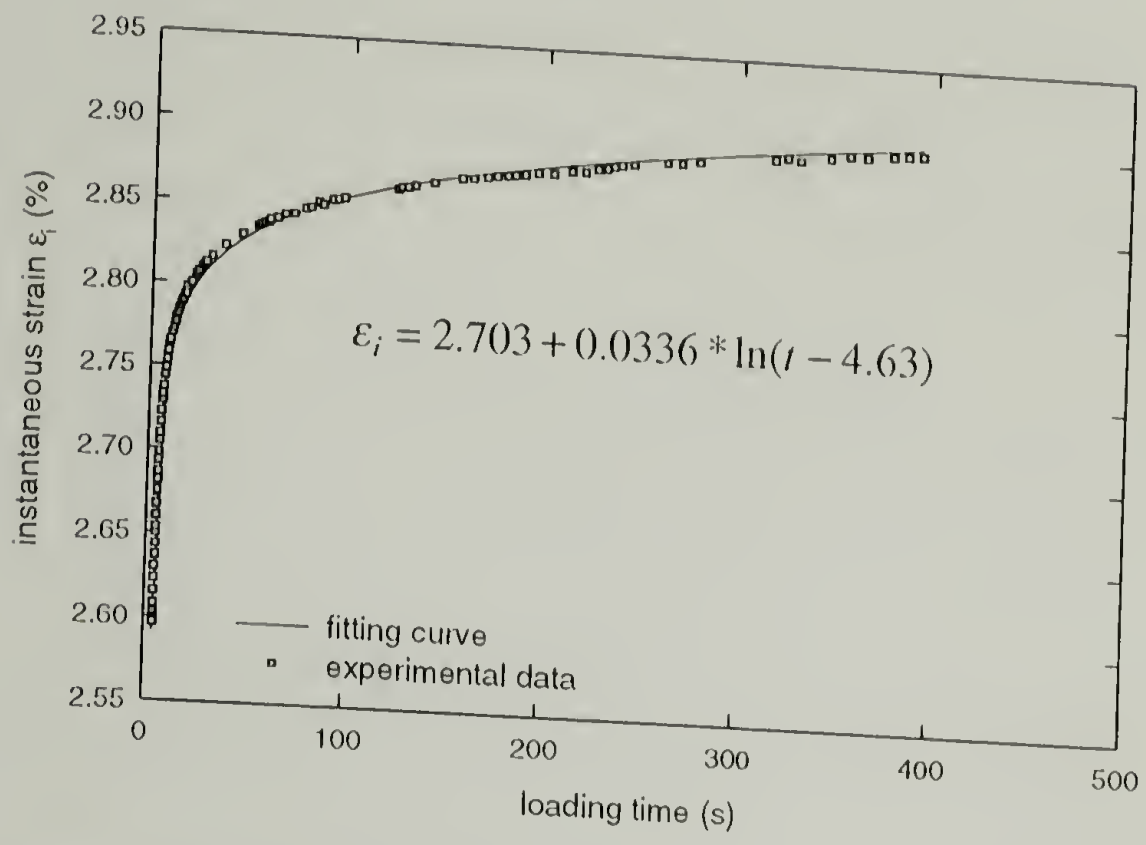

Figure 3.37 Descriptions of primary creep with time.

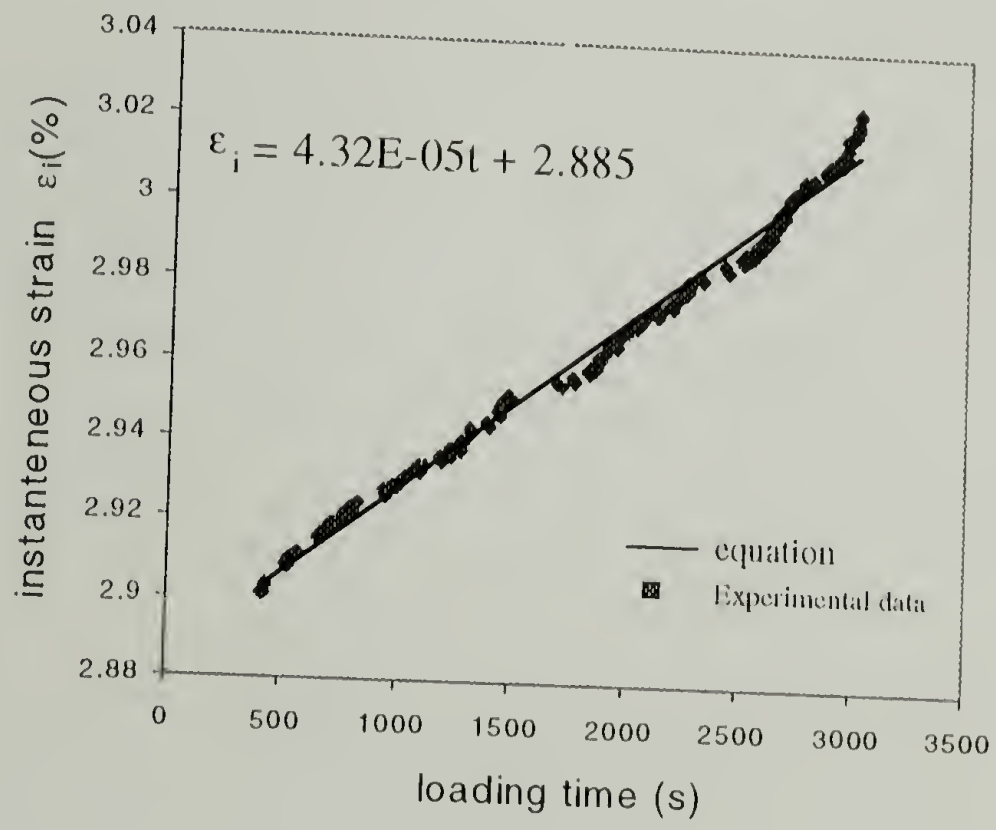

Figure 3.38 Descriptions of secondary creep with time.

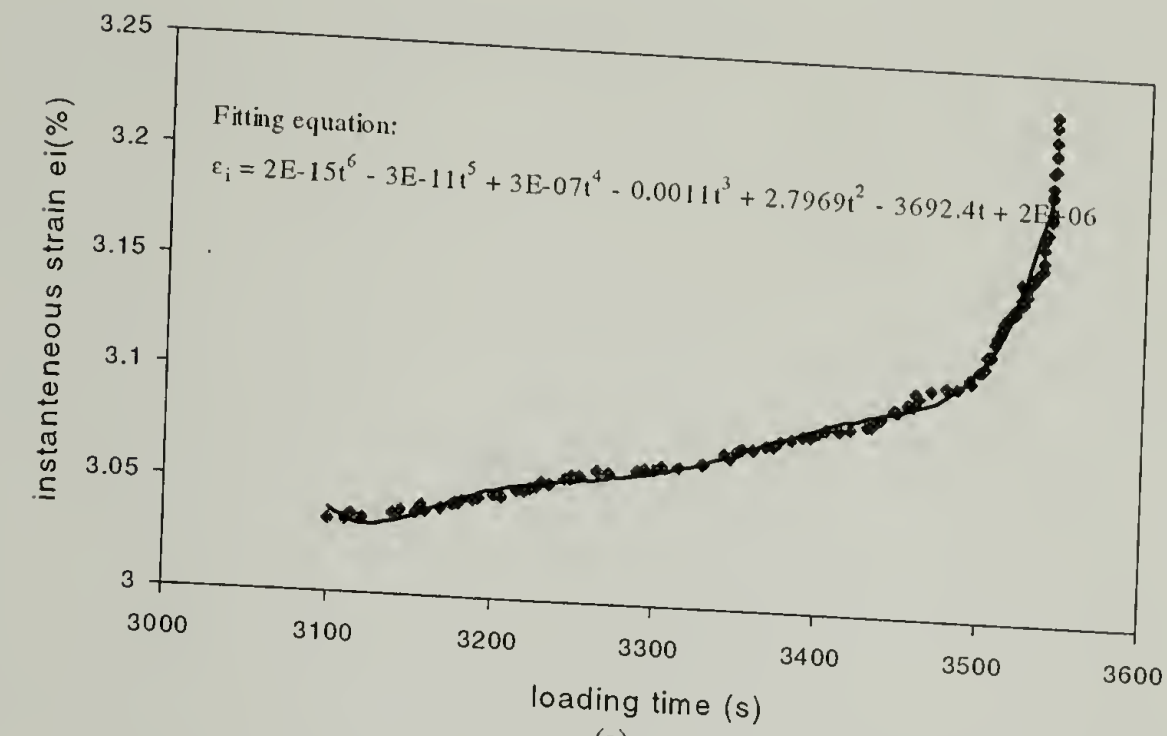

(a)

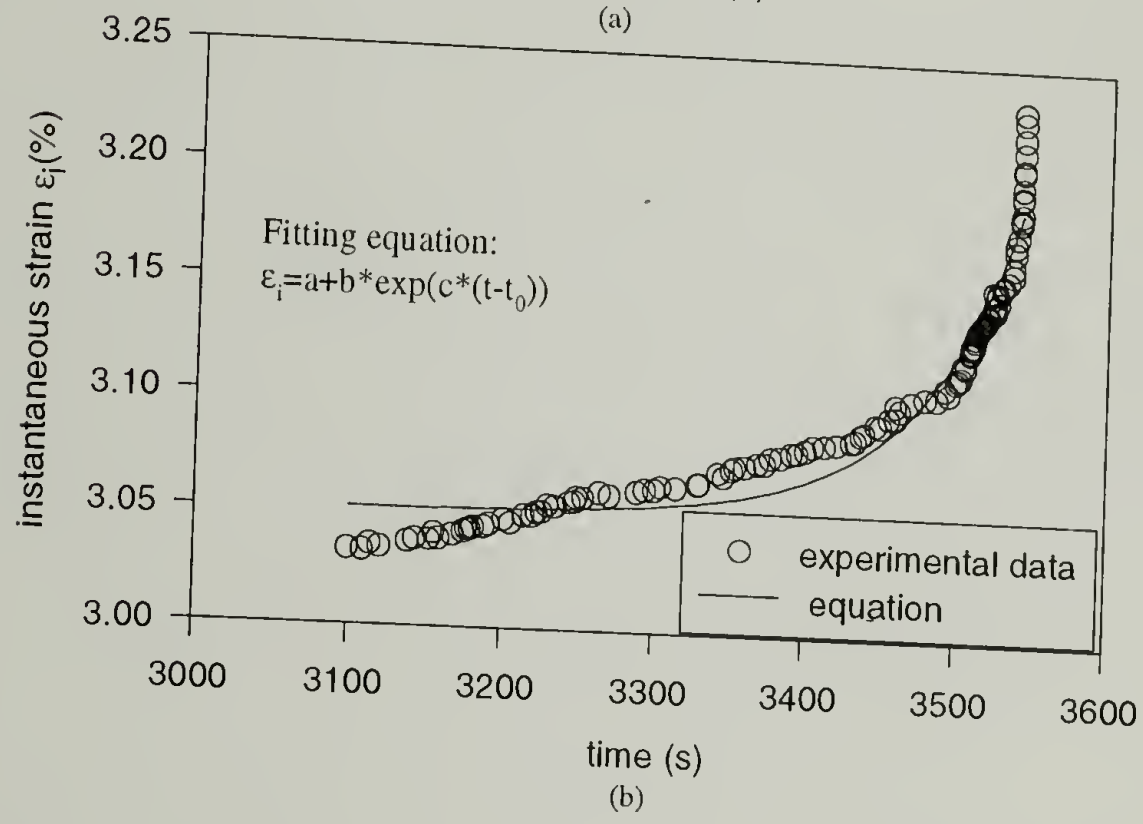

(b)

Figure 3.39 Attempts to describe the tertiary creep with time.

To understand the origin of the tertiary creep, creep of the same fiber yarns of different linear densities were tested. When a 200 denier yarn sample was used instead of a 1500 denier, its tertiary creep consumes a small percent of the total life as shown in Figure 3.40 compared to Figure 3.36. When the creep of a single filament was tested, the percentage is even smaller. This suggests that the tertiary creep must be related to the fiber geometry. It is caused by the gradual break of individual fibers increasing the stress in the remaining fibers.

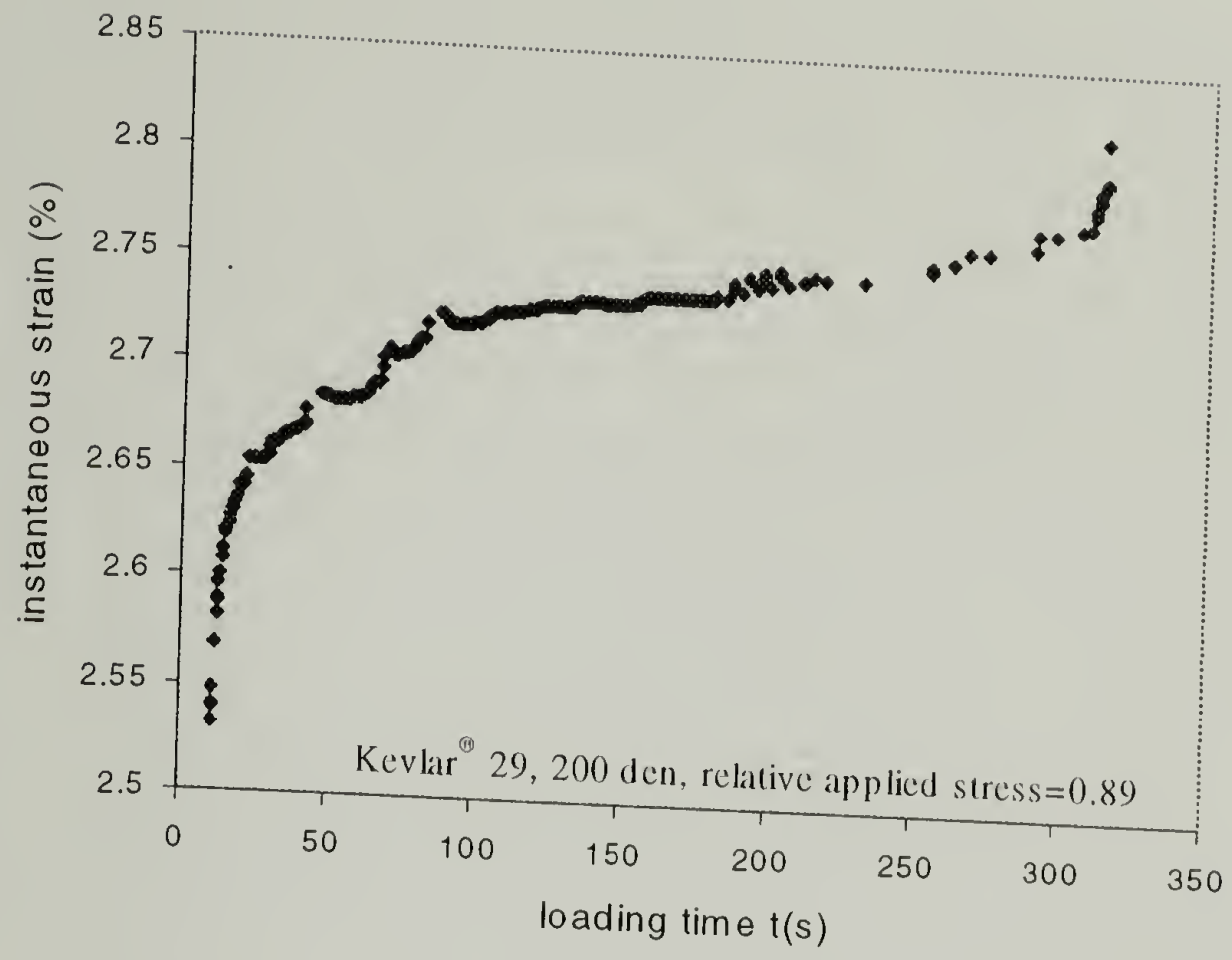

Figure 3.40 Creep deformation with loading time of a low denier yarn (200 den); it shows a shorter period of tertiary creep when compared to 1500 denier yarn; the relative stress is the ratio of the applied stress to the strength

3.4.5.2 Creep Lifetime of Different Fibers

Materials or fibers can fail under long time creep loading, even though the loading is less than the strength of the material. This kind of failure is creep failure and is termed creep lifetime.

When the changes of creep strain with the loading time under different constant stresses were compared, it was observed that the higher the applied stress the shorter the creep lifetime. It also shows that it is the secondary creep that mainly determines the creep lifetime under different creep stress and the higher the secondary creep rate, the shorter the lifetime.(Figure 3.41)

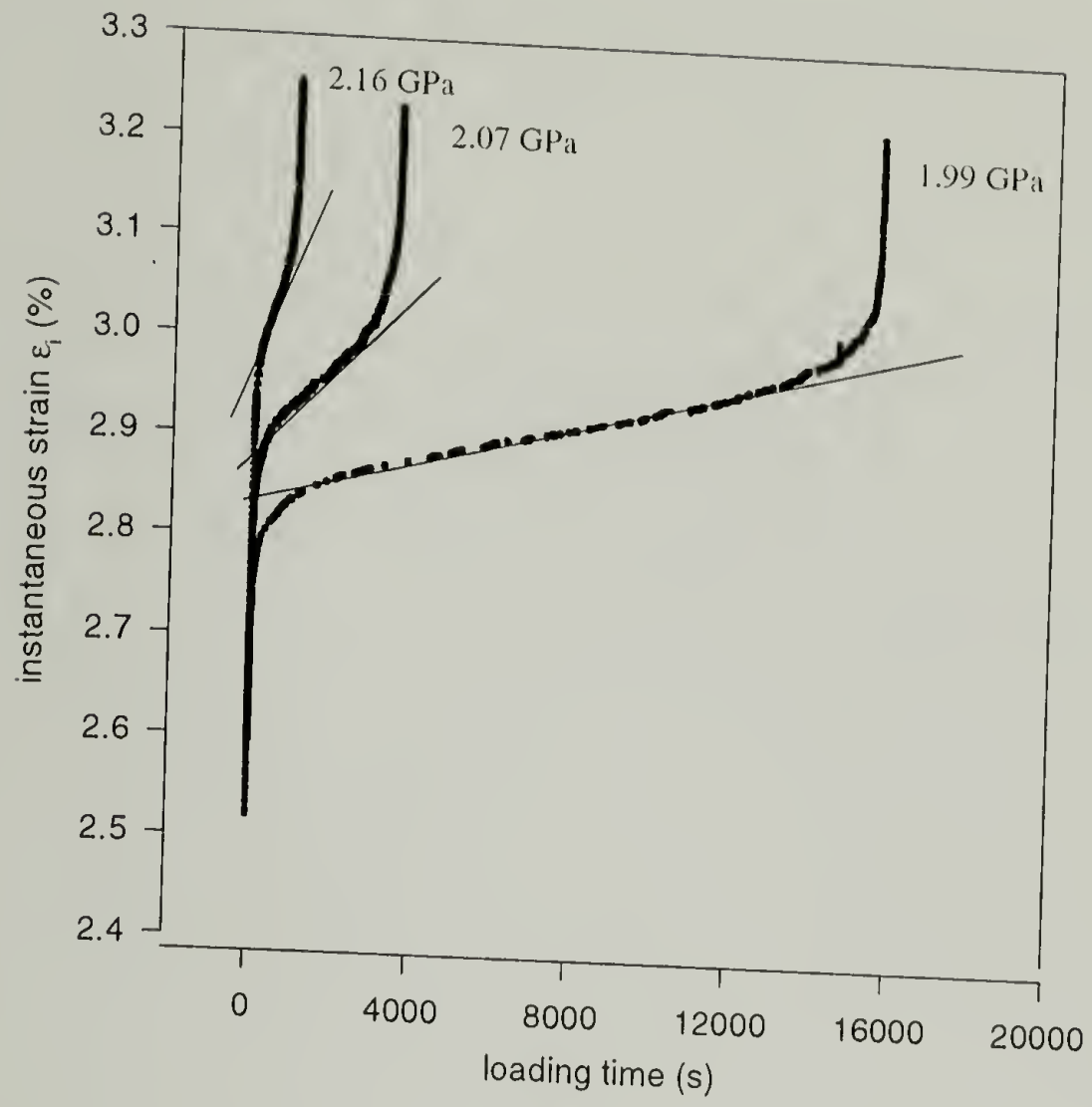

Figure 3.41 Creep strain increment with loading time for different loads; numbers in the plot are applied stresses, and lines indicate secondary creep rates

A general plot between the lifetime under creep and the applied stress is shown in Figure 3.42 for different high performance fibers. Similar to our observation of fatigue lifetime, the creep lifetime of fibers also follows a semilogarithmic rule. It is shown that the creep resistance of Nomex is better than that of Kevlar® and Technora®, and Kevlar® is better than that of Vectran® HS.

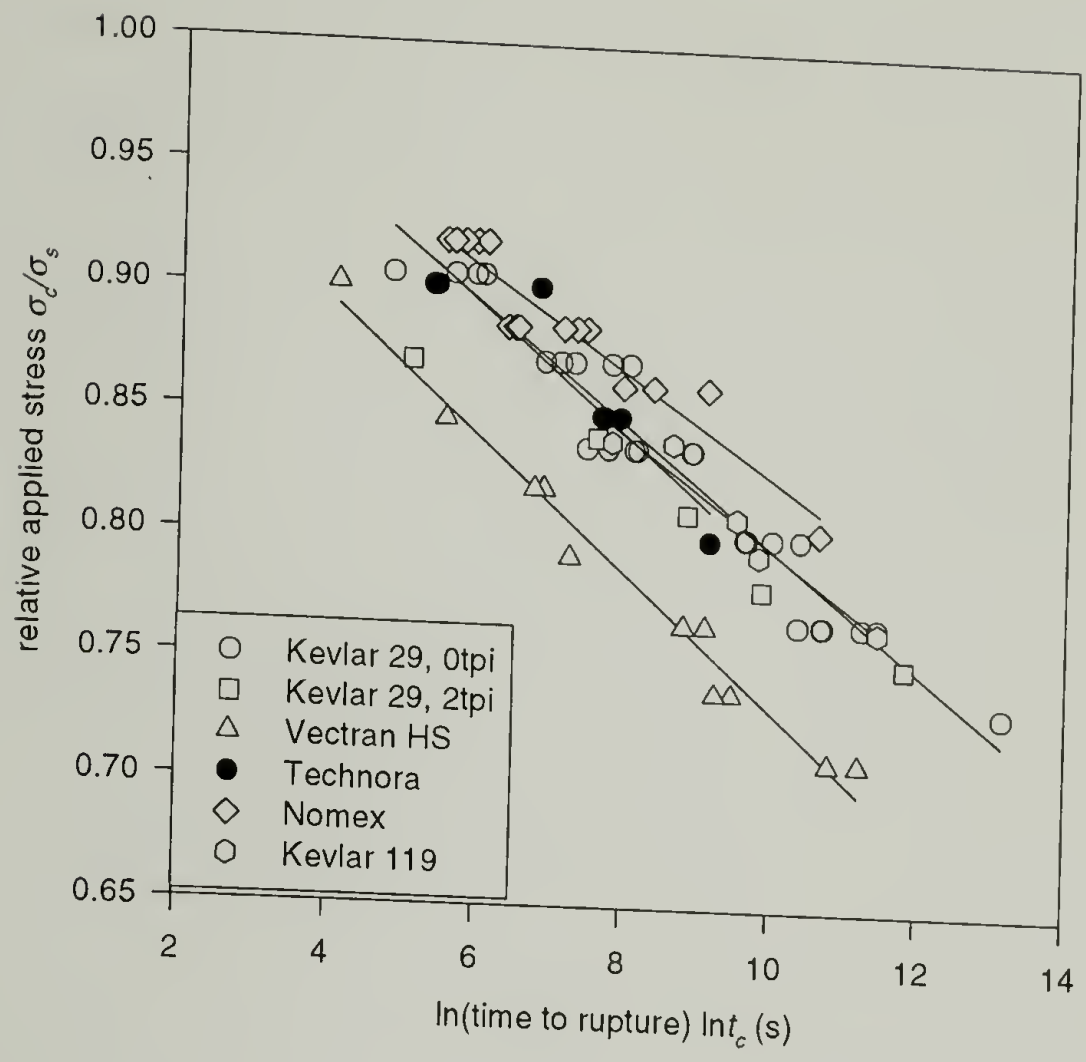

Figure 3.42 Lifetime under creep of different high performance fibers

3.4.5.3 Derivation of Creep Lifetime

The experimental observations suggest that the time to rupture under creep for Kevlar® fiber yarns is determined by the secondary creep. The summation of the duration of the primary creep and tertiary creep was found to be about 13% of the total lifetime. It is believed that the primary creep is due to reorientation through crystal rotation. The fiber deformation of the primary creep increases linearly with the logarithm of the loading time. The tertiary creep is an accelerating process that may involve stress redistribution due to the statistical variability of fiber properties, the misalignment of the filaments and the increasing stress on the remaining members. It is very difficult to describe the deformation behavior of the tertiary creep of the yarn (Figure 3.39).

The determination of yarn rupture when a critical ultimate strain is reached (Figure 3.27) makes it possible to derive the general stress dependence of the creep lifetime from the deformation behavior, exclusively from the deformation of the secondary creep. The derivation, furthermore, reflects the mechanism of the creep-rupture.

Assuming a general creep rupture of the fiber:

$$\varepsilon_c = \varepsilon_0{}' + C_a \cdot \ln(t - t_0) + C_b \cdot (t - t_0)$$

Equation 3.24

where $\varepsilon_0{}'$ is the elastic strain, C_a is the apparent primary creep rate; C_b is the secondary creep rate

1. The instantaneous secondary creep is

$$\varepsilon_c = \varepsilon_o{}'' + C_b t$$

Equation 3.25

where ε_c is the total strain, $\varepsilon_0{}''$ is the initial secondary creep strain including primary creep. (Figure 3.37)

2. Strain at break = ε_b (Figure 3.27)

3. Experiments show that

$$\ln C_b = C_d \cdot \sigma_c + C_e$$

Equation 3.26

where σ_c is the applied stress; and C_d and C_e are fitting parameters and C_d is called creep rate index and C_e is called the apparent zero creep rate. (Figure 3.43)

Equation 3.25 can be rewritten as

$$(\varepsilon_c - \varepsilon_0{}'') = C_b t$$
$$\ln(\varepsilon_c - \varepsilon_0{}'') = \ln C_b + \ln t$$

Equation 3.27

At break point, Equation 3.27 becomes

$$\ln(\varepsilon_b - \varepsilon_0'') = \ln C_b + \ln(0.85 \cdot t_c)$$

Equation 3.28

where t_c is the time to rupture under creep; and ε_b is the final strain of the secondary creep.

When $\ln C_b$ is replaced by σ_c according to Equation 3.26, Equation 3.28 can be rewritten as

$$\sigma_c = (\ln(\varepsilon_b - \varepsilon_0') - C_e - \ln 0.85)/C_d - \frac{1}{C_d} \cdot \ln t_c \qquad \text{or}$$

$$\frac{\sigma_c}{\sigma_s} = \frac{(\ln(\varepsilon_b - \varepsilon_0') - C_e - \ln 0.85)}{C_d \cdot \sigma_s} - \frac{1}{C_d \cdot \sigma_s} \cdot \ln t_c$$

Equation 3.29

Equation 3.29 has the same form as the empirical lifetime equation: (Figure 3.44)

$$\sigma_c = \sigma_{cf} \cdot (1 - C_m \cdot \ln t_c) \qquad \textbf{or}$$

$$\frac{\sigma_c}{\sigma_{cf}} = 1 - C_m \cdot \ln t_c$$

Equation 3.30

where σ_{cf} is called the creep strength of the yarn; C_m reflects the creep resistance of the yarn and is called the creep strength index.

Therefore, similar to the way fatigue was treated, two material parameters are defined to characterize the creep properties of fibers.

Creep Strength

$$\sigma_{cf} = \frac{(\ln(\varepsilon_b - \varepsilon_0') - C_e - \ln 0.85)}{C_d}$$

Creep Index

$$C_m = \frac{1}{\sigma_{cf} \cdot C_d}$$

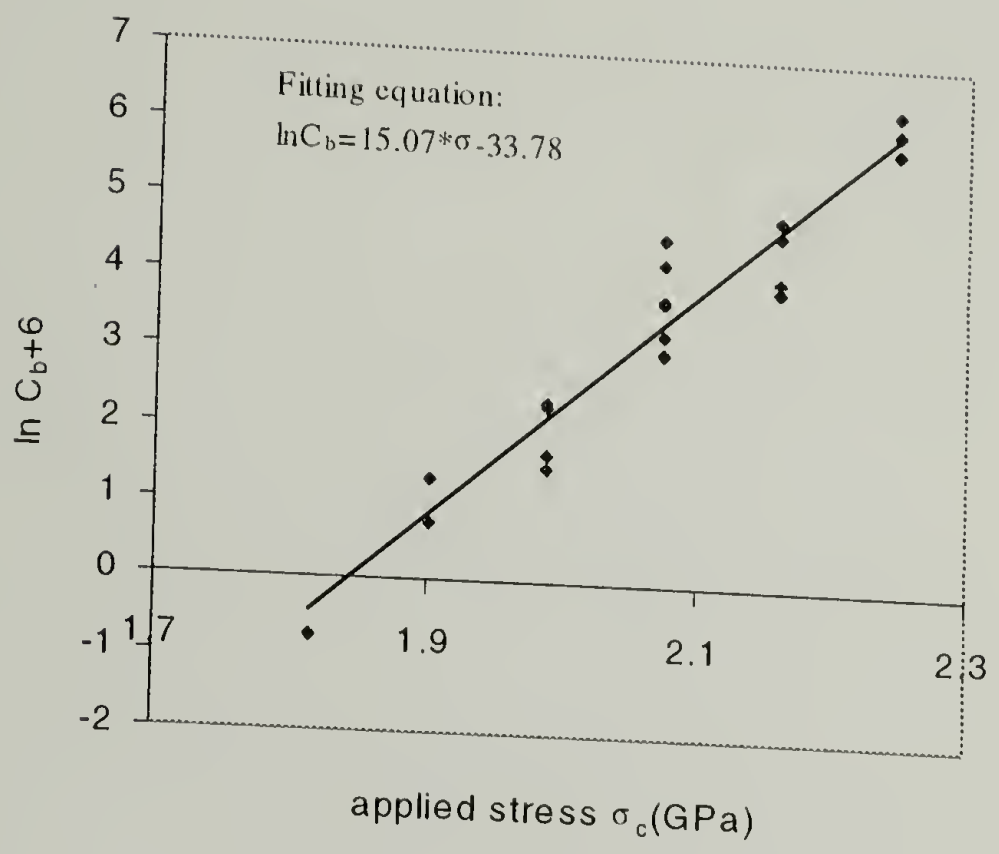

Figure 3.43 Secondary creep rate vs. the applied stress in Kevlar® 29 fiber

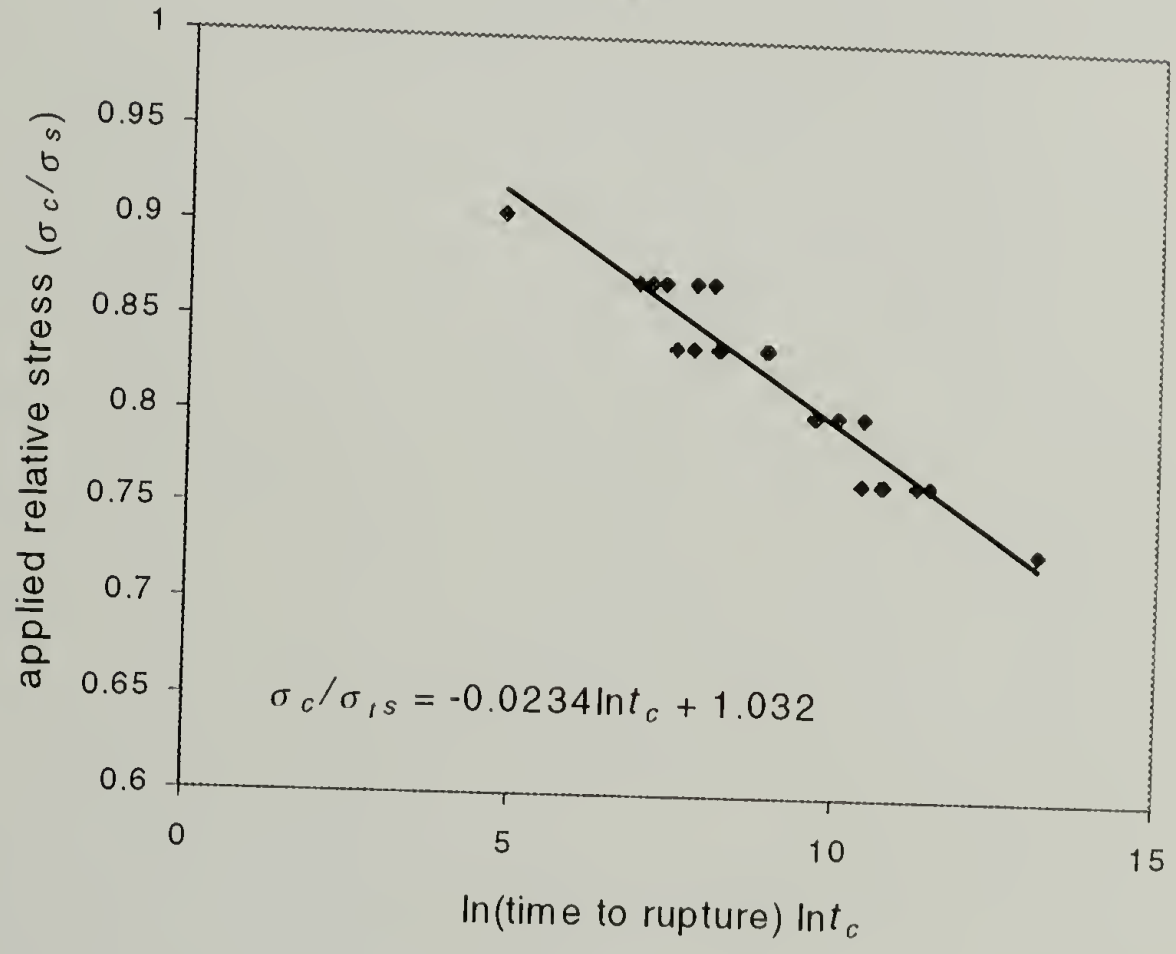

Figure 3.44 Lifetime of Kevlar® 29 yarn under creep with the applied stress level

The determination of the creep lifetime by the secondary creep was assumed in this derivation. Since this linear secondary creep was observed for Kevlar® fiber for the first time, efforts have been made to prove the correlation between the secondary creep and creep lifetime. Figure 3.45 shows that there is indeed a good correlation between the secondary creep rate and the lifetime of Kevlar® under creep. The creep lifetime decreases linearly with the secondary creep rate. This correlation is better than the correlation between the lifetime and the applied stress (Figure 3.44). This indicates that the secondary creep is inherently related to the creep lifetime.

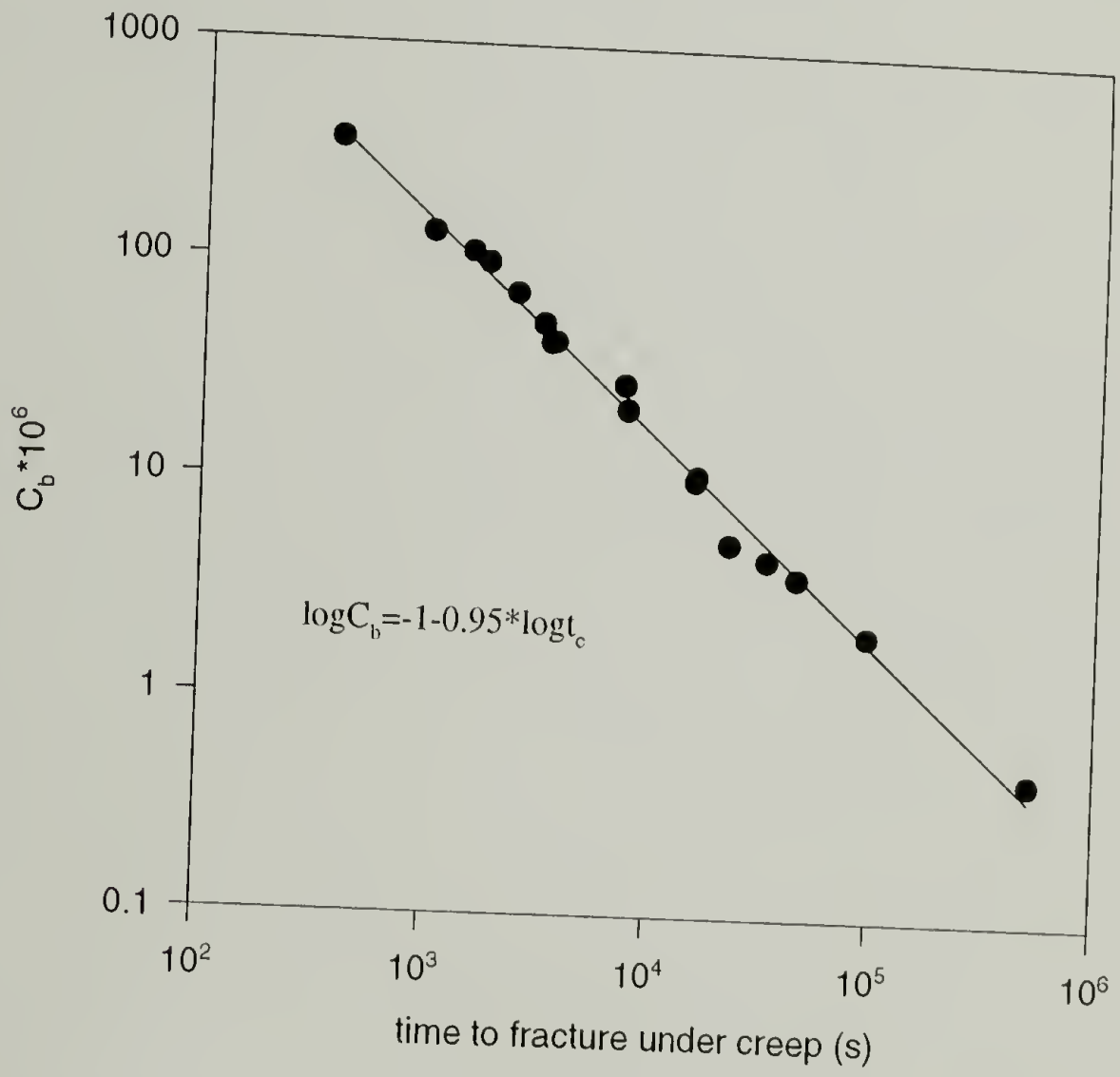

Figure 3.45 Secondary creep rate vs. lifetime under creep

Based on the above argument, the lifetime equation of Kevlar® fiber under creep can be calculated using corresponding material parameters. Such a calculation is shown in Table 3.6 and the prediction is in good agreement with the experimental results.

Table 3.6 Correlation of creep properties and material parameters

Creep life equation: $\sigma_c = \sigma_{cf}(1-C_m*\ln(t_c))$

material	Kevlar 29
creep rate index C_d (%/s.GPa)	15.07
apparent zero creep rate C_e (%/s)	-33.78
strain to break ε_b(%)	3.4
initial secondary creep strain ε_0'(%)	2.7--3.0
static strength σ_s(GPa)	2.5
predicted creep strength σ_{cf}(GPa)	2.25
experimental creep strength σ_{cf}(GPa)	2.58
predicted creep strength index C_m	0.0266
experimental creep index C_m	0.0234

There are debates about the stress dependence of the primary creep. Figure 3.46 illustrates that the primary creep rate of Kevlar® and Technora® is stress dependent. This result does not agree with those of Ferreira's. [118]

Table 3.8, Table 3.9 and Table 3.7 list the experimental results for the creep of different high performance fibers.

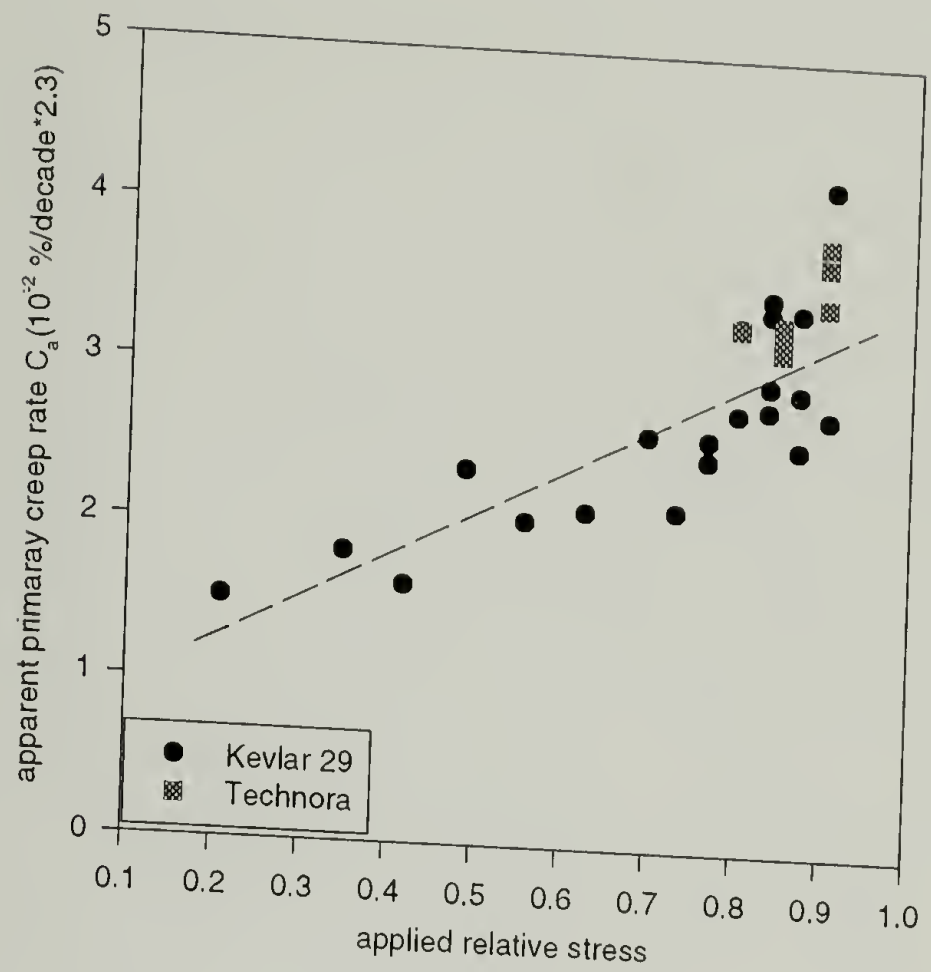

Figure 3.46 Apparent primary creep rate vs. the applied relative stress

Table 3.7 Creep results for Technora® and Vectran® HS yarns

I.D.	Test condition			Experimental observation				Fitting results primary creep: $\varepsilon_c(t) = a\ln(t-t_0)+b$			secondary creep: $\varepsilon_c(t) = C_b \cdot t+\varepsilon_0'$	
	applied load(N)	stress (GPa)	relative stress	lifetime (s)	starting strain(%)	break strain(%)	onset loading time t_0'(s)	a(10^{-2})	b	to (s)	C_b(10^{-6})	ε_0' (%)
Technora												
ctec308	308	2.58	0.80	9420	3.79	4.63	6.81	3.31	3.90	6.79	24.90	4.10
ctec3271	327	2.73	0.85	2230	3.92	4.61	7.08	3.17	4.02	7.05	80.90	4.17
ctec3272	327	2.73	0.85	2150	4.05	4.78	7.29	3.35	4.16	7.26	81.30	4.32
ctec3273	327	2.73	0.85	2810	3.90	4.58	7.02	3.23	4.01	6.99	56.00	4.19
ctec347	347	2.90	0.90	911	4.10	4.64	7.38	3.47	4.19	7.31	151.00	4.35
ctec3472	347	2.90	0.90	225	4.10	4.64	7.38	3.73	4.18	7.26	800.00	4.28
ctec3473	347	2.90	0.90	216	4.14	4.66	7.48	3.86	4.22	7.35	665.00	4.34
Vectran Hs												
cvhs513	260	2.09	0.71	74300	2.59	3.20	5.20	1.13	2.64	5.20	0.90	2.71
cvhs509	260	2.09	0.71	49300	2.76	0.00						
cvhs515	270	2.17	0.74	13000	2.52	3.07	5.11	1.36	2.57	5.15	2.29	2.67
cvhs512	270	2.17	0.74	104400	2.67	3.17	5.33	1.93	2.67	5.15	7.70	2.78
cvhs5281	280	2.26	0.77	8990	2.75	3.28						
cvhs508	280	2.26	0.77	6690	2.72	3.16						
cvhs514	290	2.34	0.79	1410	2.67	3.17	5.41	2.79	2.73	5.32	184.00	2.81
cvhs506-1	300	2.42	0.82	976	2.77	3.40	5.62	1.59	2.81	5.43	203.00	2.86
cvhs506-2	300	2.42	0.82	988	2.83	3.38	5.72	2.08	2.84	4.76	165.00	2.92
cvhs506-3	300	2.42	0.82	870	2.82	3.35	5.70	2.33	2.84	4.86	179.00	2.92
cvhs505	310	2.50	0.85	260	2.84	3.36	5.70	3.82	2.85	4.58	463.00	2.95
cvhs504	330	2.66	0.90	60	2.97	3.38	5.30	4.37	2.99	5.31	3990.00	3.00

Table 3.8 Creep results for Kevlar® 29 yarn

Kevlar 29 I.D.	Test condition			Experimental observation				Fitting results				
								primary creep: $\varepsilon_c(t) = a\ln(t-t_0)+b$			secondary creep: $\varepsilon_c(t) = C_b t+\varepsilon_0'$	
	applied load(N)	stress (GPa)	relative stress	lifetime (s)	starting strain(%)	break strain(%)	onset loading time t_0'(s)	$a(10^{-2})$	b	to (s)	$C_b(10^{-6})$	ε_0'(%)
ck29528	60	0.52	0.21				1.50	1.51	0.76	1.52		
ck29529	100	0.86	0.35				2.48	1.82	1.26	2.45		
ck29527	120	1.04	0.42				2.83	1.62	1.43	2.80		
ck29140	140	1.21	0.49				3.34	2.36	1.74	3.34		
ck29230	160	1.38	0.56				3.45	2.05	1.91	3.40		
ck29180	180	1.56	0.63				4.56	2.12	2.23	4.50		
ck29517	200	1.73	0.70	1470000+	2.25		4.60	2.61	2.35	4.63		
ck29516	210	1.82	0.73	518000	2.47	3.29	5.00	2.14	2.58	4.90	0.46	2.79
ck29220	220	1.90	0.77	45200	2.45	3.36	2.20	2.47	2.54	2.18	2.09	2.73
ck29515	220	1.90	0.77	94500	2.46	3.30	5.20	2.60	2.61	5.00	3.79	2.78
ck295220	220	1.90	0.77	32000	2.55	3.12						
K29cr132	220	1.90	0.77	76200	2.45	3.36						
k29cre06	220	1.90	0.77	44300	2.66	3.15						
ck29230	230	1.99	0.80	15600			4.70	3.32	2.62	4.50	10.80	2.83
ck29504	230	1.99	0.80	33000	2.80	3.17	2.56	2.77	2.61	2.53	4.55	2.79
ck29524	230	1.99	0.80	15400	2.45	3.04					10.30	2.76
ck29526	230	1.99	0.80	22300	2.48	3.06					5.34	2.78
ck292401	240	2.07	0.84	2370			2.40	2.80	2.77	2.37	71.80	2.89
ck292402	240	2.07	0.84	3540			4.64	3.40	2.70	4.63	43.20	2.88
ck292403	240	2.07	0.84	1760			4.60	3.50	2.69	4.60	98.50	2.83
ck29503	240	2.07	0.84	7510	2.77	3.13	5.42	2.95	2.69	5.41	21.50	2.86
ck29523	240	2.07	0.84	7310	2.56	3.13						
ck29525	240	2.07	0.84	3380								
ck292501	250	2.16	0.87	995			2.40	2.56	2.79	2.43	134.00	2.95
ck292502	250	2.16	0.87	1480			4.90	3.42	2.80	4.82	110.00	2.97
ck29502	250	2.16	0.87	3140	2.80	3.17	4.24	2.91	2.84	4.10	52.20	2.96
ck29521	250	2.16	0.87	2450	2.64	3.19						
ck295252	250	2.16	0.87	1220	2.84	3.30						
ck29501	250	2.16	0.87	383	2.77	3.13						
ck29520	260	2.25	0.91	289	2.77	3.19	2.62	2.76	2.90	2.62	600.00	3.35
ck29260	260	2.25	0.91				5.60	4.21	3.04	5.51	352.00	3.37

Table 3.9 Creep result for twisted Kevlar® 29, Nomex® and Kevlar® 119 yarns

I.D.	Test condition			Experimental observation		
	applied load(N)	stress (GPa)	relative stress	lifetime (s)	starting strain(%)	break strain(%)
Kevar 29, twist degree: 2tpi						
ck295105	250	2.16	0.75	137000	2.87	3.56
ck295102-3	260	2.25	0.78	19300	2.95	3.38
ck295102-1	270	2.33	0.81	6940	3.01	3.56
ck295101-3	280	2.42	0.84	2040	3.24	3.62
ck295101-2	290	2.51	0.87	165	3.22	3.56
ck295101-1	330	2.85	0.99	59	3.32	3.63
Nomex						
11-1	70	0.55	0.82	42400	9.13	18.39
4--1	75	0.59	0.88	9120	10.77	17.98
9--1	75	0.59	0.88	4340	11.40	19.67
10--1	75	0.59	0.88	2880	10.74	18.54
7--4	77	0.61	0.90	1730	11.37	19.36
6-1	77	0.61	0.90	1510	10.32	17.18
6-2	77	0.61	0.90	591	11.69	18.87
6-3	77	0.61	0.90	650	11.66	18.78
7--1	77	0.61	0.90	680	10.81	17.80
7--5	77	0.61	0.90	1270	12.02	20.01
2--7	80	0.63	0.93	442	13.03	19.44
2--4	80	0.63	0.93	328	14.22	19.44
7--2	80	0.63	0.93	256	12.42	18.81
7--3	80	0.63	0.93	283	13.04	19.58
2--8	80	0.63	0.93	383	13.44	19.49
Kevlar 119						
1	282	2.49	0.84	2470	3.65	4.27
2	282	2.49	0.84	5680	3.65	4.27
3	272	2.40	0.81	13700	3.52	4.27
5	267	2.36	0.80	18600	3.43	4.18
4	257	2.27	0.77	95100	3.29	4.18

Morphology Study

The fracture surfaces of the tensile broken and fatigue broken fibers have been examined by optical microscope (OM) and scanning electron microscope (SEM). Figure 3.47 shows that the characteristic feature of the fatigue-failed Kevlar® fiber is axial splitting, which is similar to that observed in a tensile failure. Figure 3.47.(b) shows the onset of the splitting. This observation is consistent with the study of other researchers on the fatigue of single filaments.[84] Generally, the fracture surfaces of tensile, creep and fatigue broken sample are similar. For Kevlar® and Vectran® fiber, the fractured ends show either long tapered fibrils or richly splitted ends. However, Nomex fiber shows blunt solid ends under tensile, creep and fatigue failure. The most salient difference between tensile and fatigue-broken filaments is in the much deeper and longer splits occurring in fatigue breaks compared to tensile breaks. All broken ends after fatigue tests show a very long fracture with extensive splitting in the longitudinal direction. For untwisted yarns, the fatigue fractured splitting length can be as long as 800 μm, while it is around 100 μm for the tensile failures.

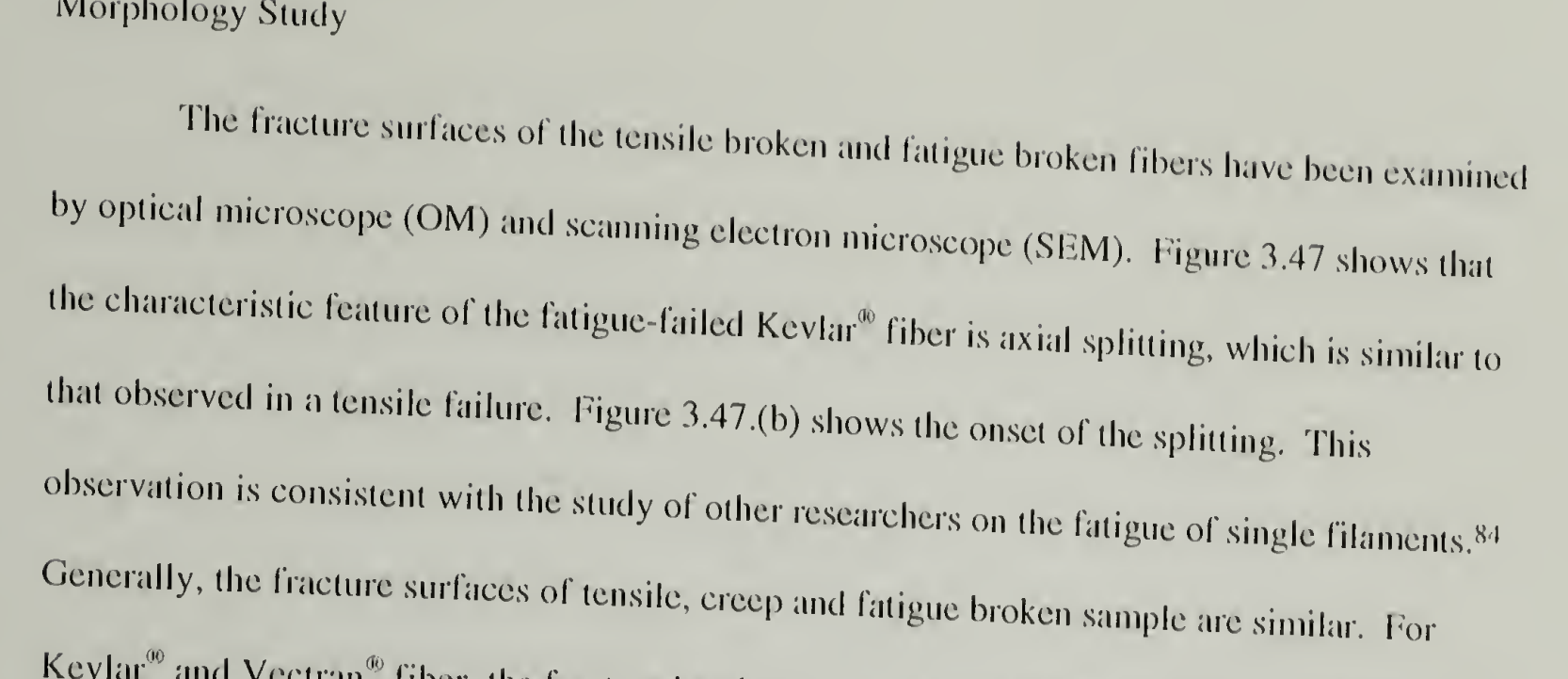

(a) (b)

Figure 3.47 Morphology of the ends of fractured fiber in fatigue; (a). a fatigue-fractured end, and (b) onset of splitting

The internal surface of a split fiber was examined. It is interesting to observe that there exists a uniform striation on the internal surface of splitted fiber shown in Figure 3.48.(a). It is suspected to be caused by the process of fatiguing. Similar parallel lines appear on fatigue fracture surfaces in many materials including metals and amorphous polymers.[124] This so-called fatigue striations was shown to relate to the advance of fatigue crack front in one cycle and the increment extent varies with the stress range. Further study is needed to confirm our speculation. Another important observation is that the thickness of the peeling skin is about 1μm.(Figure 3.48.(a)) This is in agreement with a skin-core model proposed for Kevlar® fiber.(Figure 3.48.(b))

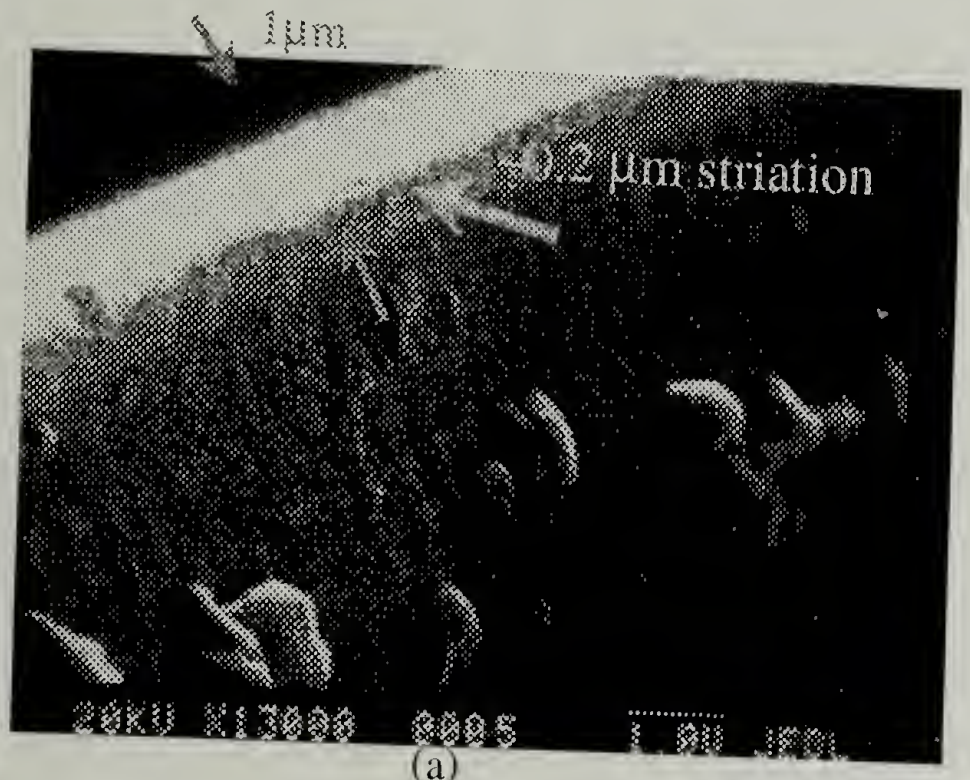

(a)

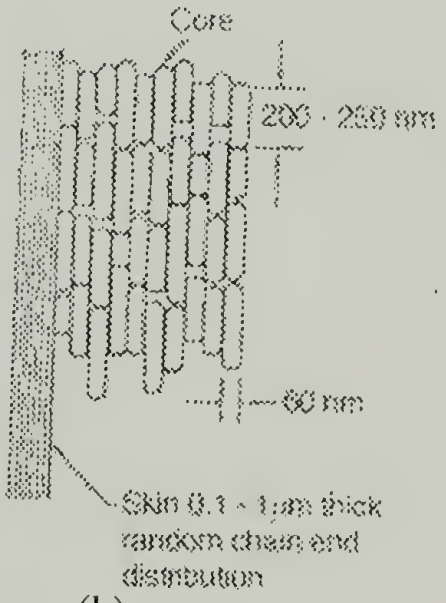

(b)

Figure 3.48 The internal surface of a fiber split under fatigue; (a). SEM picture of skin peeling, (b). proposed skin-core morphology in Kelvar[125]

3.4.7 Characterization of Post-fatigued Fibers

To help understand the influence of fatigue on the properties of high performance fibers, the properties of fibers being fatigued were characterized.

3.4.7.1 Mechanical Properties

Ferreira and coworkers found that the stress-strain curve of Kevlar® fiber changes after fatigue.[118] A three-slope stress-strain curve was claimed to characterize the effect of fatigue. Our observation is different from theirs. Figure 3.49 and Figure 3.50 are the stress-strain curves of a

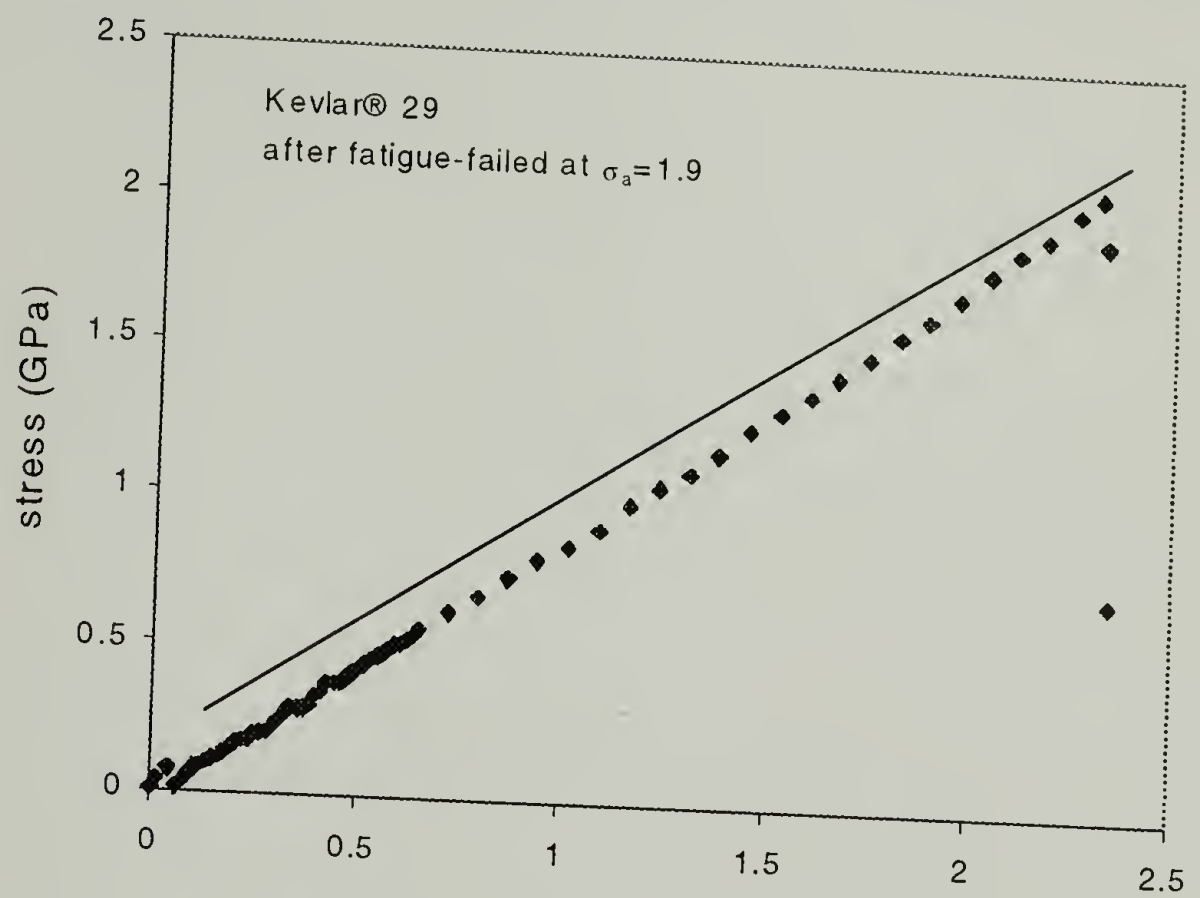

Figure 3.49 Post-fatigue characterization: stress-strain curve of one single filament

single filament and a yarn after the fiber has been fatigued. Both plots show that two slopes appear in the stress-strain curves of post-fatigued fiber, which is similar to that of an as-spun fiber and there is no decrease in modulus at high strain as shown by Ferreira and coworkers. [118]

The mechanical properties of the remaining fiber taken from the yarn failed under fatigue are shown in Table 3.10. It is found that the fiber failed in fatigue retains enhanced modulus gained in the early stage of fatigue. The shear modulus is lower after fatigue as is the tensile strength and the strain at break. It is interesting to find that the residual tensile strength is very close to the applied stress in the fatigue experiment.

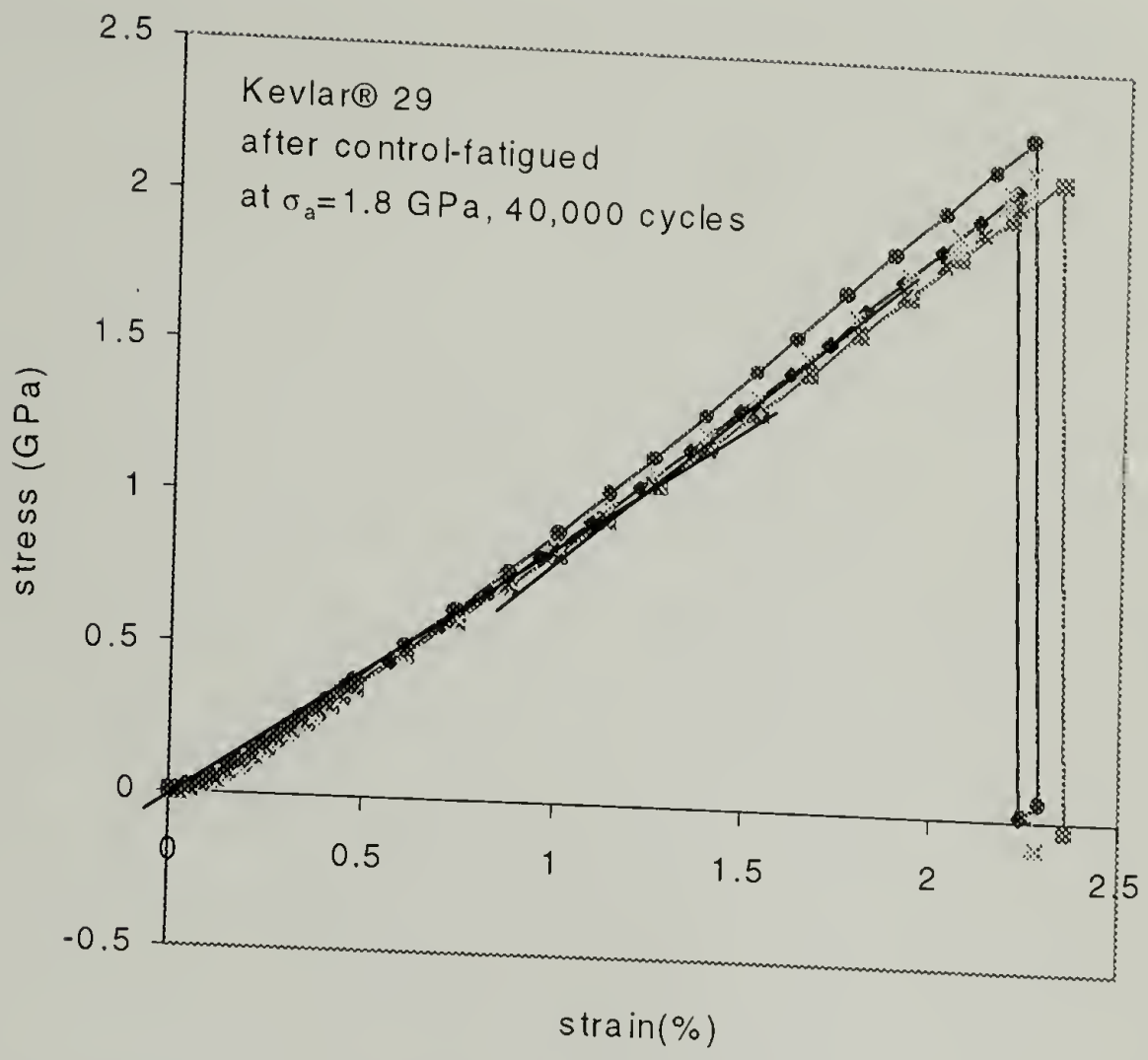

Figure 3.50 Post-fatigue characterization: yarn stress-strain curves

Table 3.10 Properties of fatigue-fractured fibers

Material	Tensile Modulus (GPa)	Shear modulus (GPa)	Tensile strength (GPa)	Strain to break(%)	Diameter (μm)
as spun fiber	82.6(0.70)	1.82(.05)	2.79(.27)	3.03(.32)	13.20
post fatigue fiber	110.2(1.13)	1.37(.13)	1.97(.51)	1.94(.59)	13.20

Test condition: single filament
Gauge length: 60 mm
strain rate: 10%/min
Instron 5564

Fatigue condition:
sine wave form
5 Hz
0-1.96 Gpa

After the fiber was exposed to limited fatigue, the mechanical properties of the fiber change as shown in Table 3.11. The trends are the same as discussed above. It should be pointed out that the inherent variation in properties in fibers makes the study difficult.

Table 3.11 Mechanical properties of fibers being fatigued for a certain time in the form of single filaments and yarn

ID	sample type	number of specimen	Load Max.Load (N)		Modulus (AutYoung) (GPa)		Stress at Max.Load (MPa)		Strain at Max.Load (%)	
			mean	cv%	mean	cv%	mean	cv%	mean	cv%
K29as K347	single filament	50	0.389	10.3	93	5.5	2920	6.9	3.38	7.7
		30	0.316	19.4	113	18.2	2350	20.7	2.13	18.5
K29as K600	yarn	20	287	1.8	93	1.2	2560	1.73	3.14	2.7
		5	249	3.8	110	3.3	2160	3.8	2.26	2

* fatigue condition: K347: 1.7-0 GPa, 100000 cycles, unfailed sample
K600:1.8-0 GPa, 40000 cycles, unfailed sample

The similarity of the values in the applied fatigue stress and the residual strength after fatigue-failure inspired us to investigate the change in the strength of fiber during fatiguing. Figure 3.51 illustrates the change in yarn properties with the number of loading cycles. Figure 3.51.(a) shows that the residual strength in the fiber after fatigue decreases with the number of loading cycles. This suggests that the strength of the fiber is consumed during fatigue. Unlike

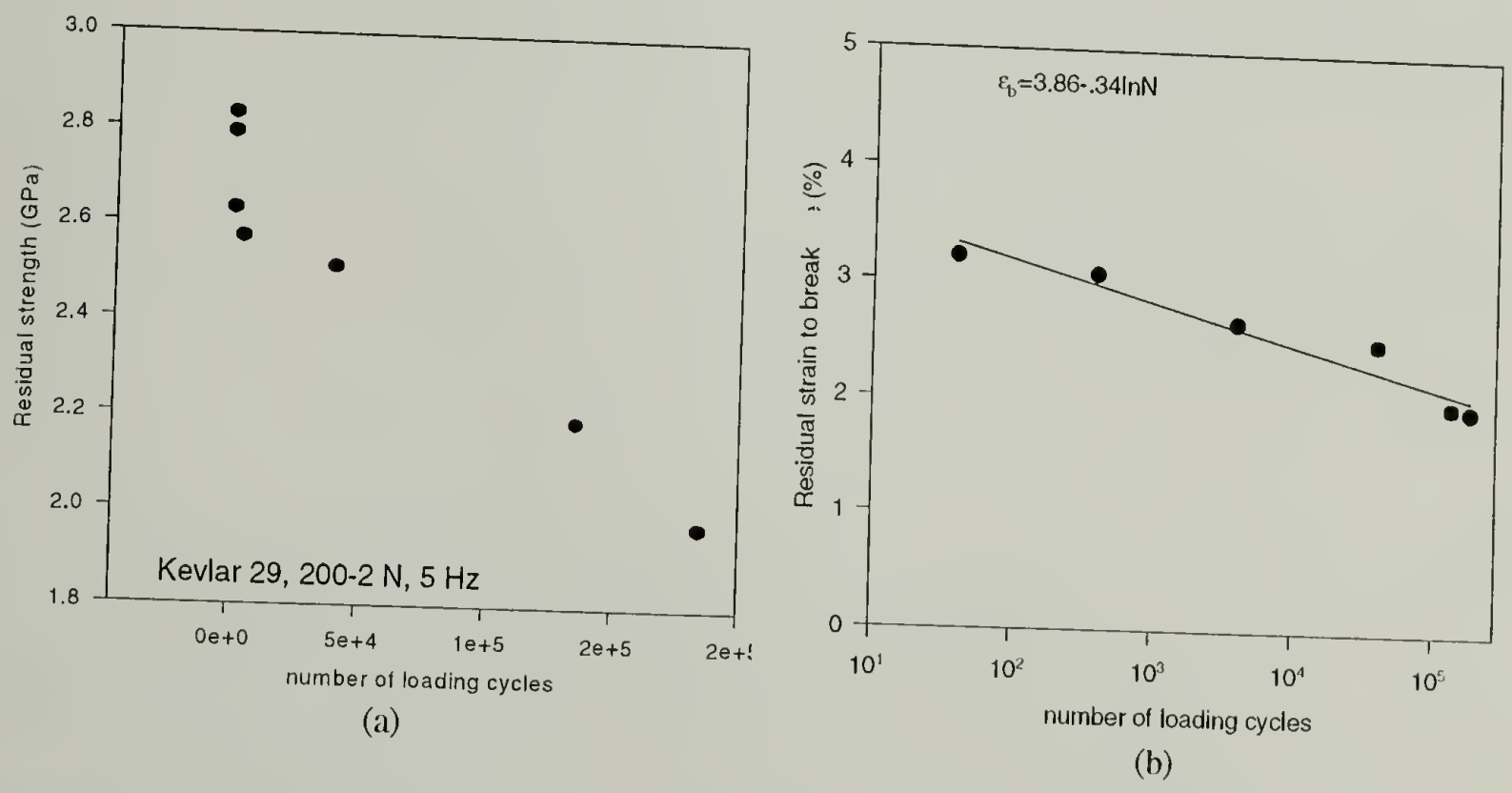

Figure 3.51 Change of yarn properties with the number of loading cycles; (a). Strength, (b). Strain at break

bulk material where the fatigue is defect dominated and is a local phenomenon, the fatigue in fibers is more macroscopic and the strength of the whole fiber deteriorates by fatigue. A decrease in the strain to break along with the number of loading cycles was expected. (Figure 3.51.(b)) It might be possible to correlate the residual strength or failure strain to the stress history of the material.

3.4.7.2 Thermal Mechanical Properties

A very intriguing finding is that the thermal shrinkage strain is strongly influenced by the fatigue history. A thermal shrinkage strain measurement was carried on a TMA (TA Instruments) on single filaments removed from the yarn at various stages of fatigue. These measurements are load sensitive. When an initial load of 2 g/den was applied, the thermal strain changes from expansion for an as spun fiber to shrinking for a fatigued sample with increasing temperature as shown in Figure 3.52. Figure 3.52 also shows that both samples have a similar thermal strain for the second heating and show a negative thermal expansion coefficient.

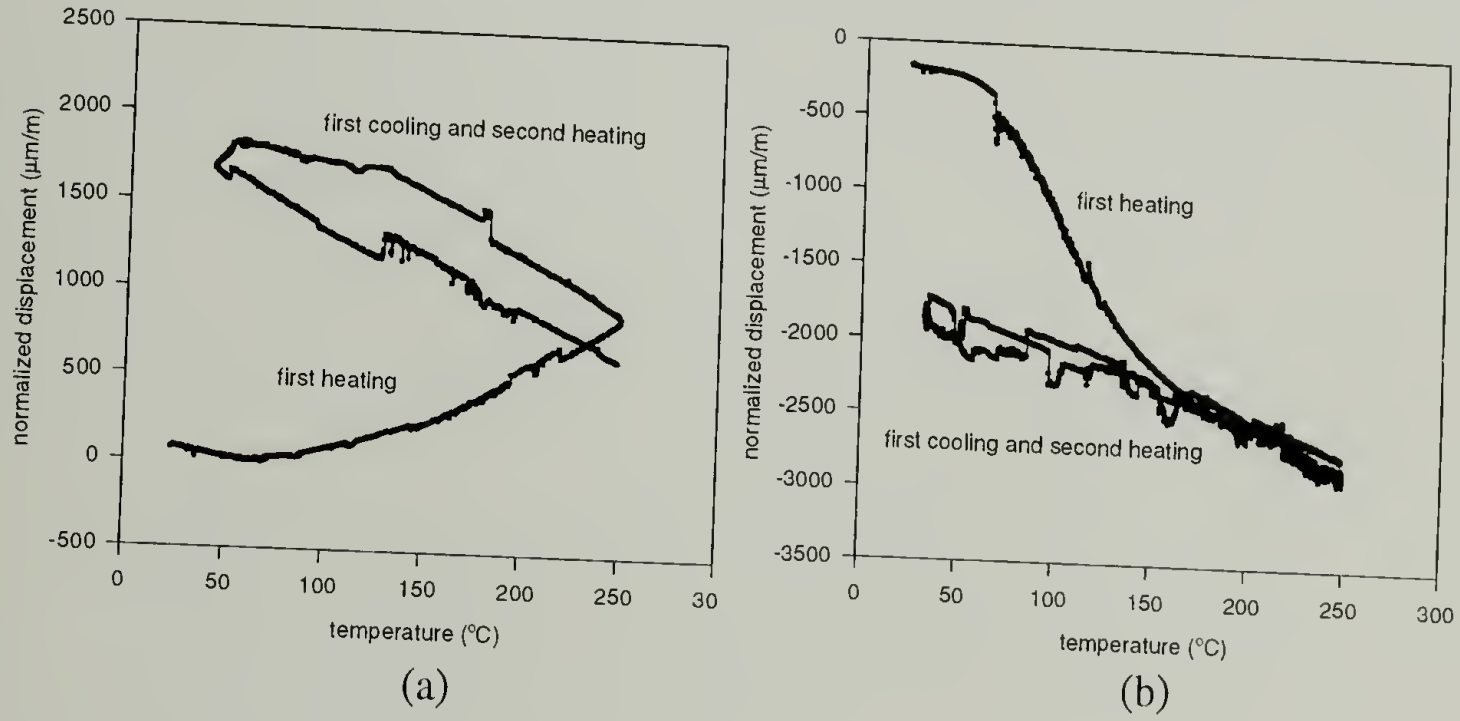

Figure 3.52 Displacement-Temperature Experiment (D-T) of the fiber; (a). As spun fiber, (b). post-fatigued fiber

Figure 3.53 compares the thermal shrinkage strains for fibers being fatigue-failed under different loading stresses. It is seen that the higher the fatigue stress, the smaller the thermal shrinkage of the fatigue-failed fiber.

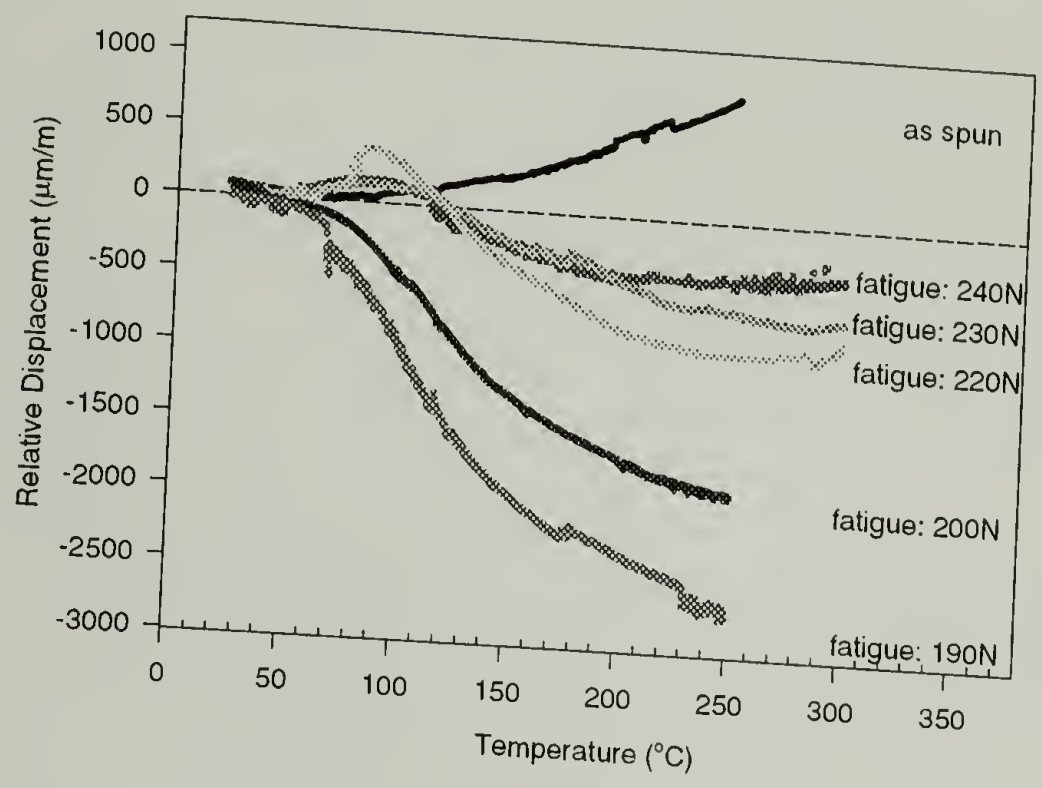

Figure 3.53 D-T Curve of Kevlar® 29 fibers fatigue broken under different applied stress amplitude; numbers in the plot are cyclic maximum loads for 1500 denier yarns

3.4.8 Correlation of Damage with Structure or Properties and Prediction of Remaining Lifetime

One objective of this study is to provide the methodology to predict the remaining lifetime after the material has been subjected to a stress history, based on an understanding of the failure mechanisms and structure-property correlations in the materials. In this part of the study, Kevlar® 29 fiber is the only material studied. Figure 3.54 illustrates our approach on how to predict the remaining lifetime in the material.

Polymeric materials retain signatures of past states. After the fiber has been used for some time, its stress and heat history can be retrieved. This topic will be discussed in detail in Chapter 5 and Chapter 7 showing that a structural characterization or a specific thermal- mechanical property measurement can detect the stress and heat history of the material.

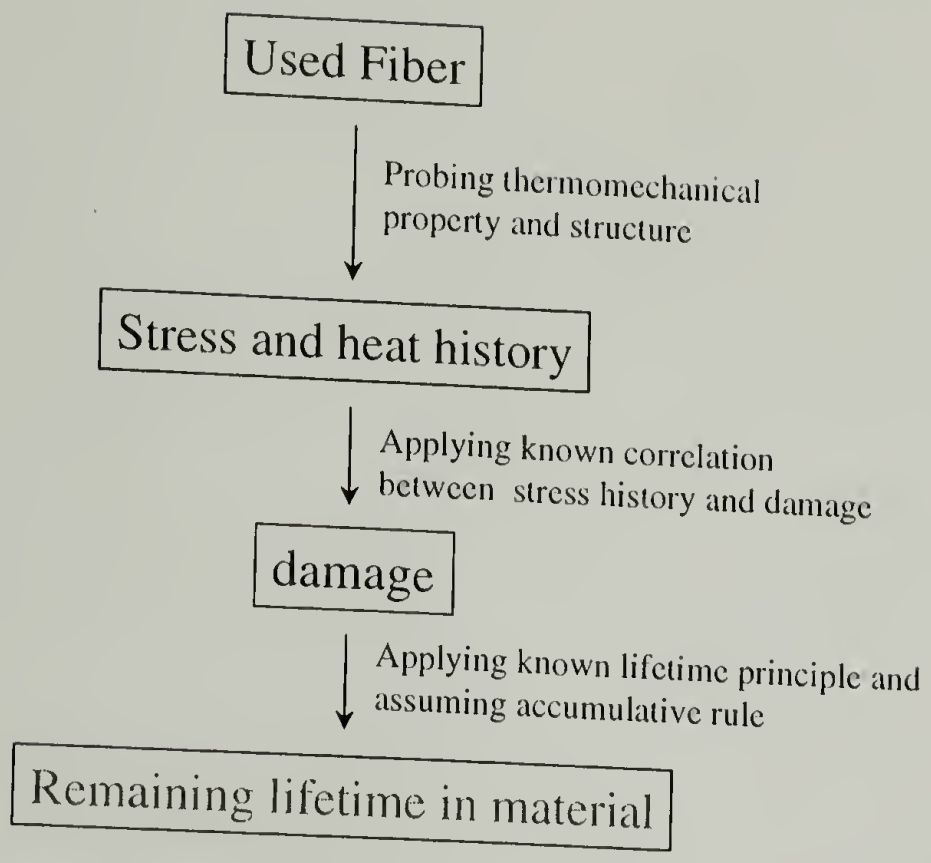

Figure 3.54 Flow diagram to predict remaining lifetime in high performance fibers

Applying known correlation between the stress history and damage, the damage in the material can be calculated. The known lifetime principle then allows us to predict the remaining material lifetime. Structure characterization can be nondestructive. However, it requires an in place X-ray diffractometry, which requires special maintenance and is expensive and difficult to use. The thermal mechanical measurement is not nondestructive, but it only requires a short piece of a single filament from the loading elements of cable or ropes. The instrument is inexpensive to use and easy to maintain.

3.4.8.1 Damage detection by Thermal Mechanical Analysis

In our study, we found that irreversible thermal force at constant strain reflects the thermal and stress history. This topic will be discussed in detail in Chapter 5. Only the conclusions will be used here.

A trace of the derivative of thermal stress with the temperature (IFTT curve, which is defined in Chapter 5) is characteristic to illustrate the thermal and stress history. The maximum

exposure temperature can be found from the peak temperature value in IFTT and the stress history can be found from a temperature at which $d\sigma/dT$ is equal to 0.15 MPa/oC that is called T_2.

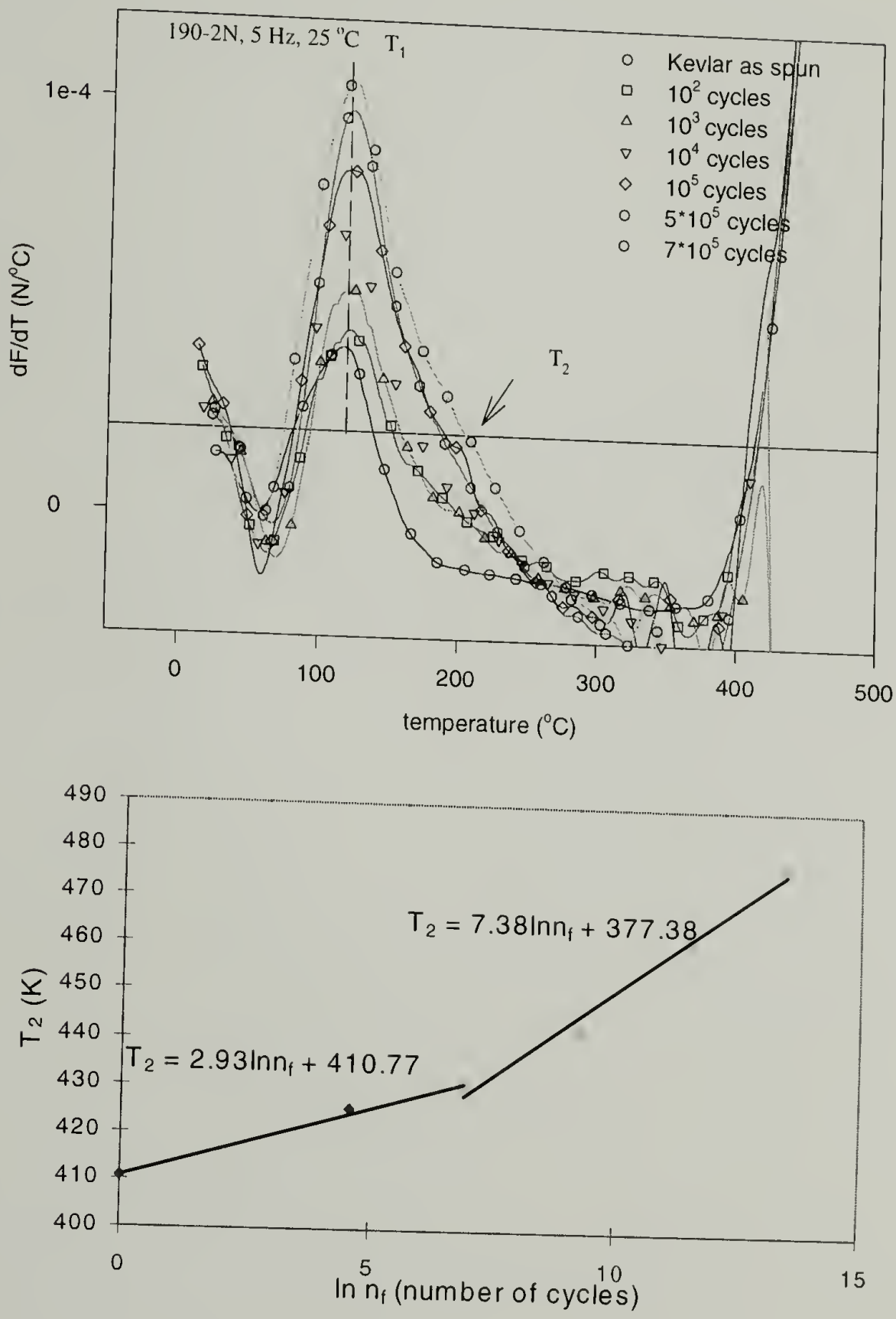

Figure 3.55 Evolution of T_2 with the time of fatigue loading

It is found that when a fatigued fiber is examined, the time of fatigue loading can be calculated. Figure 3.55 shows the IFTT curves of fibers being fatigued for different times under one stress range. The peak temperature in the IFTT curves is the same and this tells us that the fiber was fatigued at ambient temperature. When the fiber was fatigued at elevated temperature, a shift in peak temperature was observed. When T_2 is plotted against the logrithmic of number of loading cycles, a two stage linear relation was observed. (Figure 3.55) The transition point agrees with the perfection-damage transition that we discussed in 3.4.2. Using this correlation, we can tell the number of loading cycles that a fatigued fiber has experienced.

The number of loading cycles can be found from T_2 in an IFTT curve for one loading stress (1.67 GPa in the study). Figure 3.56 indicates that the characteristic temperature T_2 in thermal force measurement of fatigue-failed fibers changes with the loading stress range. This makes it difficult to determine the stress history. The fatigue stress range needs to be known to estimate the time of fatiguing. On the other hand, T_2 at the moment of failure remains unchanged when the fatigue stress is less than 2.0 GPa. (Figure 3.56) In the actual use of Kevlar® fibers, the applied stress will be lower than 2.0 GPa, which is 80% of the strength of the fiber. Therefore, T_2 is a good tool to evaluate the stress history by first assuming a certain stress range and then identifying the time of loading. Then, the remaining lifetime of the fiber can be calculated using cumulative damage rule.

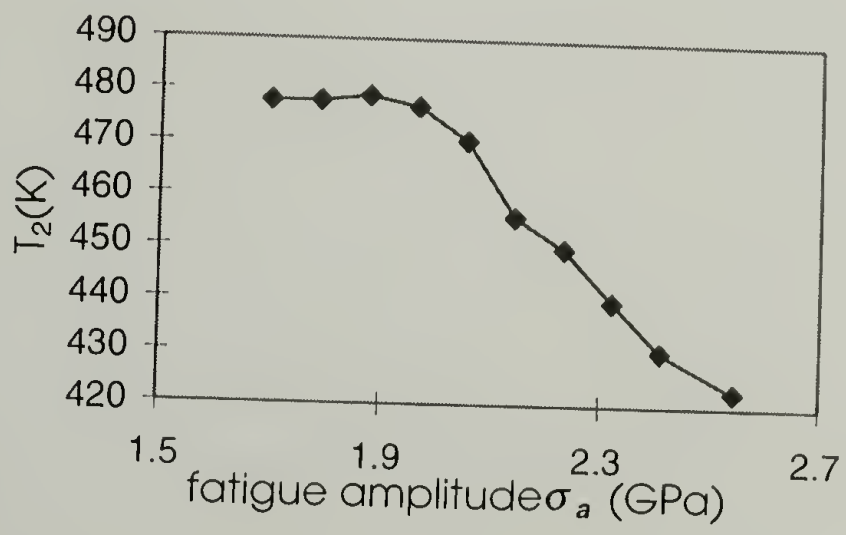

Figure 3.56 Change in T_2 of fatigue-failed sample with the corresponding fatigue amplitude

Besides thermal stress, thermal shrinkage also appears to be a very sensitive measure of the stress history of the material. Figure 3.57 correlates the maximum shrinkage strain, which is the shrinkage strain observed in the plateau region (~ 220 °C), with the number of loading cycles

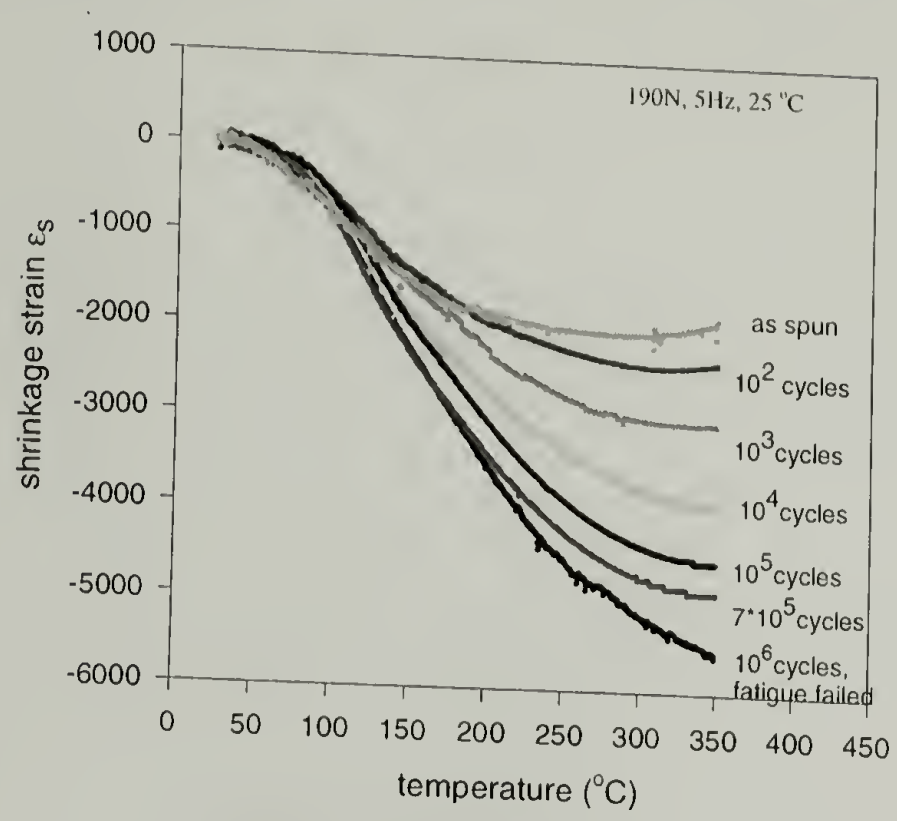

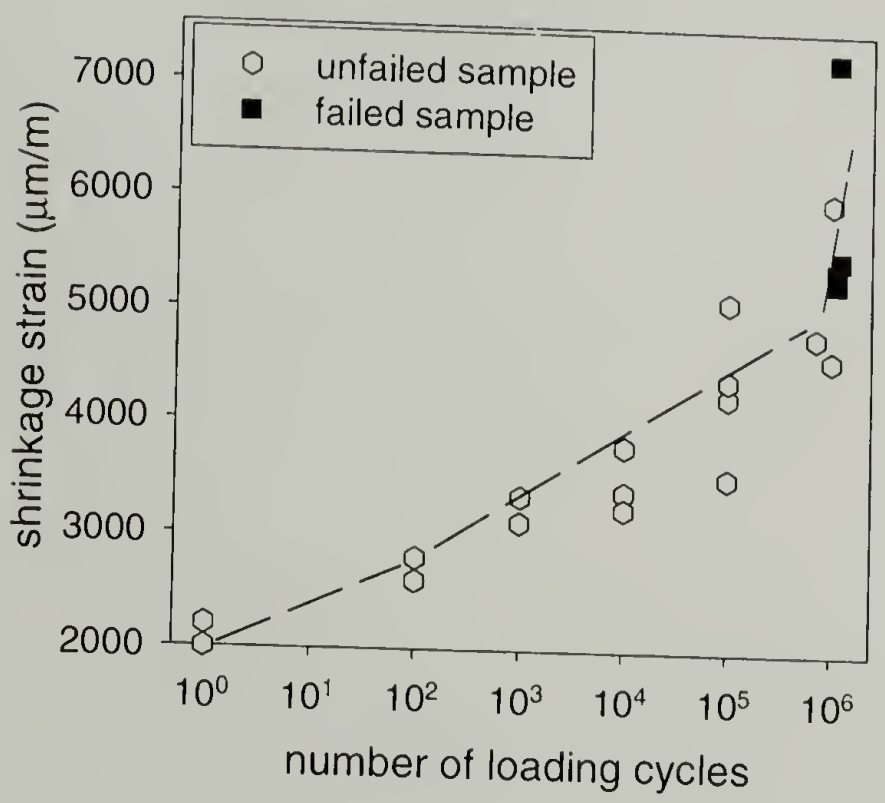

Figure 3.57 D-T behavior of Kevlar® 29 single filament being fatigued

that the fiber has seen under certain stress conditions. The thermal shrinkage for the fiber is different in Figure 3.57 from that in Figure 3.52 because the initial force applied here is smaller (< 0.1 g/den). The possible relation between thermal force and thermal shrinkage will be

discussed in Chapter 5. Although the reversible elastic thermal shrinkage and thermal force are inherently related, the thermal force and thermal shrinkage measured here are irreversible. The measurement of thermal shrinkage might be complementary to the thermal force measurement. Although no transition in perfection to damage is detected in the thermal shrinkage measurement, there is a large increase in the thermal shrinkage when the fiber under fatigue is close to failure. (Figure 3.57) This can be used to estimate the fiber's fatigue history.

3.4.8.2 Damage detection by X-ray structure characterization

We have discussed the detection of damage from thermal mechanical measurements. Another way to detect damage is through structure measurements. Kevlar® fiber is believed to be a one-phase system. The fiber is composed of imperfect crystals. The change in structure due to external stressing can be used to determine the damage. The structure-property correlation will be discussed in detail in Chapter 7. Two structure parameters are tied to the stress history: the paracrystalline parameter and the orientation angle. The structure of the fibers after limited fatigue was characterized. Figure 3.58 shows the change in these two parameters with the number of loading cycles the material has seen. In Figure 3.58, the simultaneous moduli is plotted against the moduli calculated from the two structure parameters according to a correlation function (Equation 7.11) introduced in Chapter 7. These two moduli are comparable along the whole fatigue process and this further confirms the proposed structure-property correlation. (Chapter 7) Therefore, the two structure parameters can be used to identify the fatigue history. The more interesting observation is that the change in paracrystalline parameter shows a transition from decreasing with the loading cycles to an increase as shown in Figure 3.58. This can be used as a guide in the use of the material. It probably is due to the loss of the structural integrity of the material in the late stage of fatigue.

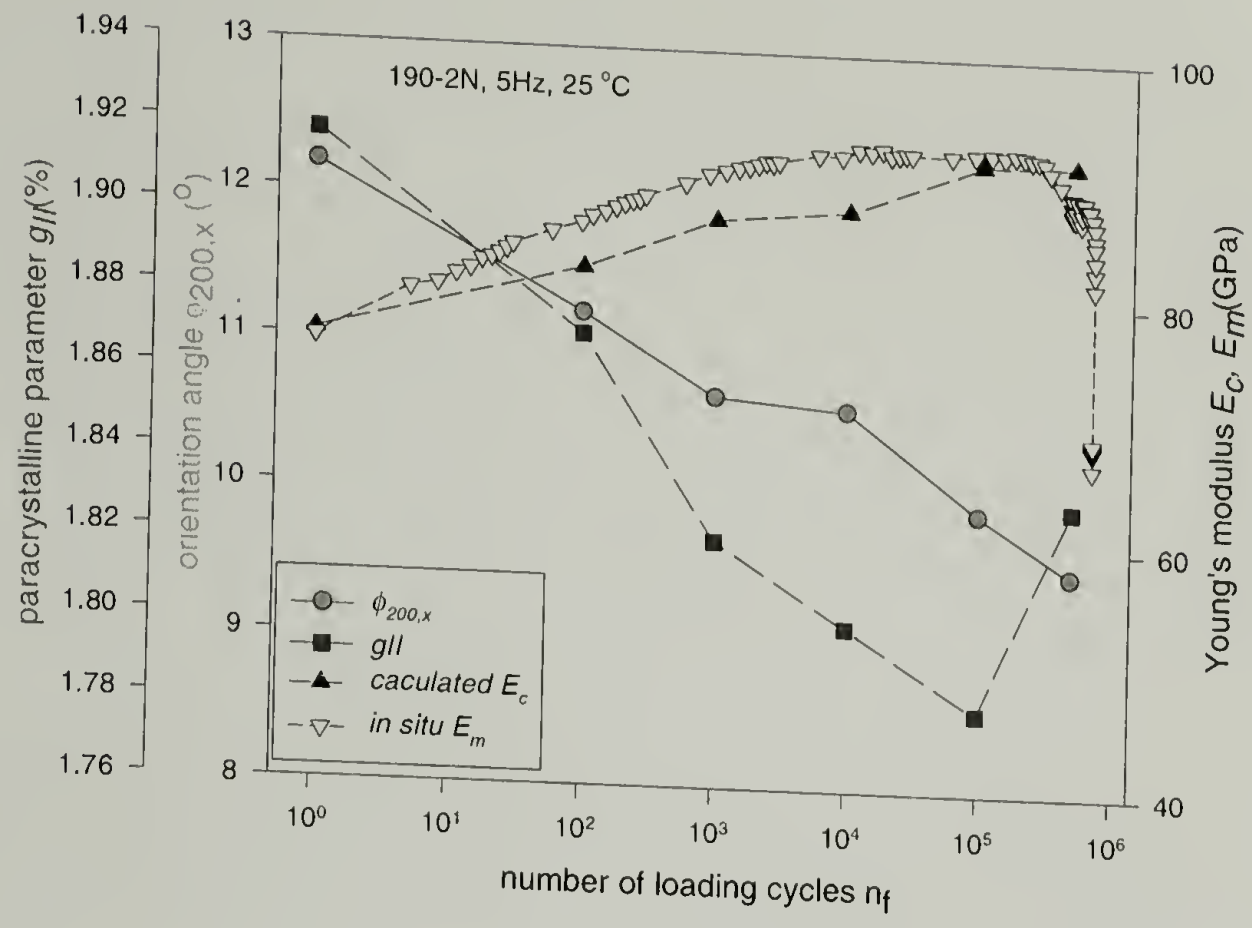

Figure 3.58 Correlating structure parameters in the fatigued fiber with the number of loading cycles

3.5 Conclusions

We have discussed the fatigue and creep behavior of high performance fiber yarns. In the study of fatigue behavior of high performance fibers, the following is concluded.

A general semilogarithmic law governs the relationship between fatigue lifetime and normalized load amplitude for these high performance fibers. Fatigue behavior is characterized by a fatigue strength and a fatigue strength index. The fatigue resistance of different fibers ranked from best poorest as: Kevlar® 29 ~ Kevlar® 119, Vectran® HS~ Technora®, Spectra® 900. The fatigue of the Kevlar® 29 and Vectran® HS exhibit frequency insensitivity in a frequency range of 0.1 to 5 Hz. There is a loading interaction phenomenon in the fatigue of Kevlar® 29 and Vectran® HS. Loading sequence affects the lifetime. The fatigue lifetime is shortened under elevated temperatures. By twisting the fiber, an improvement in tensile strength and fatigue resistance can be achieved.

A critical strain failure criterion was identified for different fibers under tensile, creep and fatigue loading.

Two methods: thermal mechanical measurements and structure characterization were proposed to detect the damage and predict the remaining lifetime in these fibers.

Unlike most bulk isotropic materials, the characteristic behavior of Kevlar® fiber yarn under stress controlled fatigue is a competition between structure perfection and fatigue damage. An increase in modulus and strength is observed during the initial phases of fatigue, while further fatiguing shortens the lifetime and lowers the strength of the material.

Fatigue strain follows a semilogarithmic equation with the number of loading cycles. The damage in the fiber is related to the fatigue strain or the permanent deformation in the fiber.

A fatigue failure model was proposed to allow the derivation of the fatigue lifetime equation from several known material constants.

Morphology studies show that axial splitting is the common mode of fatigue fracture of all the studied materials. The activation energy of fatigue strain was calculated to be 10 kJ/mol, suggesting that the process involves the break of hydrogen bonds.

Property and structural changes measured by Instron, TMA and X-ray diffraction show that the strength of the material is depleted with fatigue.

In the study of creep behavior of high performance fibers, the following has been concluded.

A general semilogarithmic law governs the relationship between creep lifetime and normalized stress in these high performance fibers. Creep behavior is characterized by a creep strength and creep strength index. Nomex exhibits the smallest creep strength index among fibers. The creep properties of Kevlar® 29, Kevlar® 49 and Technora® are similar and their creep lifetime is longer than Vectran® HS under the same stress level.

Creep strain in Kevlar® fiber is found to undergo three stages: primary, secondary and tertiary creep. The primary creep follows a semilogarithmic equation with the loading time and the secondary creep follows a linear equation with the loading time. It is the secondary creep that determines the material lifetime. A creep failure model was proposed to allow the derivation of the creep lifetime equation from several known material constants.

CHAPTER 4

TWISTED YARN MECHANICS —NEW APPROACH THROUGH COMPOSITE THEORY

4.1 Abstract

Little data exists on how twist changes the properties of high performance continuous fiber yarns. For this reason, a study has been conducted to determine the influence of twist on the strength and stiffness of a variety of high performance continuous polymeric fiber yarns. The materials investigated include Kevlar® 29, Kevlar® 49, Kevlar® 149, Vectran HS®, Spectra 900® and Technora®. Mechanical property tests demonstrate that the initial modulus of a yarn monotonically decreases with increasing twist. A model based on composite theory has been developed to elucidate the decrease in modulus as a function of both the degree of twist and the elastic constants of the fibers. The modulus values predicted by the model have good agreement with those measured by experiment. The radial shear modulus of the fiber, which is difficult to measure, can be derived from the regression parameter of experimental data by the use of the model. Such information should be useful for some specialized applications of fibers, e.g. fiber-reinforced composites. The experimental results show that the strength of these yarns can be improved by a slight twist. A high degree of twist damages the fibers and reduces the tensile strength of the yarn. The elongation to break of the yarns monotonically increases with the degree of twist.

Keywords: Twisted yarn, Young's modulus, Modeling, High performance fibers

4.2 Background

Since the 1970's, considerable effort in the fiber industry has been dedicated to finding new polymeric fibers with high performance for potential use in applications such as ropes and

cables, fiber-reinforced composites, ballistic vests, gaskets, etc. Kevlar®[2], Vectran®[126], Technora®[88] and Spectra®[127,128] are some excellent examples of high performance polymeric fibers. There have been several investigations of the properties and the structure-property relationships of these high performance fibers [30,35,38,129,130]. These fibers show high anisotropy[71,131] when compared to conventional fibers or other bulk materials. This chapter aims to illustrate the importance of material anisotropy on some macroscopic properties by studying the properties of twisted yarn.

Special geometric effects are introduced into fiber yarns in many textile applications. Twist has long been known to improve the strength of short fiber staple materials and few recognize that many threads are composed of short fibers that are held together by twist. Strands of twisted fibers have been used to control flexibility in copper and steel cable systems. Twist is also used to give continuous yarns integrity and force the assembly of single fibers to behave as a single unit. For conventional fibers such as nylon and polyester, only a small amount of twist is used because twist damages critical yarn properties. However, for some high performance fibers twist affects the yarn properties such as modulus, strength and elongation to break in a more complicated way. There are few reports describing the influence of twist on the properties of high performance polymeric fiber yarns[3,71,131]. One of the purposes of this paper is to illustrate and model the influence of twist on high performance fiber yarns.

As early as 1907, Gegauff [132] had proposed a simple analysis to correlate the twist angle of a yarn with the yarn modulus. Gegauff's derivation is given below and forms an excellent basis to expand this type of model.

The geometry of a twisted yarn is shown in the following:

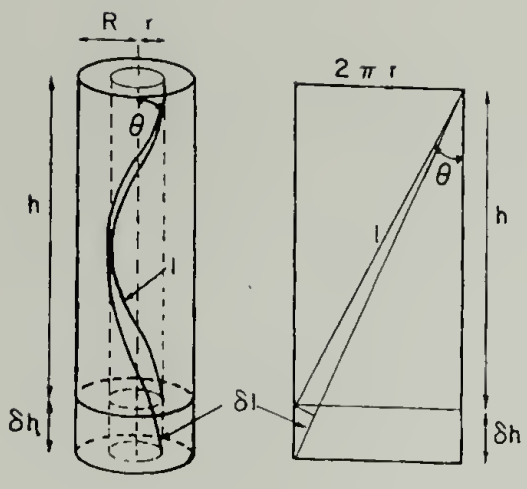

(a) (b)

$$\tan\theta = \frac{2\pi r}{h}, \tan\alpha = \frac{2\pi R}{h}$$

where, (a) is an ideal geometry of a twisted yarn, the solid curved line is a single filament, R is the radius of the yarn, r is the radial position of a single filament, h is the yarn length for 1 turn, δh is the increase in length h under stretching, θ is the angle between the path of the single filament at a radius of r and the yarn axis, and for the single filament at the radius of R, the angle is α; (b) is a flattened projection of a single filament, l is the length of a single filament at a radius of r and δl is the corresponding filament elongation.

Gegauff's classic model of twisted yarn mechanics

1. Relation of single filament extension to yarn extension

Let the yarn extension = $\varepsilon_1 = \delta h/h$,

then, the fiber path length=$l = h/\cos\theta$, and the fiber displacement = $\delta l = \delta h * \cos\theta$

Consequently: the filament extension = $\varepsilon_f = \frac{\delta l}{l} = \cos^2\theta * \frac{\delta h}{h}$

Thus: yarn extension = $\varepsilon_1 = \varepsilon_f / \cos^2\theta$

2. Axial Tensile Force

The stress along a filament in the yarn is

$$\sigma_f = E_f * \varepsilon_f$$

and an equivalent area perpendicular to the filament axis = $2\pi r dr \cos\theta$

Then at a position of radius r in the yarn, the component of tension parallel to the yarn axis resulting from the filament stress becomes,

$$= E_f \varepsilon_f (2\pi r dr \cos\theta)\cos\theta = E_f 2\pi r dr \varepsilon_1 \cos^4\theta$$

Therefore, total yarn tension = $\int_0^R E_f 2\pi r dr \varepsilon_1 \cos^4\theta = \pi R^2 \varepsilon_1 E_f \cos^2\alpha$

Thus, yarn modulus = $\hat{E} = E_f \cos^2\alpha$

However, the measured yarn modulus always shows a stronger dependency on the degree of twist than the model indicated. Platt [133] followed this approach and incorporated the effect of lateral contraction and large extension. Hearle[134] added the influence of transverse forces and neglected lateral contraction. Treloar and Riding[135] adopted an energy method instead of performing a stress analysis and considered the migration of a single filament in a twisted yarn. Freeston and Platt[136] further considered the effect of strain rate on the stress-strain behavior. White, Cheng and Spruiell[137] performed a continuum mechanics analysis including not only transverse forces but also interfilament friction. They derived a more complicated equation describing the influence of twist on yarn modulus.

$$\text{Yarn modulus} = \hat{E} = E_f * \left(\frac{1}{4} + \frac{9}{4} T_0 + \frac{3T_0}{(1-T_0)} \ln T_0^{1/2}\right)$$

in which $T_0 = \cos^2\alpha$

None of the models described above provides good agreement with experimental data, especially when yarns made from high performance fibers are considered. All of these models imply that the change in the Young's modulus of a material depends only upon the angle between the material axis and the stress direction regardless of other material properties. The first drawback of these models lays in the fact that, for an isotropic material, the modulus does not change with the relative direction of the stress with the material axis. Secondly, as shown later in

this paper, yarns made from different fiber materials behave differently at the same twist angle, which is not contained in any of the previous models. Therefore, the omission of important material characteristics, such as anisotropy, yields models that are unsatisfactory. In this paper composite theory is used to incorporate the anisotropy of the material into a new model that accurately describes the influence of twist on yarn modulus for all polymeric fibers.

4.3 Experimental

Twisted yarns were made by anchoring one end of a fixed-length of yarn and while maintaining a slight tension, rotating the other end about the yarn direction a predefined rotation. The length of the yarn after twisting was recorded and the twist in these yarns was calculated according to ASTM D 1432-92. Several terms were used to characterize the degree of twist in a yarn. Twist in turns per inch, tpi, was directly counted. A term called the Twist Multiplier (TM) is related to the yarn twist in turns/inch (tpi) and yarn Denier by the equation $TM = \frac{tpi \times \sqrt{Denier}}{73}$. The surface twist angle is the angle between the filament at the most outer layer of a twisted yarn and the yarn axis. The linear density of the yarn was measured by a microbalance to determine the yarn Denier, i.e. the weight in grams of 9000 meters of yarn. The fiber density was measured using a density-gradient column. By knowing the Denier and density, the cross-sectional area of the yarn was calculated.

The tensile testing of the twisted yarn was done using an Instron® Model 5564 testing machine according to ASTM D 2256-90. All of the tests were performed at standard conditions of 21 °C (± 1 °C) and 65% (± 2%) relative humidity. Pneumatic yarn/cord grips were used for these tests, with the effective gauge length set at 150 mm and a crosshead speed of 10 %/min. The initial modulus was calculated from the slope of the stress-strain curve in the strain range from 0.05% to 0.5 %. Griping effects were corrected by adjusting the gauge length.

4.4 Notation

Given below is a list of the principle symbols and notation used in the text. To avoid confusion and complexity, all the symbols are defined here. Referring to Figure 4.1, different structural components--a single filament, a layer of flattened twisted yarn composing of single filaments resembling to a unidirectional composite and a twisted yarn -- are utilized in this paper. The properties of a single filament are transformed first into on-axis properties and further into off-axis properties of the unidirectional composite.

For a single filament and twisted yarn, the symbols follow what are defined before.

E_f, ε_f, σ_f characterize the behavior of a single filament

ε_l, σ_l characterize the behavior of a twisted yarn

$\hat{E}(\alpha)$: apparent Young's modulus of a twisted yarn with the surface twist angle of α

For the layer of flattened twisted yarn, i.e., the unidirectional composite,

on-axis constitutive equation can be expressed by the following matrix

$$\begin{pmatrix} \varepsilon_z \\ \varepsilon_y \\ \varepsilon_s \end{pmatrix} = \begin{pmatrix} S_{zz} & S_{zy} & 0 \\ S_{yz} & S_{yy} & 0 \\ 0 & 0 & S_{ss} \end{pmatrix} \begin{pmatrix} \sigma_z \\ \sigma_y \\ \sigma_s \end{pmatrix} = \begin{pmatrix} \frac{1}{E_z} & \frac{-\nu_{zy}}{E_y} & 0 \\ \frac{-\nu_{yz}}{E_z} & \frac{1}{E_y} & 0 \\ 0 & 0 & \frac{1}{E_s} \end{pmatrix} \begin{pmatrix} \sigma_z \\ \sigma_y \\ \sigma_s \end{pmatrix}$$

off-axis constitutive equation can be expressed by the following matrix

$$\begin{pmatrix} \varepsilon_1 \\ \varepsilon_2 \\ \varepsilon_6 \end{pmatrix} = \begin{pmatrix} S_{11} & S_{12} & S_{16} \\ S_{21} & S_{22} & S_{26} \\ S_{31} & S_{32} & S_{66} \end{pmatrix} \begin{pmatrix} \sigma_1 \\ \sigma_2 \\ \sigma_6 \end{pmatrix} = \begin{pmatrix} \frac{1}{E_1} & \frac{-\nu_{12}}{E_2} & \frac{\nu_{16}}{E_3} \\ \frac{-\nu_{21}}{E_1} & \frac{1}{E_2} & \frac{\nu_{26}}{E_6} \\ \frac{-\nu_{61}}{E_1} & \frac{\nu_{62}}{E_2} & \frac{1}{E_6} \end{pmatrix} \begin{pmatrix} \sigma_1 \\ \sigma_2 \\ \sigma_6 \end{pmatrix}$$

in which,

z, *y*: principle terms of the on-axis behavior; *1,2*: principle terms of the off-axis behavior

s, 6: shear terms;

ε_i: strain; σ_i: stress; S_{ij}, E_i: compliance and engineering Young's modulus

ν_{ij}: Poisson's ratio

On-axis properties of a twisted yarn layer are the same as the properties of a single filament,

$E_z = E_f$; $E_s = E_{rz}$; $E_y = E_r$ in which E_{rz} is the shear modulus and E_r is the transverse radial modulus in a filament.

θ, α, r, R: the same meanings as previous defined in the ideal twist geometry; dominate the characteristic off-axis behavior of different yarn layers

T_0: a function of the surface twist angle, $\cos^2\alpha$

d: anisotropic ratio, $\frac{E_z}{E_s}$

E_{zc}, E_{yc}, E_{sc}: the on-axis Young's moduli and shear modulus of an unidirectional composite

E_m, G_m: the Young's modulus and shear modulus of the matrix in a composite

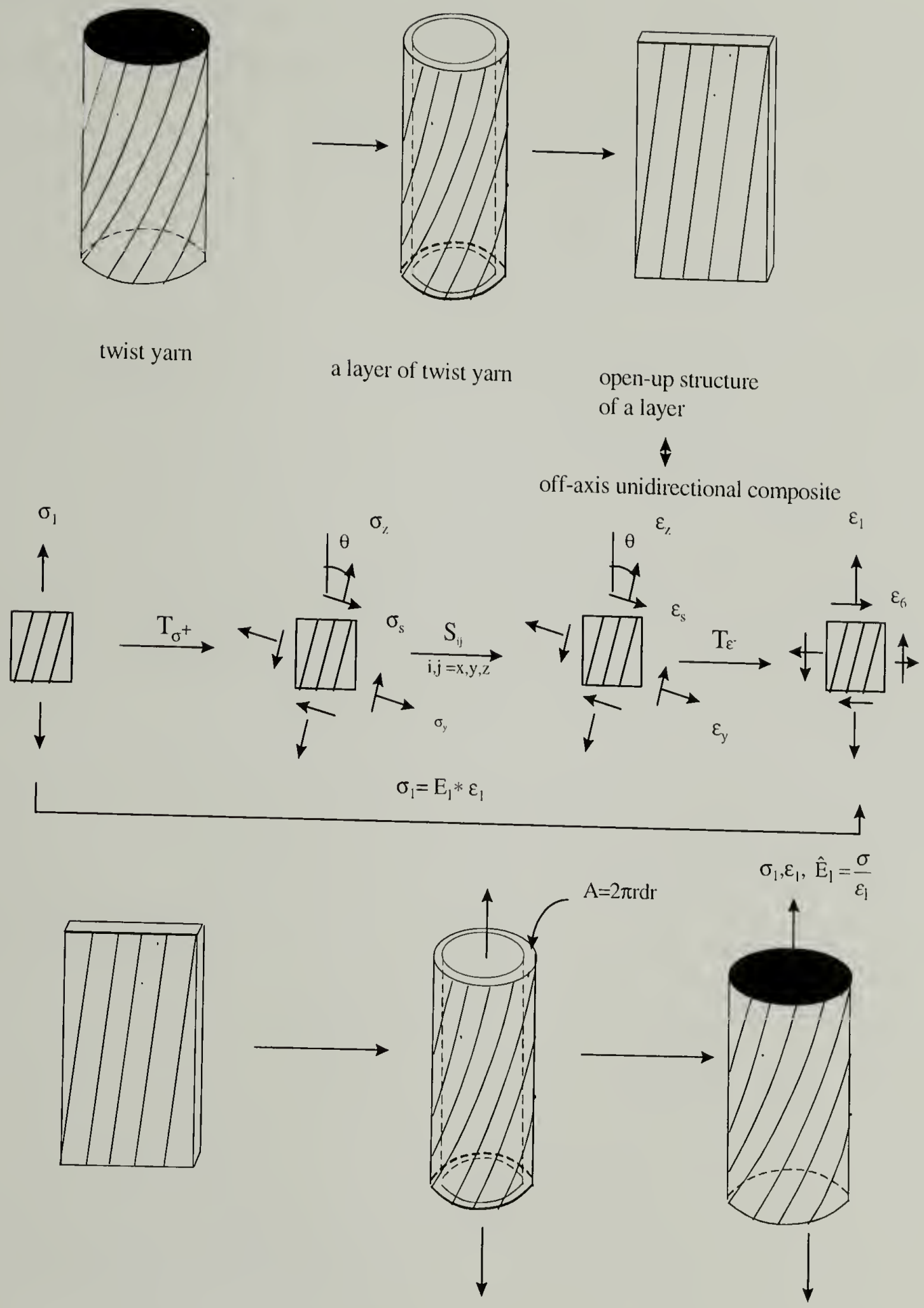

Figure 4.1 Schematic illustration of the model of calculation the twisted yarn modulus from the fiber properties

4.5 Models, Results and Discussion

4.5.1 Model Development of Modulus of Twist Yarn Using Composite Theory

The approach used to model how the yarn modulus is influenced by the degree of twist is quite straightforward. A strategy was taken as shown schematically by Figure 4.1. The notation in the following discussion will follow those in Figure 4.1. The twisted yarn was first dissected into individual loading elements, which are a series of thin-wall tubes. A tube is hypothetically cut and opened up to be a sheet structure with a preferred orientation different from that of the planar material axes. The stress-strain response of the plane was solved using orthotropic composite theory [138]. The responses of the individual elements were added via integration of the layered structures and this yields the stress-strain behavior of the yarn. In this way, the yarn modulus was derived from the single filament properties.

4.5.1.1 Single layer mechanics

A thin-walled layer of the twisted yarn was taken. The open-up structure of this layer resembles a unidirectional composite. At the radial position of r, the off-axis angle is θ, and at the radial position of R, the off-axis angle is α.

According to composite theory[138], under uniaxial stress a unidirectional composite responds as

$$\varepsilon_1 = S_{11}\sigma_1 = \frac{\sigma_1}{E_1}$$

Therefore, the off-axis modulus of a single layer $E_1 = \frac{1}{S_{11}}$,

and the off-axis stress $\sigma_1(\theta) = \frac{1}{S_{11}}\varepsilon_1$

Equation 4.1

4.5.1.2 Yarn mechanics by layer assembly

Assuming no slippage between layers because of the integrity of a twisted yarn, each layer has the same extension $\varepsilon = \varepsilon_l$ under uniaxial stress. Also assuming continuous layers along radial direction in a twisted yarn, the axial force in a yarn = $F = \int \sigma_1(\theta) dA = \int_0^R \sigma_1(\theta) 2\pi r dr$

Equation 4.2

If the yarn is treated as one body, the axial force can also be expressed as $F = \pi R^2 \hat{E} \varepsilon_1$

Equation 4.3

in which $\hat{E}$ is the apparent yarn Young's modulus. Utilizing the ideal twist geometry $\tan\theta = \frac{2\pi r}{h}$ and $\tan\alpha = \frac{2\pi R}{h}$, as well as the equality of Equation 4.2 and Equation 4.3 and the expression of $\sigma_l(\theta)$ by Eqn. 1, the apparent Young's modulus of a twisted yarn can be calculated as

$$\hat{E} = \frac{2}{\tan^2\alpha} \int_0^\alpha \frac{1}{S_{11}(\theta)} \tan\theta \sec^2\theta d\theta$$

Equation 4.4

4.5.1.3 Exact solution

According to composite theory[138], the off-axis compliance of a unidirectional composite can be expressed as

$$S_{11} = m^4 S_{zz} + n^4 S_{yy} + m^2 n^2 S_{ss} + 2m^2 n^2 S_{zy}$$

Equation 4.5

where $S_{zz} = \frac{1}{E_z}$, $S_{yy} = \frac{1}{E_y}$, $S_{ss} = \frac{1}{E_s}$, $S_{zy} = -\frac{\nu_{zy}}{E_y} = -\frac{\nu_{yz}}{E_z}$, $m = \cos\theta$, $n = \sin\theta$ and θ is the off-axis angle.

The compliance S_{11} can be expressed by moduli after rearrangement as

$$S_{11} = \frac{1}{E_y} + (\frac{1}{E_s} - \frac{2}{E_y} - \frac{2\nu_{yz}}{E_z})\cos^2\theta + (\frac{1}{E_z} + \frac{1}{E_y} - \frac{1}{E_s} + \frac{2\nu_{yz}}{E_z})\cos^4\theta$$

Equation 4.6

Substitution of Equation 4.6 into Equation 4.4 yields after integration,

Yarn modulus

$$\hat{E}(\alpha) = \frac{1}{\tan^2\alpha}\left[\frac{b}{2c^2}\ln\frac{(a+b+c)T_0^2}{(aT_0^2+bT_0+c)} - \frac{T_0-1}{cT_0} + \frac{(b^2-2ac)}{2c^2\sqrt{b^2-4ac}}\ln\frac{(2a+b-\sqrt{b^2-4ac})(2aT_0+b+\sqrt{b^2-4ac})}{(2aT_0+b-\sqrt{b^2-4ac})(2a+b+\sqrt{b^2-4ac})}\right]$$

Equation 4.7

in which, $T_0 = \cos^2\alpha$, $a = \frac{1}{E_z} + \frac{1}{E_y} - \frac{1}{E_s} + \frac{2\nu_{yz}}{E_z}$, $b = \frac{1}{E_s} - \frac{2}{E_y} - \frac{2\nu_{yz}}{E_z}$, $c = \frac{1}{E_y}$

4.5.1.4 Approximation

To reduce the rather complicated Equation 4.7 to a simpler form, several approximations have been used. Since it is generally true that a high degree of twist damages the material properties, only low twist angles are usually used in real applications. The approximations given below are valid only for this condition. Another factor used to simplify the above expression is recognition of the fact that for high performance fibers, the ratio of longitudinal modulus to the transverse modulus is usually greater than 10.

In case of low off-axis angle ($\alpha < 15^{\circ}$), $m^2 >> n^2$ $(n^2/m^2 < 7\%)$

Taking a range of $-0.5 \le \nu_{yz} < 0.5$, which was found reasonable for PPTA fiber[12] and assumed for the other fibers investigated, then

$$m^4 S_{zz} + 2m^2 n^2 S_{zy} = m^2 / E_z (m^2 - 2\nu_{yz} n^2) \approx m^4 S_{zz}.$$

For $S_{yy} \sim S_{ss}$,

$$n^4 S_{yy} + m^2 n^2 S_{ss} = n^2 (n^2 S_{yy} + m^2 S_{ss}) \approx m^2 n^2 S_{ss}.$$

Then,

$$S_{11}=m^4 S_{zz}+m^2 n^2 S_{ss}$$

Equation 4.8

Now, the anisotropic ratio is defined as $d = \frac{E_z}{E_s}$, which is the ratio of the longitudinal modulus and the shear modulus of the filament.

Through integration,

Yarn modulus,

$$\hat{E}(\alpha) = E_z * \left[\left(\frac{3T_0 + 1}{2dT_0} \right) + \frac{(1-d)^2}{d^3 \tan^2 \alpha} \ln \frac{(1-d)T_0 + d}{T_0} \right]$$

Equation 4.9

After this approximation, only a shear coupling effect is incorporated in the model to affect the properties of anisotropic materials and transverse coupling and secondary coupling are omitted.

4.5.2 Discussion of the Model for Two Extreme Cases—a Untwisted Yarn and an Isotropic Fiber Yarn

4.5.2.1 Consideration of extreme cases

4.5.2.1.1 The case of an untwisted yarn

Statement: If the yarn is untwisted, the yarn modulus should be equal to the filament modulus

If $\alpha = 0$

For Equation 4.7, it is easy to prove that: $\hat{E}(0) = E_z$

For Equation 4.9, at α=0, because $\tan\alpha = 0$, and $\ln \frac{(1-d)T_{0+}d}{T_0} = 0$

L'Hopital's Rule needs to be used which yields

$$\hat{E}(0) = E_z * \frac{1+d^2}{d^2}$$

For high performance fiber yarns, $d > 10$, then $\hat{E}(0) \approx E_z$

For conventional fibers, Equation 4.9 was modified to yield the exact answer when $\alpha = 0$:

$$\hat{E}(\alpha) = E_z * \left[\left(\frac{3T_0 + 1}{2dT_0} \right) + \frac{(1-d)^2}{d^3 \tan^2 \alpha} \ln \frac{(1-d)T_0 + d}{T_0} \right] / \left(\frac{1+d^2}{d^2} \right)$$

Equation 4.10

4.5.2.1.2 The case of an isotropic material

Statement: $E(\alpha) = E_z$ at all αs, for isotropic materials

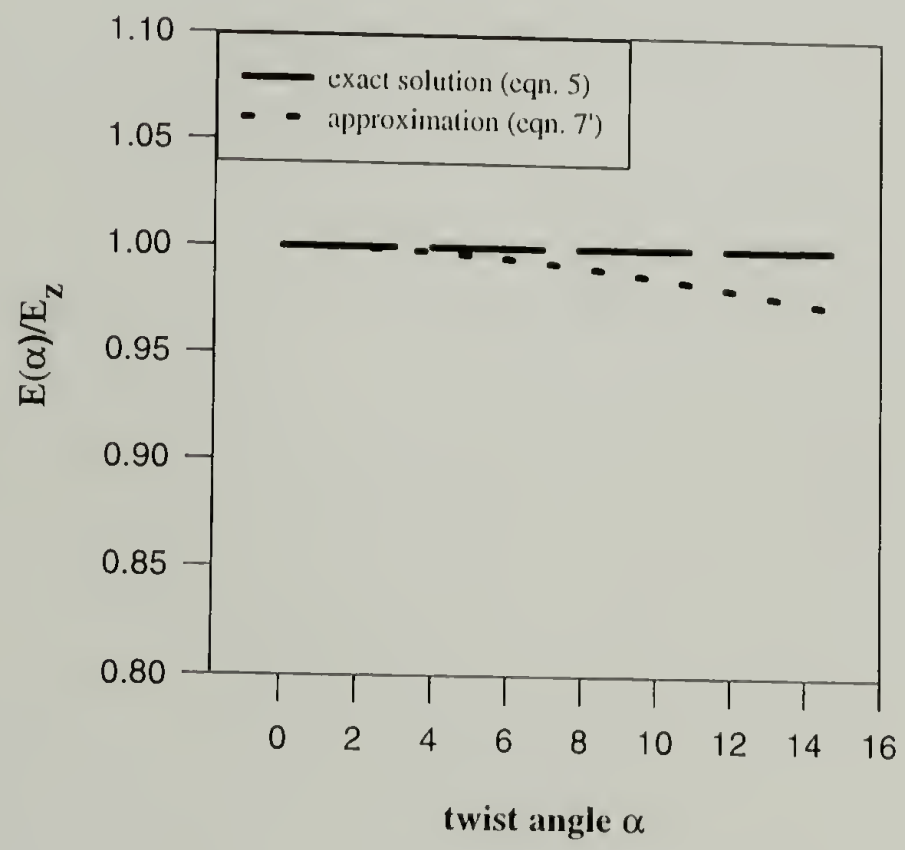

Figure 4.2 Predicted twisted yarn modulus for an isotropic material

The yarn modulus has been predicted by the model equations and the data are illustrated in Figure 4.2 for an isotropic material. It is clear that Equation 4.7 predicts a constant modulus for any twist angle and Equation 4.10, the approximate relation, gives a deviation less than 3 %.

Both predict the material properties for an isotropic material will not change with the material orientation, while the earlier models did predict a change.

4.5.3 Confirmation of the Model by Fibers with Known Properties

To confirm the proposed equations, tests were performed to determine the dependency of modulus on twist for a material with known properties, and these data were compared with the derived equations. The longitudinal properties of a fiber are easy to measure, but the transverse and shear properties are very difficult to determine. Kevlar® 49 is generally used in composite materials as a reinforcing fiber. Most of the material properties such as composite and matrix moduli and the fiber properties have been tested. From these data, it is then possible to derive several unknown material constants through valid composite equations.

According to the composite properties of a Kevlar® 49/Epoxy unidirectional composite, in which the volume content of the fiber, V_f, is 0.6 and the volume content of the matrix, V_m, is 0.4 [139]:

E_{zc} =76 GPa, E_{yc} =5.5 GPa, E_{sc} =2.3 GPa

The matrix properties of Epoxy are: E_m =3 GPa, ν =0.3, isotropic

According to the Rule of Mixtures: $E_{zc} = V_f E_z + V_m E_m$, then

$E_z = 124.7$ GPa, which is the same as that directly measured using an untwisted yarn sample.

According to the so-called Constant-Stress Rule [140]:

$$\frac{1}{E_{yc}} = \frac{V_f}{E_y} + \frac{V_m}{E_m}, \quad \frac{1}{E_{sc}} = \frac{V_f}{E_s} + \frac{V_m}{G_m},$$

$E_s = 6.9$ GPa, $E_y = 12.4$ GPa, so the anisotropic ratio: $d = 18$

By inserting these fiber properties into the equations, the twisted yarn behavior can be predicted. Figure 4.3 shows good agreements between the predicted yarn moduli by both the exact and approximate equations and the measured yarn modulus for different twist angles.

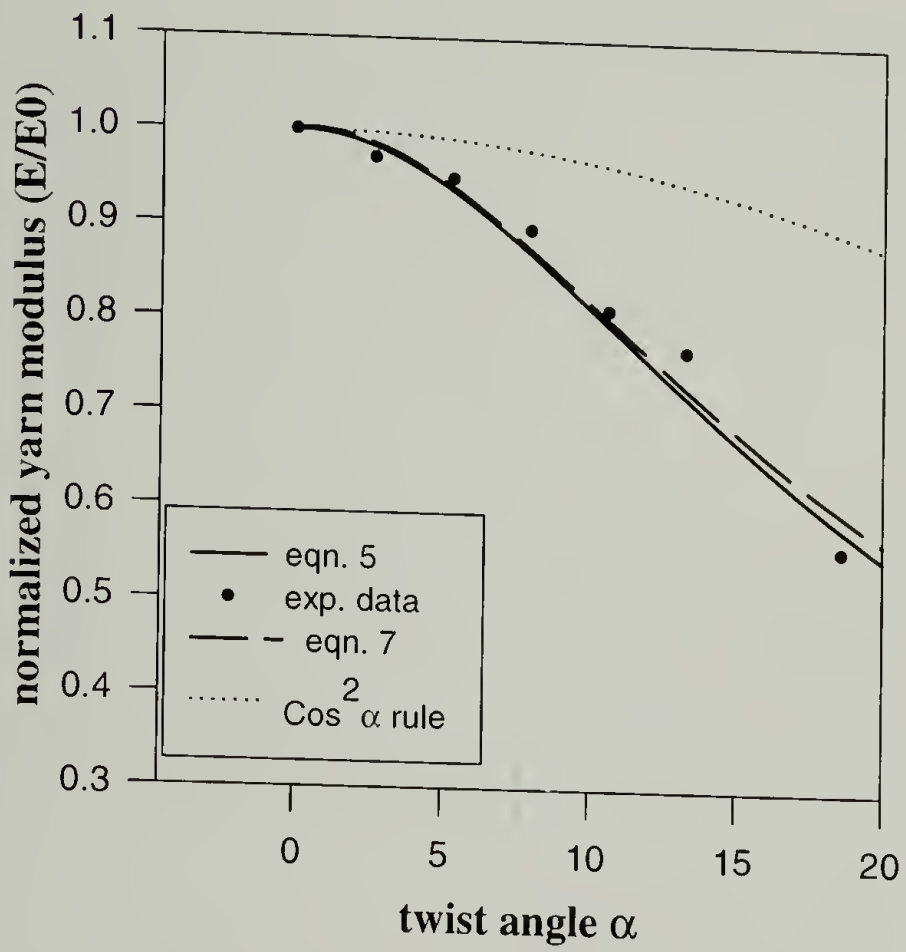

Figure 4.3 Comparison of the predicted and measured yarn modulus of Kevlar® 49 fiber

In summary, in a twisted yarn, the anisotropic ratio, which is the ratio between the axial modulus and radial shear modulus, determines how the degree of twist influences the yarn modulus, and this also is important information for fiber-reinforced composites.

In this study, the stress state has been simplified into a unidirectional stress acting along the yarn direction. As Allen[131] has already shown, because of the cylindrical orthotropy, a simple uniaxial stress state is almost impossible. Hoop and radial stresses are induced by the action of an axial stress in any cylindrically anisotropic material to form a complicated stress state. However, Allen's calculations on Kevlar® fiber indicate that the magnitudes of radial and hoop stress are less than 1% of the axial stress. Therefore, the effect of a complex stress state, as

well as the coupling effect from the transverse Young's modulus and further coupling caused by off-axis angles, can be attributed to secondary importance and that is why they could be reasonably omitted in this model.

4.5.4 An Examination of a Conventional Fiber by our Model

Others [141] claimed that an equation of $\hat{E}(\alpha) = E_z \cos^2 \alpha$ yields a good fit to the yarn modulus data of nylon fiber. It is worthwhile to compare the results from our model and the conventional "$\cos^2\alpha$" rule and further confirm our model. Ward [142] reported a full set of elastic constants for nylon fiber after careful measurements: E_z=3.45 GPa, E_y=1.37 GPa, υ_{yz}=0.48, E_s=0.61GPa. Using these elastic constants, a predicted curve can be generated by our model. Zorowski and Murayama [143] have reported a comparison of the experimental data and "$\cos^2\alpha$" rule prediction for nylon fiber. The predictions from our model and their data are shown together in Figure 4.4. Both curves describe the true behavior well because for low anisotropic ratio

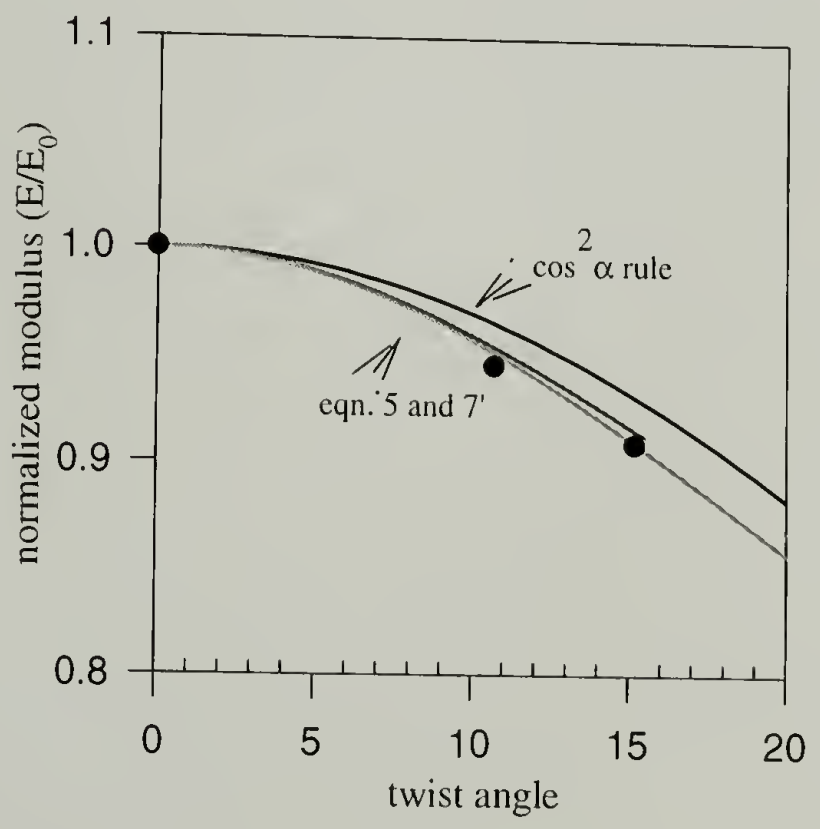

Figure 4.4 Comparison of the twist effect on yarn modulus of two models for nylon fiber, $\cos^2\alpha$ rule and our model with the experimental data [141], lines are predicted curves and dots are experimental data

materials, the coupling effect from the shear modulus does not significantly deviate the twisted yarn modulus from the earlier models. This might be one of the reasons why the importance of the anisotropic nature of the fiber did not draw enough attentions in the past.

4.5.5 Twist Effect on Yarn Properties and Applications of the Model

The influence of degree of twist on yarn properties, such as yarn modulus, yarn strength and elongation to break, has been systematically studied for several high performance fibers. The results are shown by Figure 4.5,Figure 4.6 and Figure 4.7.

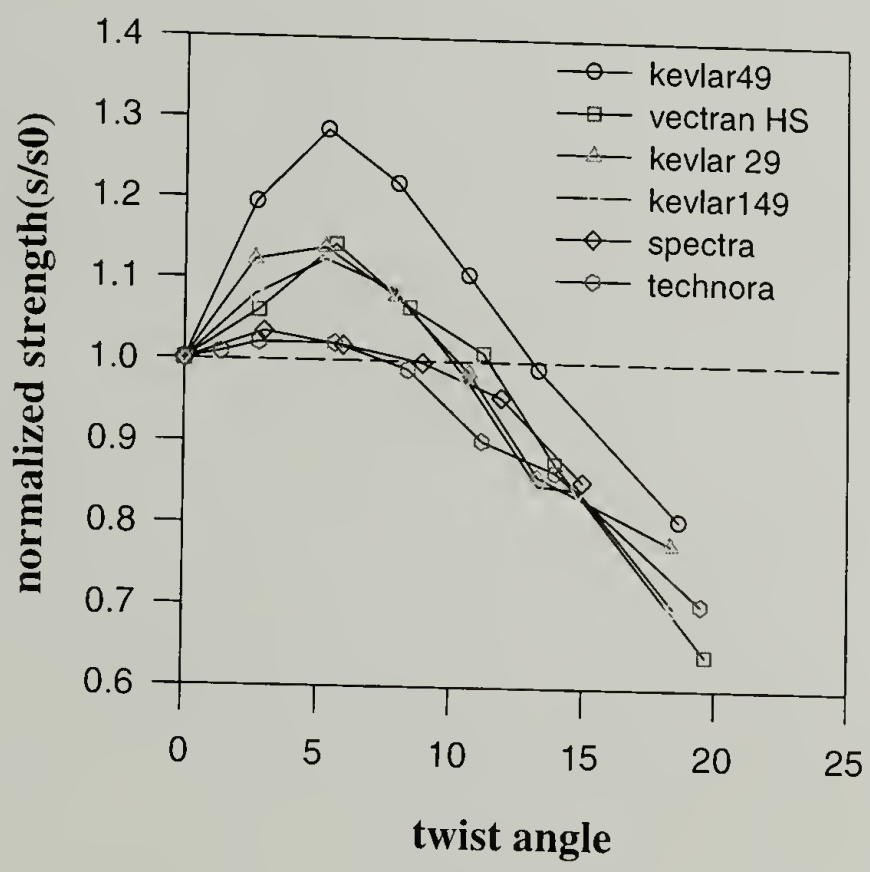

Figure 4.5 Yarn strength with the twist angle for various fibers

A general trend for the change of the yarn strength with twist angle is that there is an optimum degree of twist for the yarn to achieve maximum strength. The magnitude of the relative strength at the same twist angle depends on the material. Kevlar® 49 shows the largest increase in strength at the optimum twist degree, which is followed by Vectran® HS®, Kevlar® 29 and Kevlar® 149. Spectra®and Technora® show only a slight increase in strength. The optimum twist angle for all the material was found to be near 7 °. Generally, the elongation to break of the

twisted yarn increases with the twist degree. Again, the magnitude of the increment depends on the material, and Kevlar49® shows the largest increase while Spectra® shows almost no change.

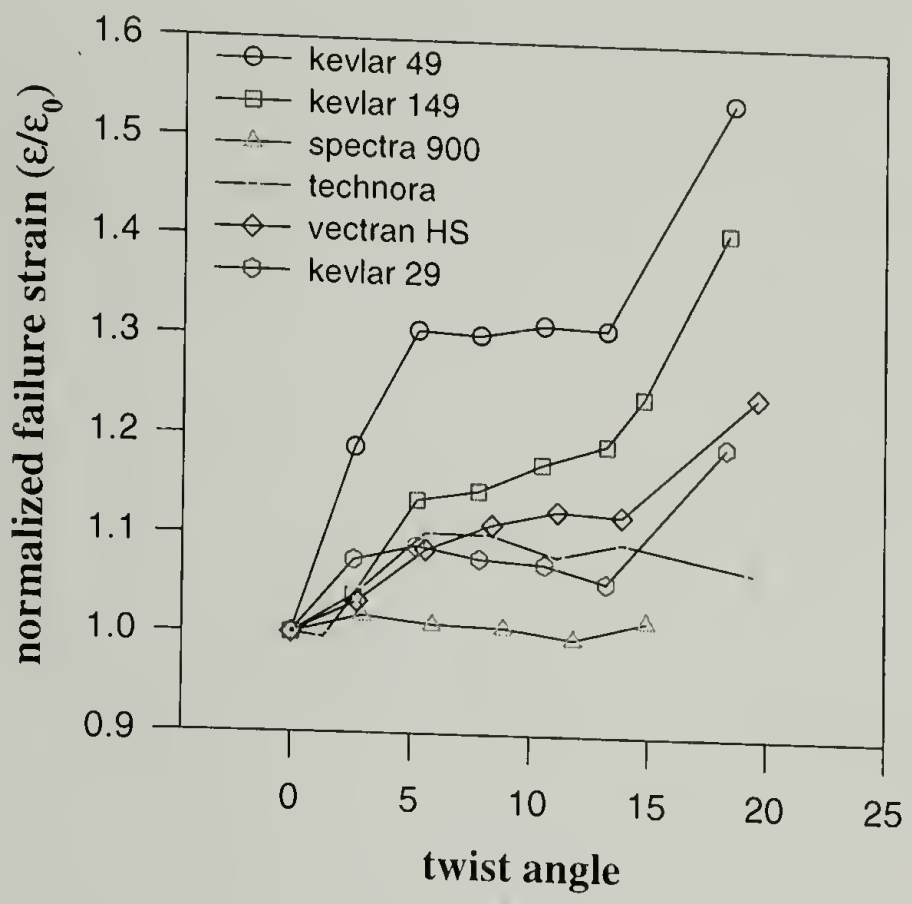

Figure 4.6 Strain to break of a yarn with the twist angle for various fibers

Extensive studies on the influence of degree of twist on strength and extensibility have been done on continuous fiber yarns of several textile fibers such as Acetate, Nylon, Viscose and Tenasco [144-146] as well as spun yarns made from staple fiber[147,148]. Generally, for yarns made from staple fiber, the strength shows a maximum while the extension to break increases with degree of twist.[147,148] For some continuous fiber yarns studied, both the strength[146] and the breaking extension[149] of twisted yarns show a maximum at certain surface twist angle. The reason for the increase in strength is likely due to an interlocking mechanism where the filaments are held together by radial forces and friction, and in effect enables a single fiber to fail more than once. It is also possible that this transverse compression alters the stress state for the material and results in a different strength in a complex failure criterion. The prediction of the strength of twisted yarn is an interesting topic[100,150,151] but will not be pursued in this paper.

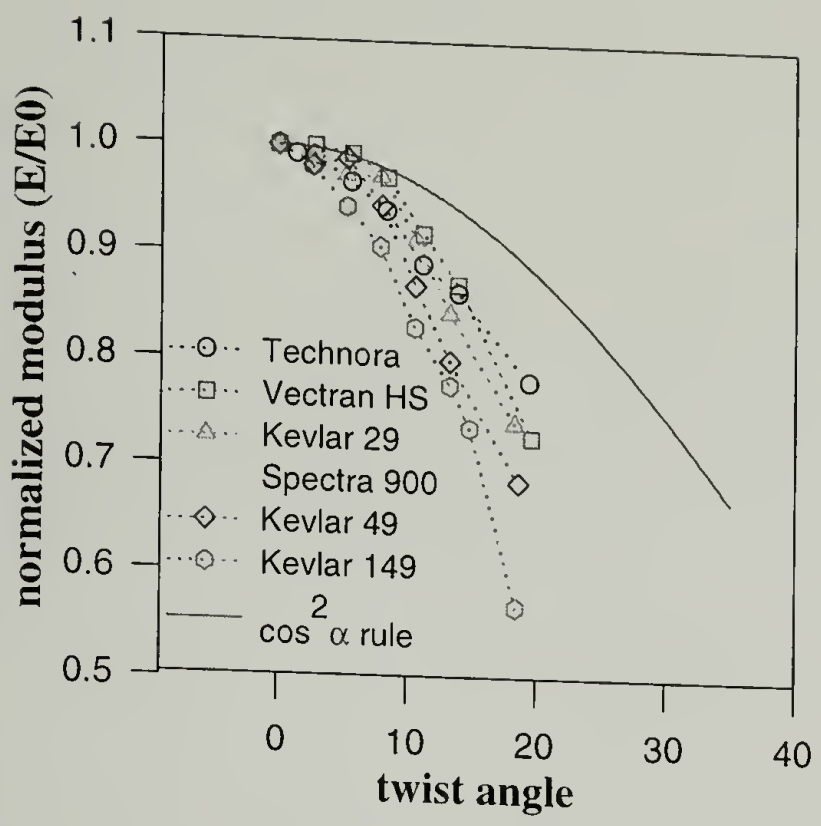

Figure 4.7. Yarn modulus changes with the twist angle for various fibers, solid line is the $\cos^2\alpha$ rule

A mathematical curve fitting procedure has been used to resolve the data for the yarn modulus as a function of twist for the other fibers using Equation 4.9. The anisotropic ratio, which was unknown for these fibers, is the only fitting parameter. After the fitting, the radial shear modulus can be calculated, as the longitudinal modulus is known from the untwisted yarn measurement. The results from this type of analysis are shown in Figure 4.8 where the agreement is quite good. The radial shear modulus for these fibers were calculated and listed in Table 4.1. These data are useful for the study of corresponding fiber-reinforced composites as well as for constructing the proper geometry for ropes and cables.

An extension of the application of the model and also a further step to confirm the model is to consider a more complicated heterogeneous twisted yarn where the twisted yarn consists of two different types of fibers. The yarn modulus of mixed fibers can be predicted according to the arrangement of the different fibers inside the yarn by using the model. Different response is

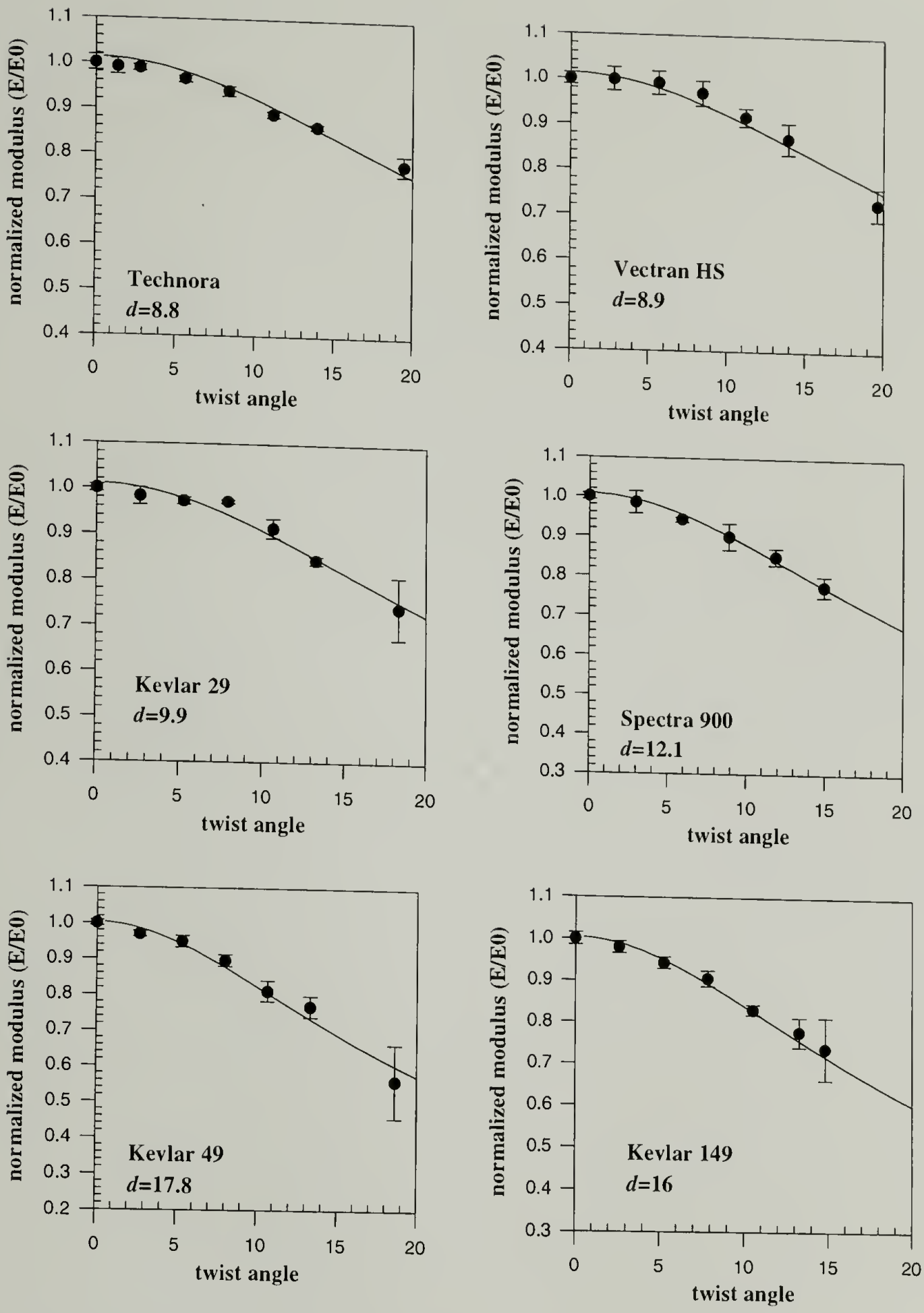

Figure 4.8 Curve fitting results of the change of yarn modulus with the twist degree for various fibers. In the plot, solid lines are fitting curves and dots are experimental data, and the fitting parameter is shown in the plot

to be expected if the arrangements of the two fibers inside the yarn are different, since the behavior is determined by the material constants and their radial placement. A heterogeneous

yarn consisting of Kevlar® 149 and Technora® was examined. Two forms of the geometry as shown by Figure 4.9 were taken: one has Kevlar® 149 fiber as the core and Technora® as the outer layer; the other has the opposite arrangement. To form a heterogeneous twisted yarn with the same twist degree distribution as a homogenous twisted yarn, the core material was twisted first to certain twist degree calculated by the radius of the core and the outer layer was twisted carefully around the core layer. The yarn moduli of these two yarns at different twist angles were measured and compared to the predicted value by using the anisotropic ratios determined earlier. The result is shown in Figure 4.10, where the experimental data and predicted values show good agreement.

Table 4.1 Anisotropic ratio and calculated radial shear modulus for different fibers

	Vectran HS	Technora	Kevlar 29	Kevlar 49	Kevlar 149	Spectra 900
$d=E_z/E_s$	8.9	8.8	9.9	17.8	16	12.1
E_s	11.9	8.3	8.9	6.5	9.2	4.5

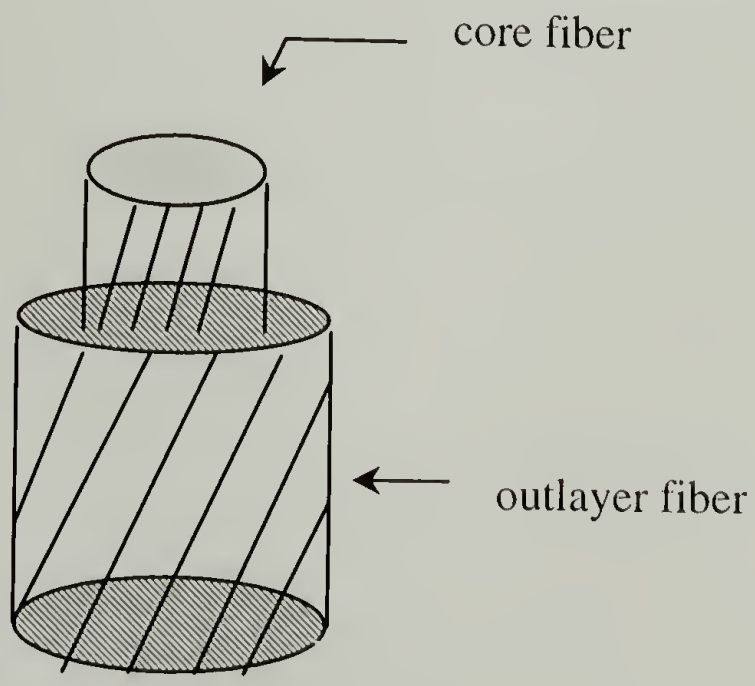

Figure 4.9 A illustration of a heterogeneous yarn; KevTe yarn has Kevar® 149 core and Technora® outer layer; TecKe yarn has Technora® core and Kevlar® 149 outer layer

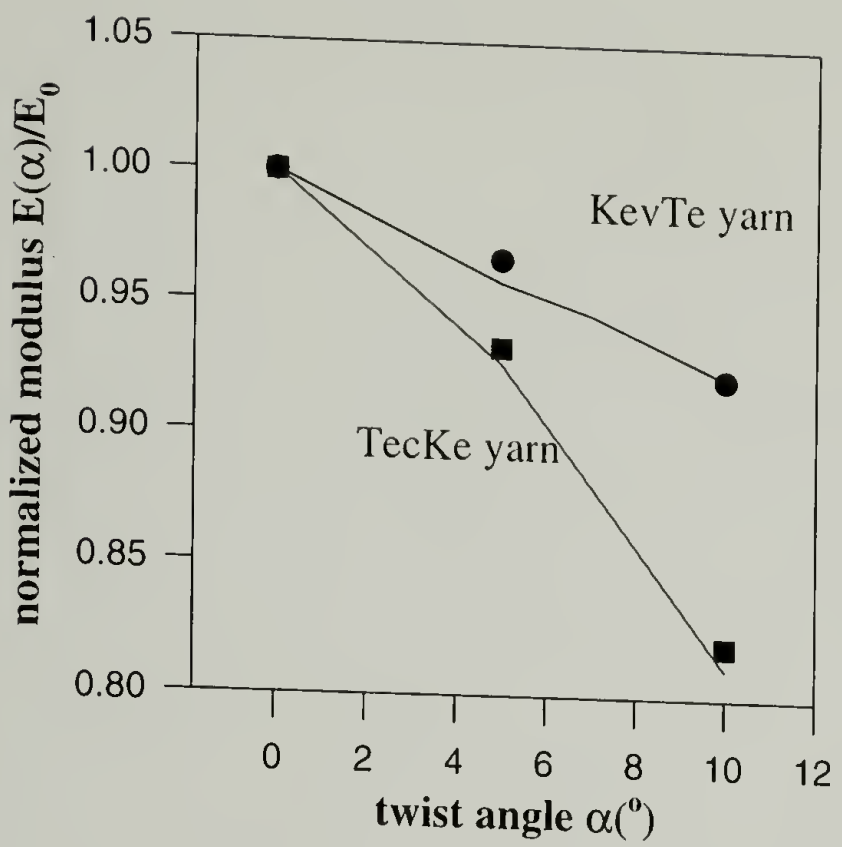

Figure 4.10 Comparison of predicted data (lines) and experimental data (dots) of the twist effect on modulus of heterogeneous yarns

4.5.6 Morphology Study of Twist Effect

The influence of twist on the yarn properties is intriguing. A morphology study was conducted to gain more understanding.

One important phenomena in the fracture of twist yarn is that there are free filaments that fall from the yarn during both tensile and fatigue tests for the twist yarn, which does not appear in the fracture of untwisted yarn. These free filaments have different lengths. The fracture ends of long free filaments (~ 20 mm) look the same as non-free filaments. However, for short free filaments (< 5 mm), two ends both show solid non-tapered ends (Figure 4.11), which implies a transverse fracture instead of longitudinal splitting.

Figure 4.11 Solid end of short free fiber from fractured twist yarn

The splitting lengths of the twist samples are longer than those observed for untwisted samples. The splitting length for tensile fracture twist samples can be as long as 600 μm while the length for untwisted sample is normally ~ 100 μm.(Figure 4.12) The splitting length does not always increase with the increasing twist degree. It is found that the splitting length for 1.55 tpi twisted yarn is much longer than that for 11.3 tpi twisted sample.

Figure 4.12 Fatigue-fractured end of a fiber in a twist yarn

For a twist sample, some bulges can be found on some points along the fiber.(Figure 4.13.(b)) It seems that a micro-fiber is first peeled and snapped back around the fiber. It indicates that there is abrasion between the filaments during the deformation of the twisted yarn. A greater extent of twisting seems to induce excessive transverse pressure that will cause the transverse deformation of the fiber.

The transverse squeezing is observed. The cross-section direction is flatten by this squeezing. (Figure 4.13.(a) and Figure 4.15

(a) (b)

Figure 4.13 Surface of a fiber from a twisted yarn after fatigue-failed. (a). Deformation of the transverse of the fiber; (b). Skin peeling and ridges on the core of the fiber

Figure 4.14 Fiber surface from a twist yarn with high twist degree (3.1 tpi) observed under optical microscope

It is believed that this longitudinal stretch-induced transverse compression acts as an interlocking mechanism to hold the fiber together. It is schematically shown in Figure 4.15. It is this compressive force improves the tensile strength and the fatigue strength of the fiber yarn. However, severe twisting causes the yarn fail by compression.

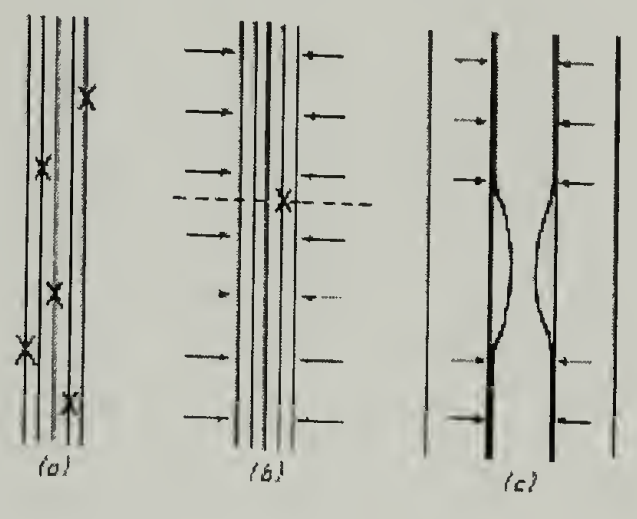

Figure 4.15 Transverse compression induced by longitudinal drawing in a twist yarn.[152]

Kinks are found on the surface along broken fibers of a twisted yarn. (Figure 4.16)Detailed examination shows microcracks on the surface. Table 4.2 summarizes our observation of the kink bands observed in twist yarns.

Table 4.2 Summary of the observation of the formation of kink bands for twist fiber yarns

Material	Kevlar 29						Vectran HS	Nomex
Test Control	pure torque, 10days	tensile failure	creep for 30 min. unde150 N	fatigue failure under 220 N	fatigue failure under 220 N	fatigue for 15 min. under 220 N	tensile failure	
Twist Degree Desprition	8.5 tpi Permanent curvature exists after untwisting. the residual twist degree is 4.5 tpi Filaments from the outer portion shows severe kinks, while those from the center shows no kinks	1.55 tpi Permanent curvature exist in the broken yarns. Kind bands always show up at cruved region of the fiber, other parts are quite smooth	3.1 tpi no kin bands were found for all the observed filaments. However the cross area was enlarged	2.07 tpi Possiblity of kink bands is 4/6 within the observed filaments. (away from the broken ends) Severe kink bands always show at the curved sections	5.65 tpi Possibility of kink bands is 8/11. otherwise same on comments on left.	2.07 tpi Possiblity of kink bands was 2/8.	3.4 tpi Filaments from the outer have more kinks than those from the center.	3.0 tjpi No kinks were found under any conditions

Figure 4.16 Kink bands observed for a filament taken from a twist yarn after the yarn was fatigued

4.6 Conclusions

An analysis based on composite theory was used to model the influence of twist on the yarn modulus. It is shown that material anisotropic ratio, which is the ratio between longitudinal modulus and radial shear modulus, is an important factor in determining the influence of twist on the yarn modulus. For high performance fibers, it is validated that a simple equation containing two variables, the twist angle and the material anisotropic ratio, can be used to predict the change of the yarn modulus with twist for a variety of fibers. From this analysis, it has been determined

Vectran HS® and Kevlar® 29. The calculated radial shear moduli provide useful information for the study of fiber-reinforced composites. Experimental results also show that there is an optimum twist angle of around 7 ° at which all the fiber yarns exhibit maximum tensile strengths, but the magnitude of the increase depends on the material. The elongation to break of the twisted yarns increases with the twist degree for all of the fiber yarns investigated.

CHAPTER 5

THERMAL MECHANICAL PROPERTY OF HIGH PERFORMANCE FIBERS AND ISO-STRAIN FORCE-TEMPERATURE EXPERIMENT (IFTT)—PROBING TRANSITIONS AND STRESS AND HEAT HISTORY IN MATERIALS

5.1 Abstract

In this part of the research, a new thermal-mechanical test method, Iso-strain Force-Temperature Test (*IFTT*) has been developed to study the thermomechanical properties of high performance fibers. Two different IFTT scans, reversible IFTT and irreversible IFTT, provide information about relaxations and transitions, and the stress and thermal history in these fibers, respectively. This information is difficult to detect by other methods due to the high crystallinity and orientation of these materials. It was shown that the thermal and stress history of Kevlar® fibers could be retrieved from the first run of the IFTT, which facilitates the prediction of the material's remaining lifetime. This memory effect originates from the relaxation process that was also observed by dynamic mechanical thermal analysis. IFTT also helps understand the processing and use of PPTA fibers. The IFTT behavior of various other materials such as PET, Teflon, PC, Technora®, Nylon, Spectra® and Vectran® was also studied.

Keywords: Iso-strain Force-Temperature Test (IFTT), first-order transition, second-order transition, stress and thermal history, processing, use temperature, DMTA, Kevlar®, Teflon®, PET, Bisphenol-A PC, Technora®, Vectran®, Spectra®, Nylon

5.2 Background and Thermodynamic Considerations

In the study of fibers, dimensional stability is an important property. Good dimensional stability is a desirable property of high performance fibers. There are two aspects of the dimensional stability: under load or under high temperature exposure. The dimensional stability

under load can be studied through creep experiments, which we discussed in Chapter 3. The dimensional stability at high temperatures is characterized by its thermal expansion coefficient and its shrinkage. The linear thermal expansion coefficient, α_1, of Kevlar® was reported to be about –3 ppm/°C. [153] Compared to this, the linear thermal expansion coefficient of aluminum is 23.1 ppm/°C.[154] However, when the thermal expansion experiment was conducted for Kevlar® 29 fiber, there is a change in its α_1 with the temperature and a difference between the heating and cooling curve (See Figure 3.51). This indicates that the response of the thermal strain to the heating is not pure thermo-elasticity and extra thermal activity complicates the situation. A detailed study suggests that the thermal mechanical behavior of a polymeric fiber is strongly influenced by the thermal and stress history of the material.

This understanding has been recognized by several researchers. For deformed polyethylene, an irreversible stress drop has been attributed to the modification of the molecular structure that was frozen in during deformation.[155,156] When studying polyurethane elastomeric fibers, Wang and co-authors[157] associated the shrinkage force with the soft segment and the stress drop with the rearrangement of the hard segment. In the study of Nylon 6,6, PET and polypropylene fiber, the thermal stress was also observed.[158] Pottick studied the thermal force of Kevlar® and PBZT fibers and used it to characterize fibers' thermal stability.[159]

In our study, the thermal force in the material was measured in an Iso-strain Force-Temperature Test (IFTT). A theoretic derivation has been provided to show that the thermal force is a better indication of thermal transitions and the thermal and stress history in the fibers than the quantity of thermal strain. A detailed thermal force study of high performance fibers and several polymeric films is reported.

5.2.1 Reversible thermodynamics—Transitions

For a purely elastic material, the thermal transitions, such as first or second order transitions can be detected by the change of its thermal elastic stress with the temperature. The following shows thermodynamically how to detect the transitions from the thermal elastic stress.

For a reversible process, considering the existence of only hydrostatic pressure and uniaxial force, the first law of thermodynamics yields

$$\delta W = -pdV + fdl, \qquad dU = TdS - pdV + fdl$$
$$\because H = U + pV,$$

at ambient pressure P,

$$dH = dU + pdV = TdS + fdl$$
$$\because G = H - T \cdot S$$
$$\therefore dG = fdl - SdT$$
$$fdl = -TdS + dH$$

Equation 5.1

where G is the Gibbs' free energy, H is the enthalpy, T is the temperature, S is the entropy, V is the volume, l is the length and f is the force. Then, the thermally induced force, f, is related to the change in Gibbs' free energy as follows:

$$f = \left(\frac{\partial G}{\partial l}\right)_T$$
$$\left.\frac{\partial f}{\partial T}\right|_l = \left(\frac{\partial}{\partial T}\left(\frac{\partial G}{\partial l}\right)_T\right)_l = -\left(\frac{\partial S}{\partial l}\right)_T$$

Equation 5.2

According to definitions, a transition is first-order if there is a in the first derivative of Gibbs' free energy, and the transition is second-order if there is a discontinuity in the second

derivative of Gibbs' free energy. There will then be discontinuity in $f = \left(\frac{\partial G}{\partial l}\right)_T$ for a first-order transition; and a discontinuity in $\left.\frac{\partial f}{\partial T}\right|_l = \left(\frac{\partial}{\partial T}(\frac{\partial G}{\partial l})_T\right)_l$ for a second-order transition.

This derivation is parallel to that for DSC measurements. It is known that in a DSC trace of heat capacity with temperature, a peak indicates a first-order transition and a step change in the heat capacity dictates a second-order transition. A typical DSC trace is shown in Figure 5.1. Similarly, in an IFTT trace, the $\frac{\partial f}{\partial T}$ is plotted with T, and a peak in $\frac{\partial f}{\partial T}$ ~T curve indicates a first-order transition whereas a step change indicates a second-order transition.

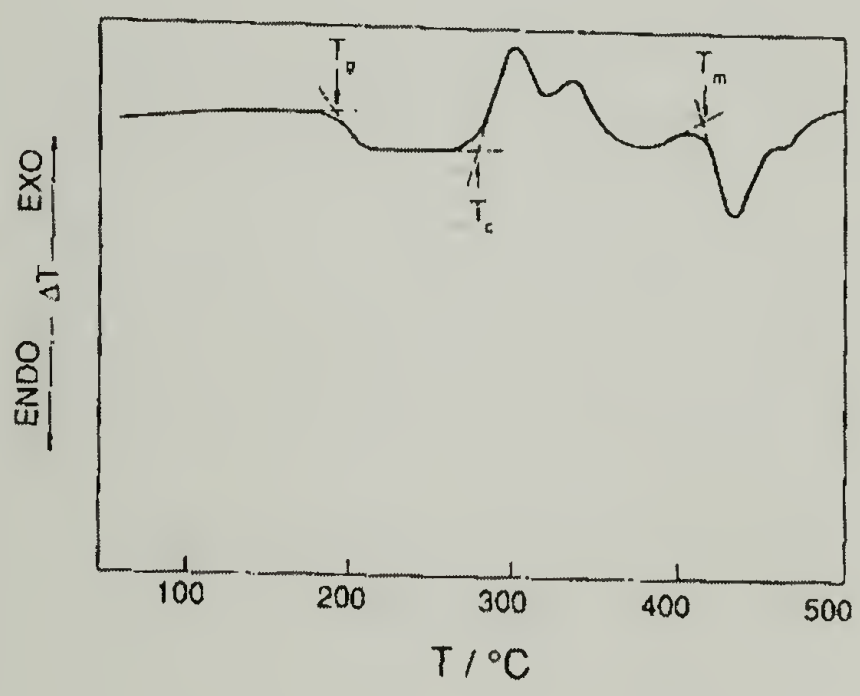

Figure 5.1 DSC curve of a polymer glass.[160]

The thermal force and thermal strain is interrelated through thermodynamic laws. For isotropic material, the following relation exists:

$$(\frac{\partial f}{\partial T})_{P,l} = -(\frac{\partial f}{\partial l})_{P,T}(\frac{\partial l}{\partial T})_{P,f} = -E \cdot \alpha \cdot V$$

Equation 5.3

where E is the modulus and α is the thermal expansion coefficient. Then, the measurement of $\frac{\partial f}{\partial T}$ and α are interrelated through the modulus.

However, the situation is complex in anisotropic materials. For an anisotropic material, the thermally induced stress per degree of temperature, $\left.\frac{\partial \sigma_i}{\partial T}\right|_{\varepsilon_i}$, is related to the change in entropy with strain,[161]

$$\left.\frac{\partial \sigma_i}{\partial T}\right|_{\varepsilon_i} = -\frac{1}{V}\left.\frac{\partial S}{\partial \varepsilon_i}\right|_T$$

Equation 5.4

The thermal expansion coefficient for an anisotropic material can be expressed as

$$\alpha_i = -\frac{1}{V}\sum_{j=1}^{6}\frac{\partial S}{\partial \varepsilon_i}C^T{}_{ij}$$

Equation 5.5

The temperature dependence of the isothermal stiffness moduli, $(C_{ij}{}^T)^{-1}$, is

$$(C_{ij}{}^T)^{-1} = \frac{1}{V}\left[\frac{\partial^2 A}{\partial \varepsilon_i \partial \varepsilon_j}\right]_{T,\varepsilon_k \neq i,j} = \frac{1}{V}\left[\frac{\partial^2 U}{\partial \varepsilon_i \partial \varepsilon_j}\right]_{T,\varepsilon_k \neq i,j} - \frac{T}{V}\left[\frac{\partial^2 S}{\partial \varepsilon_i \partial \varepsilon_j}\right]_{T,\varepsilon_k \neq i,j}$$

Equation 5.6

where A is the Helmholtz free energy, ε_i is the strain.

Equation 5.4 is the same as Equation 5.2. It shows that in an anisotropic material, $\left.\frac{\partial \sigma_i}{\partial T}\right|_{\varepsilon_i}$ still indicates the second derivative of Gibbs' free energy. While the combination of Equation 5.5 and Equation 5.6 does not yield a clear expression related to the second derivative

of Gibbs' free energy. Therefore, $\left.\frac{\partial \sigma_i}{\partial T}\right|_{\varepsilon_i}$ is a better quantity than α_i to represent the characteristic change in the Gibbs' free energy related to the first- and second- order transitions.

An example to support the conclusion that indeed the thermal force profile represents the thermal transitions is easy to find in the polymer textbook, which was not recognized by others. The thermal force of nature rubber was measured along with the temperature. Figure 5.2 shows a discontinuity in the first derivative of thermal stress to temperature at around 210 K that is exactly the glass transition of the rubber.

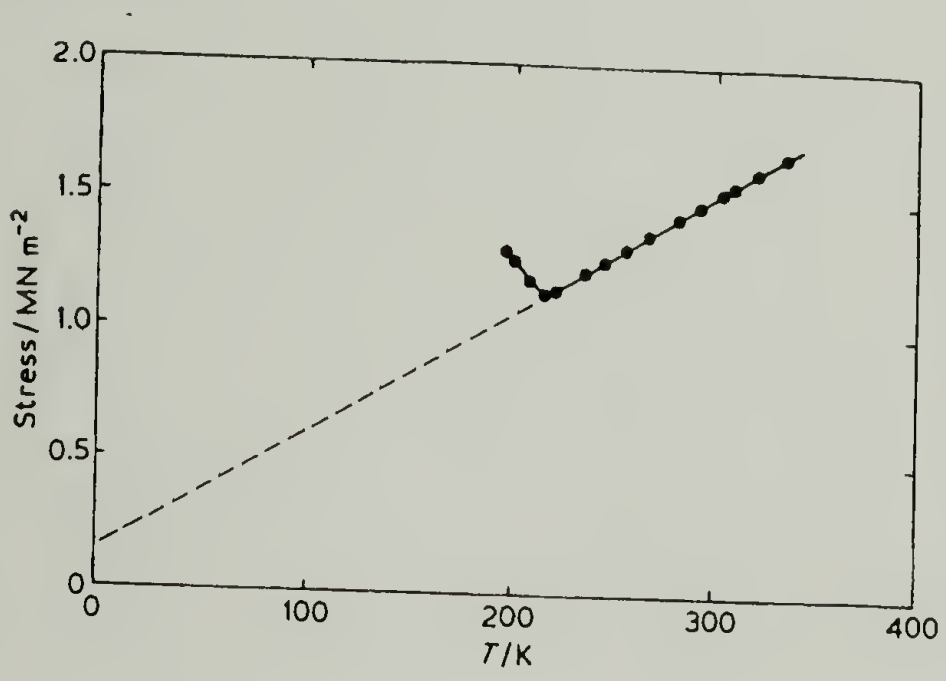

Figure 5.2 Thermal elastic force in natural rubber.[162]

5.2.2 Irreversible thermal mechanical behavior-- Influence of heat and stress history

As we mentioned earlier, the IFTT curves of the first heating and the second heating of a Kevlar® fiber are different. It is seen that the second heating and all subsequent heatings are reversible when the maximum temperature of those heatings is lower than that in the first heating. This difference of IFTT curves from the first to second heatings is common to many polymers. The IFTT curve of a material hence composites of two parts: a reversible part and an irreversible part. The irreversible part is see during the first heating. The reversible part is observed during

the first cooling or following heating. We believe that the irreversible part of IFTT is influenced by the thermal and stress history of the material.

For a material with latent energy from a previous processing, i.e. cold work, part of the latent energy can be released upon heating the material. This phenomenon might be associated with other phenomena found in the polymeric materials: volume relaxation, enthalpy relaxation[163] or delayed elasticity[164].

An illustration of a possible change of internal energy with the temperature is shown as follows:

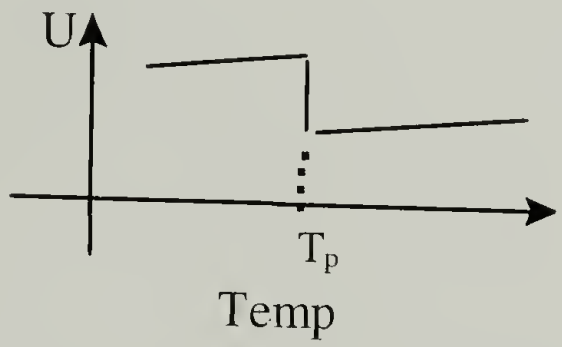

Assuming the releasing of the stored internal energy takes the form of a thermal stress or a strain, the generated thermal stress or strain will be related to the change in internal energy by

$$\Delta U = -\frac{1}{2} * E_T * \varepsilon_T{}^2 = -\frac{\sigma_T{}^2}{2 * E_T}$$

Then $\sigma(T)$ will change during heating, depending on the shape of $U \sim T$.

5.3 Experimental

The materials investigated include Kevlar®, Technora®, Spectra®, Vectran®, PET and Nylon in the form of fiber; and PET, Bisphenol-A PC and Teflon in the form of film.

Figure 5.3 shows the setup of the experiment. The experiment is an Iso-strain Force Temperature Test (**IFTT**). In the experiment, the thermally induced force is measured while a single filament or film is heated at constant elongation. Conditions used in this study unless

otherwise specified are constant strain: 0.03 % and heating rate: 10 °C/min. The experiment are typically run using a DuPont TMA. Single fiber samples are typically used.

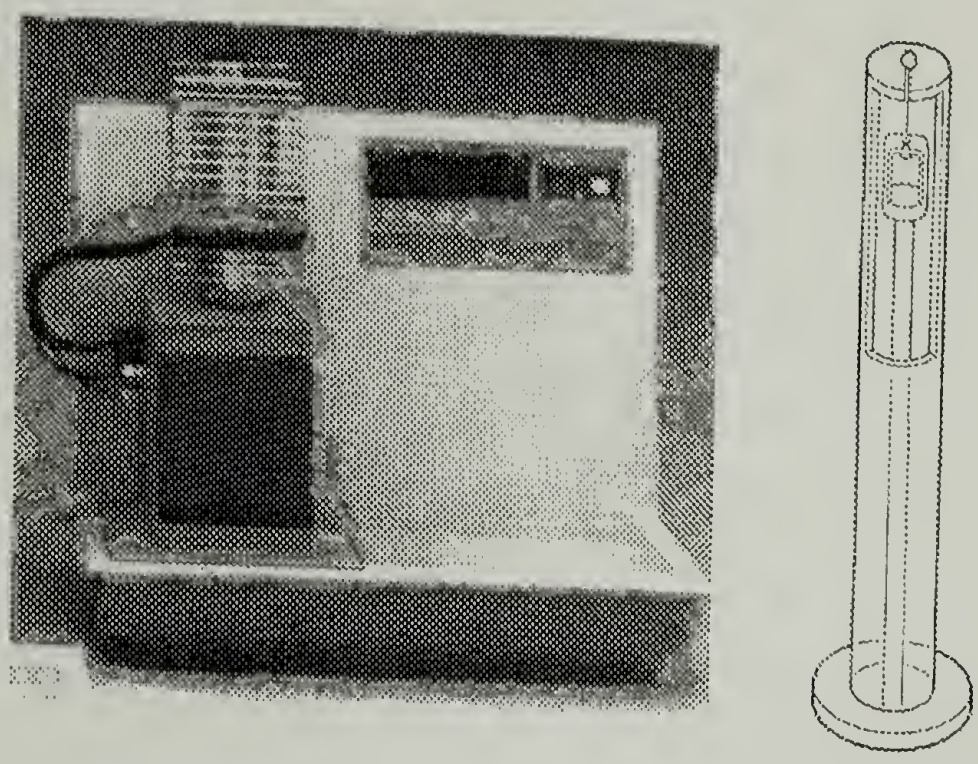

(a) (b)

Figure 5.3 Setup of an IFTT experiment; (a). instrument, (b). probe setup

An IFTT plot refers to the plot of the first derivative of thermal force dF/dT with the temperature.

5.4 Results and Discussion

Figure 5.4 and Figure 5.5 summarizes the characteristic features of the transitions and the history of stress and heat in an IFTT curve that have been observed in our study. The transitions being observed includes the adsorption and desorption of a solvent, first-order crystal-crystal transformation, second-order glass transition and first-order melting. The thermal and stress history probed by IFTT includes cold drawing, annealing or relaxing, thermal set and cold crystallization.

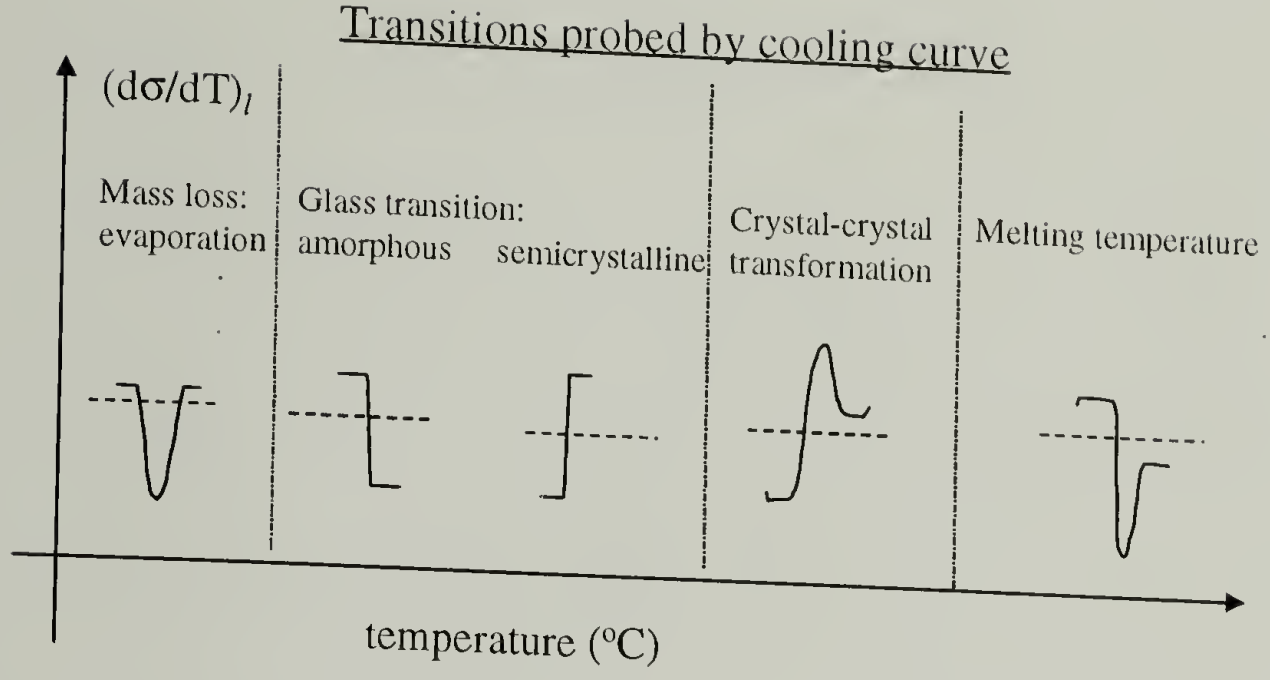

Figure 5.4 Schematic IFTT curves reflecting transitions

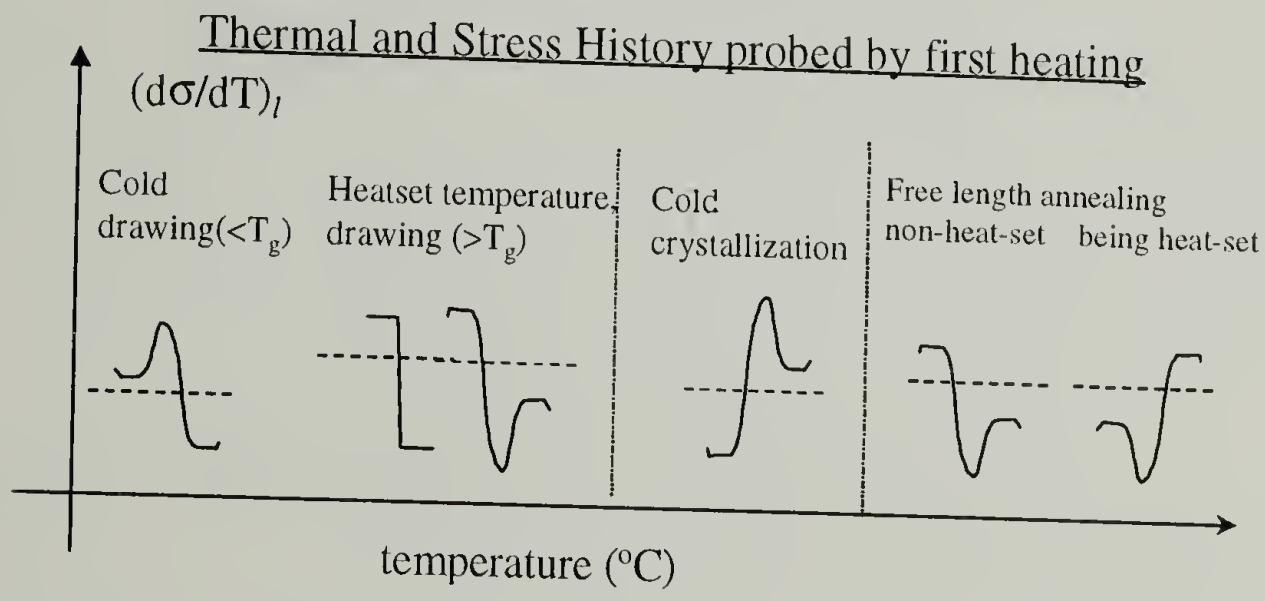

Figure 5.5 Schematic IFTT curves reflecting thermal and stress history

5.4.1 Thermal Mechanical Property and IFTTs of Anisotropic Materials

It is found in our study that IFTT is a general tool that can be used to study the transitions and the thermal and stress history in a material. This method shows higher sensitivity than conventional heat measurement such as DSC. It is especially helpful in the thermal study of anisotropic materials.

5.4.1.1 Transitions Probed by Reversible IFTTs

5.4.1.1.1 Adsorption and Desorption of Water

It is known that residual water exists in PPTA fiber after the spinning and drying of the fiber. Some of the water is in the intercrystalline region and can be removed and regained relative easily. IFTT was used to study the removal and regain of the water in Kevlar® fibers. In the IFTT curve of an as-received Kevlar® 29 fiber, a downward peak appears around 60 °C and is attributed to the residual water. (Figure 5.6) This peak disappears after the sample is dried in vacuum at low temperature. Figure 5.6 shows the appearance and disappearance of this peak in the *dF/dT~ T* curve in Kevlar® 29 fiber.

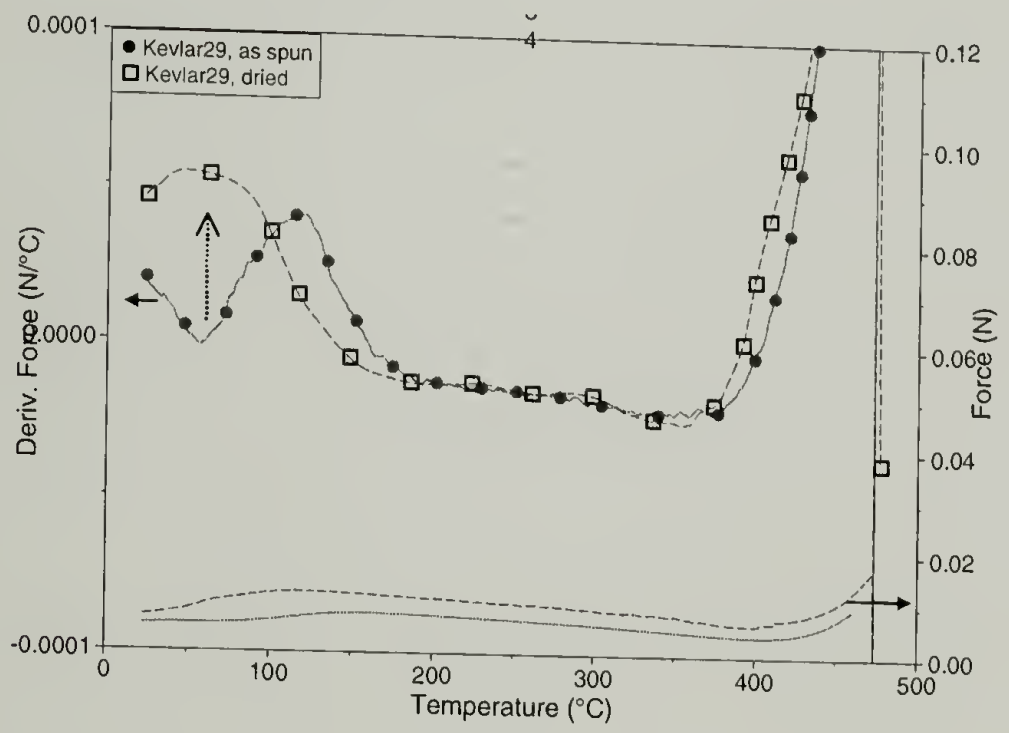

Figure 5.6 Desorption and adsorption of water probed by IFTT in as received Kevlar® 29 fiber;

This water accessibility within the structure remains when the fiber is stretched at high temperature. Figure 5.7 indicates similar water desorption or absorption in a Kevlar® fiber stretched at 250 °C.

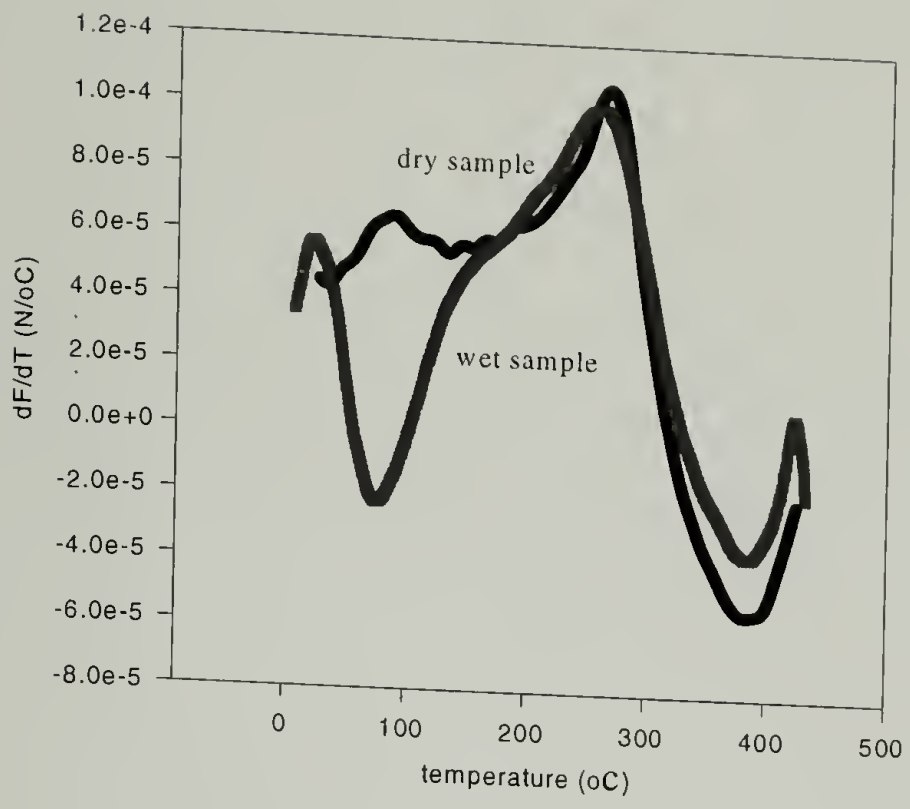

Figure 5.7 Desorption and adsorption of water probed by IFTT in thermal-stretched Kevlar® fiber.

5.4.1.1.2 First-order crystal-crystal transformation

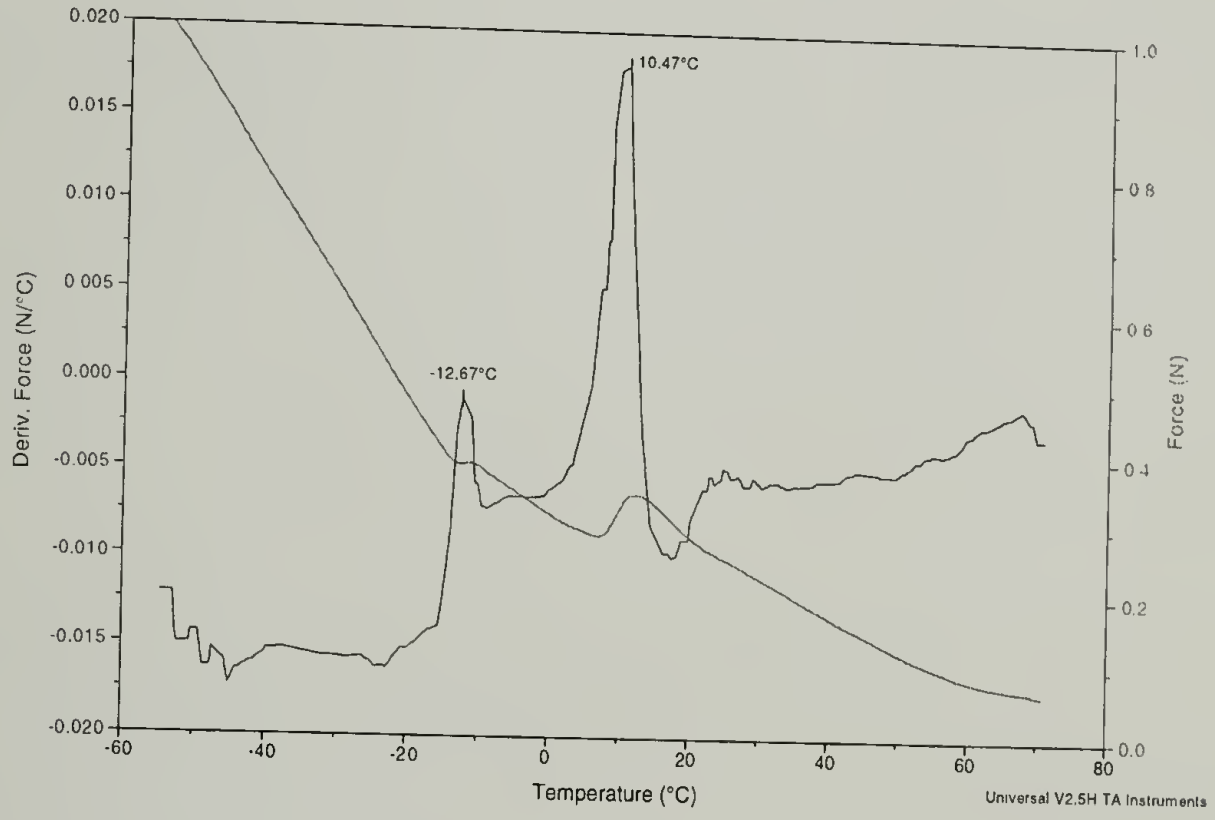

Figure 5.8 Two first-order crystal-crystal transformations in poly(tetrafluoroethylene) strip probed by IFTT.

X-ray diffraction study of Teflon suggests an existence of two crystal-crystal transformations around room temperature. [165-167] This can be detected by IFTT scan. Figure 5.8 shows that an IFTT curve of a Teflon film has two distinctive peaks around room temperature corresponding to the claimed crystal-crystal transformations. The peaks indicate that the transitions are first order.

It appears that IFTT scans have much higher resolution than other thermal analysis tools. To probe the transitions in Teflon, DMTA tests were conducted. Figure 5.9 is a DMTA spectrum of Teflon, while only one broad peak in tanδ appears. It was concluded by other researcher that the two first-order thermal transitions happen at 19 and 30 °C respectively. However, our IFTT indicates the transitions happen at –12 and 10 °C. The difference might be due to the heating rate used in the experiment. It should also mentioned that we are measuring a new equilibrium property where DMTA has no thermodynamic basis.

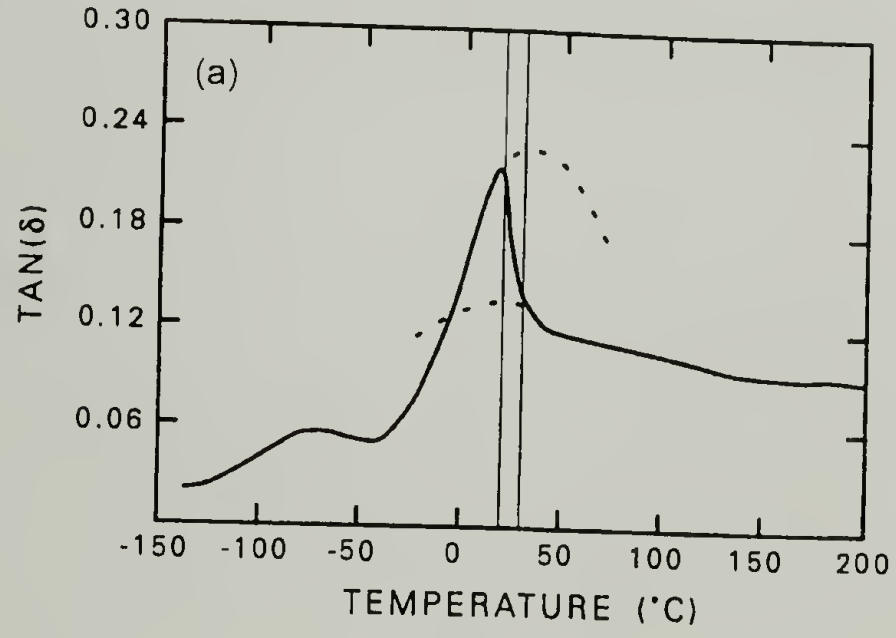

Figure 5.9 Tanδ profile by DMTA for Teflon[168]

5.4.1.1.3 Glass Transition in Semi-crystalline Polymers

In the processing of semi-crystalline polymer, the polymer is often heat set at a temperature higher than the glass transition and below the melting point to improve the thermal stability of the material. After the material has been heat set, its glass transition is difficult to

detect using DSC. Figure 5.10 is a DSC trace of biaxial stretched PET film. The glass transition could not be seen in the plot.

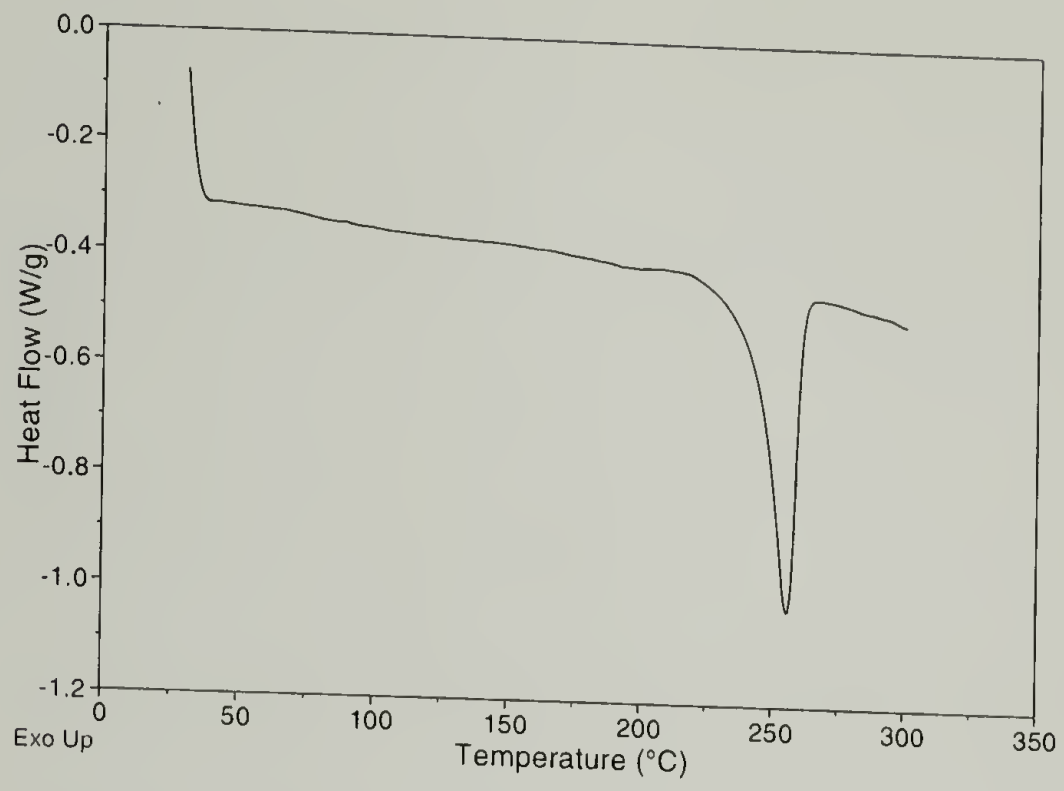

Figure 5.10 DSC of biaxial stretched PET film. 10 °C/min

The glass transition of the semi-crystalline polymer is very important to determine the

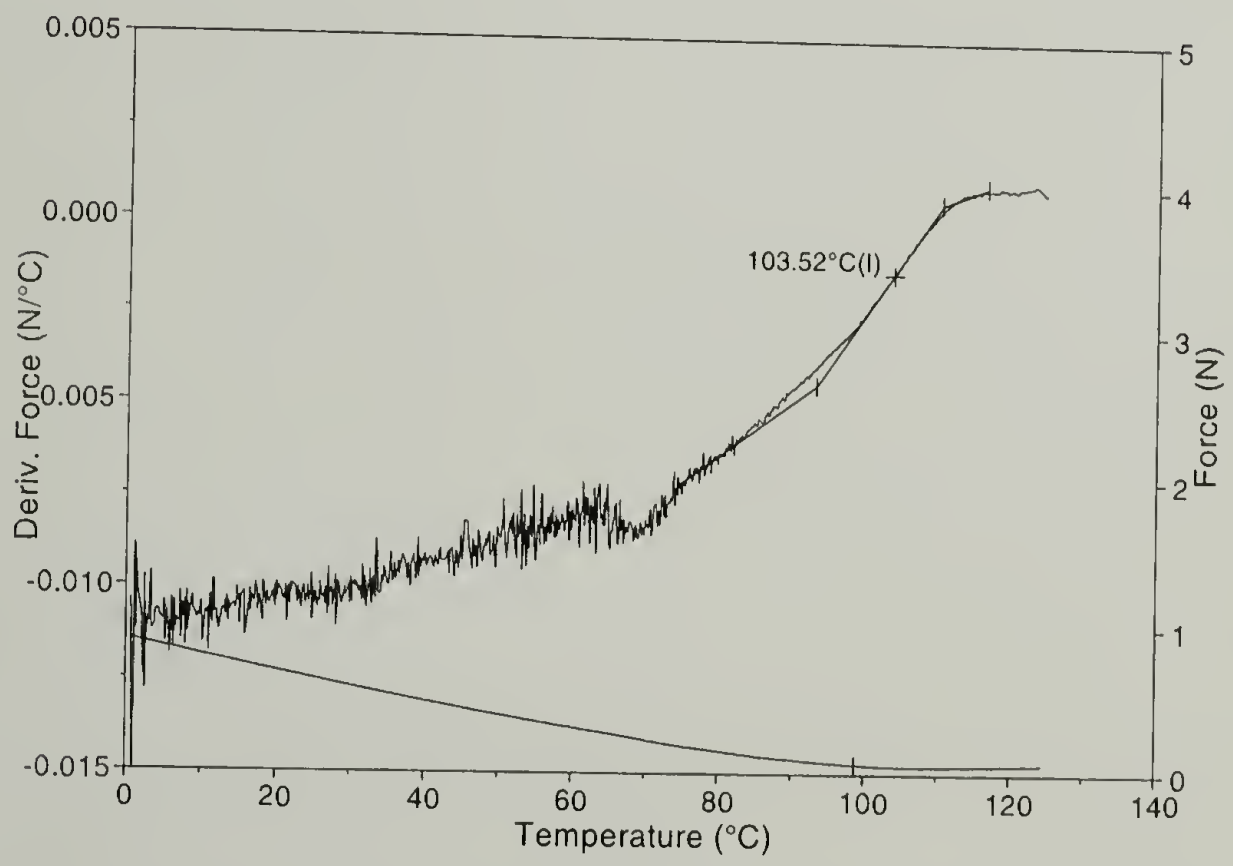

Figure 5.11 Second-order glass transition in biaxial stretched PET film detected by IFTT.

properties of the material. The glass transition can be detected using IFTT. Figure 5.11 is an IFTT of a biaxial stretched PET film. A step transition in an IFTT is seen at about 103 °C, which indicates the glass transition.

IFTT generally has better sensitivity than other thermal analysis tools such as DSC and DMTA. The reason is because that IFTT is a force-measurement method. For anisotropic materials, force measurements are usually easier than heat measurements. Also, there is a huge difference between work and heat.

5.4.1.2 Thermal and Stress History Probed by Irreversible IFTTS

In the processing of fiber or films, treatments utilizing various temperature and stress are often adopted to achieve desired properties. Several commonly used treatment methods are:

1. Annealing, where the sample is kept stress-free at a specified temperature for a specified time;
2. Cold drawing, where the sample is drawn by stress at a temperature usually lower than the glass transition;
3. Heat set, where the sample is constrained at a temperature usually higher than the glass transition and lower than the melting point; and
4. Heat stretching, where the sample is drawn under stress at high temperature.

To be able to control the properties, the processing conditions need to be precisely controlled. In addition, sometimes one wants to know what processing conditions a material has been exposed, or what will be a good processing condition to use.

Through our study, we found that thermal and stress history has a strong influence on the irreversible IFTT behavior of the material. It is possible to retrieve from the IFTT curves the processing conditions for some materials.

5.4.1.2.1 Annealing Temperature of pre-heatset materials

After a pre-heatset material has been annealed at a temperature lower than the heatset temperature, its IFTT curve shows characteristic features.

Figure 5.12 shows that the IFTT trace of a PET fiber changes after the fiber has been annealed.

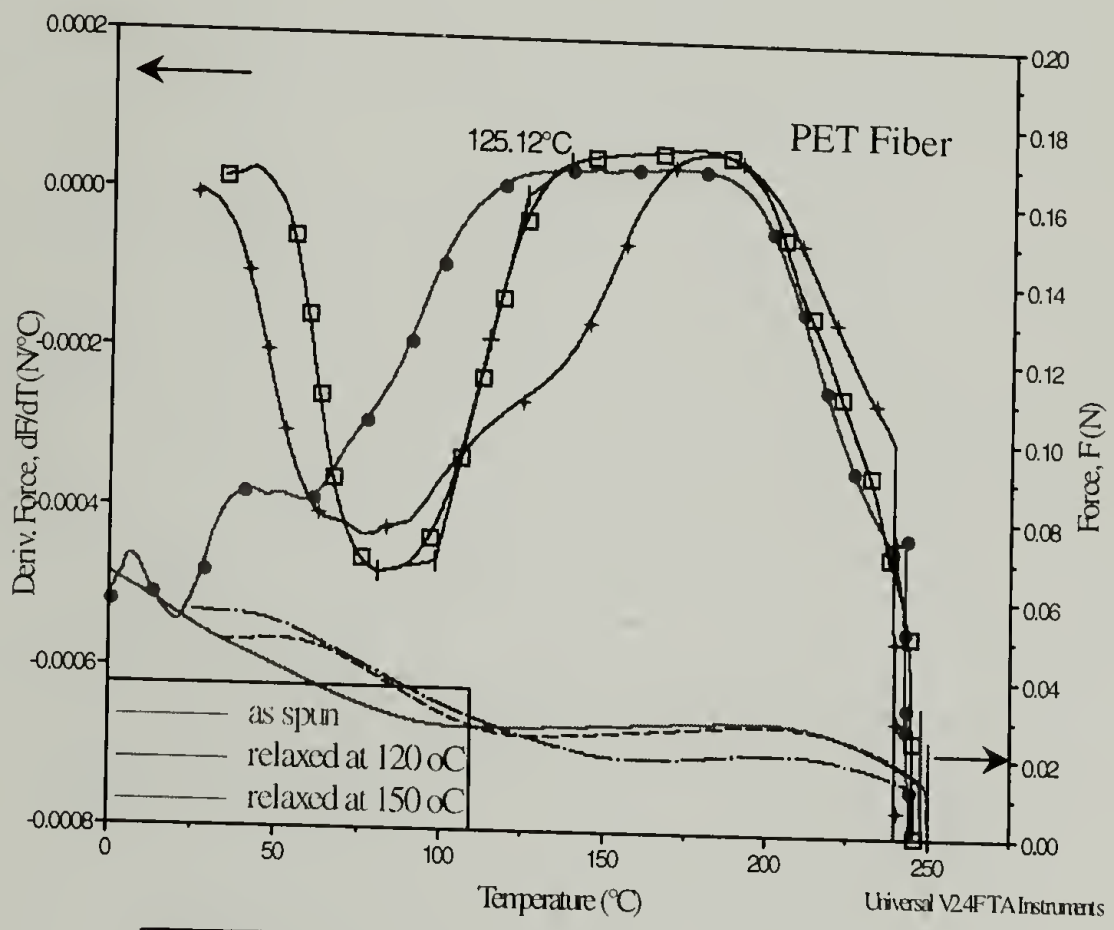

PET fiber		
annealing temperature	120 °C	150 °C
transition temperature in IFTT	125 °C	155 °C

Figure 5.12 Influence of thermal annealing on the IFTT behaviors of pre-heat-stretched PET fiber.

A step like feature appears around 100 °C in the as-received fiber. This step feature moves to 125 °C for the fiber being annealed at 120 °C and further 150 °C for the fiber being annealed at 155 °C. By examining this step change, the annealing temperature of the fiber can be determined.

Figure 5.13 shows the change in IFFT curves of Spectra® fiber after the fiber has been annealed. For the as-received fiber, a step like feature appears at about 70 °C (midpoint of the

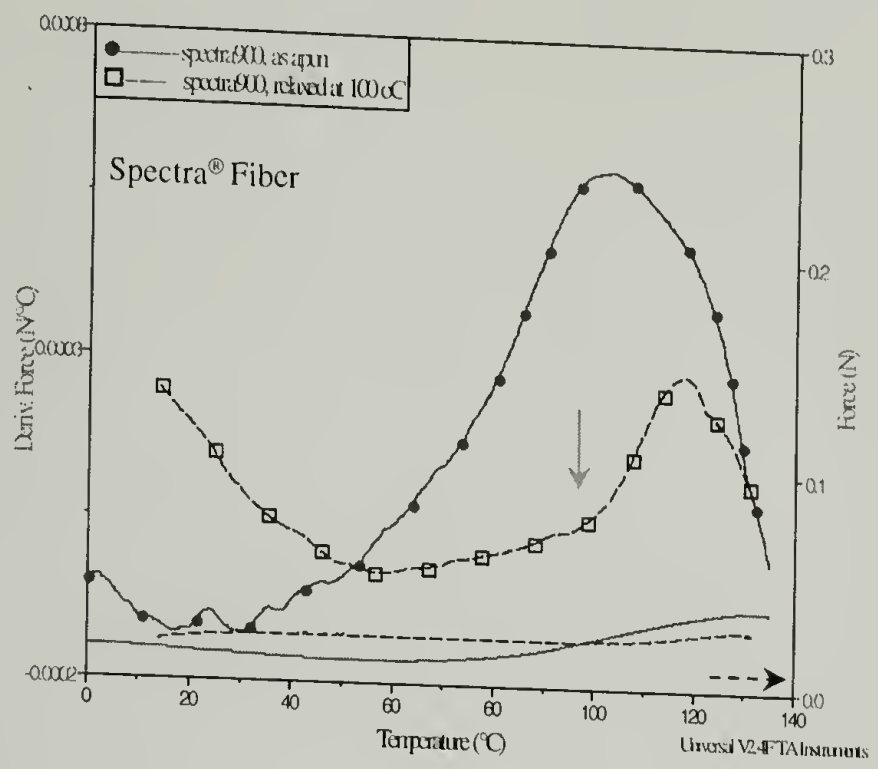

Figure 5.13 Influence of thermal annealing on the IFTT behaviors of pre-heat-stretched UHMW polyethylene fiber

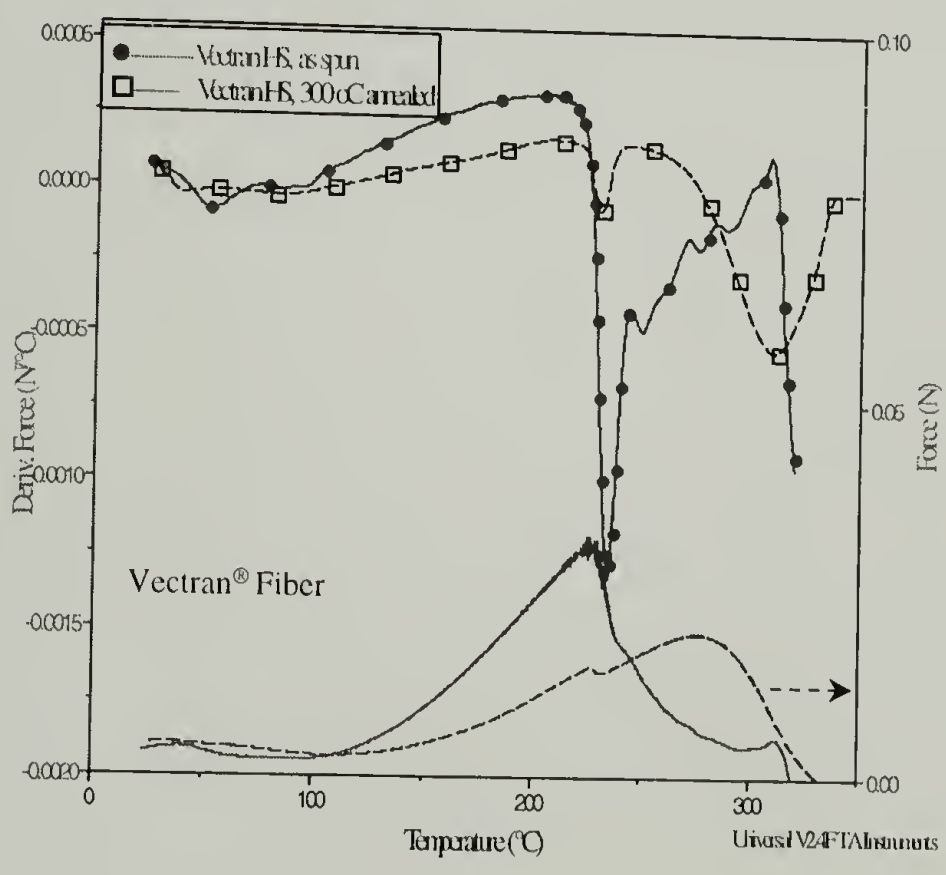

Figure 5.14 Influence of thermal annealing on the IFTT behavior of Vectran® HS fiber

step change). When the fiber is annealed at 100 °C, this step change moves to 100 °C. This feature enables the detection of the annealing temperature for the Spectra® fiber.

For Vectran® HS fiber, thermal annealing also brings characteristic changes in its IFTT plot. As shown in Figure 5.14, thermal annealing of Vectran® HS at 300 °C moves a peak at 240 °C before annealing to 300 °C.

5.4.1.2.2 Temperature of Heat set, Cold drawing and Heat stretching

Heat set, cold drawing and heat stretching are the same in the sense that the material is subjected to stress at elevated temperature. The temperature in the processing can be found using IFTT.

Figure 5.15 shows that the IFTT curve of Nylon fiber changes after the fiber has been heat stretched. A new step change appears with a peak value of 150 °C in its IFTT after the Nylon fiber has been stretched at 150 °C.

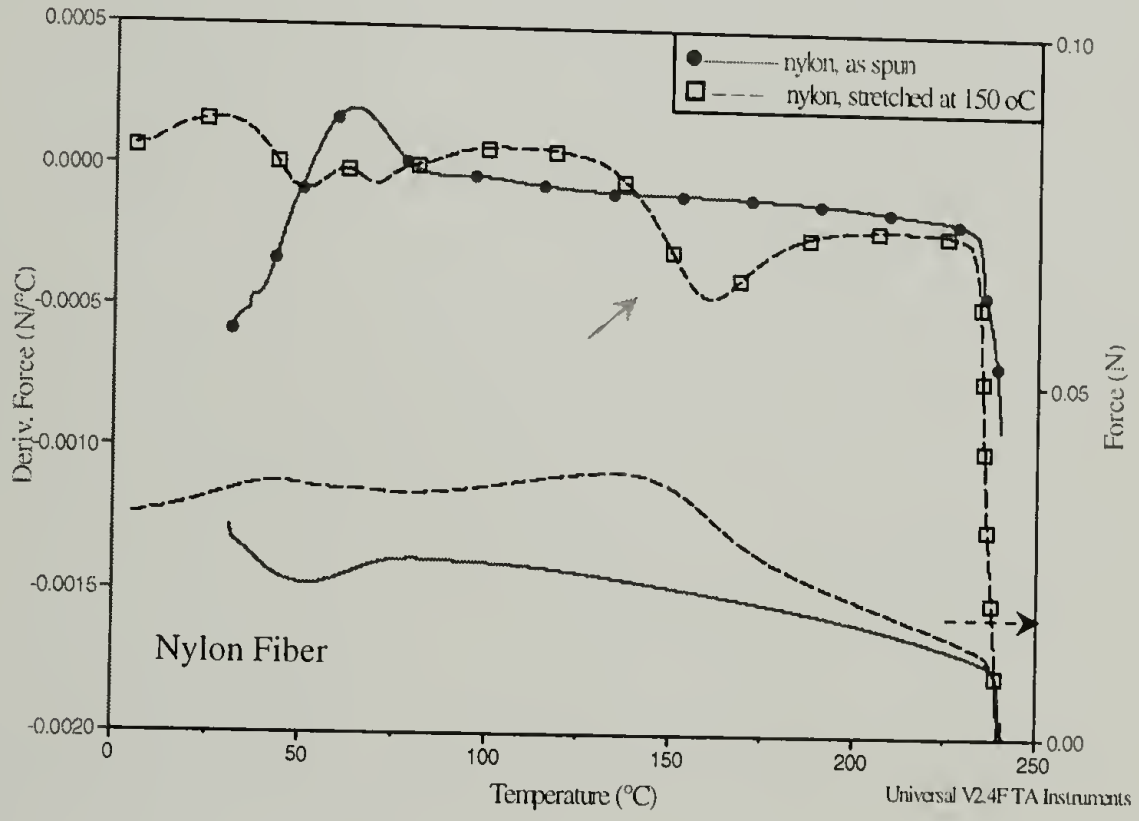

Figure 5.15 Influence of heat stretching on the IFTT behaviors of Nylon fiber.

Figure 5.17 shows the characteristic IFTT curves of heated and constrained PET film. It indicates that a peak temperature in its IFTT the constraint temperature.

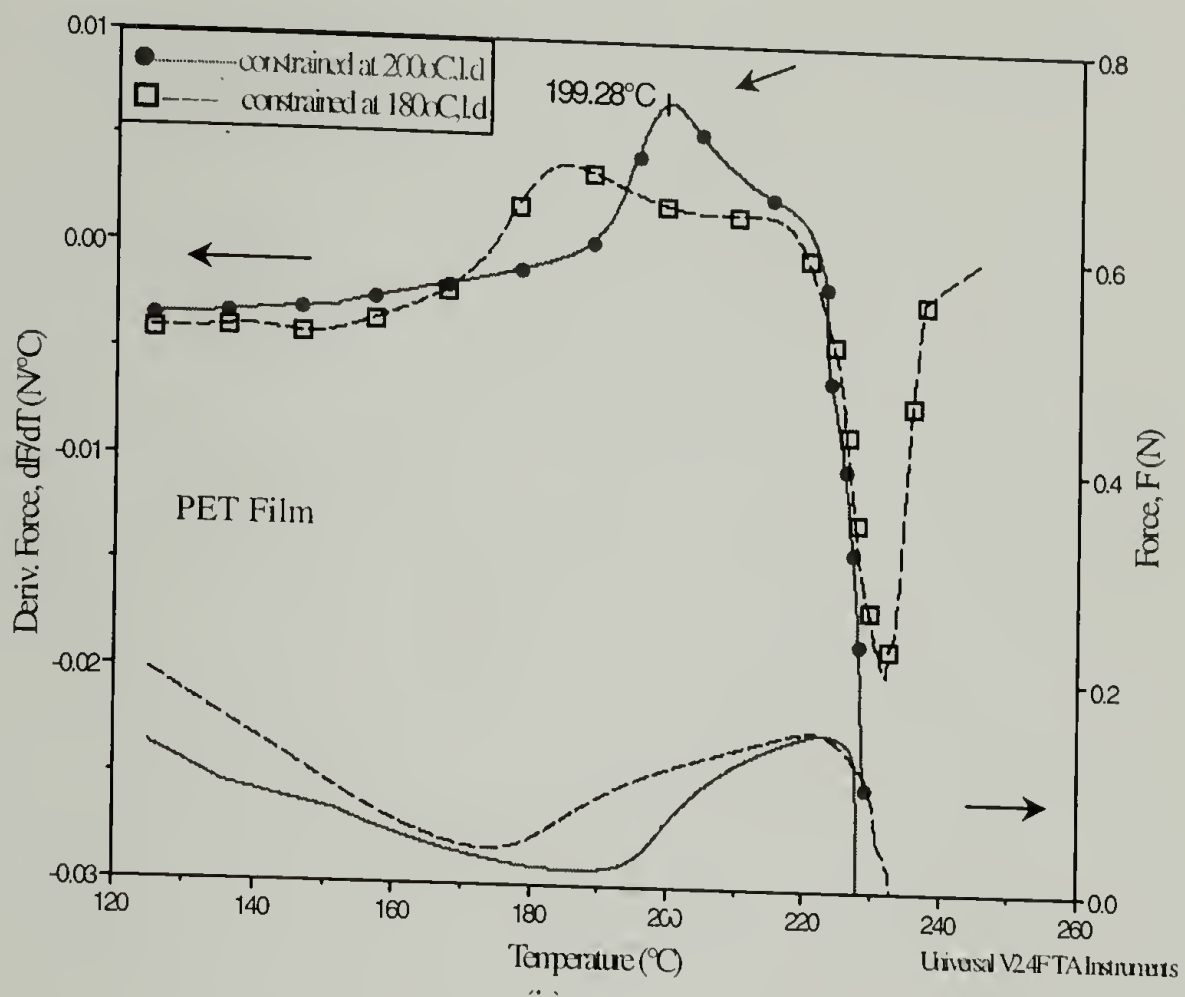

Figure 5.16 Influence of heat stretching on the IFTT behaviors of PET film; ld indicates the machine direction

Technora® fiber is believed to have no thermal transitions below its decomposition temperature. Figure 5.18 compares its IFTT curves after different treatment conditions including annealing and heat stretching. The IFTT curve of as received Technora® has a peak around 60 °C similar to that in Kevlar® 29 fiber. It is also attributed to the residual water and was not seen for heat-treated fibers. Technora® has a very similar chemical structure to Kevlar®. Only that the nonlinearity of the copolymer component prevents an ordered crystal structure as in Kevlar®. The IFTT curve of as-received Technora® has two high temperature peaks at about 380 °C and 460 °C, respectively. These two peaks indicate two relaxation processes in the material. The

peak at 380 °C is similar as the one in Kevlar® shown in Figure 5.21 and it is suspected to have the same origin. The peak at 460 °C might be caused by the copolymer segment.

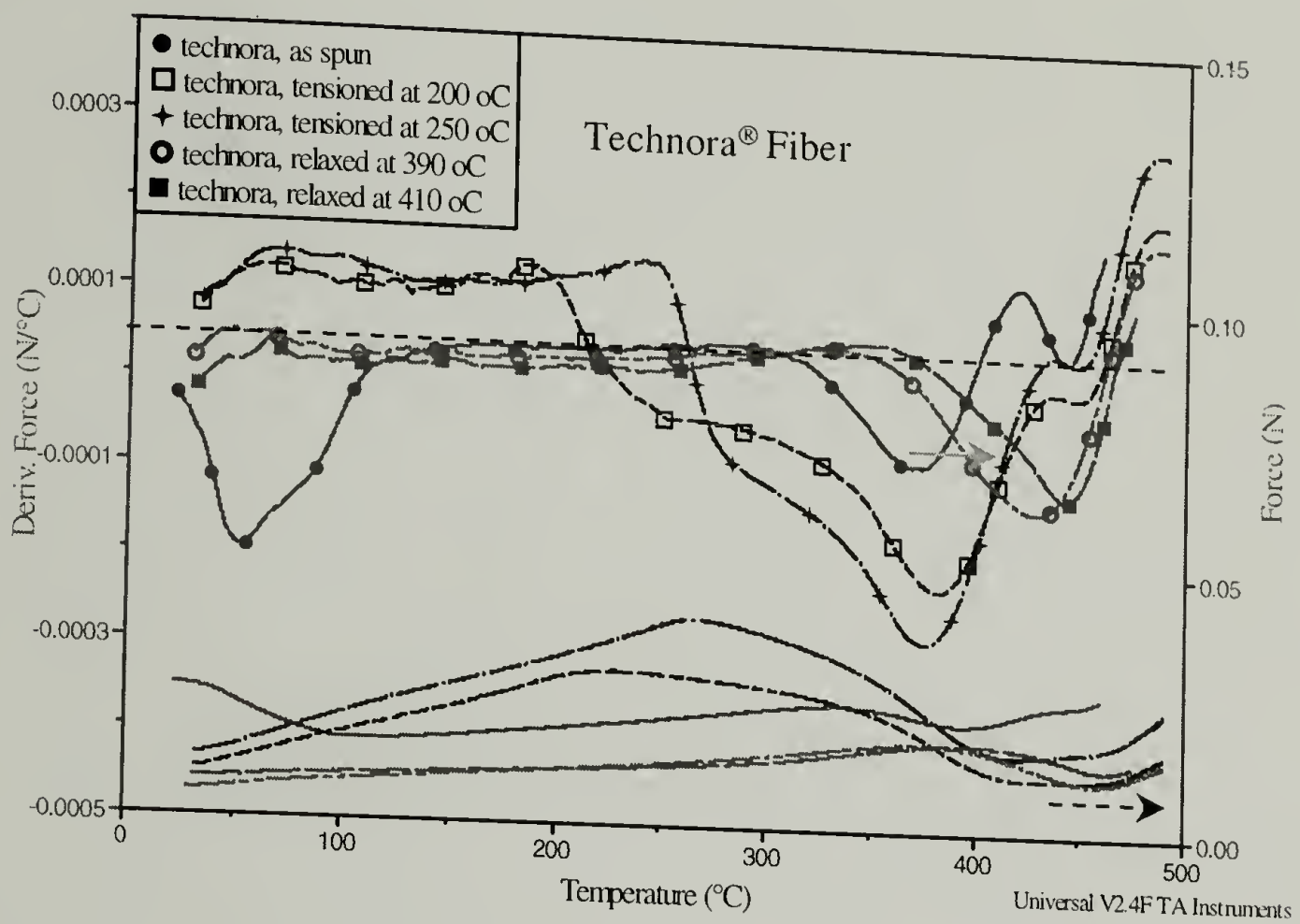

Figure 5.17 Change in IFTT behavior of Technora® fibers being treated differently by thermal annealing or heat stretching

Two treatments have been done to Technora®. After the fiber has been heat stretched, a step feature appears in its IFTT. Shown in Figure 5.17, a Technora® fiber being stretched at a temperature of 250 °C has a step change of *dF/dT* at 270 °C, while the IFTT curve at higher temperature remains unchanged. There is good correlation between the stretching temperature and the step change temperature. Annealing at the temperature higher than the first relaxation temperature erases the first peak in *dF/dT*. In the meantime, the second peak temperature is moved to the new higher annealing temperature.

The thermal stress in Bisphenol A PC has been studied by many researchers. Adams and Farris[169] have shown that a cold drawing of PC at room temperature creates large thermal force,

which can cause failure when the material is heated, if the material kept constrained. Our study shows that when PC film was cold-drawn at room temperature, a peak in dF/dT appears at about 63 °C.(Figure 5.18) Why the peak temperature appears at 63 °C is not clear.

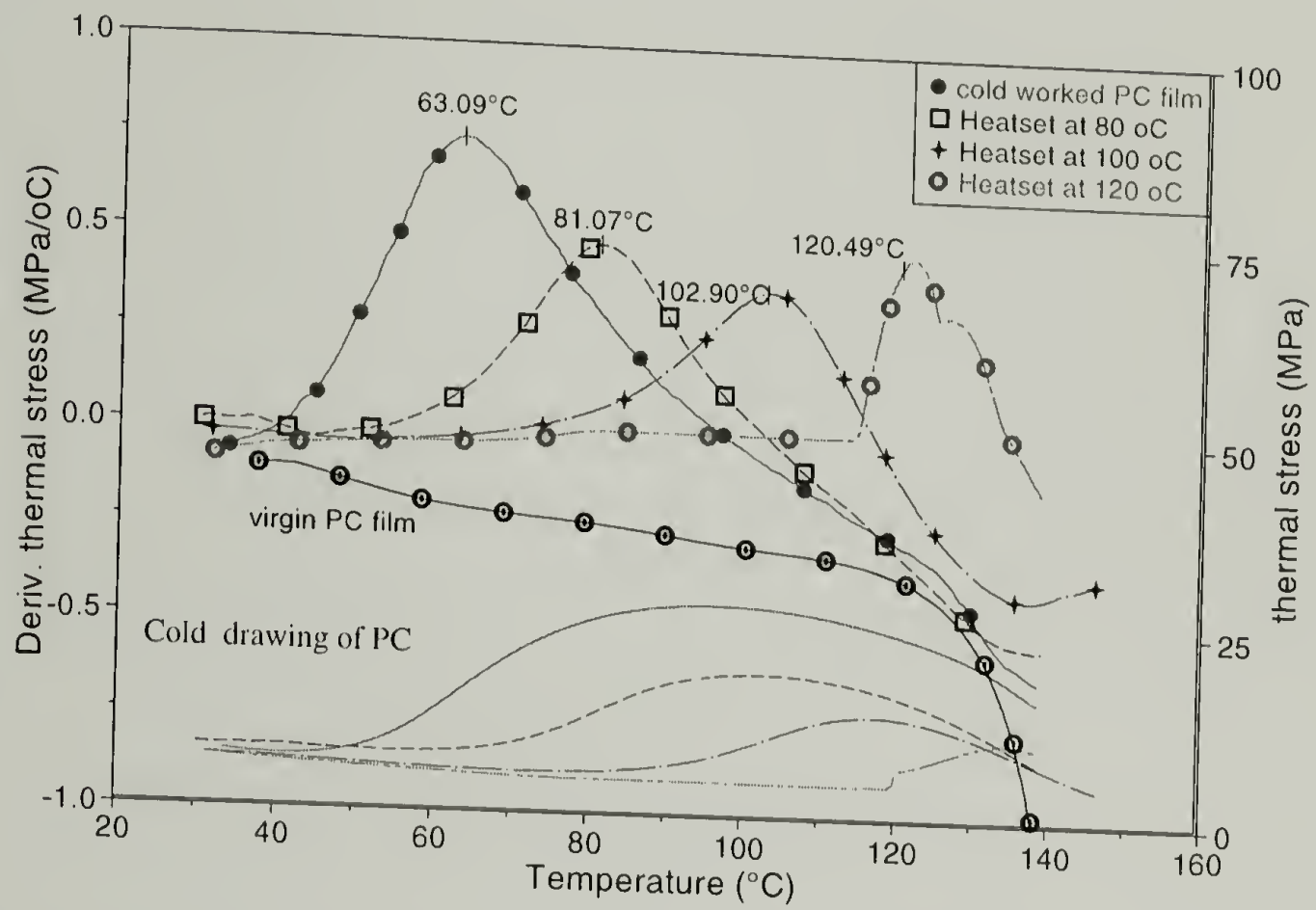

Figure 5.18 Influence of heat-set on the IFTT behaviors of cold-drawn PC film

When the cold-drawn PC was constrained at different temperatures, the dF/dT peak temperature moves. The new dF/dT temperature corresponds well to the constraining temperature.

5.4.2 Influence of Experimental Conditions on the IFTT Behavior

In an IFTT experiment, the applied initial load, the value of the constant strain, and the heating temperature affect the experimental results in a similar way as the influence of heating in the DSC measurements. In our study, Kevlar® 29 fiber was used as model material to study the influence of experimental conditions.

Figure 5.19 shows the influence of heating rate on the IFTT behavior of Kevlar® fibers. It is seen that the higher the heating rate, the higher the transition temperature. This is similar to the heating rate effect on the DSC transitions. An "equilibrium" transition temperature can be calculated from the extrapolation of the peak temperature of different heating rates to zero heating rate.

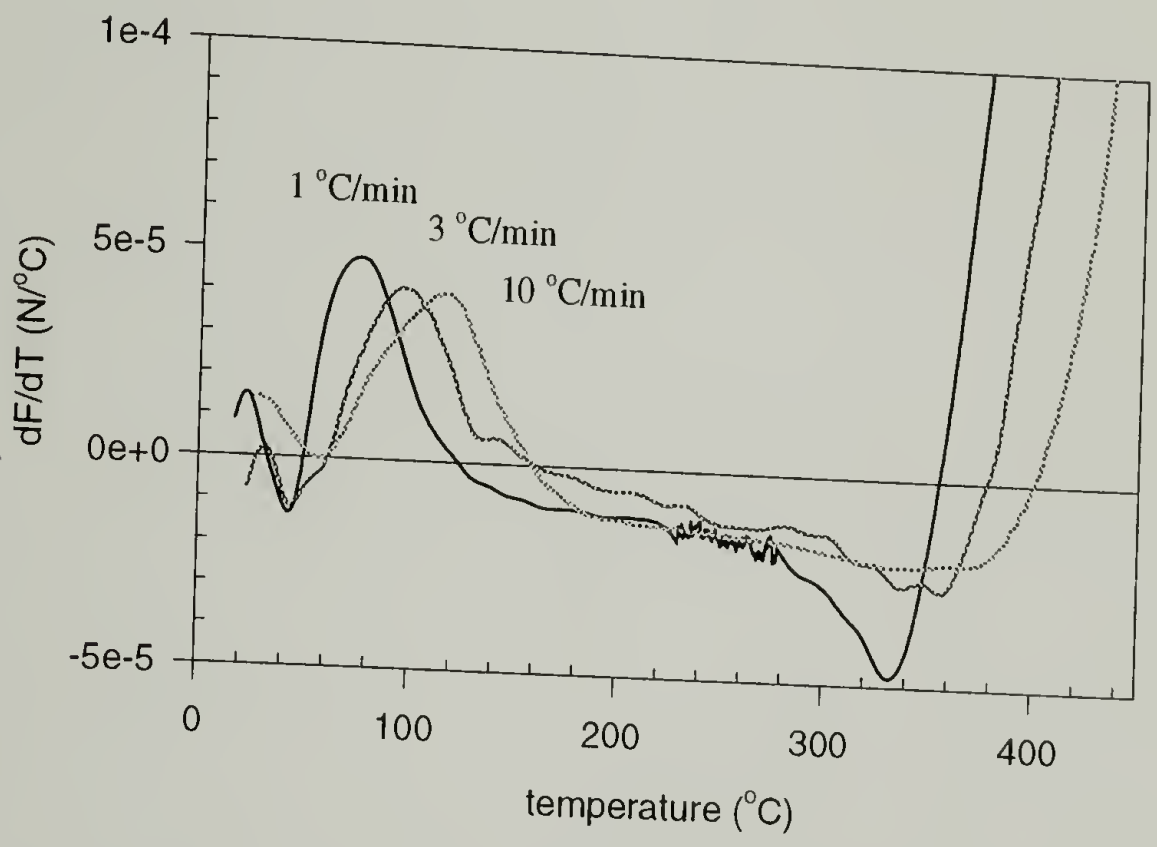

Figure 5.19 *IFTT* behavior in Kevlar® fiber affected by the heating rate.

Figure 5.20 shows that the strain level affects the IFTT behavior of Kevlar® fibers. The higher the strain level, the higher the peak temperature. This is an important observation. When the F-T plot is examined, there is larger difference for different strain levels. At higher strain levels, the stress-temperature derivative is negative at all temperatures, while at lower strain levels, the derivative of stress undergoes a transition from positive to negative. At first this was hard to understand. However, when the dF/dT ~ T is plotted, the curves look similar with only a vertical peak shift. The difference in F-T plots is simply due to the additional force acting on the material.

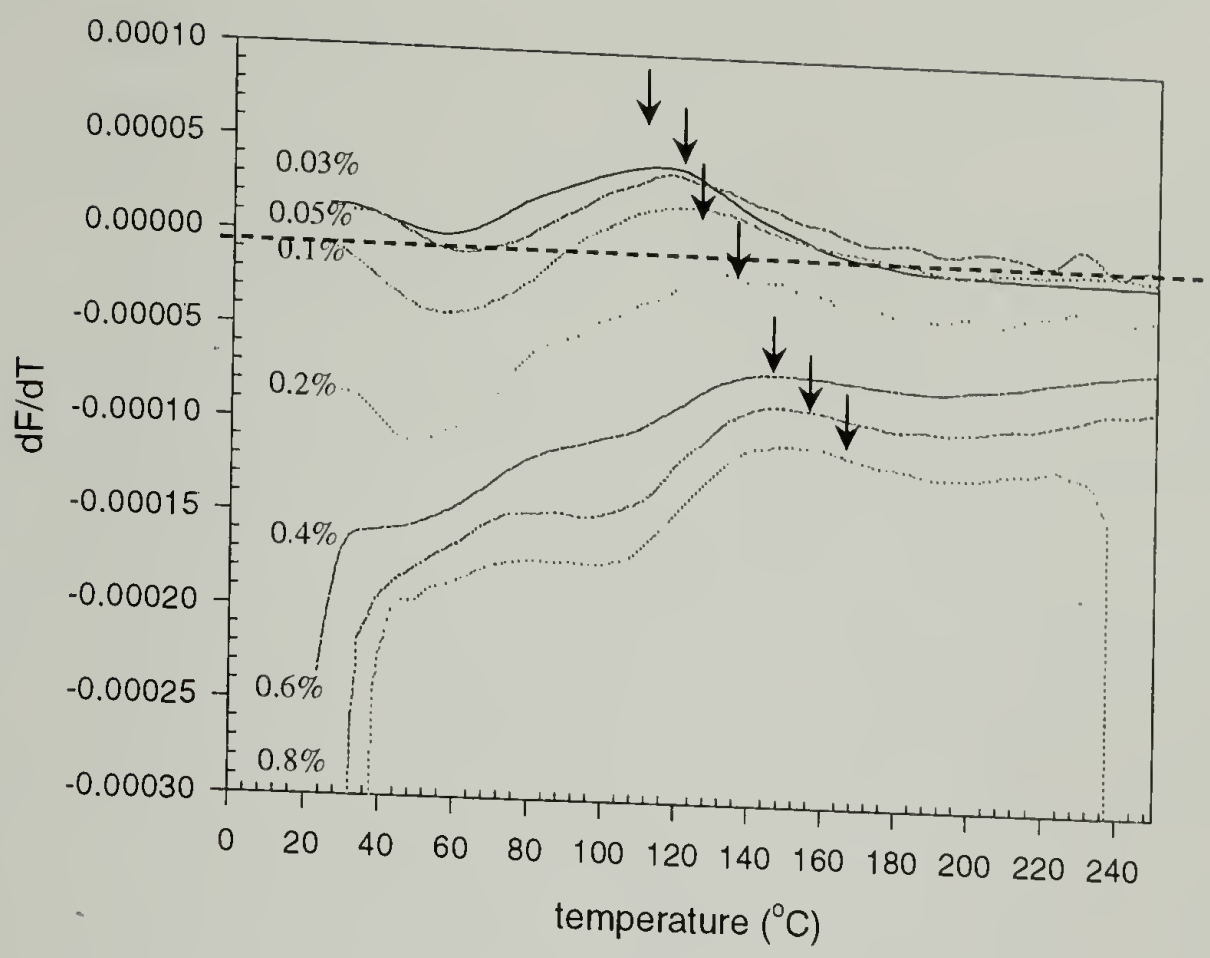

Figure 5.20 *IFTT* behavior in Kevlar® fiber affected by the strain level

It was observed that the transition temperature does not move with the strain level when the initial strain is smaller than 0.03%. Therefore, in order to probe the true transition temperature and enhance the signal-to-noise ratio, a strain level of 0.03% is used through our study.

5.4.3 IFTT Behavior of PPTA Fibers

The study of the thermal-mechanical properties and IFTT behavior of materials was initiated first by a desire to understand the thermal properties of PPTA fiber. Since PPTA is a lytropic liquid crystalline polymer, its thermal studies by other thermal analysis tools such as DSC, TGA and DMTA provide very limited information. The thermal mechanical properties of PPTA fiber was studied by IFTT and found to be very informative.

Figure 5.21 is a typical IFTT curve of PPTA fiber. There are three features in the dF/dT ~ T trace of this figure: two peaks at about 60 °C and 100 °C respectively and a step change at about 400 °C. Thermal and stress history, humidity and the type of commercial fiber affect these

three features, such as changing the profile of the curve, the temperature of the peak or step transition, or change the amplitude of the peak. We will discuss these effects in detail in this section and also explore the molecular origin of these phenomena.

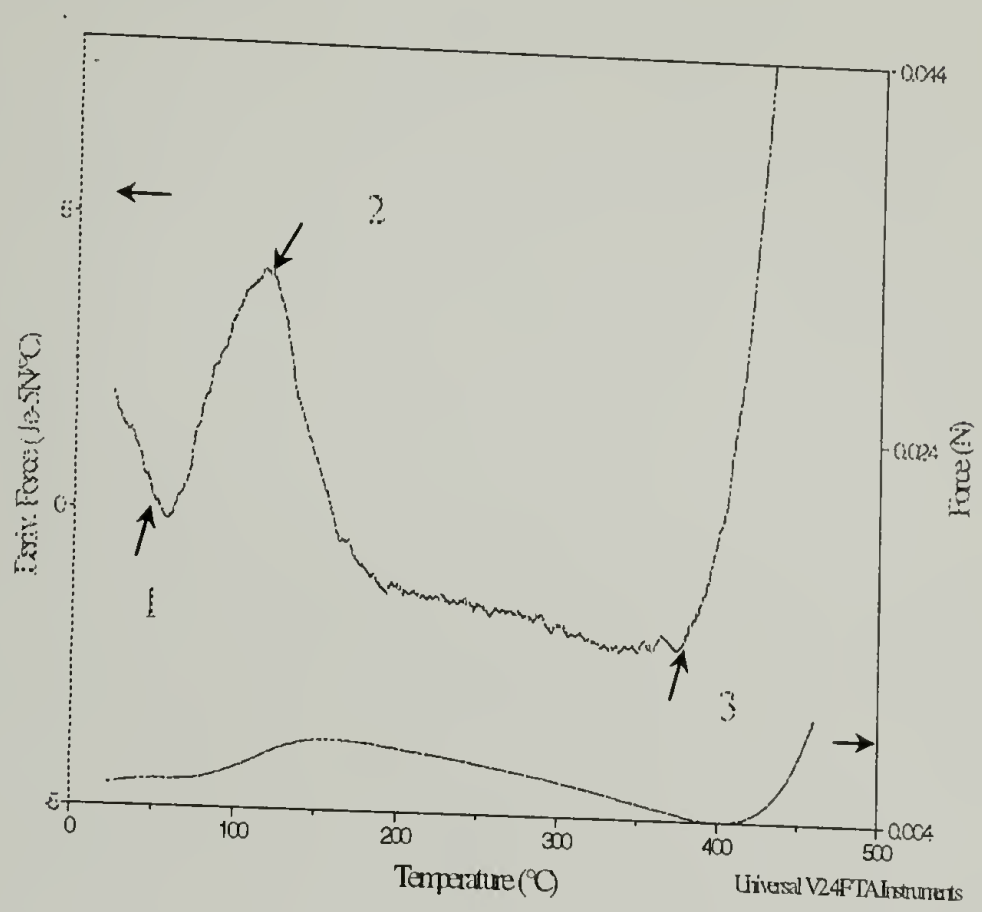

Figure 5.21 *IFTT* curve of Kevlar® 29 as spun fiber showing three characteristic features indicated by numbers in the plot

To identify the origin of these features, other thermal analysis have been done. Figure 5.22 is a TGA diagram of Kevlar® 29 fiber. There are two step weight losses at temperatures close to the first and third feature temperatures in the IFTT curve. It indicates that the first peak and third step change in IFTT curve are associated with the residual water in the material. The first peak is related to the removal of water between crystals; while the third step change involves the water within the crystal region.

Dynamic thermal mechanical analysis was also used in Kevlar® fiber. Figure 5.23 is the DMTA spectrum of Kevlar® 29 fiber. It shows that residual water affects the DMTA spectrum of Kevlar®, while a second heating eliminates the influence from the water. For the first time, a

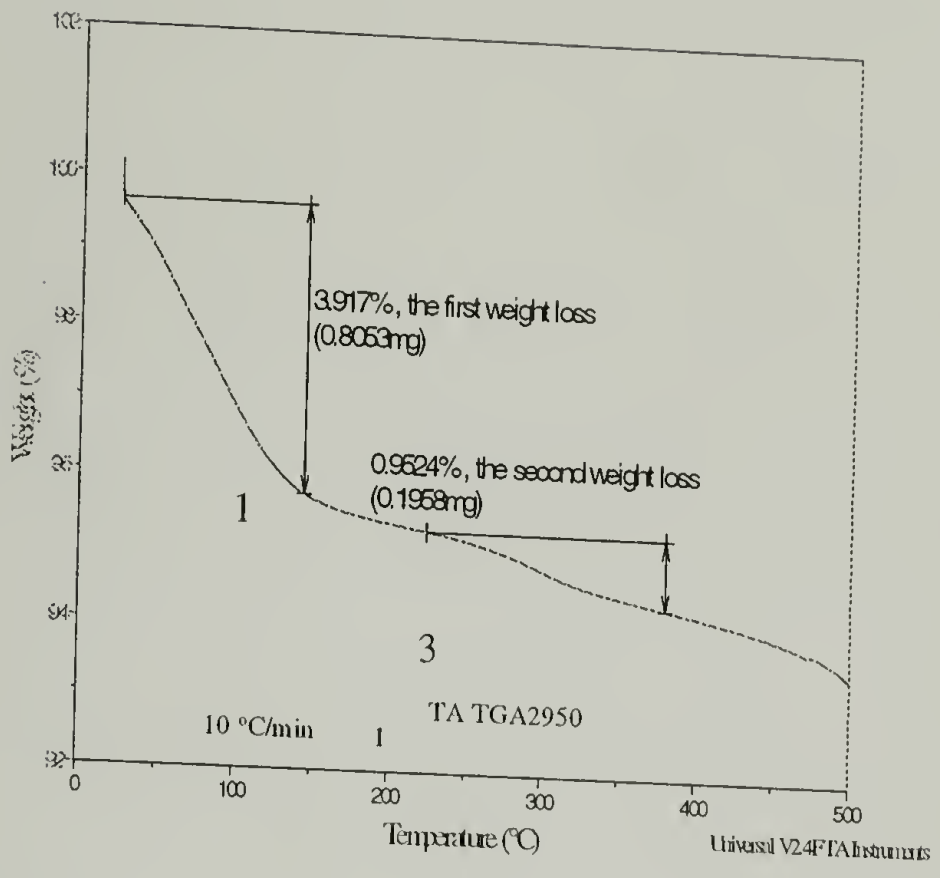

Figure 5.22 Thermal gravitometry diagram of Kevlar® 29 fiber.

tanδ peak around 220 °C is observed and this peak is reversible indicating a relaxation process. This relaxation is suspected to have the same mechanism as that causes the second peak in the

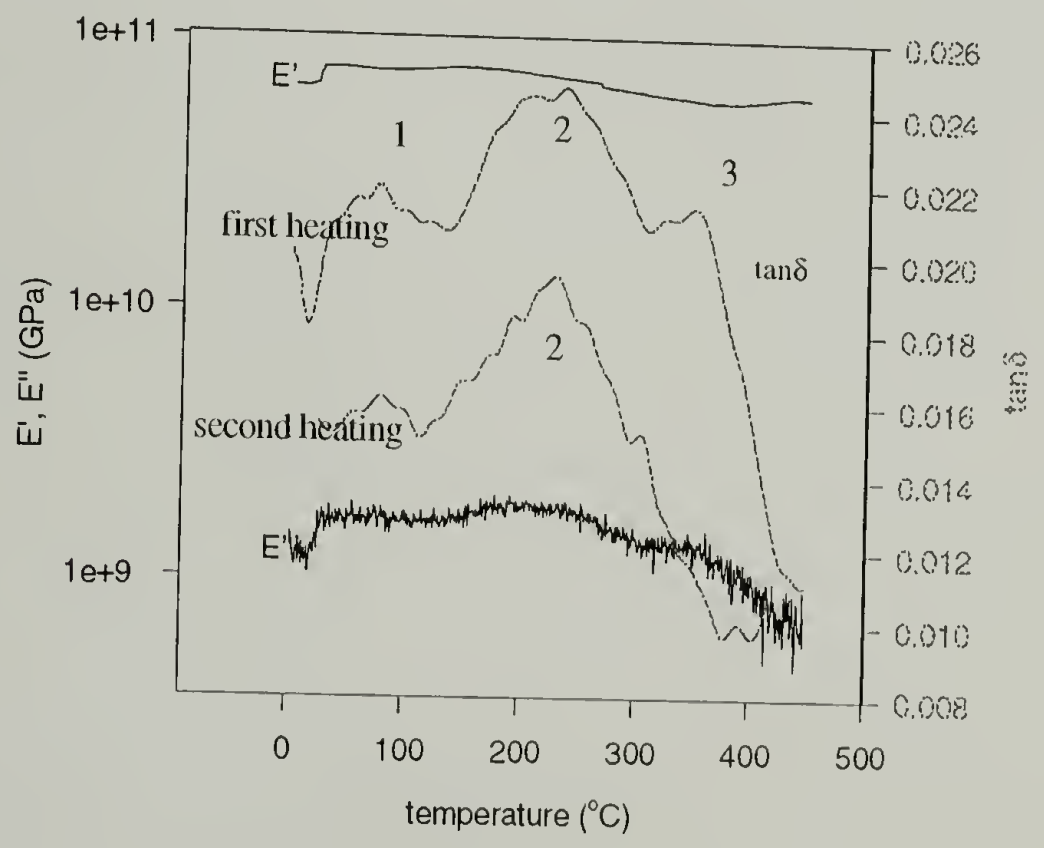

Figure 5.23 *DMTA* study of Kevlar® 29 fiber; (a). DMTA trace, Rheometric Mark IV, 0.2%, 1Hz, 5 °C/min

IFTT of Kevlar®. We speculate that the reason this feature appears corresponding to some stress or thermal history is that an inherent relaxation is modified by the stress and thermal history.

The activation energy of this relaxation was calculated using the measurements done at various frequencies. Figure 5.24 shows the Arrhenius plot. The activation energy is 27 kcal/mol.

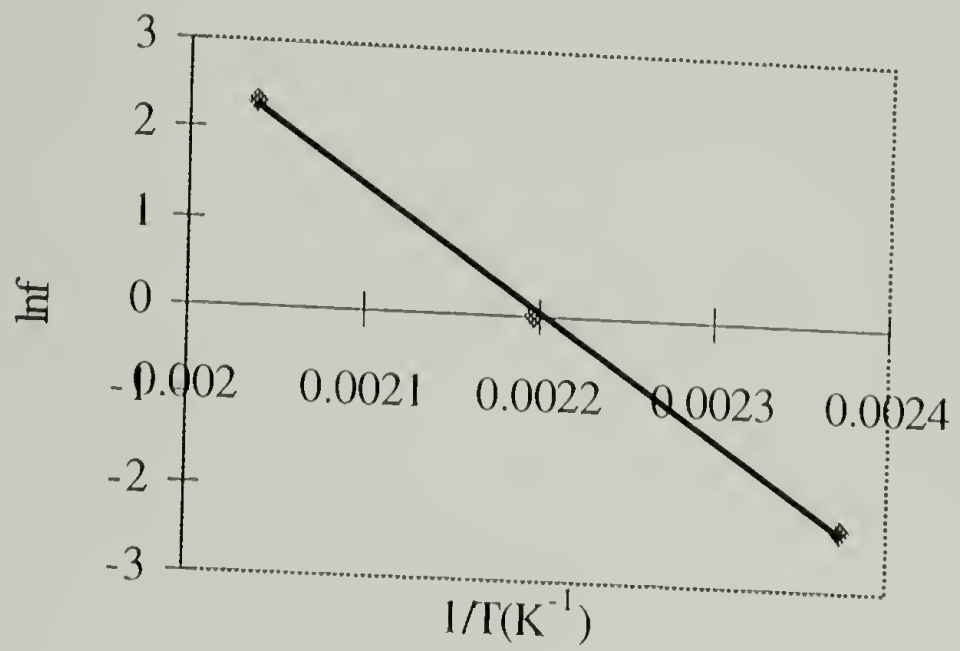

Figure 5.24 Arrhenius plot of the relaxation in Kevlar® fiber

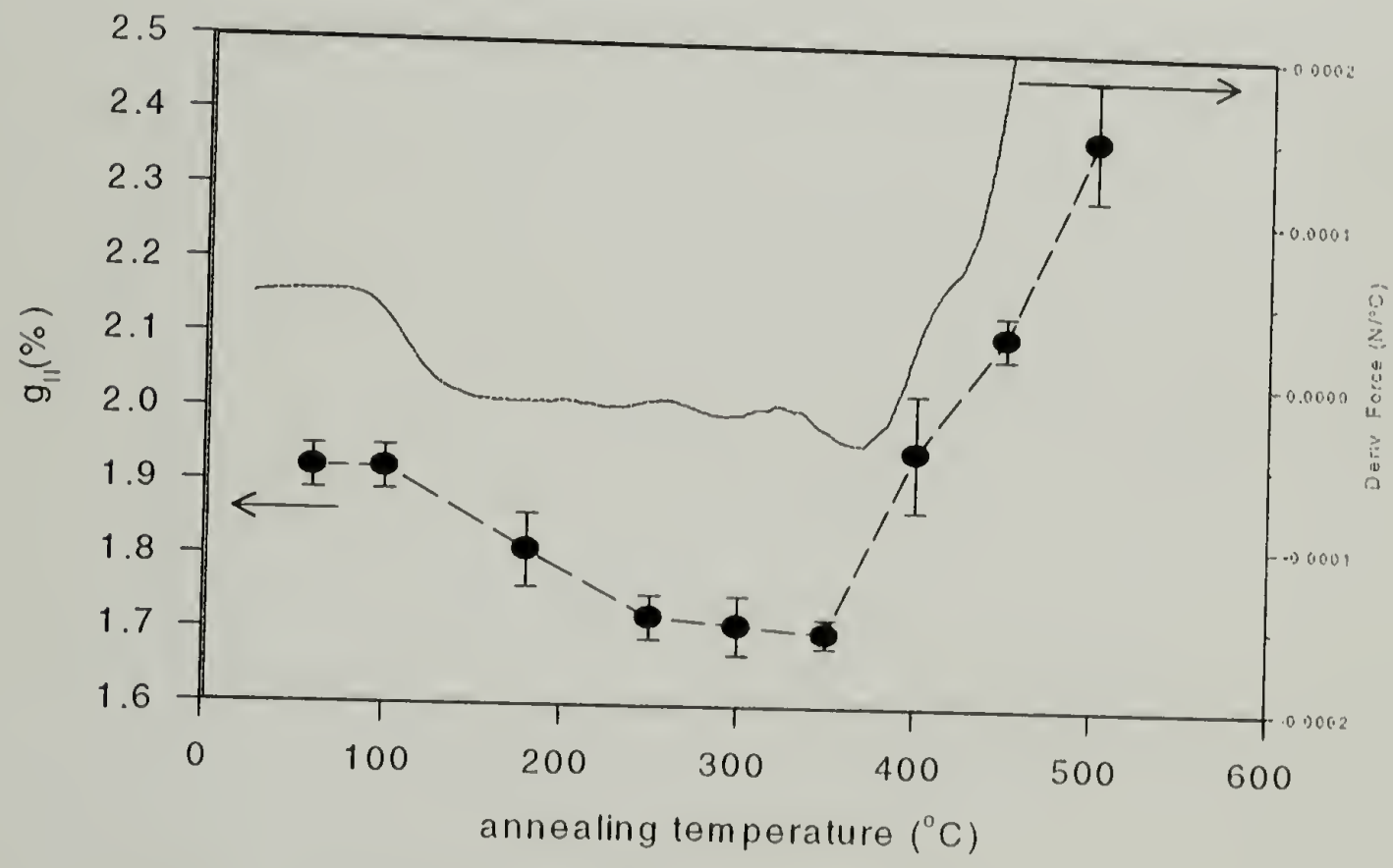

Figure 5.25 Comparison of the change in dF/dT and the paracrystalline parameter with temperature in Kevlar® fiber.

If the change of dF/dT with temperature is compared with the change of the paracrystalline parameter with temperature as in Figure 5.25, these two are very similar. This suggests that the IFTT behavior represents the structure change inside the material.

In Chapter 7, the structural difference among different types of Kevlar® fibers is discussed. Kevlar® 149 is shown to have different chain conformation from Kevlar® 29(Figure 7.9). The meridional scan of the X-ray diffraction of a fiber being treated above temperature 350 °C, which is higher than the relaxation temperature, is similar to that of Kevlar® 149. This similarity suggests that the mechanism of the relaxation is that first the hydrogen bond between the polymeric chains and the residual water is broken and then it reforms between polymeric chains. Experiments were designed to examine this hypothesis. The fiber was treated with high temperature and pressurized water. Because of the presence of liquid water, the driving force to break hydrogen bonds due to the leaving of gas vapor is destroyed. Thus, the break of hydrogen bonds between polymeric chains and residual water is prevented so that the change in chain conformation is inhibited. Figure 5.26 confirmed this hypothesis. The 2nd peak in the IFTT curve was unchanged with the treatment temperature if the fiber was treated in the presence of liquid water. This result is very different from that of fibers treated in an inert gas environment (Figure 5.35).

Similarly as we introduced in 5.4.1.1, a reversible part of IFTT of PPTA fiber can be abstracted from a cyclic heating experiment. This reversible part, which is shown in Figure 5.27, gives us the same information obtained from the DMTA experiment.

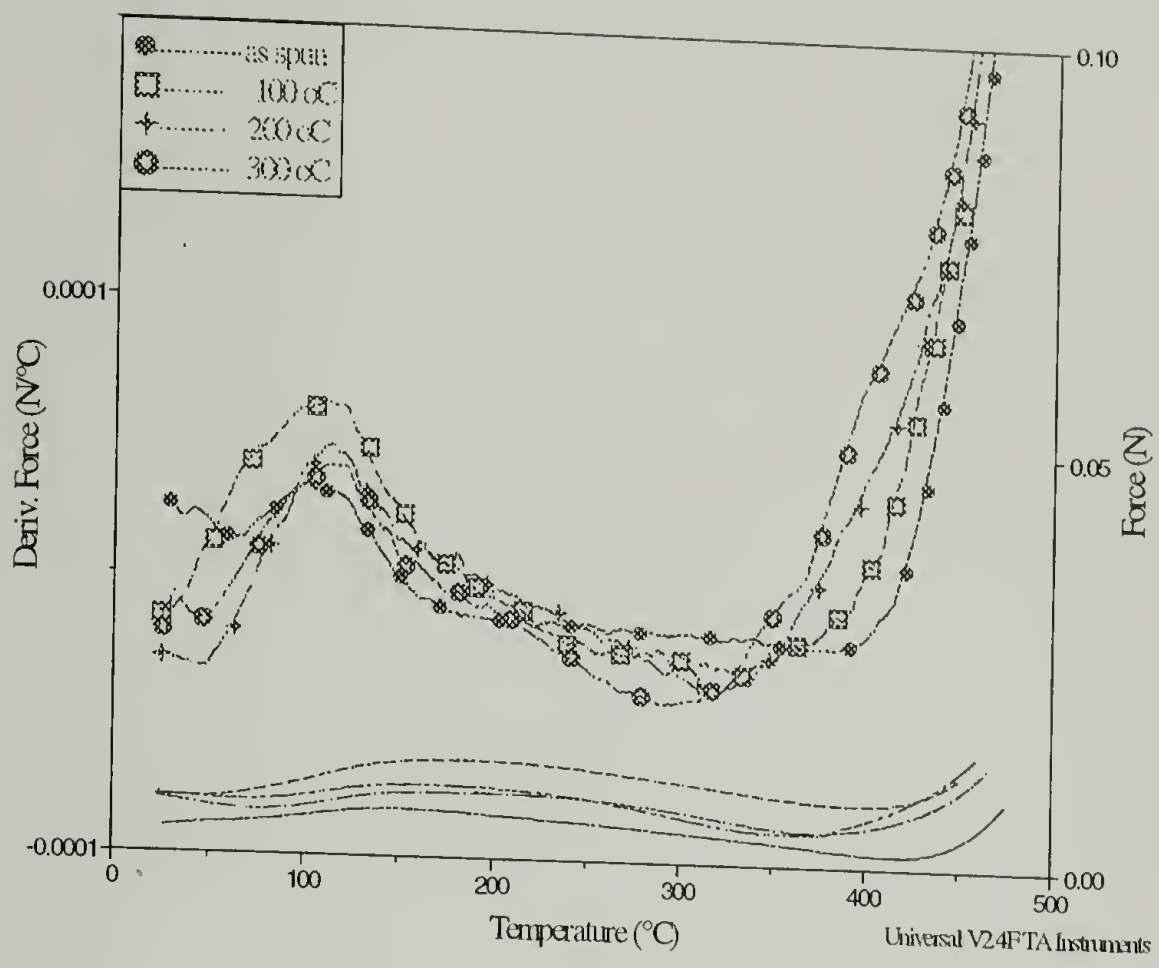

Figure 5.26 *IFTT* curves of Kevlar® fibers subjected to different temperatures in the presence of saturated water

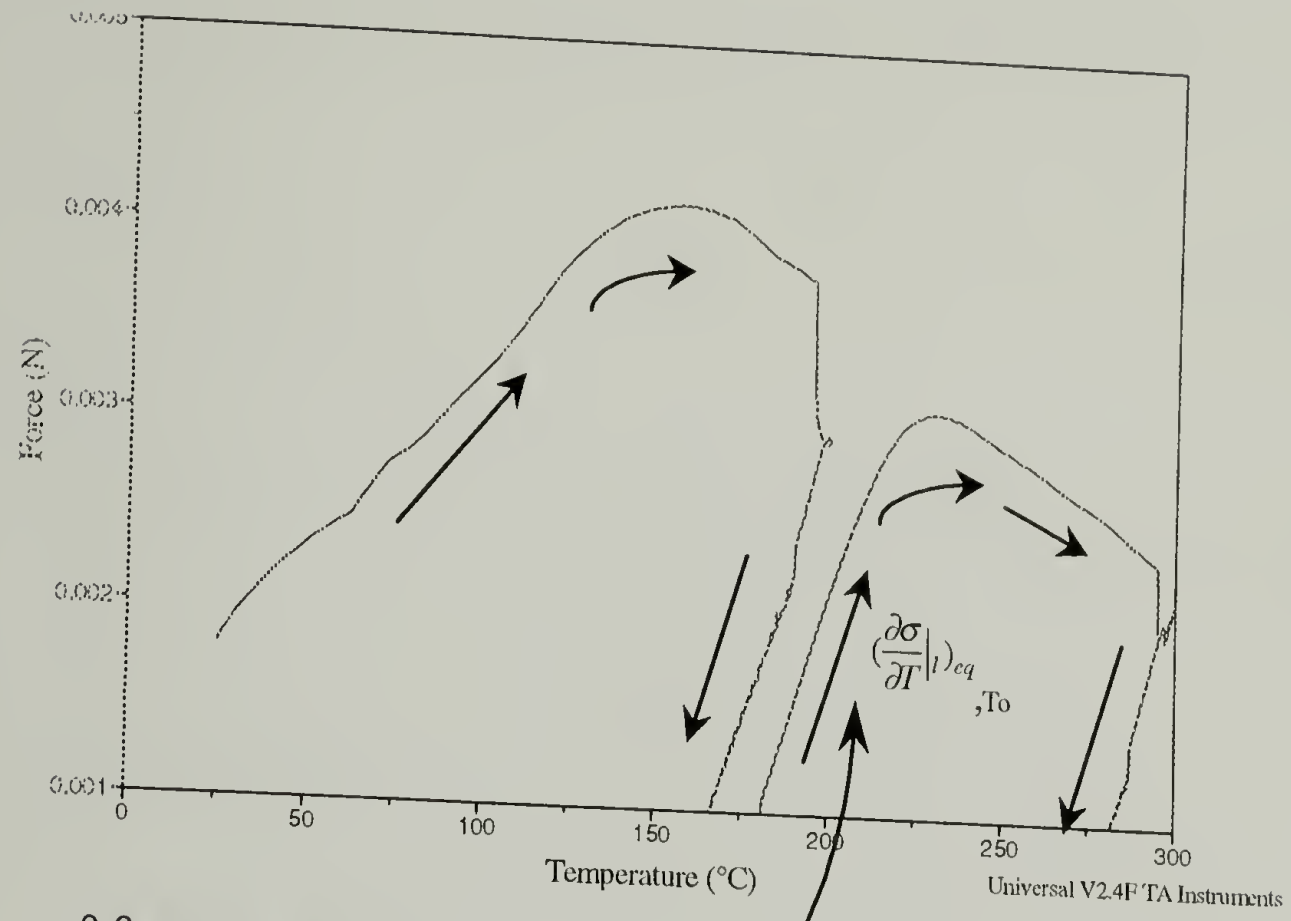

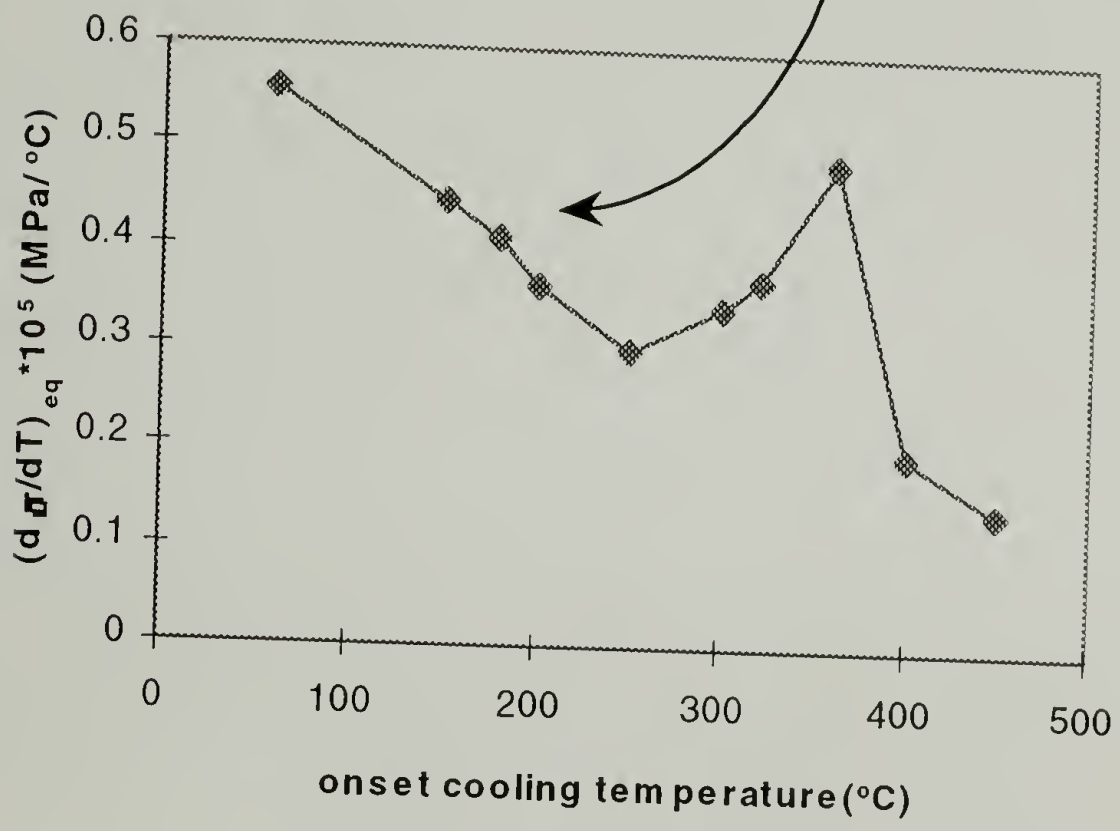

Figure 5.27 A reversible IFTT curve for Kevlar® fiber indicating a relaxation at the same temperature as suggested by DMTA. (a). A close look at how one point in the reversible IFTT curve is determined by a cyclic heating IFTT; (b). The resultant reversible IFTT curve of Kevlar® fiber

5.4.4 Probing the Processing, and Monitoring the Exposure history of PPTA Fibers

It has been demonstrated that IFTT can provide information about the stress and thermal history in a material. In this part of the discussion, IFTT is shown helpful to identify the processing and to monitor the exposure of PPTA fibers.

5.4.4.1 Controlled Post-treatment and its Effect on IFTT behavior—Correlation between Processing and Properties

To be able to probe the processing condition using IFTT, the relation between the IFTT curve and processing conditions was investigated. It was done through controlled post-treatment. The conventional methods of post-treatments of fiber are thermal annealing and heat stretching.

Figure 5.28 shows a typical IFTT curve of a fiber after it is heat-stretched. The general feature of the curve is not very different from that of the as received fiber. This suggests that Kevlar® 29 fiber has been stretched during its process. The peak temperature of the second peak in a heat-stretched fiber moves to higher temperature compared to that of the as received.

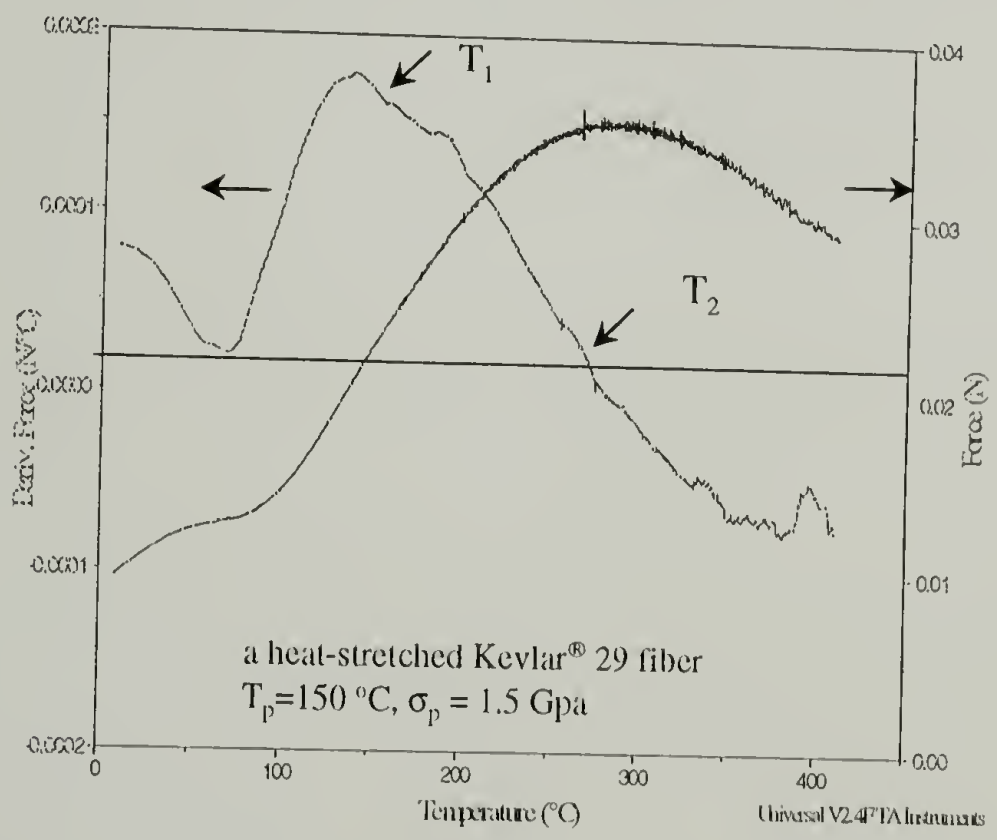

Figure 5.28 A characteristic IFTT curves of heat-stretched Kevlar® fiber. In the plot, T_1 is the temperature at which the absolute value of $(d\sigma/dT)_f$ reaches maximum, and T_2 is the temperature at which $(d\sigma/dT)_f = 0.15 MPa/^{\circ}C$.

Figure 5.29 shows a typical IFTT curve of a fiber after it is annealed. The curve changes from an upward peak into a downward peak compared to that of the as received fiber.

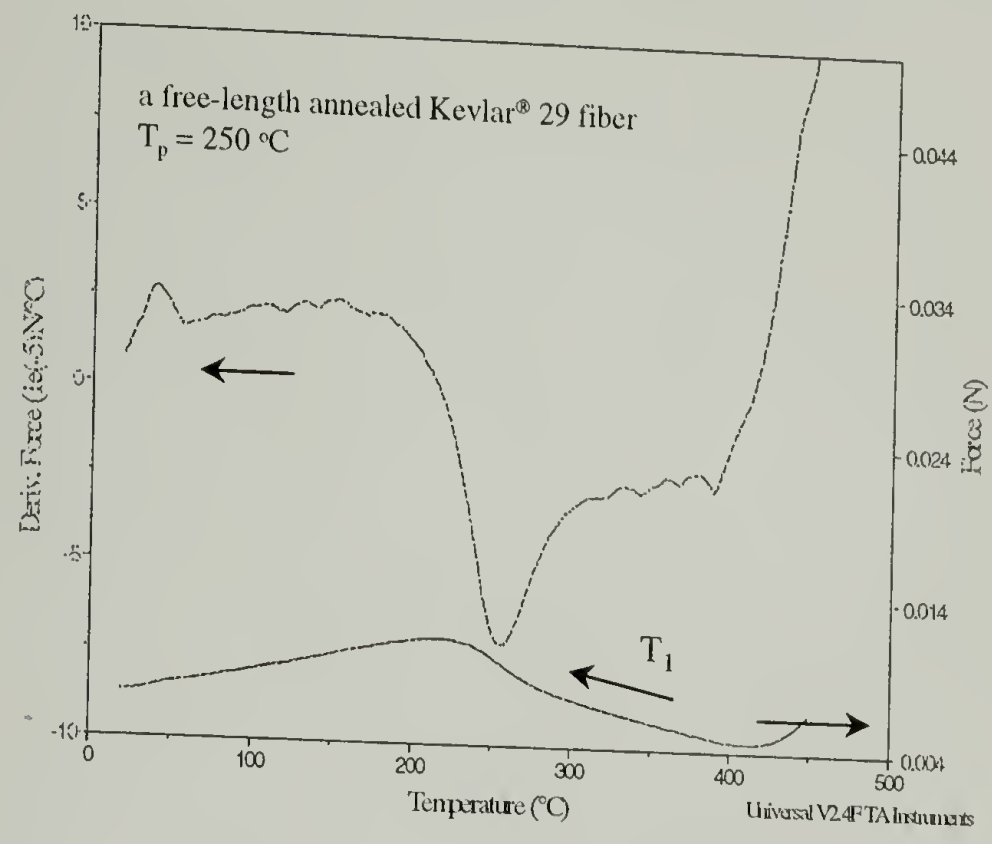

Figure 5.29 A characteristic IFTT curve of annealed Kevlar® fibers. T_1 is the temperature at which the absolute value of $(d\sigma/dT)_l$ reaches maximum. The annealing temperature was T_p=250 °C

5.4.4.1.1 Correlation of IFTT Properties with the Heat-stretching Condition

Figure 5.30 illustrates the correlation between the heat-stretching condition and the IFTT properties. For the fiber heat-stretched at T_p under tension of σ_p, the temperature T_1 at dF/dT=Max. in its *IFTT* curve is equal to T_p.(Figure 5.30.(b)) The temperature at $(\partial\sigma/\partial T)_l$=0.15MPa/°C, T_2, characterizes the applied tension σ_p during the treatment. $T_1 = T_p$ for treatment under different applied stresses at T_p.

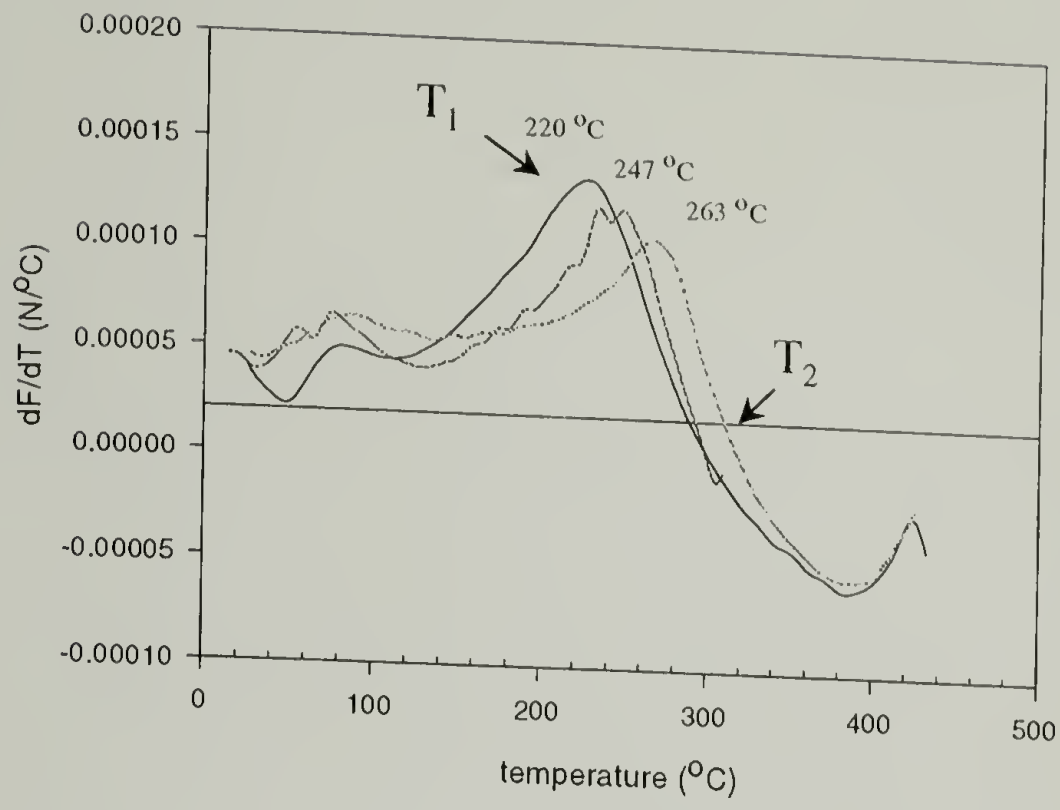

(a)

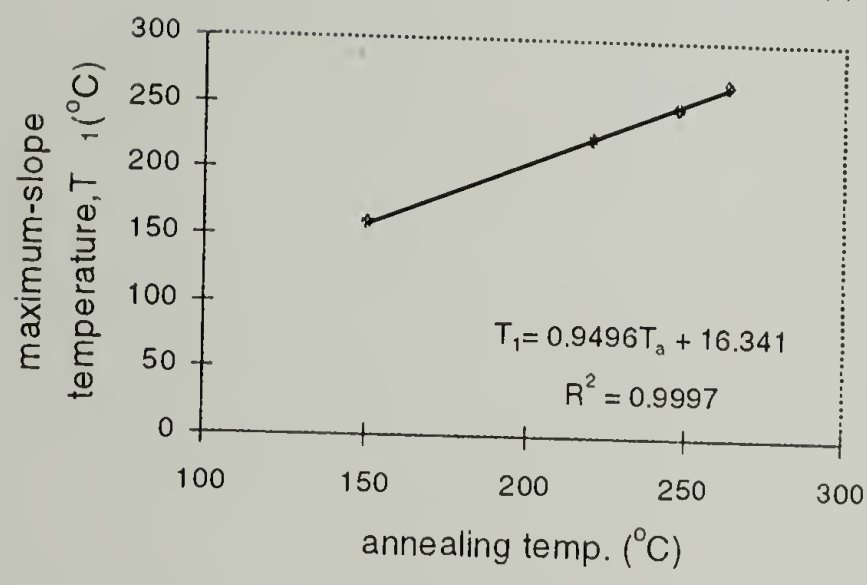

(b)

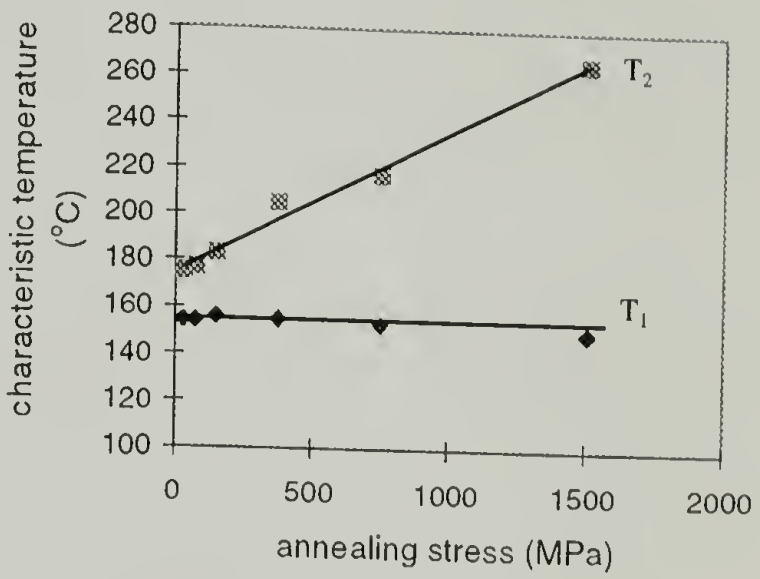

(c)

Figure 5.30 Influence of the stretching temperature and stress on the IFTT behavior of Kevlar® fibers. (a). IFTT curves of fibers being stretched at different temperatures; legends in the plot are stretching temperatures. (b). Correlation between the peak temperature T_1 in IFTT curves and the stretching temperature. (c). Correlation between the characteristic temperature T_2 with the applied stretching stress.

The choice of T_2 is empirical. Intuitively, it was thought that the amplitude of the second peak should be related to the applied tension during the treatment. However, Figure 5.31 shows that the IFTT curve of a heat-stretched fiber relaxes with time. A careful examination identified that T_2, which is the temperature where $(\partial\sigma/\partial T)_1$=0.15MPa/°C, remains unchanged.

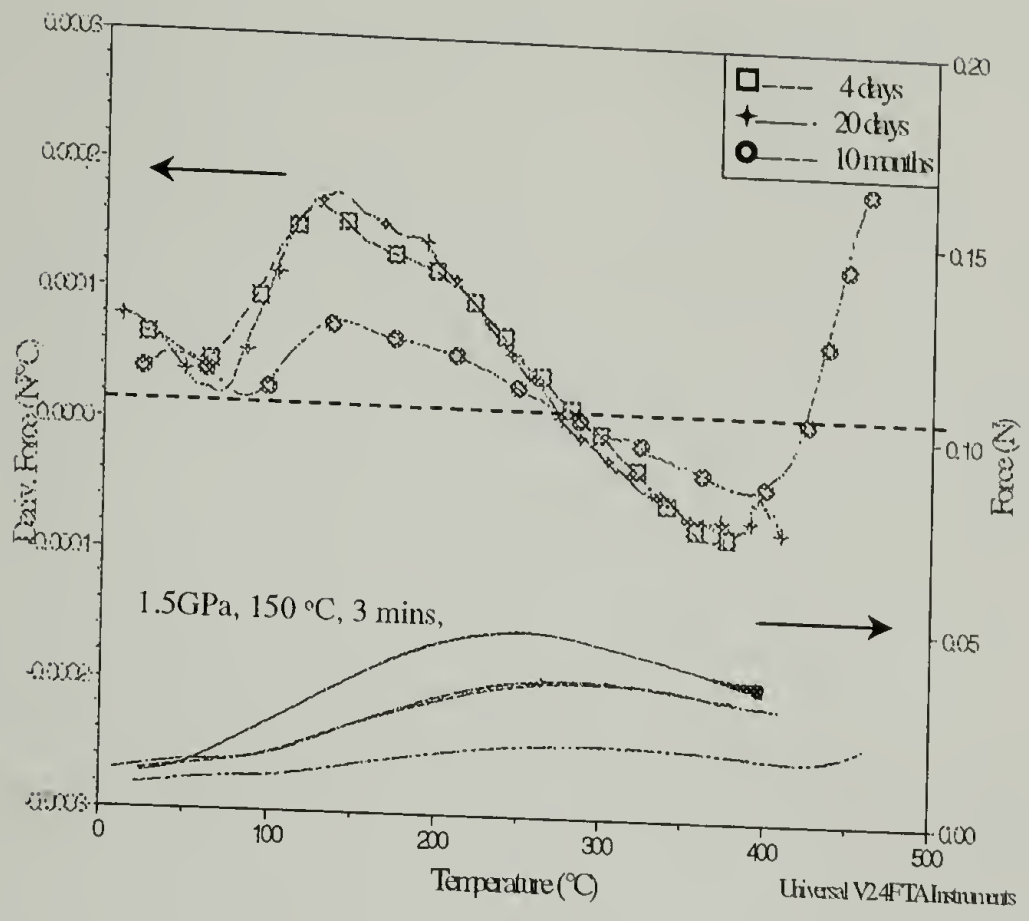

Figure 5.31 Influence of relaxation time in the IFTT behavior of Kevlar® fibers. (a). Fiber being heat-stretched; (b). Fiber being stress-fatigued

This potential correlation of T_2 and the applied stress was also supported by the IFTT study of a fatigued fiber. Fatiguing is just a stretching at room temperature. After the Kevlar® 29 fiber was fatigued, the fiber was tested after different relaxation times. Figure 5.32 is the IFTT curves of a fatigued fiber at different relaxation times. It is seen that the amplitude of the peak dF/dT decreases with the relaxation time, while the T_2 remains unchanged. Thus, the correlation between the T_2 and the stress history is established. This result is not only used in the probing of heat-stretching conditions but also used in the detecting the fatigue damage of fibers discussed in Chapter 3.

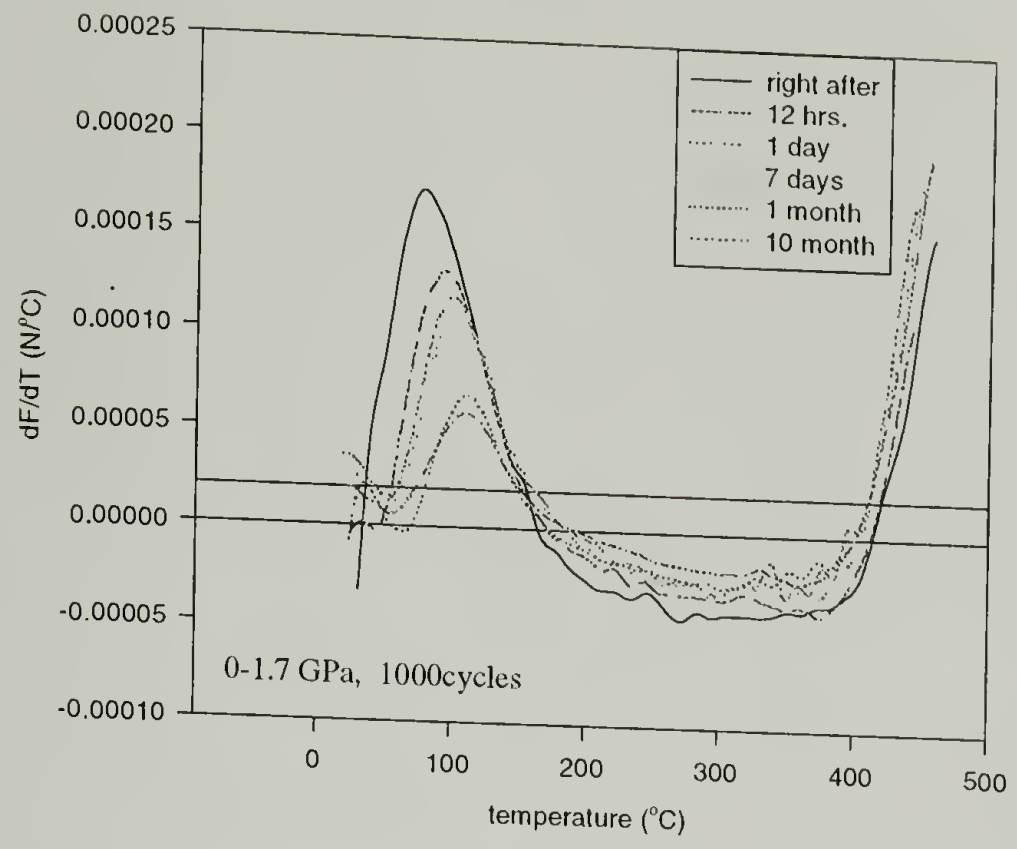

Figure 5.32 Influence of relaxation time in the IFTT behavior of Kevlar® fibers. (a). Fiber being heat-stretched; (b). Fiber being stress-fatigued

5.4.4.1.2 Correlation of IFTT Properties with the Thermal-annealing Condition

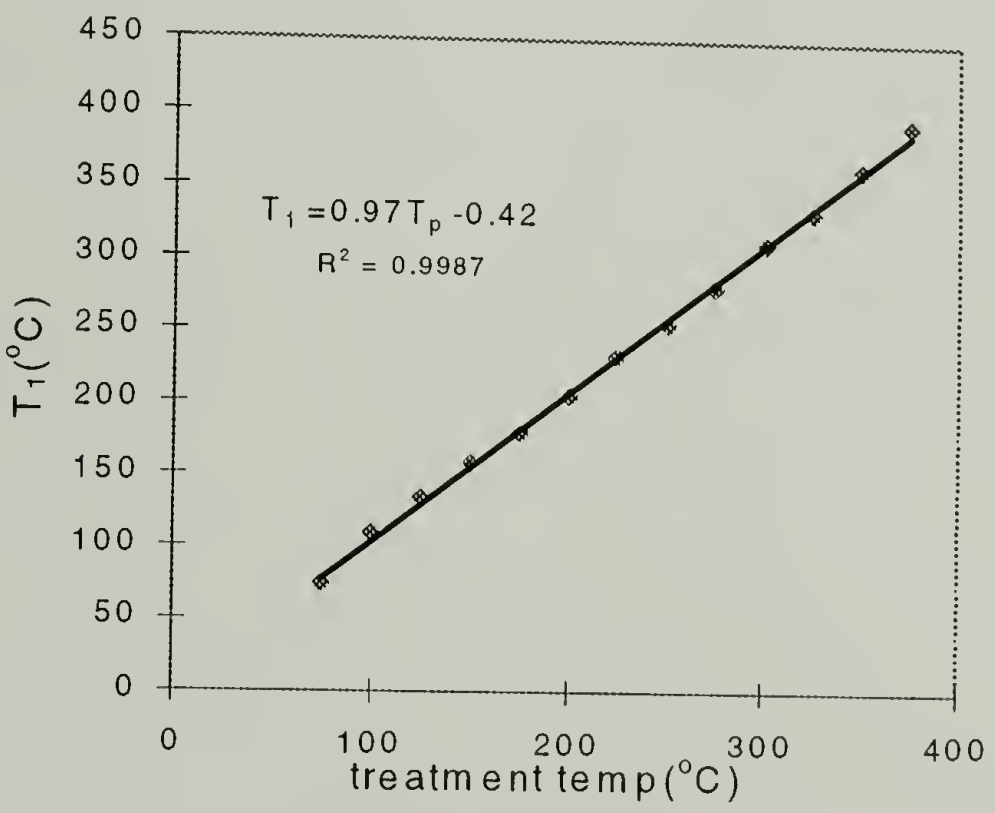

Figure 5.33 Correlation between the peak temperature T_1 in a *IFTT* curve and the free-length annealing temperature T_p

Figure 5.33 illustrates the correlation between thermal annealing condition and the IFTT properties. For free-length annealing, the downward peak temperature in IFTT curve, T_1, equals the annealing temperature T_p.

5.4.4.2 Application of Processing-property Correlation to Probe the Post-treatment Condition of Commercial Kevlar® Fibers

DuPont supplies different types of Kevlar® fibers: Kevlar®29, Kevlar® 49 and Kevlar® 149, just to name a few. These fibers have different properties: different modulus and strength. It is believed that the starting material for the different types of Kevlar® is the same and it is the post-treatment thus yields the different properties. Figure 5.34 illustrates the IFTT behaviors for different types of Kevlar.

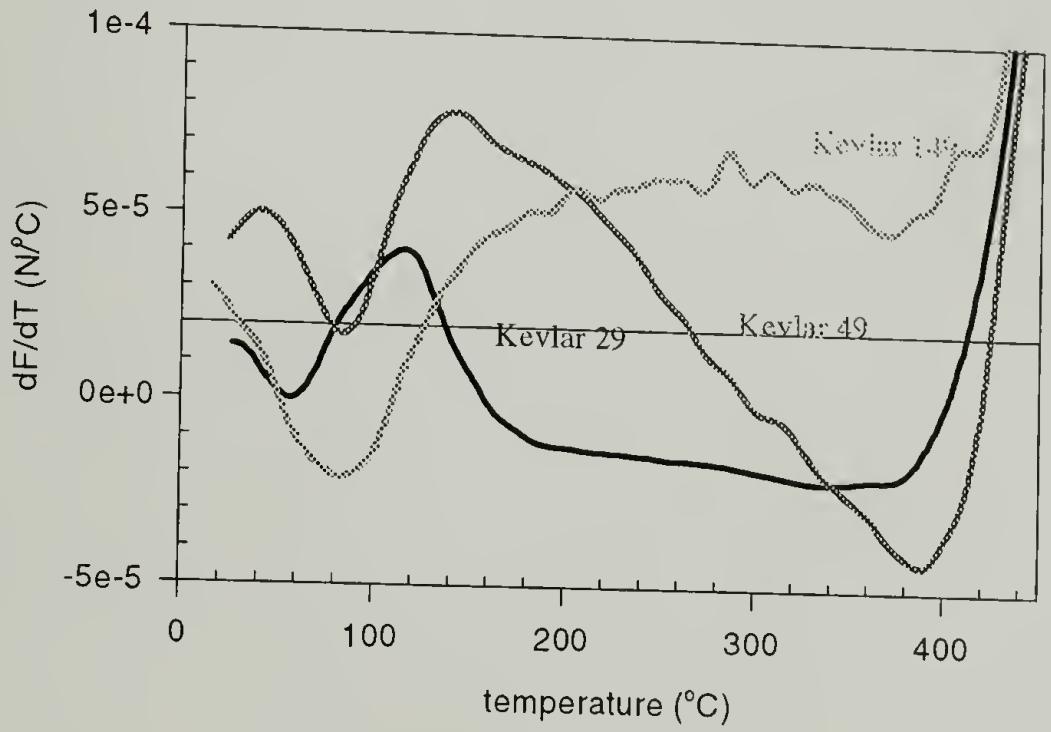

Figure 5.34 *IFTT* curves of various Kevlar® single fibers

Using the correlation that we introduced above, the post-treatment conditions for Kevlar® 49 and Kevlar® 149 were retrieved and are listed in Table 5.1.

Table 5.1 Retrieved processing conditions for Kevlar® 49 and 149 from their IFTT curves

	heat-stretch temperature(oC)	stretching stress(MPa)
Kevlar 49	150	1520
Kevlar 149	370	760

Kevlar® fibers were treated under the conditions in Table 5.1 that were determined by the IFTT. After treatment, the properties of the treated fiber were measured. Table 5.2 compares the properties of the treated Kevlar® 29 fiber, termed Mimic, and those of the commercial fibers. It shows that the mimicking fibers have similar property as the commercial ones.

Table 5.2 Property comparison of commercial fibers and fibers treated using retrieved processing condition

	starting material Kevlar® 29	Kevlar® 49	Mimic-49	Kevlar® 149	Mimic-149
modulus* (GPa)	79	113	116	138	140
strength (GPa)	2.5	2.4	2.39	2.15	2.25
elongation to break(%)	3.1	2.47	2.42	1.5	1.53

*initial modulus in the strain range of 0.05%-0.5%

5.4.4.3 Monitoring the Use of PPTA Fiber at Elevated Temperature

In addition to probing the processing of the PPTA fiber, the IFTT can also be used to monitor the use of PPTA fiber at elevated temperatures.

If the PPTA fiber is exposed to elevated temperature in use, its IFTT behavior changes. The exposure temperature can be found from its IFTT curve. Figure 5.35 shows the change in the IFTT caused by different exposure temperatures.

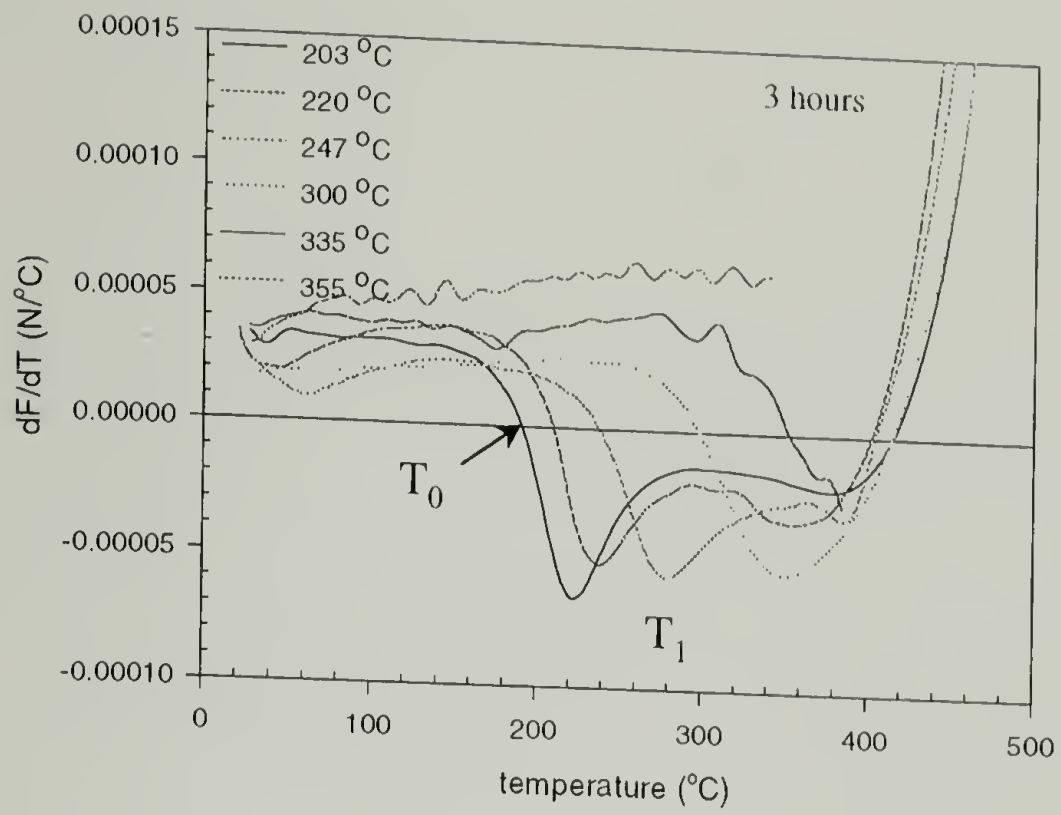

Figure 5.35 IFTT traces of fibers exposed to different temperatures

The IFTT curves are not different from those treated by annealing. The difference is only in the time. It is found that the exposure time affects the corresponding IFTT behavior of the fiber. Although the profile does not change, the characteristic temperature changes with the exposure time. Figure 5.36 shows this change.

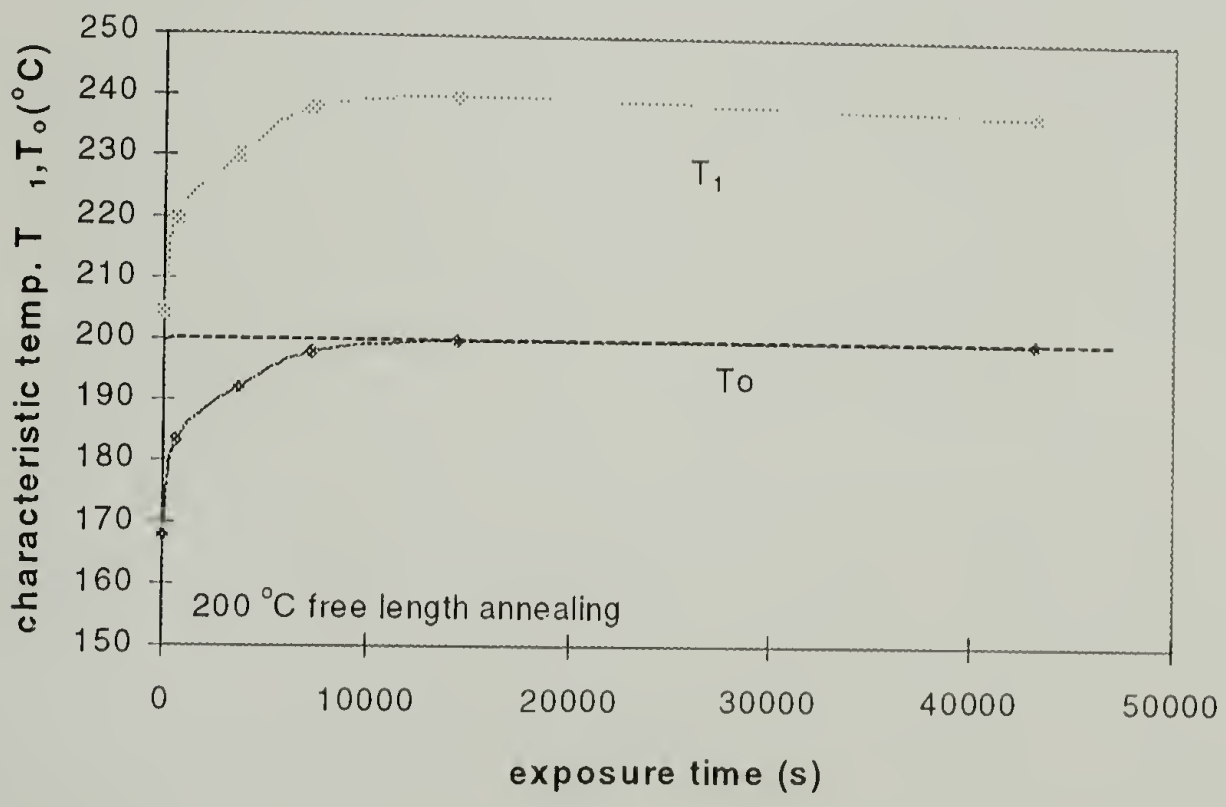

Figure 5.36 Change in characteristic temperatures of IFTT with the exposure time

When the fiber experiences only a short time of the high temperature, T_1, where dF/dT=negative maximum, equals to the exposure temperature. This is exactly the same as in a treatment of annealing. Then as the exposure time increases, T_1 moves to higher temperature, while another temperature T_0, where dF/dT=0 also moves accordingly. After 2.5 hrs of exposure, both temperatures plateau. Figure 5.37 illustrates a good correlation between the exposure temperature and the temperature at $(\partial\sigma/\partial T)=0$ in the IFTT curve. The temperature at $(\partial\sigma/\partial T)_f=0$, T_o, in the *IFTT* curve is equal to the temperature to which the fiber has been exposed to: $T_o=T_e$.

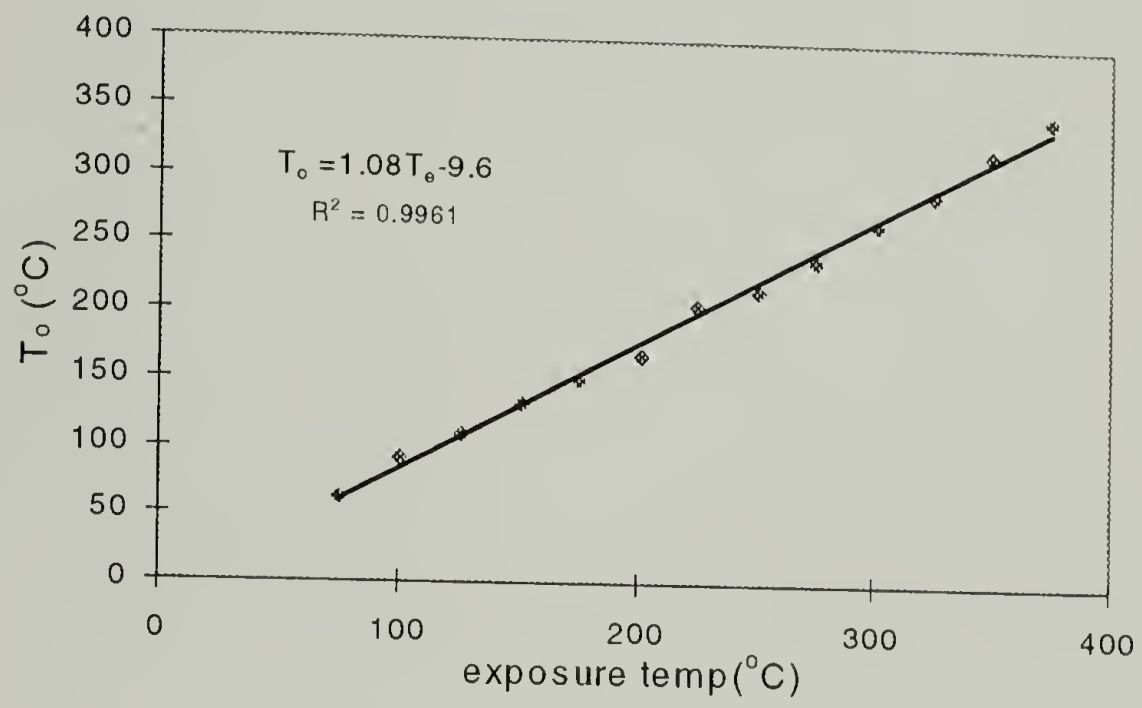

Figure 5.37 Correlation of T_0 in IFTT curve with the maximum exposure temperature T_e that the fiber has seen

5.5 Conclusions

We have demonstrated that the Iso-strain force-temperature test (*IFTT*) is a valuable tool to probe transitions and relaxations, and the thermal and stress history of materials, especially anisotropic material such as fiber and film. The measurement method has a thermodynamic derivation. It is shown that this method has higher sensitivity than some other thermal analysis tools such as DSC and DMTA.

Thermal transitions such as first order crystal-crystal transformation and second-order glass transition in various materials were detected using IFTT.

The thermal and stress history of a material is shown to leave a characteristic signature in its IFTT curve. The investigated materials include: PET in the form of fiber and film; Bisphenol-A PC in the form of film; and Kevlar®,Technora®, Spectra®, Vectran®, and Nylon in the form of fiber.

The IFTT behavior of PPTA fiber was extensively investigated. IFTT curve of PPTA fiber reflects the structure change within the material. It can be used to locate the processing conditions for commercial fibers. It can also be used to monitor the use of the fiber.

A characteristic temperature in *IFTT* can indicate the state of the post-fatigued material and can be used to predict residual material lifetime.

CHAPTER 6

EVOLUTION OF STRUCTURE AND PROPERTIES WITH POST-TREATMENT IN PPTA FIBERS

6.1 Abstract

The evolution of the mechanical properties and structure of PPTA fibers with different post-treatment methods involving heat, tension, hydrostatic pressure, and different environments was systematically investigated. Wide-angle x-ray diffraction measurements reveal that the crystal structure of PPTA fiber is not stable and changes upon post-treatment. The cooperative changes in the modulus and two structure parameters--the misorientation angle and the paracrystalline parameter -- indicate a direct structure-property correlation. After studying free-length annealing and heat-tensioning of fibers, several structure parameters--the *c*-dimension lattice constant, the paracrystalline parameter, the intensity ratio between (110) and (200), and the orientation angle--were found to be affected greatly by the tension applied during heat stretching; while other structure parameters such as the apparent crystal size, equatorial crystallinity and the *a, b* dimensions of the lattice constant are insensitive to the applied tension but determined by the applied temperature and time. A sudden change in the crystal structure at 400 °C suggests an α-relaxation in the crystalline region, which is supported by DMTA and TMA measurements.

Keywords: poly (*p*-phenylene terephthalamide) Kevlar® fibers, structure and properties, wide-angle x-ray diffraction

6.2 Background

Poly(p-phenylene terephthamide) (PPTA) fiber is known to have very high modulus and strength and good thermal stability. [2] The properties of the fiber can be greatly enhanced through post-treatment. In order to achieve better performance, it is important to understand what structure

change is caused by post-treatment and how this structure change relates to the property enhancement. In recent years several studies were made on the structure-property relation. [29,34,41,42] However, no systematic study of the structure change with post-treatment has been reported.

Wu et al [54] studied the crystal structure change of PPTA fiber under annealing temperatures ranged from 380°C to 480°C at either no-tension or constant-tension modes. They proposed a residual-stress free *c*-dimension of a crystal. Then, an increase in the *c*-dimension was observed for all treatments. The higher the tension, the bigger the increment; and the higher the annealing temperature, the smaller the increment. They also discussed the change in the apparent crystal size along the *c*-axis and the degree of orientation. Lee and coworkers did a similar study on the structure and property development of PPTA during heat treatment under tension. [42] They observed a correlation between the modulus and the orientation as well as the pleating. Other structure parameters such as crystal size and paracrystllinity were found to be irrelevant. It was reported that the fiber tenacity does not change much at low and intermediate temperatures for short time annealing but drops when the temperature exceeds 450°C and degradation occurs. [32] Several hours' exposure to high temperature deteriorates the strength but does not affect the modulus much. [55] The crystallites were found to grow laterally along the *b*-axis upon thermal annealing. [56]

Different researchers have focused exclusively on certain structure parameters, narrow range of treatment temperature or specific experimental methods in their study of the structure change upon post-treatment. In this paper, the change in the properties and structure of PPTA fibers were studied over a wide range of temperature from 180 °C to 500 °C. In addition, different post-treatment conditions including tension, hydrostatic pressure with inert gas or water were utilized. Then all relative structure parameters were investigated. Our experiments disclose the instability of the crystal structure of PPTA and an α-relaxation around 400 °C in the crystalline

region. Our results strongly indicate the modulus of the fiber is determined by the combination of the orientation and the paracrystalline parameter.

6.3 Experimental

Five different post-treatment methods were used to alter the properties and structure of the fiber:

Free length annealing where loose fiber yarns were placed inside a glass container and put in an oven with a nitrogen purge at a fixed temperature.

Tensioning annealing where fiber yarns were put through a home-made heat-treatment apparatus where a dead weight was used for constant tension with a controlled heating time.

Pressure-tensioning annealing where fiber yarns were sealed in the same home-made heat-treatment apparatus and pretension was controlled by a tension-control device with silicon oil as the pressurizing agent.

Pressured steam annealing where fiber yarns were put in a heatable high pressure vessel and where water was injected to achieve saturated water/steam at the heat treatment temperature.

Pressure annealing where a P-V-T rig was used to hold the sample and mercury was used as the pressurizing agent. The conditions explored are listed in the following table:

Table 6.1 Post treatment conditions for PPTA fibers

	Temperature (°C)	Time (Mins.)	Tension (MPa)	Hydrostatic pressure (MPa)	Media
Free Length Annealing	varied 180 °C-500 °C	180	0	0	N_2
Tensioning Annealing	varied 180 °C-370 °C	3	varied	0	N_2
Pressure Tensioning Annealing	250 °C,	1.5	800	90	silicon oil
Pressure Steam Annealing	varied 100 °C-300 °C	120	0	saturated steam	H_2O
Pressure Annealing	260 °C	240	0	130	mercury

The methods of evaluating property and structure were described in detail in Chapter 7. To gain better statistics, yarn tests were conducted. Single filament tests were used only when yarn samples were not available. At least three samples were tested for each condition. The mechanical properties were measured by an Instron® and MTS® tester. The initial modulus, which is the modulus in the strain range of 0.1%-0.5%, the strength and the break strain were recorded. The structure was characterized using wide-angle X-ray diffraction. The structure parameters investigated include lattice constants, *a, b, c*; paracrystalline parameter, g_{II}; equatorial x-ray diffraction crystallinity, *X*; intensity ratio, I_{110}/I_{200}; different apparent crystal sizes (*ACS*) of planes (*00l*), (110) and (200); and the (200) orientation angle, $\phi_{200,x}$. A Simens® D500 diffractometer, Simens® two-dimensional area detector and Statton® Camera were used.

The following table lists the statistics of different measurements for structure characterization and error bars will not be included in the section on results and discussion.

Table 6.2 Statistics in structure measurements

	Lattice Constant Å	Paracrystalline parameter g_{II},%	Equatorial crystallinity *X*, %	Intensity ratio I_{110}/I_{200}
standard deviation*	0.003	0.04	4	0.03
	Apparent crystal size (110),(200) nm	(*00l*), nm	(200) orientation angle, degrees	
standard deviation*	0.2	7	0.3	

* listed numbers are the maximum standard deviation in the measurement of different samples

Dupont TMA 2950 and Rheometric Mark IV DMTA were used for thermo-mechanical measurements.

6.4 Results and Discussion

Table 6.3 summaries the properties and structure parameters of the post-treated fibers.

Table 6.3 Datasheet for the annealing of Kevlar® fiber

Treatment condition			Property			Structure									
Temp. (°C)	Tension (GPa)	Condition	Modulus (GPa)	Tenacity (GPa)	strain to break (%)	Lattice Constant a, Å	b, Å	c, Å	g_{II}[1] (%)	X[2] (%)	I_{110}/I_{200}[3]	Apparent crystal size (002) nm	(110) nm	(200) nm	$\phi_{200,x}$ °
Free-length annealing															
Kevlar 29 as spun			78	2.58	3.1	7.75	5.23	12.838	1.92	76	0.70	656	52	46	12.2
180	0	N_2	78	2.28	3.1	7.81	5.23	12.838	1.81	75	0.69	735	61	48	12.8
200	0		78	2.2	3.1	7.81	5.23	12.838	1.78	77	0.67	734	63	48	13.0
250	0		77	1.68	2.4	7.84	5.22	12.836	1.72	72	0.67	920	71	52	13.6
300	0	2hrs.	78	1.55	2.2	7.86	5.21	12.840	1.68	74	0.66	800	77	54	13.1
300	0		75	1.65	2.3	7.87	5.22	12.852	1.74	77	0.65	815	80	56	14.0
350	0		71	1.2	2.11	7.86	5.21	12.852	1.70	74	0.67	820	84	59	14.7
350	0	10hrs	76	1.1	2	7.96	5.20	12.854	1.70	76	0.73	500	85	61	14.3
400	0		56	0.54	0.9	7.87	5.20	12.824	1.91	74	0.77	418	90	63	15.0
450	0	15min.	66	0.83	1.55	7.87	5.20	12.830	1.99	72	0.75	400	82	60	14.6
450	0	30min.	61	0.4	0.92	7.87	5.18	12.830	1.80	70	0.75	321	85	62	15.8
450	0	45min.	60	0.21	0.6	7.85	5.19	12.800	1.89	70	0.75	221	86	62	15.1
450	0		40	0.1	0.5	7.85	5.18	12.718	2.13	60	0.75	154	86	62	20.9
500	0	10hrs	42	0.05	0.2	7.88	5.19	12.740	2.38	41	0.87	150	93	68	21.0
Kevlar 119 as spun			61	2.96	4.10	7.75	5.22	12.820	1.91	75	0.74	609	50	45	16.2
450	0	15min.	55	0.87	1.58	7.87	5.19	12.820	1.88	75	0.66	650	91	66	17.7
450	0	30min.	49	0.48	0.8	7.87	5.19	12.820	1.94	75	0.70	735	61	66	18.0
450	0	45min.	50	0.21	0.4	7.87	5.19	12.820	2.06	75	0.72	450	92	67	18.1
Kevlar 49 as spun			113	2.40	2.47	7.78	5.23	12.880	1.66	77	0.61	737	66	51	6.8
450	0	30min.	90	0.82	0.9	7.88	5.19	12.870	1.75	69	0.68	700	95	67	9.8
Kevlar 149 as spun			138	2.15	1.50	7.90	5.19	12.920	1.40	77	0.60	1548	123	76	6.4
450	0	15min.	120	0.24	0.2	7.87	5.18	12.910	1.50	99	0.63	1500	125	80	7.2
Kevlar 29, heat tension															
180	0.92	3min	105	2.45	2.5	7.81	5.23	12.880	1.65	77	0.56	700	64	50	8.2
180	1.2	3min	108	2.4	2.4	7.81	5.23	12.880	1.60	77	0.52	658	65	50	
180	1.5	3mins	116	2.39	2.42	7.81	5.23	12.888	1.55	77	0.48	730	65	50	6.9
230	1.2	3min	110	2.38	2.44	7.84	5.22	12.890	1.57	77	0.51	800	75	53	8.7
230	1.5	1.5min	113	2.38	2.2	7.84	5.22	12.880	1.68	77	0.48	850	75	53	7.2
370	0.76	1min	140	2.25	1.53										
Kevlar 29, pressure-heat-tension															
250	<0.8 1min.	90MPa, SiO_2	80	2.5	2.9	7.75	5.23	12.852	1.87	72	0.65	1800	57	50	10.7
260	0	130MPa Hg	101	0.25	0.3	7.77	5.22	12.846	1.99	80	0.71	1800	79	62	8.2
Kevlar 29, pressurized steam															
100	0	0.1MPa	78	2.2	2.4	7.75	5.23	12.838	1.93	77	0.70	658	55	48	12.2
204	0	1.1MPa	78	1.85	2.05	7.75	5.23	12.838	1.95	75	0.74	1500	61	45	11.9
300	0	9.8MPa	92	1.75	2.1	7.75	5.23	12.838	2.04	71	0.67	600	64	51	11.3

treatment time unless otherwise noted: 3 hrs.

[1]: paracrystalline parameter; [2]: equatorial crystallinity

[3]:intensity ratio of two diffraction peaks

6.4.1 Free-length Annealing

6.4.1.1 Mechanical Properties

Upon free length annealing, the modulus of Kevlar® 29 fiber decreases slightly with the annealing temperature until 400 °C and then drops rapidly as shown by Figure 6.1. The strength of the fiber starts to deteriorate rapidly when the annealing temperature is higher than 250 °C. After being annealed at 450 °C for 30 minutes, the modulus drops by 46% and the strength decreases by 80%. The color of the fiber also becomes darker when the annealing temperature is above 400 °C. This result is similar to the annealing study on Kevlar® 49 observed by Hindeleh [29].

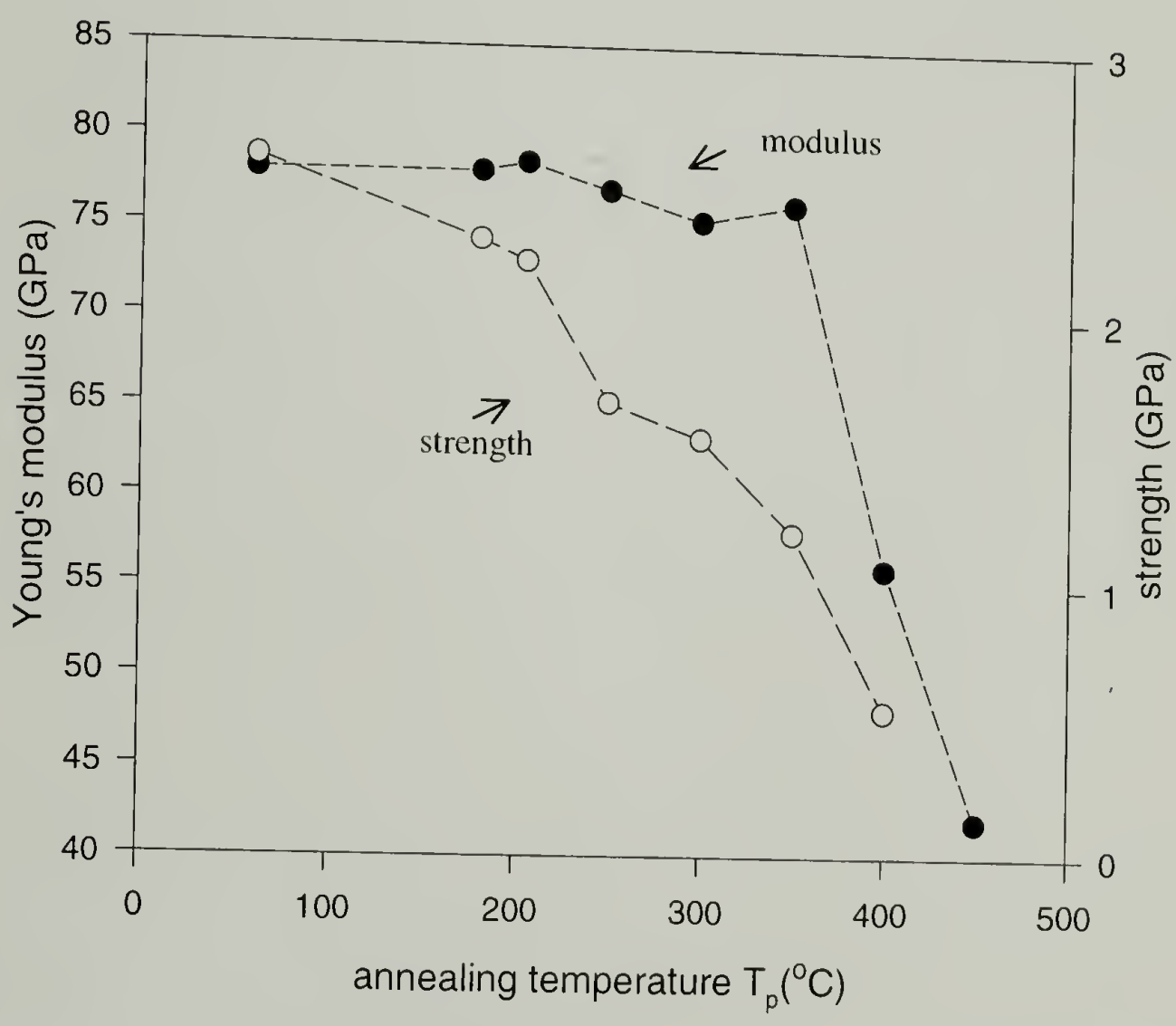

Figure 6.1 Properties of the fiber under different annealing temperatures in free-length annealing; close circles are modulus and open circles are strength

6.4.1.2 Lattice Parameters

A typical diffraction pattern of Kevlar® fiber is shown in Figure 6.2. Its corresponding meridional and equatorial scans are shown in Figure 6.3.

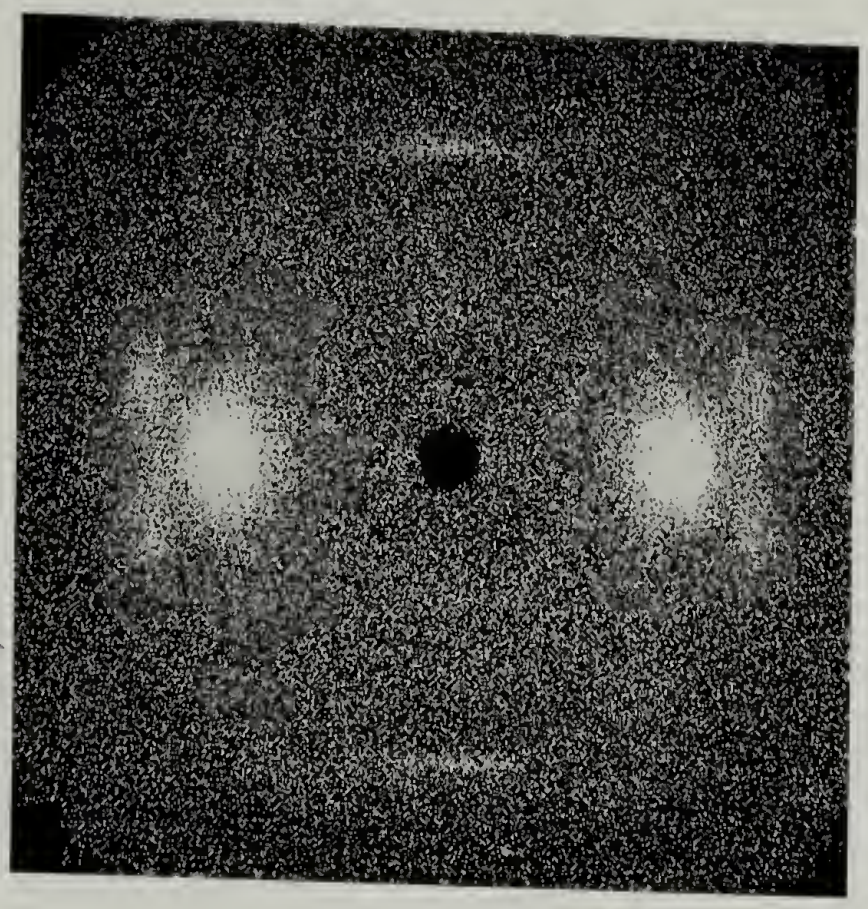

Figure 6.2 WAXD pattern of Kevlar® 29 fiber

The lattice constants of PPTA crystal have been carefully examined by wide angle x-ray diffraction. The high orientation of PPTA fiber makes the measurement of the lattice *c*-dimension difficult. The sample was titled at certain angle to allow the *c*-axis to intercept with the Ewald sphere. The c-dimension was calculated from the regression of 3 orders of meridional diffraction as illustrated in Figure 6.4. It was found that the *c*-dimension of PPTA crystal changes upon annealing. Figure 6.5 shows that the *c*-dimension is relatively constant when the annealing temperature is lower than 250 °C. Then the *c*-dimension increases with the annealing temperature until 350 °C and decreases rapidly afterwards. This data suggests that the crystal structure of PPTA is not thermally stable. This is not difficult to understand. Because PPTA is a lytropic liquid crystalline polymer, the ordered structure can be formed in the liquid crystal state. This ordered structure is probably frozen via coagulation and is not an equilibrium state.

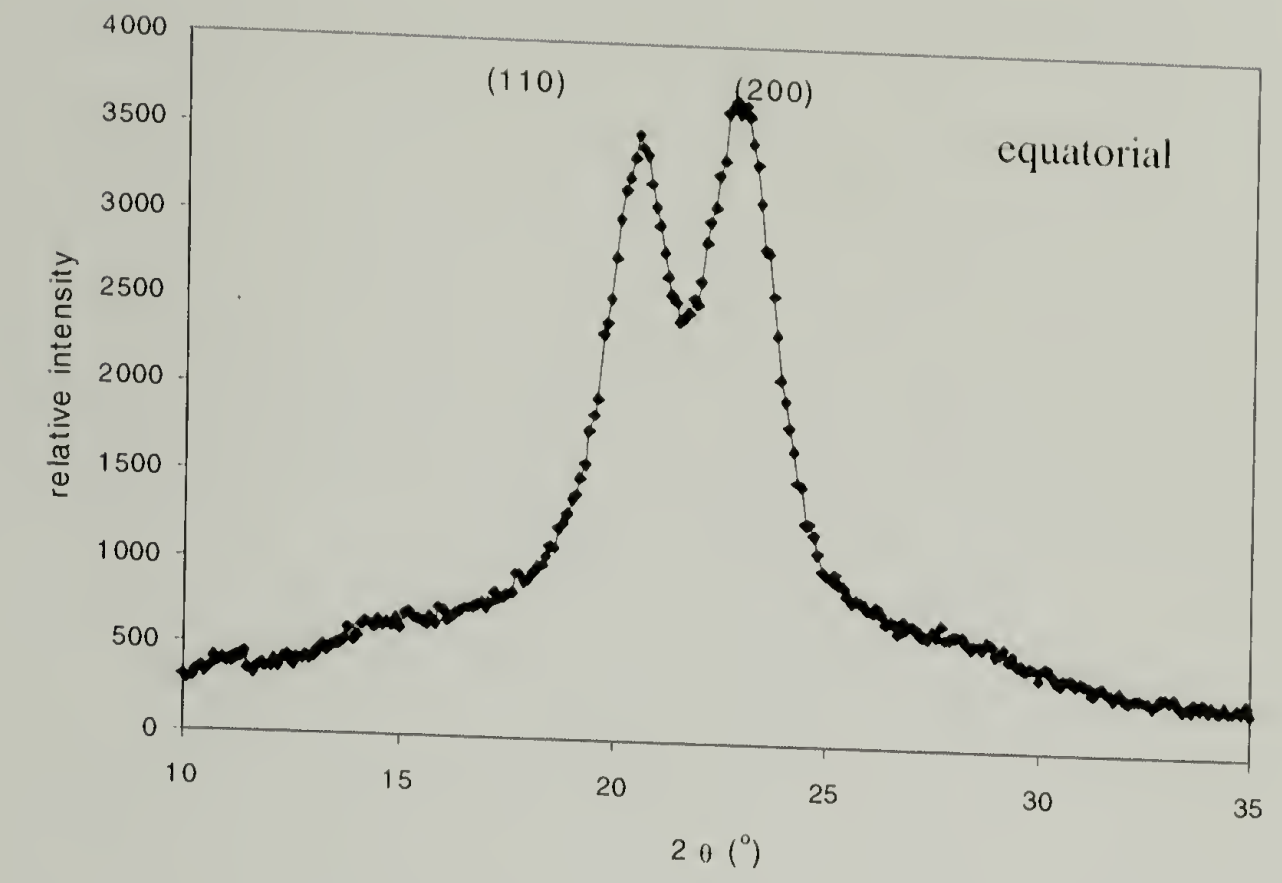

(a)

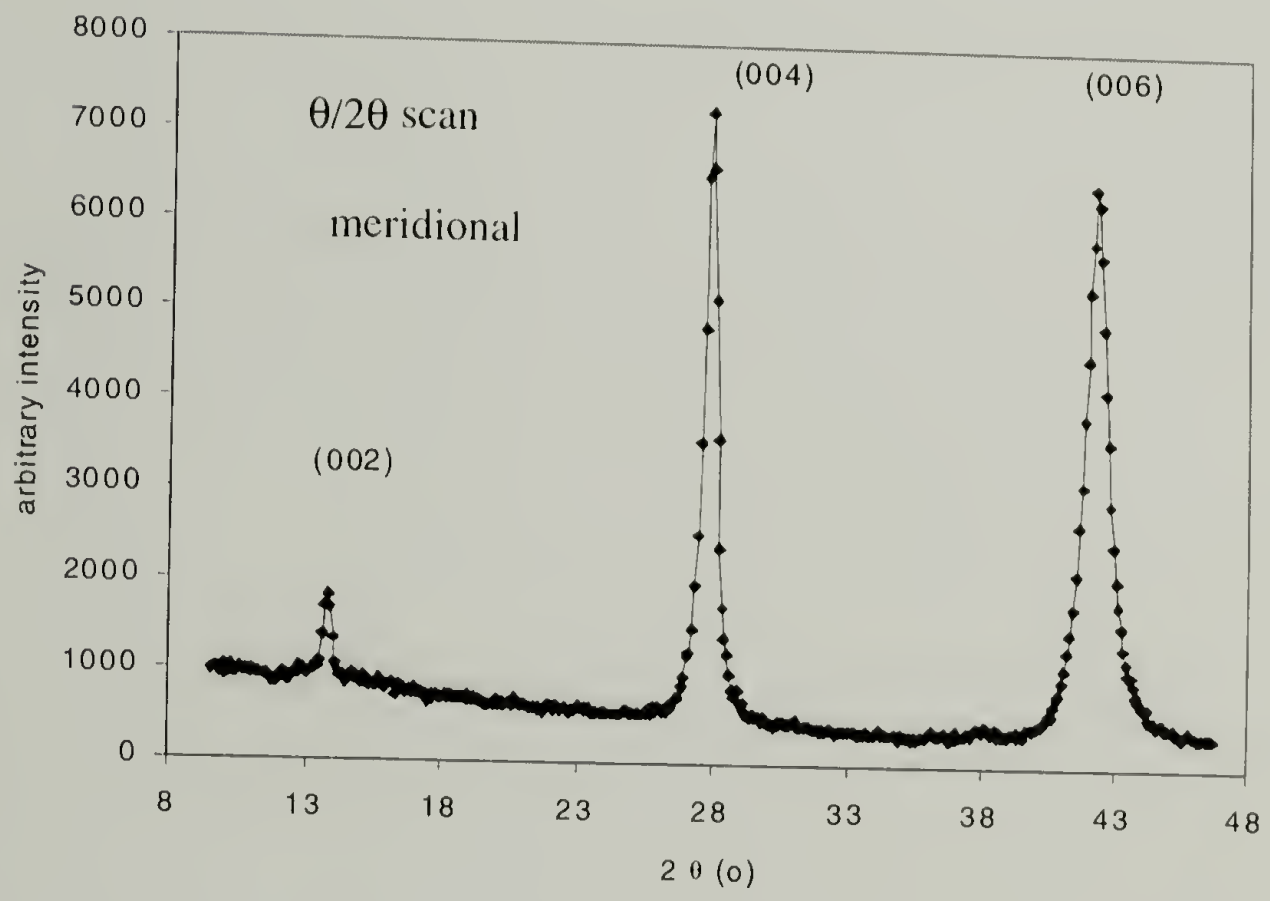

(b)

Figure 6.3 Typical diffraction scans for Kevlar® fiber; (a) equatorial scan, (b) meridional scan

Therefore any post-treatment serves as an evolution in the crystal's metastable state. As the strong intramolecular interaction overcomes the weaker intermolecular forces, namely

hydrogen bonding and van der Waals interactions in the case of PPTA, the polymer crystal is rearranged. The external force is applied directly to the chain and the crystal dimension is changed due to the deformation of a single chain.

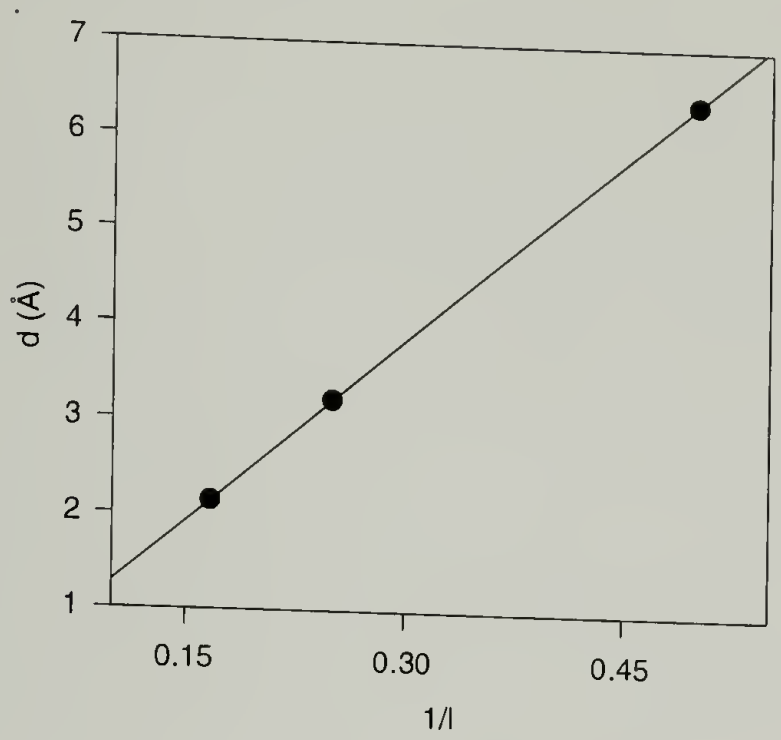

Figure 6.4 Calculation of *c* from several orders of meridional diffraction

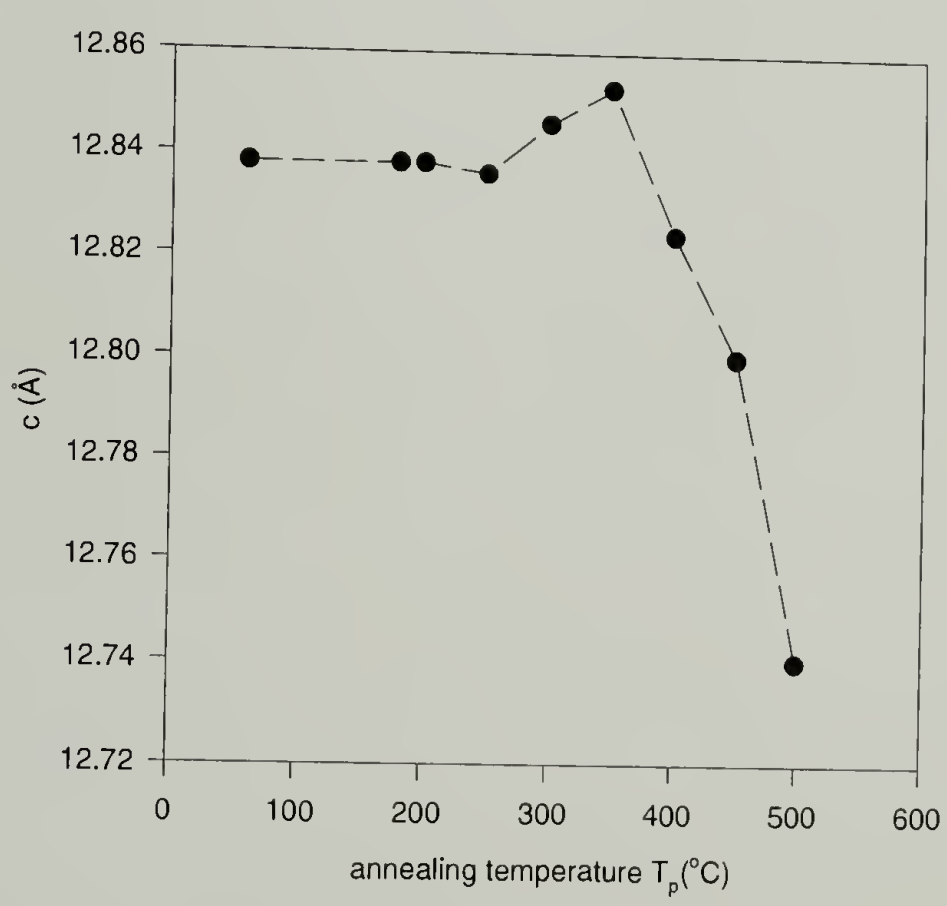

Figure 6.5 Change of the lattice *c*-dimension with the annealing temperature in the study of free-length annealing

This structure instability was also observed by Haraguchi and coworkers in their study on the PPTA film. [170] Haraguchi attributed that instability to the metastable crystal form II of PPTA film made by coagulating with water. Our study shows that the instability of PPTA crystals is more general. A thermal expansion experiment was conducted in order to compare the microscopic permanent deformation with the macroscopic deformation.

Figure 6.6 is the thermal expansion curve of Kevlar® 29 as spun fiber. There is a strong resemblance between the change of *c*-dimension measured by x-ray diffraction and the thermal expansion coefficient with annealing temperature. Therefore, the change in thermal expansion coefficient α represents the structural change in the material due to high temperature annealing.

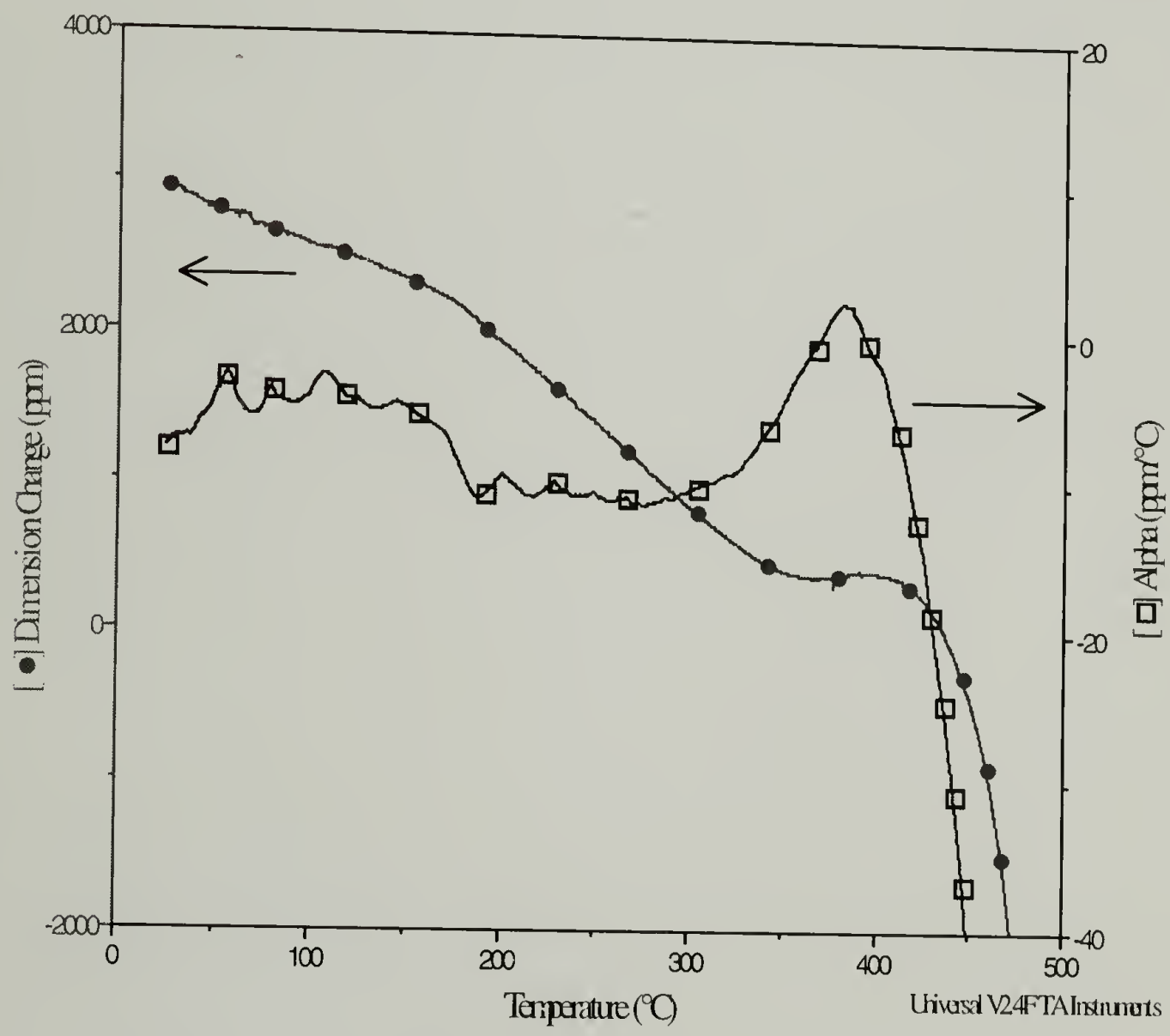

Figure 6.6 Dimension change of Kevlar® 29 as spun fiber upon heating; close symbols are dimension and open symbols are linear thermal expansion coefficient α; heating rate: 10 °C/min

There are also slight changes in the *a*-, *b*- lattice dimensions. Figure 6.11(c) reveals that the *a*-dimension increases with annealing temperature while *b*-dimension decreases. The change in crystal structure when the annealing temperature lower than 350 °C can be represented by Figure 6.7. In a PPTA crystal, hydrogen bonding is along *b*-direction and van del Waals force along *a*-direction. There is water bound to the polymer chain through hydrogen bonding when the fiber is coagulated. Upon heating, this bound water is removed and gives mobility to the chains to form new hydrogen bonds. Therefore, the *b*-dimension is shortened.

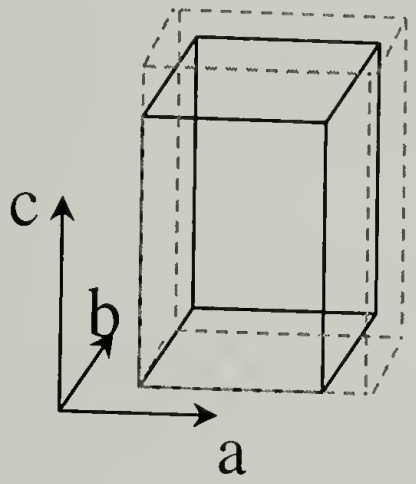

Figure 6.7 Change of the unit cell upon annealing; solid line: as spun and dash line: annealed

6.4.1.3 Paracrystalline Structure

The imperfection of PPTA crystal is found to be described by the paracrystal.[33-35] The concept of paracrystallinity was first introduced by Hosemann.[166] Three parameters of the dimension of the unit cell, the electron-density distribution within the cell and the crystal size can characterize an ideal crystal. If the dimension of the unit cell and the electron-density distribution vary statistically from cell to cell, a paracrystallinity measure is needed. As in PPTA fiber, a conformational distribution can cause the paracrystallinity. Therefore, the information of paracrystalline structure will be very helpful in understanding the deformation mechanism under

different loading modes. The broadening effect in a paracrystal can be described by the following equation:

$$(\delta_s)_0^2 = (\delta s)_c^2 + (\delta s)_{II}^2 = \frac{1}{\bar{L}_{hkl}^2} + \frac{(\pi g_{II})^4 n^4}{d_{hkl}^2}$$

in which δ_s is the broadening of the diffraction peak, L is the crystal size, g_{II} is the paracrystalline parameter, n is the order of the diffraction peak, d_{hkl} is the dimension of the first order diffraction palne

A typical plot between the peak width and the diffraction order for PPTA crystal is shown in Figure 6.8 and its paracrystalline parameter g_{II} can be calculated accordingly. The paracrystalline parameter of PPTA fiber was found to change with the annealing temperature as shown in Figure 6.9. The paracrystalline parameter first decreases with the annealing temperature and increases rapidly when the annealing temperature is higher than 350 °C. Figure 6.9 also shows that the intensity ratio of the diffraction peak of (110) to (200) changes in the same way as the paracrystalline parameter. The I_{110}/I_{200} was shown to be an important structure aspect in studying the structure change due to water desorption, although the nature of this ratio remains unclear. [59] Both Figure 6.5 and Figure 6.9 show two transitions at 250 °C and 350 °C respectively. This tells us that several structure parameters--the lattice *c*-dimension, the paracrystalline parameter and the intensity ratio of I_{110}/I_{200}--undergo a cooperative change when the material is annealed. The analysis of the change of these three parameters yields a nonlinear chain model to describe the paracrystal in PPTA. (See Chapter 7) Upon heating, the molecular chain tends to move to a more extended conformation, which may involve the transformation of *gauche* to *trans* conformation. Then when the temperature reaches 350 °C, there is a sudden contraction of the chain causing a rapid decrease in the lattice *c*-dimension. In addition, these structure changes are frozen by cooling because of the long relaxation time.

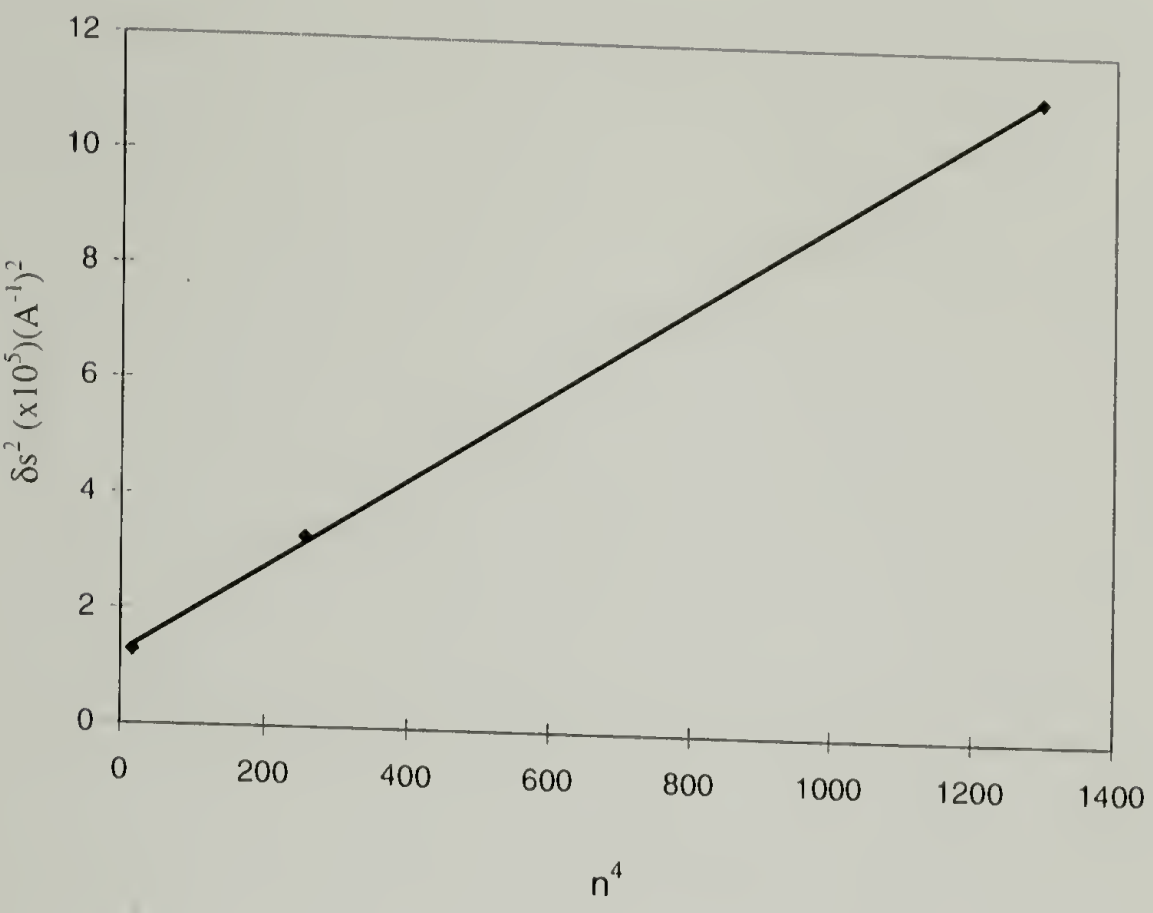

Figure 6.8 The Square of the peak breadth vs. the 4th power of the reflection order describing paracrystalline disorder in Kevlar® 29

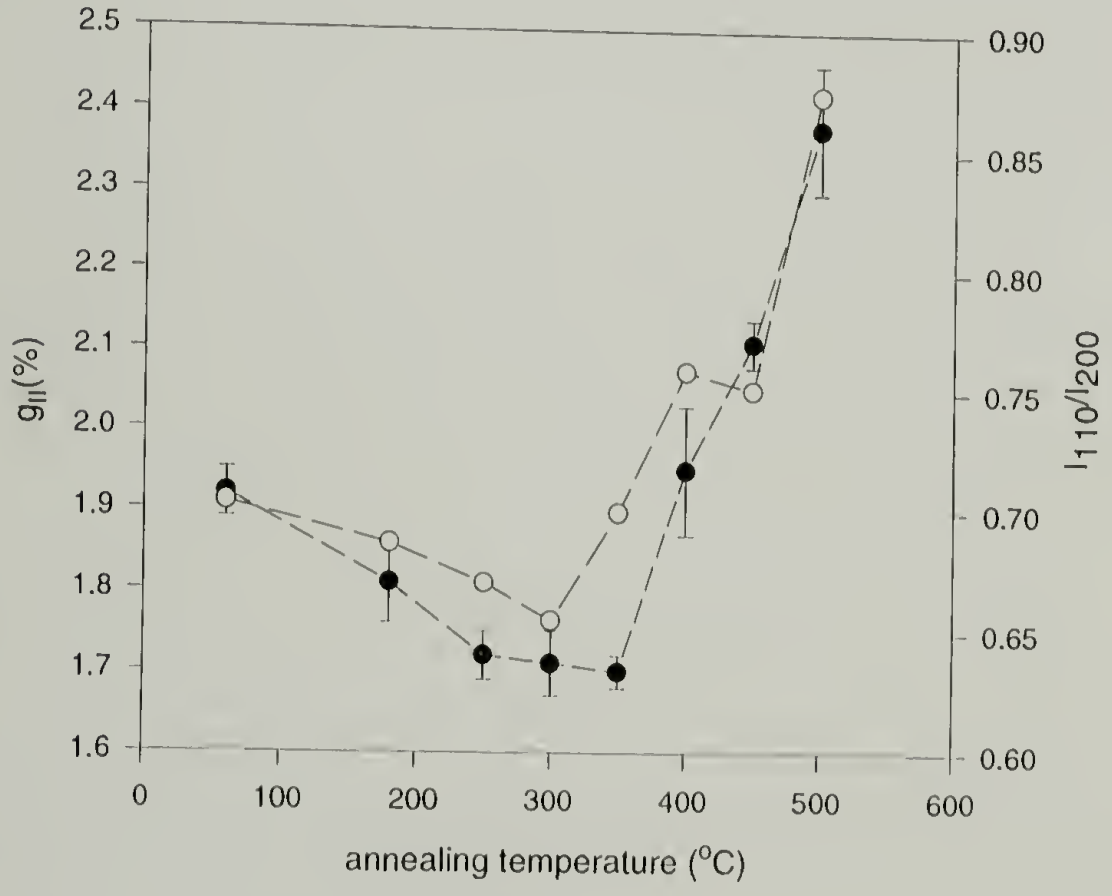

Figure 6.9 Paracrystalline parameter g_{II} and intensity ratio I_{110}/I_{200} under different annealing temperatures in the study of free-length annealing; close circles are g_{II} and open circles are I_{110}/I_{200}

The thermal study of PPTA fiber is difficult to conduct and rare. Hindeleh and Abdo concluded that PPTA has a glass transition at 370 °C from a DTA trace. [29] Our result suggests that the structure of PPTA gains certain mobility around 350 °C. The big change in the crystal structure at 350 °C indicates that the local rearrangement happens within or on the surface of the crystalline region. The transition at 350 °C may be attributed to an α-relaxation in the crystalline region and the transition at about 200 °C is a β-relaxation in the crystalline region. It is possible that the mobility is enhanced by the relaxation in the amorphous phase, if there is such content existing in the PPTA. To further study the relaxations in PPTA fiber, DMTA measurements were performed. Figure 6.10 is a DMTA spectrum of a Kevlar® 29 as spun single filament. Three peaks appear in its tanδ trace. The first peak associates with the removal of water from the intercrystalline region where the crystal structure remains unchanged. The second and third peaks correspond well to the transitions observed by x-ray diffraction.

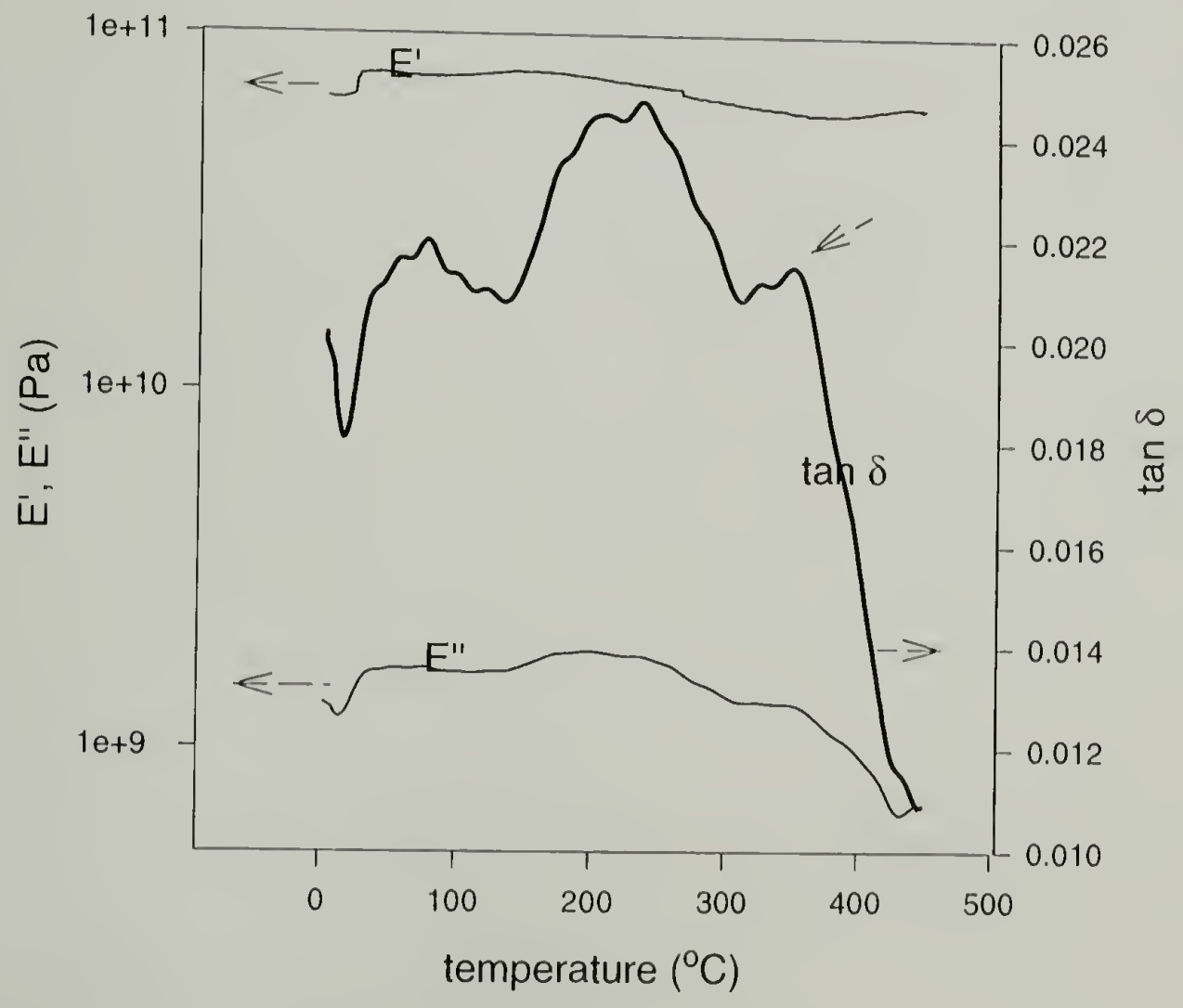

Figure 6.10 DMTA spectrum of Kevlar® 29 as spun fiber; heating rate: 5 °C/min

6.4.1.4 Apparent crystal sizes (ACS)

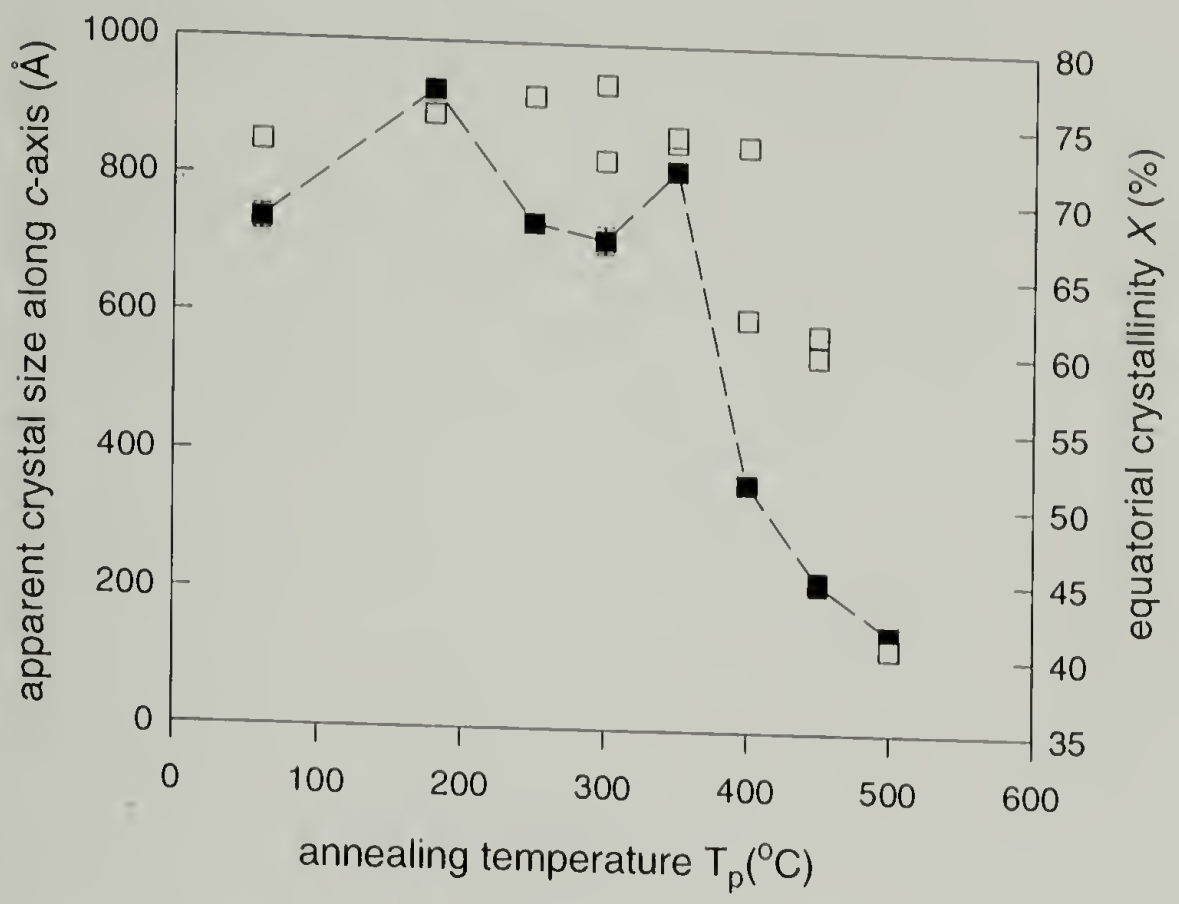

Figure 6.11 Change of the transverse structure of the crystal in Kevlar® 29 fiber with the annealing temperature in free-length annealing; in Plot (a), close symbols are the apparent crystal size along c-axis and open symbols are equatorial crystallinity *X*; (b) transverse apparent crystal sizes; (c) transverse lattice constants

Heat annealing can largely change crystal sizes. Figure 6.11(b) shows that the apparent crystal sizes of (110) and (200) increase monotonically with the annealing temperature. The apparent crystal size of (110) increases faster than (200). This was also observed by other researches. [29,50,59] However, Hindeleh and Abdo reported that the transverse apparent crystal sizes decrease when the annealing temperature is higher than 400 °C. Figure 6.11(a) shows that the apparent crystal size along *c*-axis does not change with the annealing temperature until 350 °C after which the apparent crystal size along c-axis starts to decrease. Figure 6.11(a) also includes the effect of the annealing temperature on equatorial crystallinity. The change in the equatorial crystallinity with the annealing temperature is similar to the change in the apparent crystal size along c-axis.

6.4.1.5 Orientation

When the modulus change due to free-length annealing is compared with the structure changes discussed, there is no good correlation. The reason is because of another important structure parameter in PPTA fiber: misorientation of the crystals. It is found that there is a loss of orientation when the annealing temperature increases and the orientation of the crystals deteriorates after 400 °C as shown in Figure 6.12. The modulus of the fiber is shown to be determined mainly by the misorientation of the crystals. Meanwhile, a careful analysis suggests that paracrystalline structure also contributes to the modulus of the fiber. The modulus of the fiber can be calculated from the orientation angle and the paracrystalline parameter of the crystals, as shown in Chapter 7.

The free-length annealing at 450 °C of other commercial Kevlar® fibers, Kevlar® 119, Kevlar® 49 and Kevlar® 149, were also performed. Table 6.3 shows that all different fibers have the same transverse lattice constants and apparent crystal sizes after annealing. Their orientation angle and paracrystalline parameter increase but are not the same after annealing.

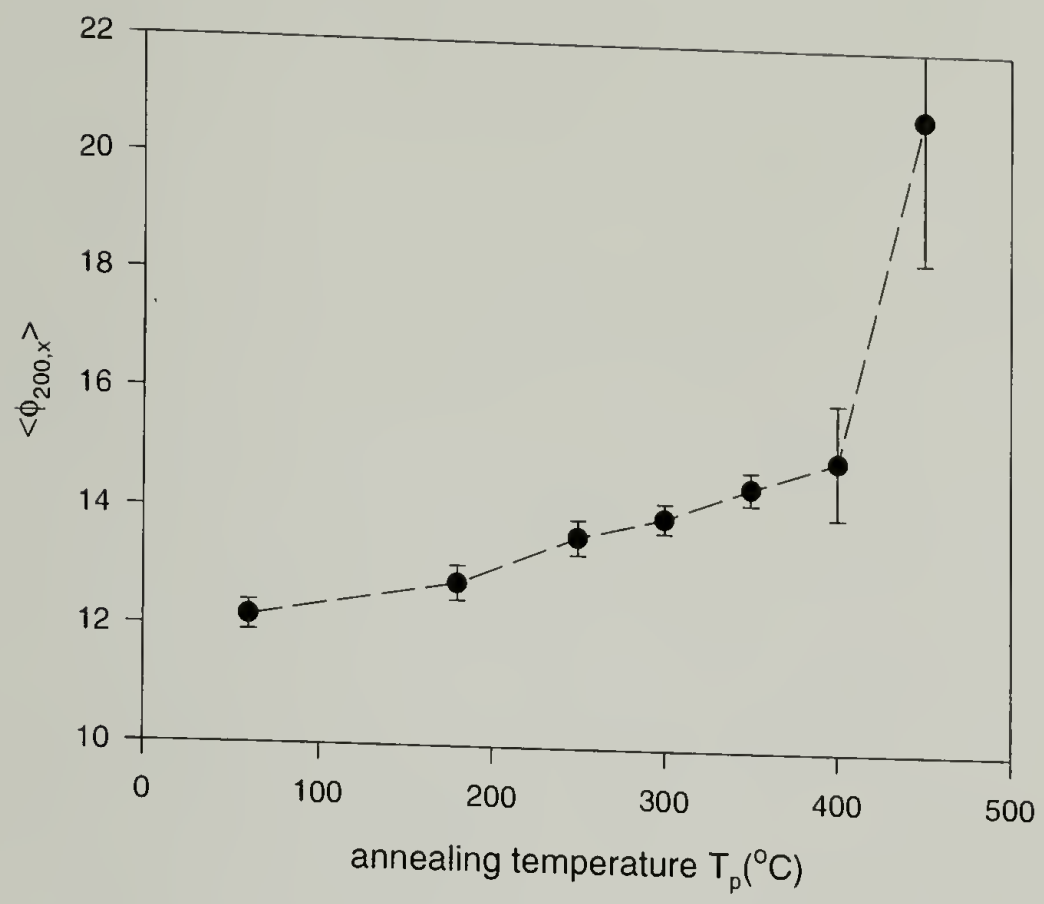

Figure 6.12 Orientation angle $\phi_{200,x}$ under different annealing temperatures in free-length annealing

6.4.2 Tensioning Annealing

It is well known that PPTA fibers can be heat-treated under tension to improve the modulus. It is important to understand the structure change during this process.

6.4.2.1 Mechanical Properties

It is illustrated in Figure 6.13 that the modulus of the fiber can be greatly enhanced by the heat tensioning while its strength remains relatively unchanged. By applying a tension of 60% of its strength at elevated temperature, the modulus of the fiber can be increased by 50%. The increase in the modulus is almost linear with the applied tension for a constant stretching temperature. The applied temperature does not have a strong effect on the increase in the modulus when the temperature is low. However, the modulus is doubled when the fiber was treated at a much higher temperature (370 °C).

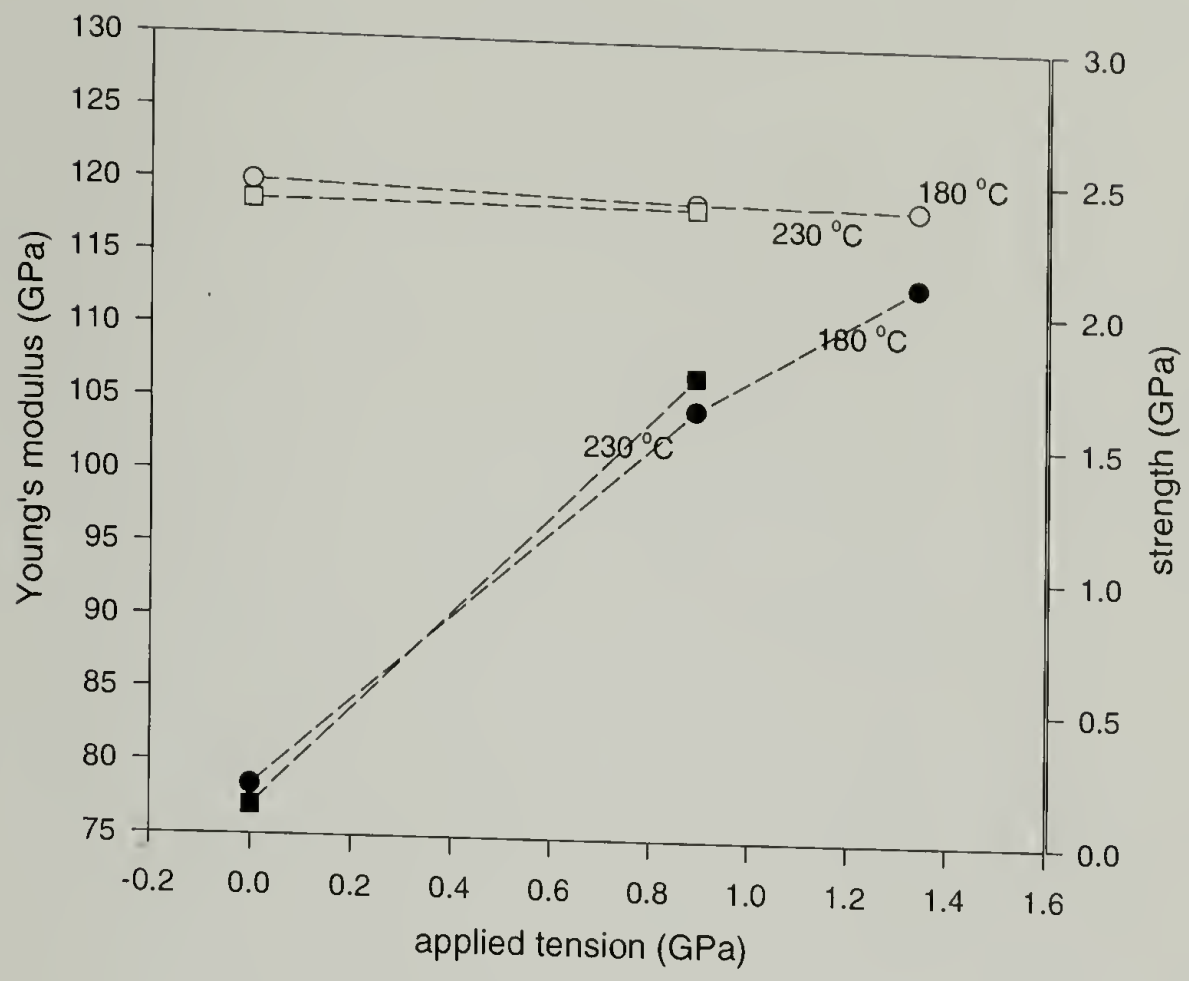

Figure 6.13 Change of the properties of the fiber with applied tension in heat- tensioning; close circles are modulus and open circles are strength; numbers in the plot are treatment temperatures

6.4.2.2 Structure

The structure of the crystal and its packing are changed with the heat tensioning. The *c*-dimension of lattice constants increases with the applied tension at constant treatment temperature. (Figure 6.14) Cooperatively, the paracrystalline parameter decreases as shown by Figure 6.15. Figure 6.15 also illustrates that the orientation angle decreases with the applied tension at constant treatment temperature. For a modulus increase by 50%, the *c*-dimension increases by 0.4% and the orientation angle changes from 12.2° to 7.0°. The change in the orientation angle can cause a fiber to elongate by 1.5% if the crystal orientation contributes to the deformation. In our heat stretching experiments, a permanent deformation of 1.9% was observed when the resultant fiber has a modulus increase of 50%. Therefore, the deformation of the fiber is caused by the combination of two mechanisms: the elongation and the rotation of the crystal.

Our study supplements the deformation mechanism of crystal rotation for PPTA proposed by Ericksen. [62]

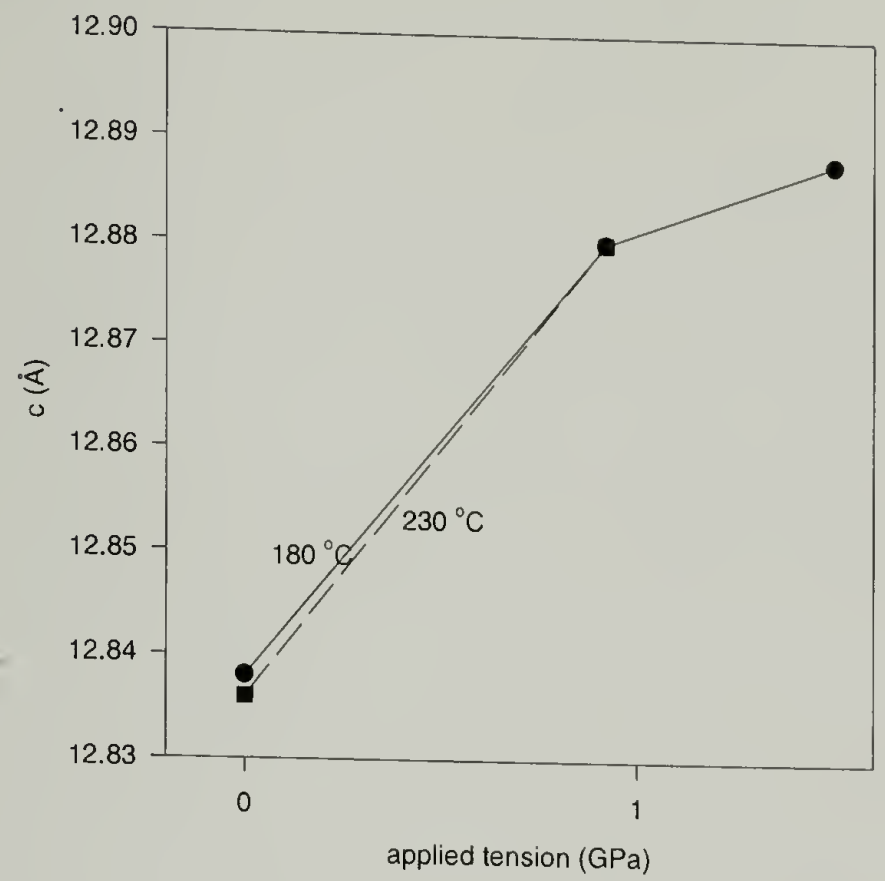

Figure 6.14 Lattice *c*-dimension changing with applied tension in heat-tensioning; close circles are crystals treated at 180 °C and open circles are crystals treated at 230 °C

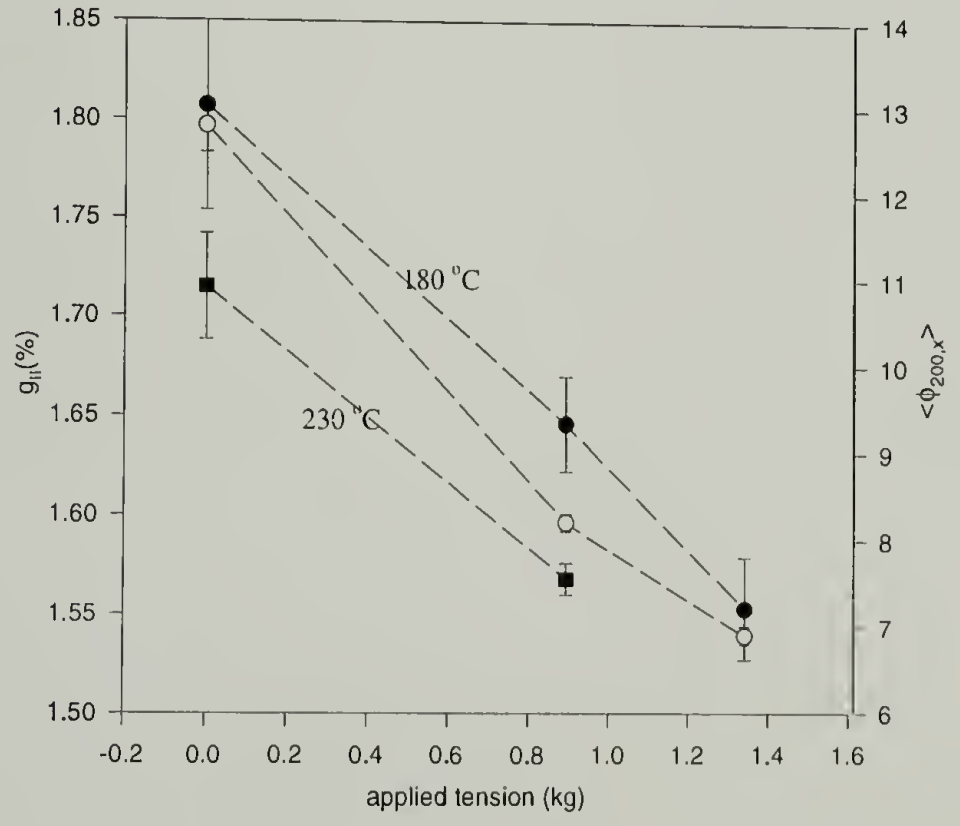

Figure 6.15 Change of the paracrystalline parameter g_{II} and the orientation angle with applied tension in heat-tensioning; close circles are g_{II} and open circles are $\phi_{200,x}$; numbers in the plot are treatment temperatures

It has been shown from the property-structure correlation (See Chapter 7) that the smaller the orientation angle and the paracrystalline parameter, the higher the modulus. The results of free-length annealing suggest that the orientation angle increases and the paracrystalline parameter decreases upon heating. A decrease in the paracrystalline parameter means the crystal becomes more perfect. This indicates that, naturally, crystals tend to de-orient while the crystal becomes more perfect upon heating. Because of the competition between two processes, the modulus of the fiber remains relatively unchanged over a wide range of annealing temperatures. When a tension is applied along with heating and the tension is high enough to

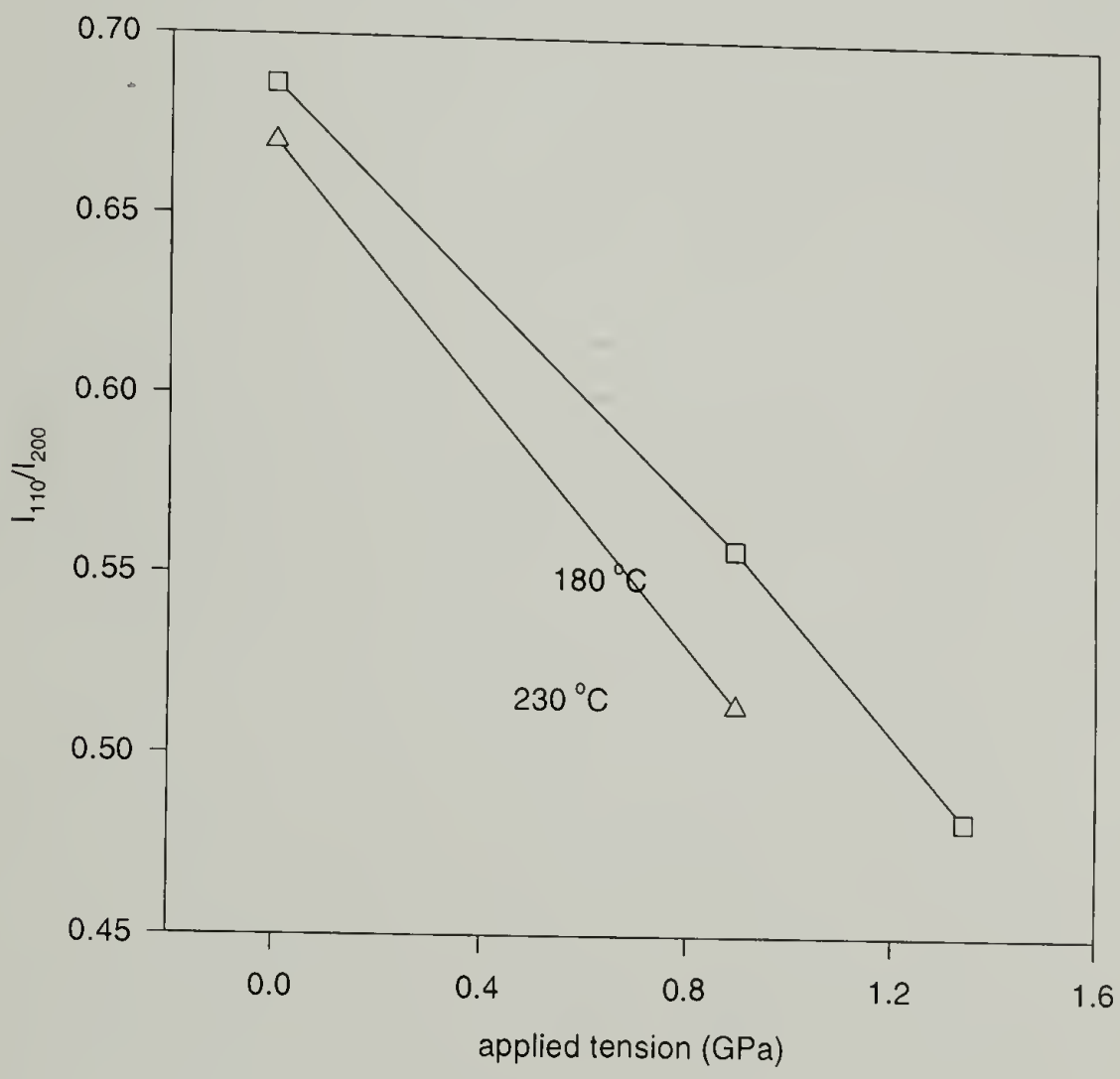

Figure 6.16 Change of intensity ratio, *I110/I200*, with applied tension in heat-tensioning; numbers in the plot are treatment temperatures

overcome the tendency of de-orientation of crystals and additionally forces crystals to realign, the properties of the fiber can be improved due to two beneficiary effects, reorientation and

perfection of the crystal as indicated in Figure 6.13. This is the structural reason for the property enhancement by heat tensioning post-treatment.

Other structure changes were also observed. Figure 6.16 indicates that the I_{110}/I_{200} decreases linearly with the applied tension. While they increase largely with the treatment temperature shown in the study of free-length annealing, the apparent crystal sizes are almost unchanged by the applied tension. The equatorial crystallinity does not change systematically with the applied tension. The lattice constants along *a*-, *b*-direction are also unchanged.

These structure characterizations clearly suggest that some structure parameters--the orientation angle, the lattice c-dimension, the paracrystalline parameter and the intensity ratio I_{110}/I_{200}--are closely related to the properties of the fiber, while the modulus of the fiber is insensitive to the *a, b*- lattice constants and apparent crystal sizes.

A heat-tensioning experiment at 370 °C yields a fiber with a modulus increase of 100% while its structure characterization was not performed due to the small quantity of the sample. (Table 6.3) This large increase in the modulus could not be achieved by tensioning at lower temperature. It is suspected that the enhancement in property is limited by the molecular chain dynamics. Two relaxations were detected in PPTA fiber: one around 250 °C and the other around 350 °C as introduced above. These two relaxations provide two windows of temperature for post-treatment. One processing window is the temperature ranges from 100 °C to 350 °C and the other is above 350 °C but lower than the degradation temperature. The achievable properties of two processing windows are different because the achievable structures are different. Considering the processing temperature between 100 °C and 350 °C, the applied tension is more important than the treatment temperature. The higher the applied tension, the better the orientation and the more perfect the crystal, therefore the higher the modulus. Meanwhile, the treatment temperature and time determine the transverse apparent crystal sizes. Our study shows a trend of decreasing strength with the increasing transverse crystal sizes. (See Chapter 7)

Therefore, low temperature, around 180 °C, high tensioning and short time are good to achieve strong and relatively stiff fiber. In order to achieve super-high modulus, the processing temperature needs to be above 350 °C and may results in a sacrifice in strength due to thermal degradation.

6.4.3 Pressure Annealing

6.4.3.1 Change in Structure and Property

In order to explore the possibility of new processing routes and to also better understand the structure response to the external stimuli, different pressure annealing experiments were

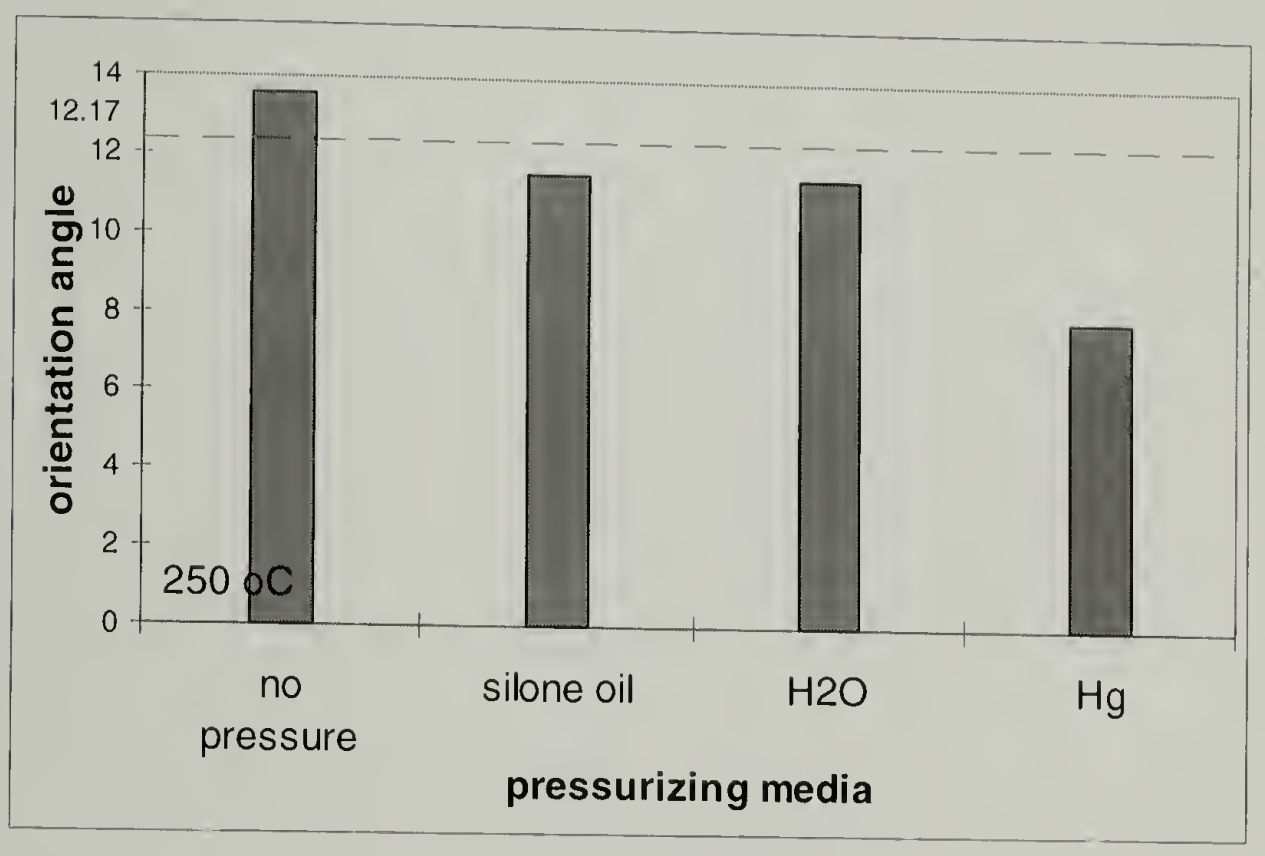

Figure 6.17 Effect of different pressurizing media on the orientation of the fiber in pressure-annealing

conducted. Pressure annealing, pressure-tensioning, and pressurized steam annealing of Kevlar® 29 fiber were studied. It is shown in Table 6.3 that the presence of hydrostatic pressure helps to reorient the crystals. The orientation angles of the fibers being treated using different pressurizing media all decrease as shown by Figure 6.17. Without tensioning, an external hydrostatic pressure of 130 MPa decreases the orientation angle to 8.2° from 13.4° for fibers

annealed without pressure. Since the modulus of the fiber is mainly determined by the orientation, it provides a different way other than heat-tensioning to achieve high stiffness.

Our results show that the hydrostatic pressure prevents the change of the crystal structure. The *a-*, *b-* lattice dimensions do not change after the fiber's being pressure annealed, pressure-tensioning annealed and pressurized steam annealed at high temperatures, which is quite different from annealing without pressure. The paracrystalline parameter of the crystal after being pressure-annealed is much bigger than that annealed without pressure at the same temperature. Tensioning along with pressuring helps to decrease the paracrystalline parameter.

In terms of properties, the fiber being pressure annealed shows higher modulus than free-length annealing but not as high as those achieved through heat-tensioning. One reason is because the applied hydrostatic pressure is much lower than the applied tension. The change of the structure due to hydrostatic pressure is not difficult to understand. The fiber is highly anisotropic and the transverse modulus of the fiber is much lower than the longitudinal modulus. The hydrostatic pressure causes larger deformation transversely than longitudinally so that the crystal is reoriented by pushing on the crystal transversely instead of stretching the crystal longitudinally. The decrease in the density of the fiber that is usually observed for the change of the crystal structure, which happens in annealing without pressure, is prevented by the hydrostatic pressure. Hence, the change in the crystal structure is relatively small. The densification was observed for the fiber being treated under pressures higher than 100MPa using mercury as the pressurizing medium.

6.4.3.2 Morphology

The diameter of the pressure-treated fiber is smaller under optical microscope and SEM (Figure 17(a)). This needs to be further confirmed by density measurements. In addition, some interaction between mercury and the fiber was observed. It is shown in Figure 17 (b) and (c) that

the fiber undergoes a brittle failure and the fracture end of the fiber becomes blunt instead of a generic fibrillar structure, which are common in the failure of PPTA fiber. In addition, a close investigation of the surface of the fiber being Hg-pressure-treated reveals a rich ridge-like feature. (Figure 6.18(d)) More study needs to be conducted to investigate the possibility of pressure-induced Hg-catalyzed degradation.

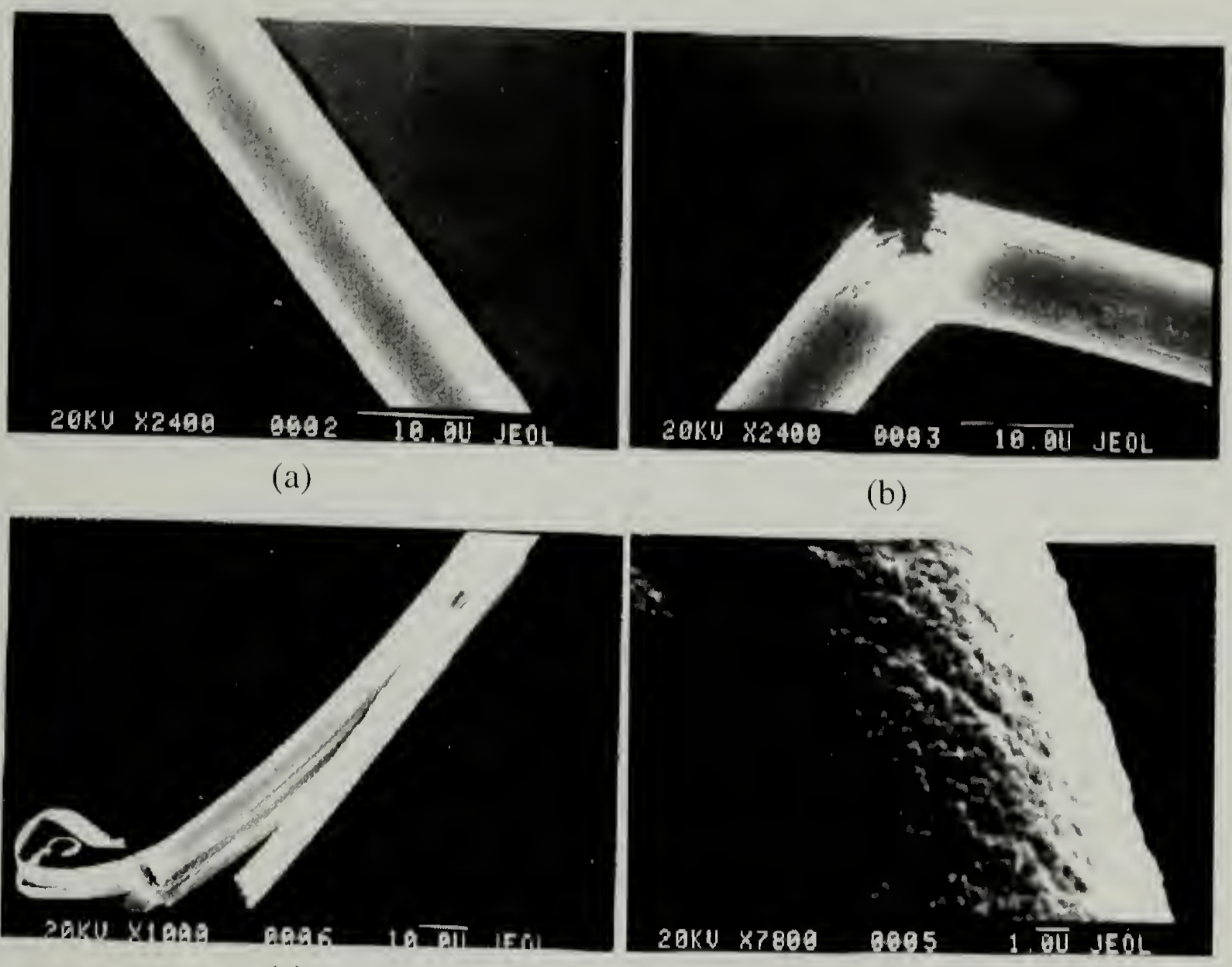

Figure 6.18 SEM pictures of a Kevlar® 29 fiber pressure-annealed in Hg; (a) a treated fiber; (b) bending of the treated fiber; (c) a fracture end of the treated fiber; (d) the surface of the treated fiber

The relaxation of the structure is suspected to be associated with the breaking of hydrogen bonds between the bound water and the polymer chain. Water was used as the pressurizing medium to study the role of water in the relaxation. It is found that the presence of

saturated water/steam during annealing prevents the change in the structure. It is shown in Table I that, when the fiber was annealed under saturated water at different temperatures, not only did the lattice constants remain unchanged but so did the transverse apparent crystal sizes and the intensity ratio I_{110}/I_{200}. This convinces us that the pressurized water during annealing suppresses the break of hydrogen bonds and inhibits the conformation change of the chain so as to keep the crystal structure unchanged.

6.5 Conclusions

From the study of properties and structure of the post-treated Kevlar® fiber, the following was found:

Under free-length annealing, the modulus of the fiber slowly decreases with the annealing temperature until 350 °C, then drops fast while the strength of the fiber decreases with the annealing temperature and time. The crystal structure of PPTA fiber is not stable and changes with the annealing temperature. The transverse crystal sizes increase with the annealing temperature monotonically. The lattice *c*-dimension, g_{II}, I_{110}/I_{200}, longitudinal crystal size and equatorial crystallinity show a cooperative change. Their change indicates two relaxations in the crystalline region which is supported by DMTA and TMA measurements. The crystal orientation decreases with increasing annealing temperature.

Under heat-tensioning, the modulus increases linearly with the applied tension at constant treatment temperature, while the strength remains unchanged. The lattice *c*-dimension increases largely with the applied tension while the transverse unit cell dimensions and crystal sizes are insensitive to the applied tension. The g_{II} and I_{110}/I_{200} show a cooperative decrease with the applied tension and the crystal orientation improves with increasing applied tension. The deformation of the fiber is due to the elongation and rotation of the crystals.

Under pressure annealing, pressure-tensioning annealing and pressurized steam annealing, the modulus increases with the applied pressure and the crystal orientation improves with the applied pressure. Meanwhile, the change of crystal structure under pressure is much smaller than that caused by tension. The presence of pressurized water prevents the structure change. It suggests that the relaxation of the structure is associated with the bound water.

CHAPTER 7

STRUCTURE-PROPERTY CORRELATION OF PPTA FIBERS

7.1 Abstract

The mechanical properties and structure parameters of various PPTA fibers have been investigated using WAXD to illustrate the property-structure correlation. The mechanical properties examined are modulus E and strength σ; and the structure parameters studied include orientation angle $\phi_{200,x}$, lattice constants a, b, c, paracrystalline parameter $g_{II,}$, apparent crystal sizes ACS_{110}, $ACS_{200,}$ ACS_{001}, intensity ratio I_{110}/I_{200} and transverse crystallinity X. Among the studied structure parameters, the c, g_{II} and I_{110}/I_{200} are found to be interrelated and their change indicates the non-reversible chain deformation due to post-treatment. It is concluded that the fiber modulus is determined by the combination of the orientation of the crystallites and the paracrystalline parameter through the following equation:

$$1/E_f = (1/E_0 + D_1 g_{II}^2) + A\langle \sin^2 \phi \rangle$$

Equation 7.1

in which E_f is the fiber modulus, g_{II} is the paracrystalline parameter and ϕ is the orientation angle, and E_0, D_1 and A are material constants. These correlations support our proposed morphology model where the crystallites are formed from nonlinear chains and packed with an orientation distribution. The strength-property correlation has also been studied. In addition, different types of Kevlar® fibers, Kevlar®119, Kevlar®29, Kevlar®49 and Kevlar®149, have been shown to have different structures. Especially, the absence of the (001) diffraction distinguishes the structure of Kevlar® 149 from the other Kevlar® fibers.

Keywords: poly(*p*-phenylene terephthalamide) Kevlar® fibers, structure-property relation, wide angle x-ray diffraction

7.2 Background

The discovery of the poly(p-phenylene terephthalamide) (PPTA) fiber in 1972 brought much excitement to the polymer field.[2] Its high performance enables a wide range of applications in fiber-reinforced composites, cables and ropes, ballistic fabrics and pulps.[3] Its superior properties also draw continuous interests in its structure-property relation.[29,34,41,42] However, the appearance of new types of Kevlar® fiber, namely Kevlar® 149, challenges the universal applicability of these correlations. This section of the research aims to shed light on a new property-structure correlation in Kevlar® fibers.

A great deal of research has been done to determine the structure of PPTA. [29-33,35-38] It is reported that PPTA is a highly crystalline polymer. Although the crystallinity of Kevlar® 29 fiber is 68% according to Hindeleh's measurement,[29] a single phase structure with crystalline imperfection describes its morphology better[33]. The crystal structure of PPTA shown by Northolt and Aartsen is a pseudo-orthorhombic.[30,31] Panar and coworkers suggested a paracrystalline structure of the crystal with a second order distortion g_{II} of 2.5% along *c*-axis.[33] These imperfect crystals are packed to form pleated sheets and those pleats were observed using polarized optical microscopy. Transmission electron microscopy and micro x-ray diffraction measurements showed that pleated sheets are formed in the hydrogen-bond direction and arranged radially.[36,37,38] Finally, a rich fibrillar structure is formed. A skin-core morphology is common due to processing.[40] With regard to achieving good properties, spinning and post treatment are crucial. The properties of PPTA fibers were shown to be sensitive to the temperature and tension in post treatment. [32,42,54,55]

In the study of structure-property relationship, Northolt first proposed that the fiber compliance changes with the disorientation angle on the basis of a single-phase structural model:[41]

$$S_{33} = e_3^{-1} + A\langle \sin^2 \phi \rangle + B\langle \sin^4 \phi \rangle$$

in which, S_{33} is the fiber compliance along the fiber axis, e_3 is the crystal modulus along c-direction and ϕ is the orientation angle of crystals. Independently, Barton showed a good correlation between the modulus and the paracrystalline parameter.[34] On the other hand, after a thermal annealing and aging study, Hindeleh and Abdo concluded that the fiber modulus increases but the strength and elongation decrease with increasing crystallinity.[29] Recently, Lee and co-authors post-treated Kevlar® fibers under different temperatures and tensions and carried out mechanical testing and x-ray measurements. Their experimental results illustrated a relation between the modulus and the orientation function and the removal of pleats. Meanwhile other structural features—paracrystalline parameter, axial and transverse crystallite sizes—do not dominate the material stiffness.[42] While there are several studies on the modulus-structure relation, the study on strength-structure correlation is rare. Allen and coworkers concluded that the tensile strength of PPTA fibers is determined by the orientation and the strength anisotropy in the polymer. [74] The fiber patentees of DuPont believed that the perfection of the radial arrangement gives improved tenacity.[43]

The study on the structure-property correlation has not been carried out in a systematic way. Different researchers focused on specific structure parameters exclusively and did not examine other structure parameters during their study. Therefore, the structure-property correlation were reexamined in this paper through a full mapping approach. In our experiment, the properties and structure of as-spun fibers were changed widely utilizing different treatment conditions including different temperature, tension, hydrostatic pressure with inert gas or water. Then, the properties and structure of the altered fibers were carefully measured and all relative structure parameters were investigated. Our experimental results strongly indicate the modulus of the fiber is determined by the combination of the misorientation and the paracrystalline

parameter. This modulus determination is attributed to a combination of local orientation and macro-orientation. A morphology model has been proposed and provides good agreement with experimental results.

7.3 Experimental

Four different fibers, Kevlar® 29, Kevlar® 119, Kevlar® 49 and Kevlar® 149 were subjected to different post-treatment conditions described in Chapter 6. After different treatments, their mechanical properties and structure were characterized.

To gain better statistics, yarn specimens were used for mechanical property tests. Single filament tests were used only when yarn samples were not available. Five repeat tests were done for yarn specimens and ten for single filaments. The tensile testing of yarn specimens was done using an Instron® model 5564 testing machine according to ASTM D 2256-90. All of the tests were performed at standard conditions of 21 °C (± 1 °C) and 65% (± 2%) relative humidity. Pneumatic yarn/cord grips were used for the yarn tests, with an effective gauge length set at 150 mm and a cross-head speed of 10 %/min. Single filament tests were performed on a MTS® tester. The sample gauge length was 25 mm and the cross-head speed was also 10%/min. Griping effects were corrected by adjusting the gauge length. Initial modulus was calculated for a strain range of 0.05% to 0.5%, where the stress-strain curve is linear. The coefficients of variation (cv) are 1.5% in the measurement of the modulus E and 3% in the strength σ and the strain to break.

The structure characterization was done using wide-angle X-ray diffraction. The structure parameters investigated include lattice constants, a,b,c; paracrystalline parameter, g_{II}; equatorial x-ray diffraction crystallinity, X; intensity ratio, I_{110}/I_{200}; different apparent crystal sizes (ACS) of planes ($00l$), (110) and (200); and (200) orientation angle, $\phi_{200,x}$.

Crystallite orientation was studied using CuK_α radiation equipped with a crystal monochromator and a Simens two-dimensional area detector. Specimens were prepared by aligning bundles under slight tension and then holding them together by epoxy. The applicability of the bundled sample was confirmed by the agreement in the orientation of the bundled sample with that of the single filament obtained by a Statton Camera. The (200) orientation angle was taken as the full width in angles at the half maximum intensity(FWHM) of the azimuthal scan of the (200) diffraction to simplify the calculation. The integrated azimuthal scan was curve-fitted using "Microcal™ Origin™" so as to calculate the integral width. Northolt[41] elucidated that this (200) orientation angle represents the misorientation between the crystallites and the fiber axis. Five specimens for each type of fiber sample were measured.

Other structure parameters were obtained using CuK_α radiation and a Simens D500 diffractometer. A receiving slit of 0.15° was used. Corundum powder with 1 micron size was used as the standard sample to calibrate the angle and evaluate the instrumental broadening. A Lorentzian profile was assumed for the peaks. Then the instrumental broadening in FWHM is 0.26°. Samples for the diffractometer were prepared by aligning 1000 filaments and confining them into a thickness of about 100 microns. The width of the sample is 2 mm. Three specimens were measured using the diffractometer for each type of fiber sample. The diffracted intensity distribution as a function of two times of the Bragg angle θ was first corrected for background, polarization, Lorentz, and adsorption factors.[171] The polarization factor P is

$P = 1/2 \cdot (1 + \cos^2 2\theta)$, the Lorentz factor L is $L = 2/\sin 2\theta$, and the adsorption factor is

$A = \dfrac{\exp(\mu t(1 - \sec 2\theta) - 1}{\mu t(1 - \sec 2\theta)}$ (normal-beam transmission) and $A = \dfrac{\sec\theta}{\exp(-\mu t(1 - \sec\theta))}$

(symmetrical transmission)

where θ is the Bragg angle, t is the thickness of the specimen and μ is the linear absorption coefficient, which was calculated to be 8.43.

The *c*-dimension of the lattice constants, apparent crystal size along *c*-axis and paracrystalline parameter g_{II} were obtained from the meridional scan of the fiber. The meridional scan was done at a $\theta/2\theta$ scan, symmetrical transmission mode. Scan times were constant for all samples and the number of counts at the maximum intensity of one peak was above 2000. The apparent crystal size along *c*-axis and the paracrystalline parameter were derived using (002),(004), and (006) diffraction peaks from the following equation:[172]

$$(\delta_s)_0^2 = (\delta s)_c^2 + (\delta s)_{II}^2 = \frac{1}{\bar{L}_{hkl}^2} + \frac{(\pi g_{II})^4 n^4}{d_{hkl}^2}$$

in which δ_s is the broadening of the diffraction peak, L is the crystal size, g_{II} is the paracrystalline parameter, n is the order of the diffraction peak, d_{hkl} is the dimension of the first order diffraction palne

Peak widths were determined using a regression analysis.

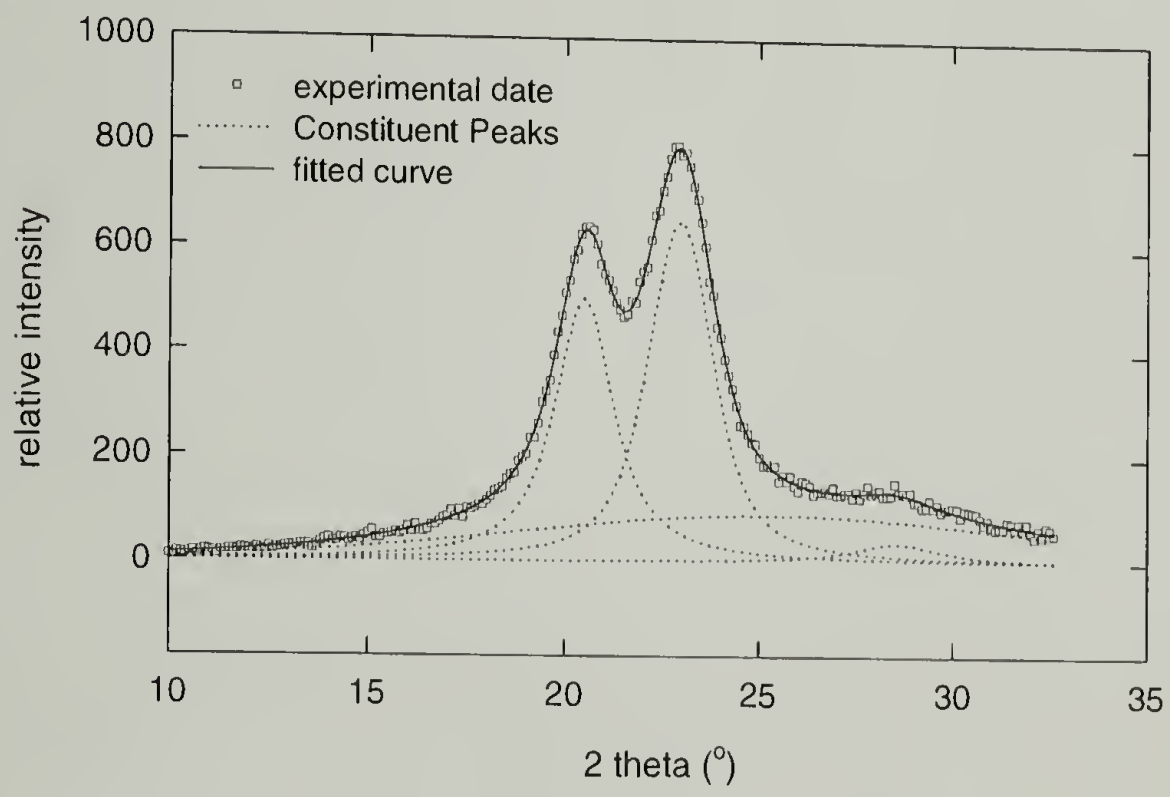

Figure 7.1 Peak Deconvolution of an equatorial scan of Kevlar® fiber after corrections

The *a, b*-dimensions of lattice constants, (110) and (200) apparent crystal sizes, equatorial crystallinity and I_{110}/I_{200} were obtained from the equatorial scan, which was performed at a normal-beam transmission mode. The scanning range of 2θ is from 10 to 35°. After

corrections, the intensity profile was resolved into 3 peaks, (110), (200) and (211), and an amorphous part. Voigt's function was assumed for peaks. Figure 7.1 shows how the two peaks were resolved and good fitting was achieved.

Then, the FWHM and the integrated intensity of the peaks were calculated. The apparent crystal sizes were calculated using the Scherrer equation. The equatorial crystallinity is defined as $X = \sum I_i / (\sum I_i + I_a)$, where I_i is the integrated intensity of a diffraction peak and I_a is the integrated intensity of the amorphous regions.

7.4 Results and Discussion

7.4.1 Structure-Property Correlation

The results of the structure and property evolution in PPTA fibers with post-treatment was systematically presented in Chapter 6. The resultant fibers have moduli in the range of 40 GPa to 138 GPa and the strength in the range of 86 MPa to 2.85 GPa. The goal is to construct the correlation between the property and structure utilizing these fibers. After the properties and structure parameters were measured, correlation plots between the modulus E and each of the following structure parameters, a, b, c, g_{II}, ACS_{110}, ACS_{200}, ACS_{001}, X, I_{110}/I_{200}, $\phi_{200,x}$ have been made. The plots that show scattered data exclude the correlation between the modulus for the structure parameters, a, b, ACS_{110}, ACS_{200} and ACS_{001}. Our experiments also did not yield meaningful correlation between the modulus and the equatorial crystallinity and this result contradicts what was suggested by Hindeleh and Abdo[29]. The large experimental variability in this measurement of crystallinity inhibits a precise analysis. However, it is worthwhile to point out that the equatorial "crystallinity" does not represent the total crystallinity. Our experimental results suggest that a single phase imperfect-crystalline structure best describes the morphology of PPTA fiber better. The so-called equatorial "crystallinity" may reveal other structure information.

Contrary to the insensitivity of the modulus to some structure parameters, other structure parameters strongly influence the modulus. Figure 7.2 shows that the modulus of the fiber is related to several structure parameters: the crystallite orientation, the paracrystalline parameter and the *c*-dimension of the lattice constants. There is an overall trend in that the modulus increases with the decrease in the misorientation angle and paracrystalline parameter, and the increase in the *c*-dimension.

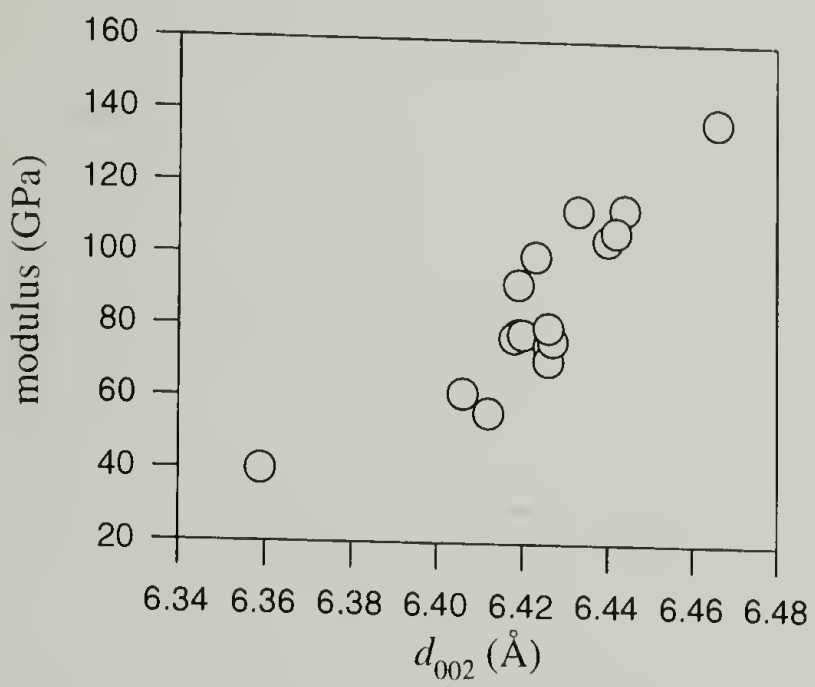

Figure 7.2 Observed relationship between the initial axial modulus and different structure parameters: (a) interplanar spacing d_{002}; (b) orientation angle $\phi_{200,x}$; (c) paracrystalline parameter g_{II}.

Experiments were conducted to examine if the crystalline orientation is related to the paracrystalline parameter. Northolt[41] proposed the correlation between the modulus and the orientation angle based on molecular mechanics. His argument is sound and analogous to contemporary composite theory. Meanwhile Barton's[34] correlation of the modulus with the paracrystalline parameter is a phenomenological result. Our results indicate that the orientation and the paracrystalline parameter are independent. During our post-treatment study, it was found that the paracrystalline parameter is more sensitive to post-treatment temperature while the orientation is more sensitive to the applied tension. Figure 7.3 illustrates different trends in the change of the orientation angle and the paracrystalline parameter with the treatment temperature under different tensions.

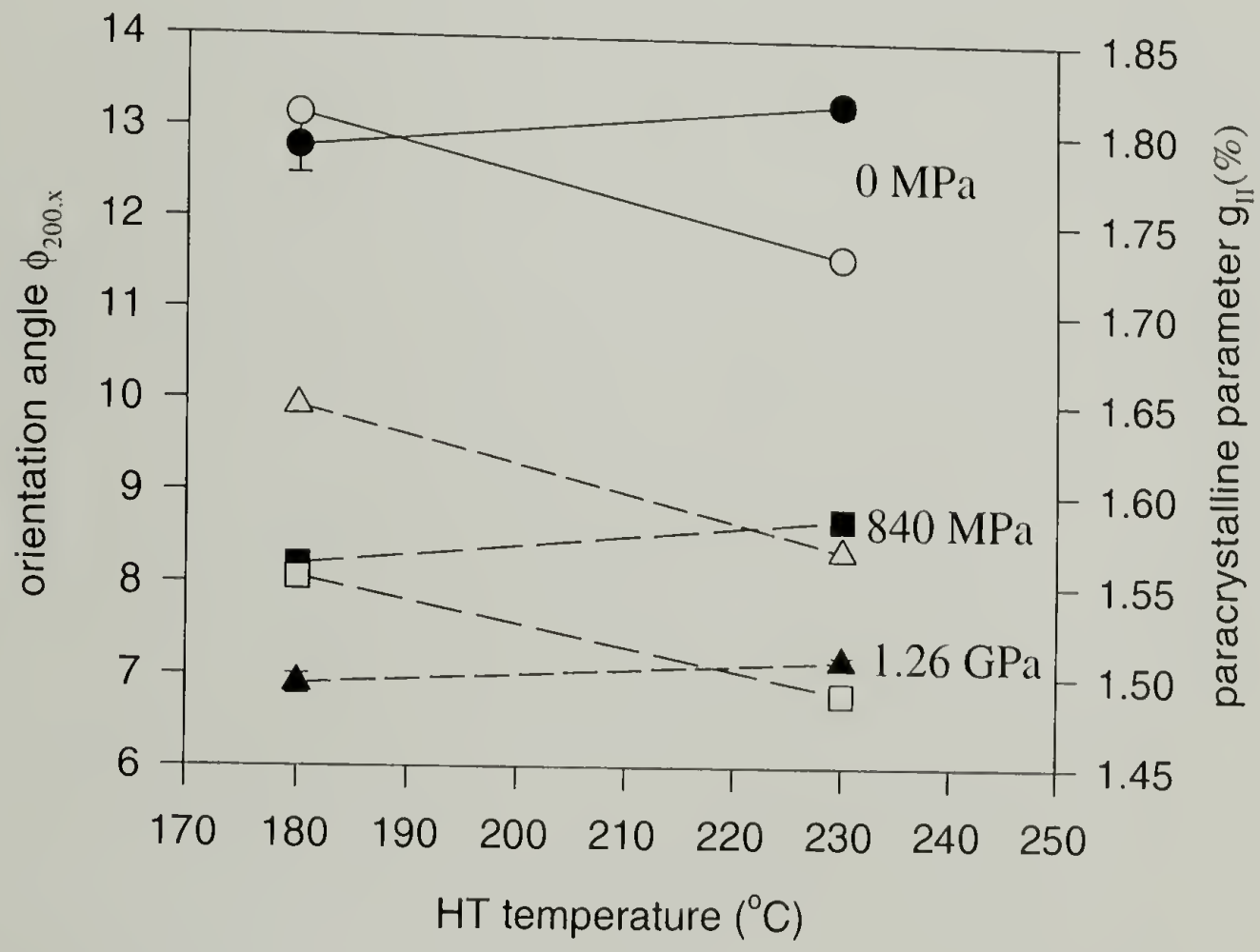

Figure 7.3 Changes of the orientation (closed symbols) and paracrystalline parameter (open symbols) when fibers are subjected to elevated temperature and tension. The tensioning stresses are shown in the plot and the treatment time for zero stress is 3 hours and 3 minutes for the other conditions.

One interesting finding in our study is that the *c*-dimension lattice constant is different for the fibers obtained for different post-treatment conditions. This observation is explained as follows. Because PPTA is a lytropic liquid crystalline polymer, the ordered structure in the fiber is formed from the liquid crystal state. This ordered structure is probably frozen via coagulation and is not an equilibrium state. Therefore any post-treatment enables an evolution in the crystal's metastable state as the strong intramolecular interaction overcomes the weaker intermolecular forces, namely hydrogen bonding and van der Waals force in the case of PPTA. In this sense, polymer crystals are not much different from single chain conformation. Hence, the concept of the deformation of a single chain is used to elucidate some observations of the crystal structure in the later discussions.

7.4.1.1 Correlation between Paracrystalline Parameter and Unit Cell c-dimension and a New Molecular Model for PPTA Paracrystal

During our post-treatment study, it was found that there are cooperative changes among structure parameters of *c*-dimension, paracrystalline parameter and I_{110}/I_{200}. Under some post-treatment conditions, the *a, b*,-dimensions of lattice constants do not change, while *c*-dimension changes as well as the I_{110}/I_{200}. A plot between the I_{110}/I_{200} and d_{002} for these samples clearly indicates that the I_{110}/I_{200} decreases with increasing d_{002} (Figure 7.4). A second order polynomial accordingly represents the data well while the fitting is simply intuitive. The change in the I_{110}/I_{200} may be caused by the change in the setting angle which is caused by the change in the chain conformation. It is worthwhile to emphasize again that this correlation only holds under the condition that the *a-, b*-dimensions do not change. Certain post-treatment conditions change the *a-, b*- dimensions of the fibers and then their structure parameters do not fit on the curve.

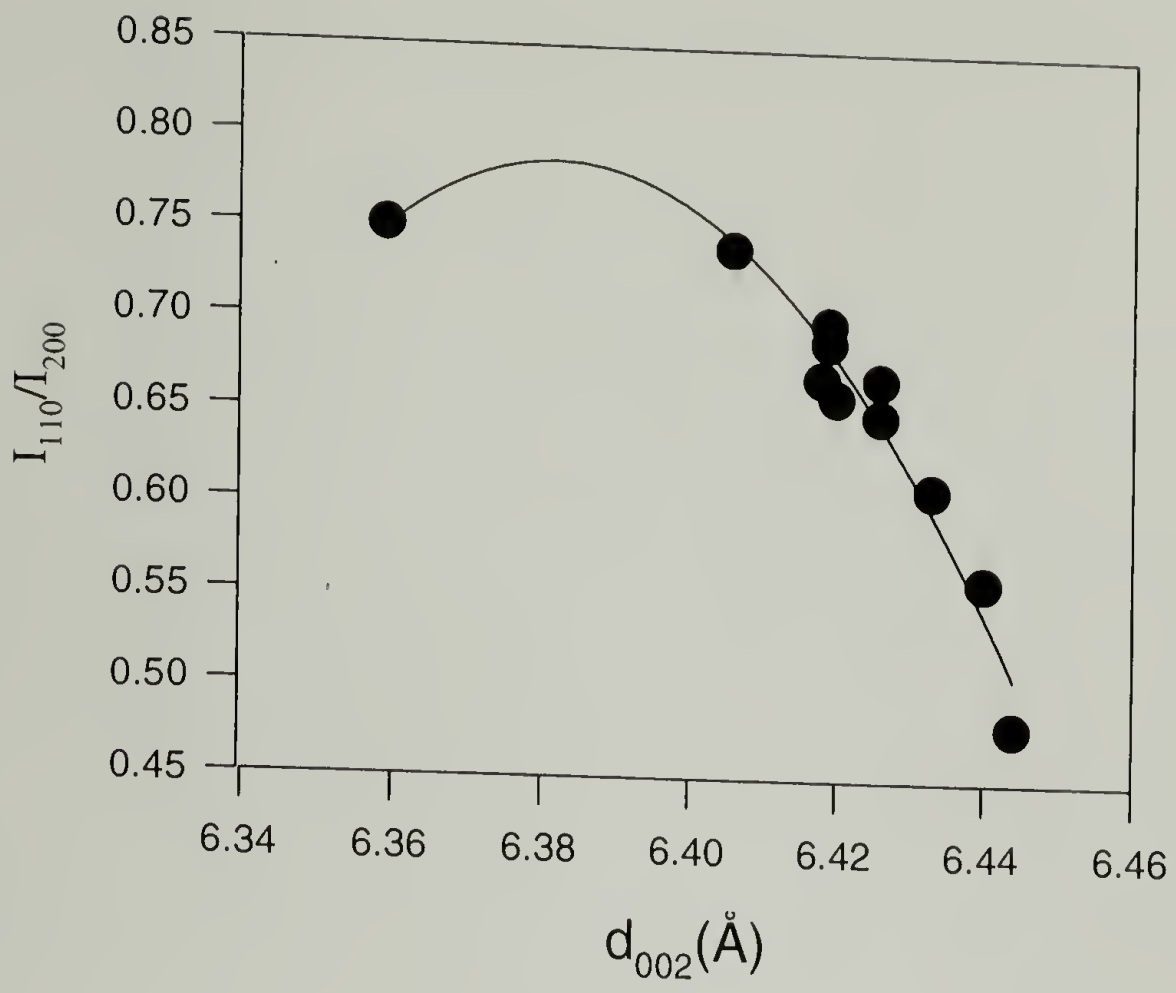

Figure 7.4 Observed relationship between two structure parameters: intensity ratio I_{110}/I_{200} *vs.* d_{002}. The points in the plot are experimental data and the line is a second order polynomial.

In contrast, a more general correlation between the paracrystalline parameter and the *c*-dimension was observed. As shown by Figure 7.5, using the structure parameters obtained for all the fiber samples, there is a linear relation between the g_{II}^2 and d_{002}^2 expressed by the following equation,

$$g_{II}^2 = 87.23 - 2.04 * d_{002}^2$$

Equation 7.2

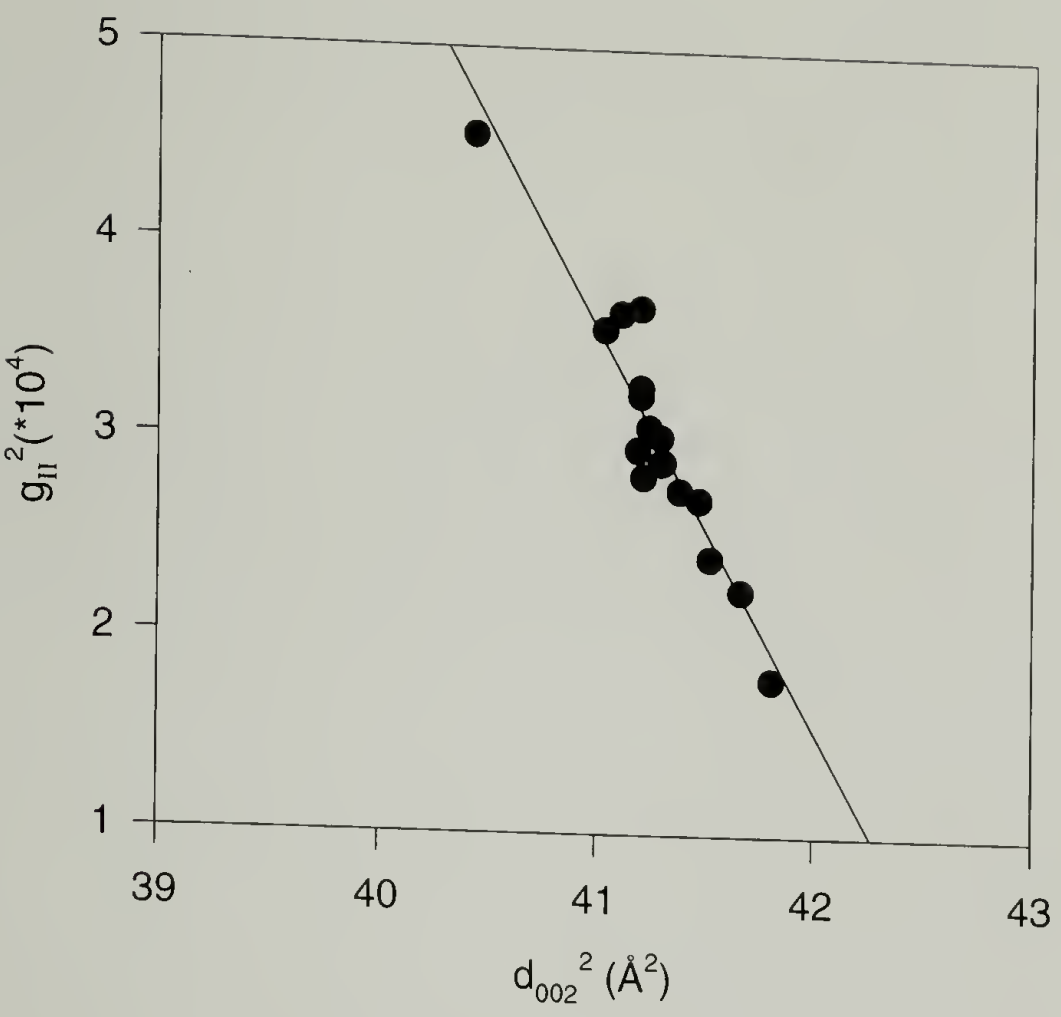

Figure 7.5 Observed relationship between two structure parameters: paracrystalline parameter *vs.* d_{002}. The points in the plot are experimental data and the line is a linear regression curve.

This correlation is explained by the morphology and deformation model of the crystal shown by Figure 7.6(a). To realize the concept of the paracrystal[166] in PPTA, the variation in the dimension of the unit cell and the electron-density distribution from cell to cell is postulated to be due to the nonlinearity of the PPTA chain since PPTA is a rigid-rod polymer. Ideally, the nonlinear chain can be treated as a sinusoidal curve with the amplitude h representing the degree of the chain nonlinearity, which is proportional to the paracrystalline parameter g_{II} in the crystal structure, and the period l corresponding to the lattice constant along c-axis, which is d_{00l}. Under any post-treatment condition, the chain conformation evolves with a change in the h and l while the contour length of the chain is conserved. For this condition, the following mathematical equation is obtained:

$$2\pi^2 h^2 + l^2 = L^2$$

Equation 7.3

in which, L is the contour length of the chain in one period.

More generally, for any shape of a periodical function, the above equation becomes

$$A_1 h^2 + B_1 l^2 = C_1 L^2$$

Equation 7.4

where, A_1, B_1, C_1 are constants related to the shape of the periodic function

Equation 7.4 predicts a linear relation between g_{II}^2 and d_{002}^2, which well explains the experimental observation.

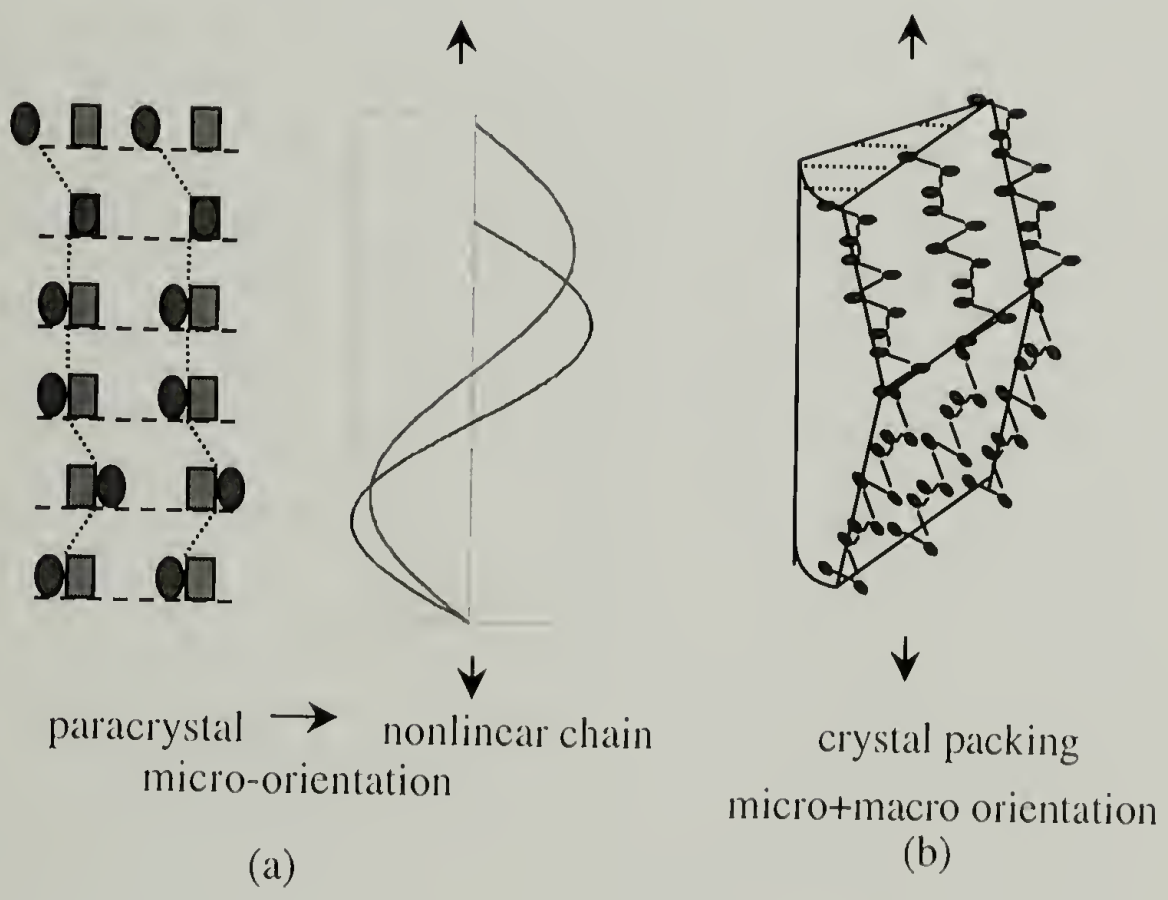

Figure 7.6 A morphological model for the deformation of Kevlar® fiber: (a) a model of nonlinear chain, (b) a model of a crystallite aggregate.

It can therefore be concluded that the change in the structure parameters of d_{001}, g_{II} and I_{110}/I_{200} are interrelated. All three of these parameters are indicators of the same phenomena of chain deformation. The increase in d_{001} means a decrease in g_{II} and I_{110}/I_{200}. Therefore, our

results suggest the crystal structure changes during post-treatment. The structure change originates from the crystal deformation. The crystal deforms accordingly with the chain deformation, which is mainly the lengthening of the bent structure caused by the conformation of the chain. Furthermore, the change in the structure during the post-treatment is preserved and it is this change in structure that leads to the change in the properties. The preservation of the structure from elevated temperature and tensioning is related to the hydrogen bonding formed between two chains. It can be proposed that the hydrogen bonding is broken at elevated temperature or under high tension and then reforms once the fiber is cooled and released from tensioning to inhibit the relaxation of the newly formed conformation. The change in the I_{110}/I_{200} was also observed in the moisture sorption of the Kevlar® fibers.[59] It is reported that the I_{110}/I_{200} increases with the drying of the wet fiber and decreases again when the fiber regains moisture. An increase in paracrystalline parameter in the dried samples was also shown without any discussion. That result is consistent with this result.

7.4.1.2 Correlation between fiber modulus and two structure parameters: Misorientation and Paracrystallinity

The morphology model is developed further as shown by Figure 7.6(b) to constitute the relation between the fiber modulus and structure. The finite crystallites are packed together to form a crystal aggregate with a distribution in orientation. In addition, the crystallites are packed in a series to resemble a pleat structure. Using this morphological model, a relation between the fiber modulus and the structure is derived as follows.

The modulus of the crystallite

To simplify the calculation, the nonlinear chain is now represented by a hinged bent beam as shown in Figure 7.7. Under axial stress P, there will be bending and stretching of the structure.

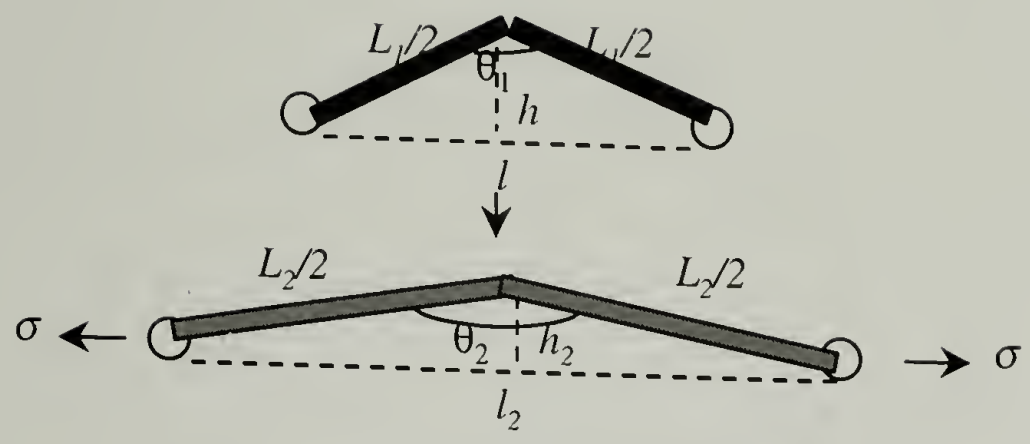

Figure 7.7 Deformation of a hinged bent beam.

Defining $\Delta\theta = \theta_1 - \theta_2$, in which θ_1 is the initial bending angle, θ_2 is the final bending angle, the bending of the structure under stress σ follows

$$\Delta\theta = \tau \cdot \sigma \cdot h_2$$

Equation 7.5

where σ is the applied axial stress, h_2 is the deflection at the middle of the beam from the center line after loading, τ is material constant.

Then, under loading, the total contour length becomes

$$L_2 = L_1 + L_1 \cdot \sigma \cdot \sin(\theta_2 / 2) / E_0$$

Equation 7.6

where L_1 is the initial contour length, and E_0 is the Young's modulus of a linear chain.

Therefore, when the $\Delta\theta$ is small (<<1), the elongation of the structure entity is

$$\begin{aligned}\varepsilon &= (l_2 - l_1)/l_1 \\ &= [(\Delta\theta/2)\cos(\theta_1/2) + \sigma/E_0 \sin^2(\theta_1/2)]/\sin(\theta_1/2)\end{aligned}$$

Equation 7.7

Substituting $\sin(\theta_1/2) = (1-(2h/L_1)^2)^{0.5}$ and $\cos(\theta_1/2) = 2h/L_1$, where h is the initial deflection at the mid point without load, into Equation 7.7 and defining the modulus of the structure entity as $E = \sigma/\varepsilon$, the modulus E becomes

$$E = (1 - (2h / L_1)^2)^{0.5} / [1 / E_0 + (\tau / l - 4 / E_0 L_1^{\ 2}) h^2]$$

Equation 7.8

Equation 7.8 can be simplified when $h << L_1$, and rewritten as

$$1 / E = 1 / E_0 + D \cdot h^2$$

Equation 7.9

where $D = (\tau / l - 4 / E_0 l^2)$

Equation 7.9 shows that the crystallite modulus changes with the nonlinearity of the chain.

The modulus of the fiber

The fiber modulus is determined by the modulus of the crystallite and the orientation distribution of the crystallites based on the aggregate model. Northolt and Aartsen's[41] equation introduced earlier is adopted to describe the orientation effect on the modulus:

$$S_{33} = e_3^{-1} + A\langle \sin^2 \phi \rangle + B\langle \sin^4 \phi \rangle$$

Equation 7.10

Then, this equation needs to be modified to incorporate the effect of the nonlinearity of the chain conformation. As indicated in Figure 7.6(b), e_3 in the Equation 7.10 needs to be replaced by the crystallite modulus E expressed by equation (9). The combination of Equation 7.9and Equation 7.10, expressing h by g_{II} and omitting the higher order term of $<sin^4\phi>$ yields a new equation to describe the fiber modulus:

$$1 / E_f = (1 / E_0 + D_1 g_{II}^{\ 2}) + A\langle \sin^2 \phi \rangle$$

Equation 7.11

in which, E_f is the fiber modulus, D_1 and A are material constants. The addition of the $<sin^4\phi>$ term does not increase the accuracy of the expression in describing the experimental data.

Our experimental results confirm our hypothesis of the morphology. Using Equation 7.11, a least square regression was performed on the modulus and corresponding structure parameters of all the different Kevlar® fibers that were modified by post treatments. The regression equation is

$$1/E_f = 0.004(1+0.31g_{II}^2)+0.102\cdot\left\langle \sin^2\phi \right\rangle$$

Equation 7.12

in which E_f is the fiber modulus in GPa, g_{II} is the paracrystalline parameter in % and ϕ is the orientation angle.

Figure 7.8 shows the excellent fit by plotting the experimental modulus with the modulus calculated from Equation 7.12. In Equation 7.12, the regression parameter A, which is 0.102, is close to the calculated value.[41] In addition, Equation 7.12 yields a linear chain modulus of 250 GPa which is close to the theoretical crystal modulus.[173] Equation 7.12 indicates that the fiber modulus is dominated by orientation distribution in the low orientation region. However, to achieve high modulus, the crystallites not only need to be highly oriented, but also the nonlinearity of the chain conformation needs to be reduced. While the paracrystalline parameter is more sensitive to the post-treatment temperature and the orientation is sensitive to the applied tension, the combination and control of the post-treatment condition provides a broad window to obtain fibers with different tailored properties. The modulus-structure correlation obtained for PPTA fibers should also help to investigate other rigid-rod fibers such as Technora®, Vectran®, polyimide fibers and PBO.

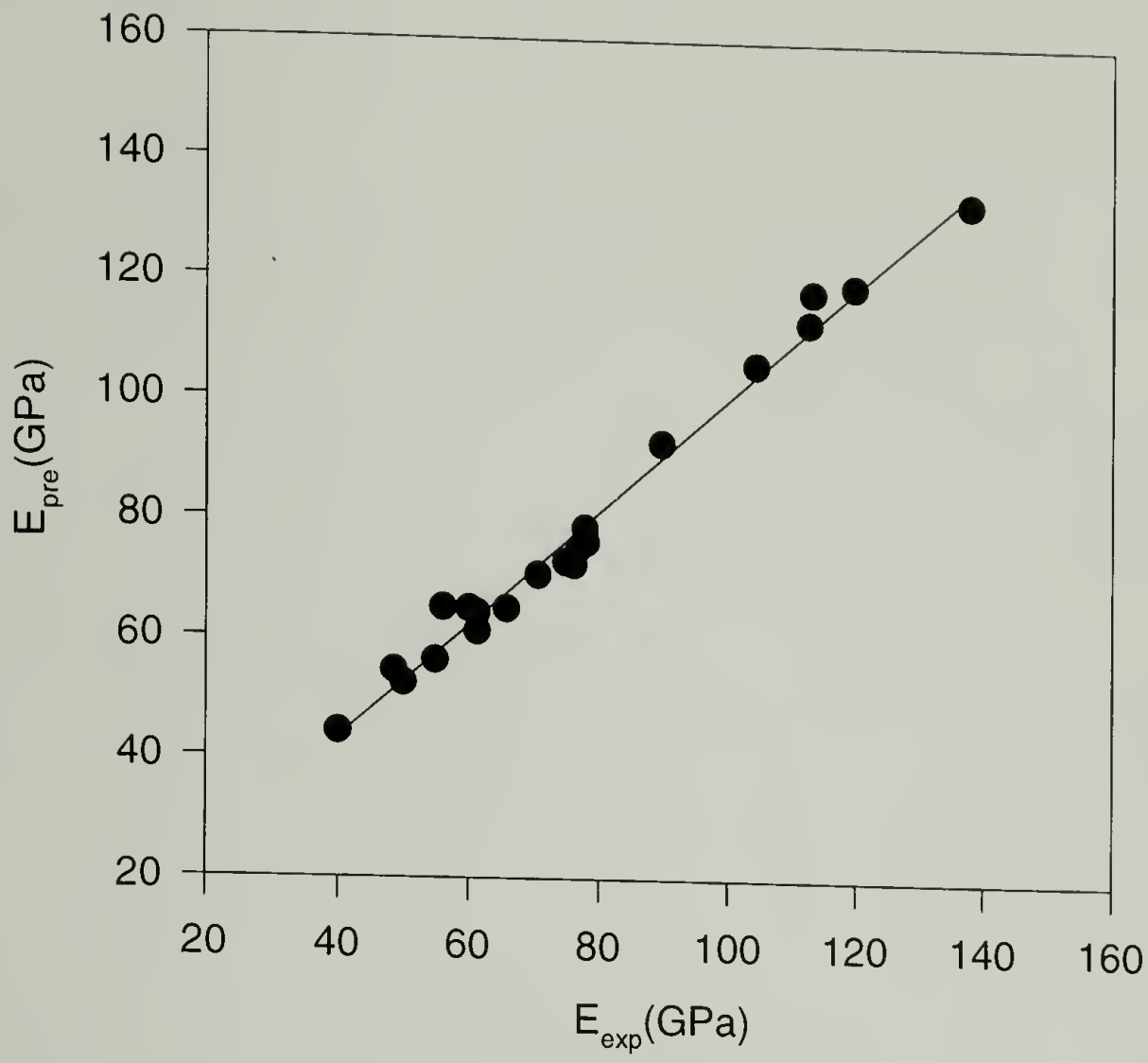

Figure 7.8 A comparison of the experimentally-measured modulus and the predicted modulus

The strength-structure relationship of different PPTA fibers was also investigated and no general correlation was obtained. However, certain correlations exist for the fibers obtained from post-treating one starting material, Kevlar® 29, under temperature and tension. Figure 7.9 shows that the strength of the treated fiber decreases with the increase in the transverse crystal sizes. This observation is consistent with what happens to metals where small crystals produce materials with high yield stress[174]. It is reasonable because PPTA is a single phase structure and the strength is determined by how the crystallites are packed. Further investigation is needed to validate this assumption.

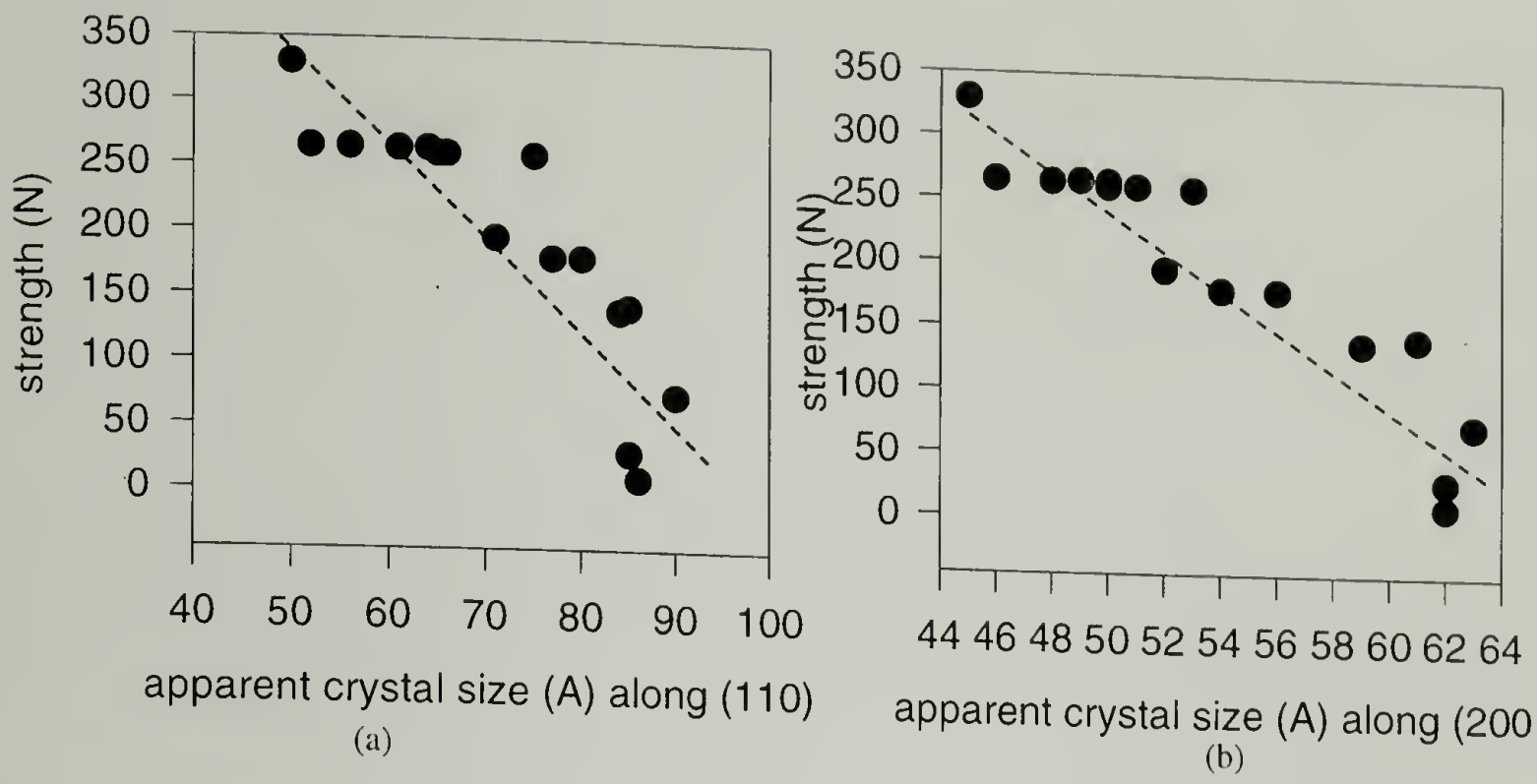

Figure 7.9 The decrease in the strength of the fibers with the increasing transverse apparent crystal size for treated Kevlar® 29 fibers: (a) ACS along (110), (b) ACS along (200).

7.4.2 Different Types of Kevlar® Fibers: Structure and Properties

The structure-property correlation in PPTA fibers has been discussed in the previous section. The obtained correlation has been utilized to explain the structural reasons for the property discrepancy among different types of Kevlar® fibers produced by DuPont.

Table 7.1 compares the property and structure of different types of Kevlar® fibers. It is shown that the modulus of Kevlar® 149 is 2.3 times of that of Kevlar® 119, while the strength of Kevlar® 149 is 73% of that of Kevlar® 119. When comparing the modulus and strength of different types of Kevlar®, they follow a reversal in order, for the modulus, Kevlar® 149 > Kevlar® 49 > Kevlar® 29 > Kevlar® 119 and for the strength, Kevlar® 149 < Kevlar® 49 < Kevlar® 29 < Kevlar® 119.

The table clearly suggests that the structure parameters determine the property differences. As listed in the table, the orientation in Kevlar® 149 is better than Kevlar® 49, while the orientation in Kevlar® 49 is better than Kevlar® 29 and Kevlar® 29 is better than Kevlar® 119.

In addition, the g_{II} of different fibers shows that Kevlar® 149 < Kevlar® 49 < Kevlar® 29 < Kevlar® 119; and the *c* dimension and I_{110}/I_{200} differ in a cooperative way consistent with our previous observation. It was confirmed by our data that both the orientation and the paracrystalline parameter need to be considered to explain the high modulus of Kevlar® 149.

Table 7.1 The property and structure parameters of different types of Kevlar® fibers.

		Kevlar 119	Kevlar 29	Kevlar 49	Kevlar 149
Property	Modulus (GPa)	61±1	78±1	113±2	138±2
	Tenacity (GPa)	2.96±0.09	2.58±0.07	2.40±0.07	2.15±0.06
	Break strain (%)	4.1±0.1	3.1±0.1	2.47±0.1	1.5±0.1
	Energy to break point (J)	1.27±0.03	0.95±.03	1.23±.04	0.36±.01
Structure	Lattice Constant				
	a, Å	7.750±0.003	7.748±0.003	7.784±0.003	7.904±0.003
	b, Å	5.224±0.003	5.232±0.003	5.232±0.003	5.188±0.003
	c, Å	12.82±0.01	12.84±0.01	12.88±0.01	12.92±0.01
	Paracrystalline parameter g_{II},%	1.91±0.02	1.92±0.02	1.66±0.04	1.40±0.03
	Equatorial X-ray diffraction crystallinity X, %	75.20	75.70	77.00	77.00
	Intensity ratio, I_{110}/I_{200}	0.74±0.03	0.70±0.02	0.61±0.02	0.60±0.02
	Apparent crystal size, nm				
	(002)	609	656	737	1548
	(110)	50	52	66	123
	(200)	45	46	51	76
	(200) orientation angle, degrees	16.2±0.2	12.2±0.3	6.8±0.1	6.4±0.2

The table also reveals that the transverse crystal sizes increase from Kevlar® 119 to Kevlar® 29, then Kevlar® 49 and then Kevlar® 149. This is in agreement with our observation of the structure difference among fibers of different strengths. There are also other structure differences among different fibers. Although the *a, b* dimensions of Kevlar® 119, Kevlar® 29 and Kevlar® 49 are the same within error, the *a* becomes bigger and *b* becomes smaller for Kevlar® 149 compared to others. In addition, the axial crystal size of Kevlar® 149 is much larger.

In order to elucidate the fine structure difference in these fibers, a synchrotron source was utilized to obtain detailed diffraction patterns of different fibers. It is clear from the patterns

that Kevlar® 119, Kevlar® 29 and Kevlar® 49 have a trace diffraction intensity of the (001) diffraction, while the trace of (001) diffraction disappears in the diffraction pattern of Kevlar® 149. Figure 7.10(a) compares the meridional scans of Kevlar® 29 and Kevlar® 149. The

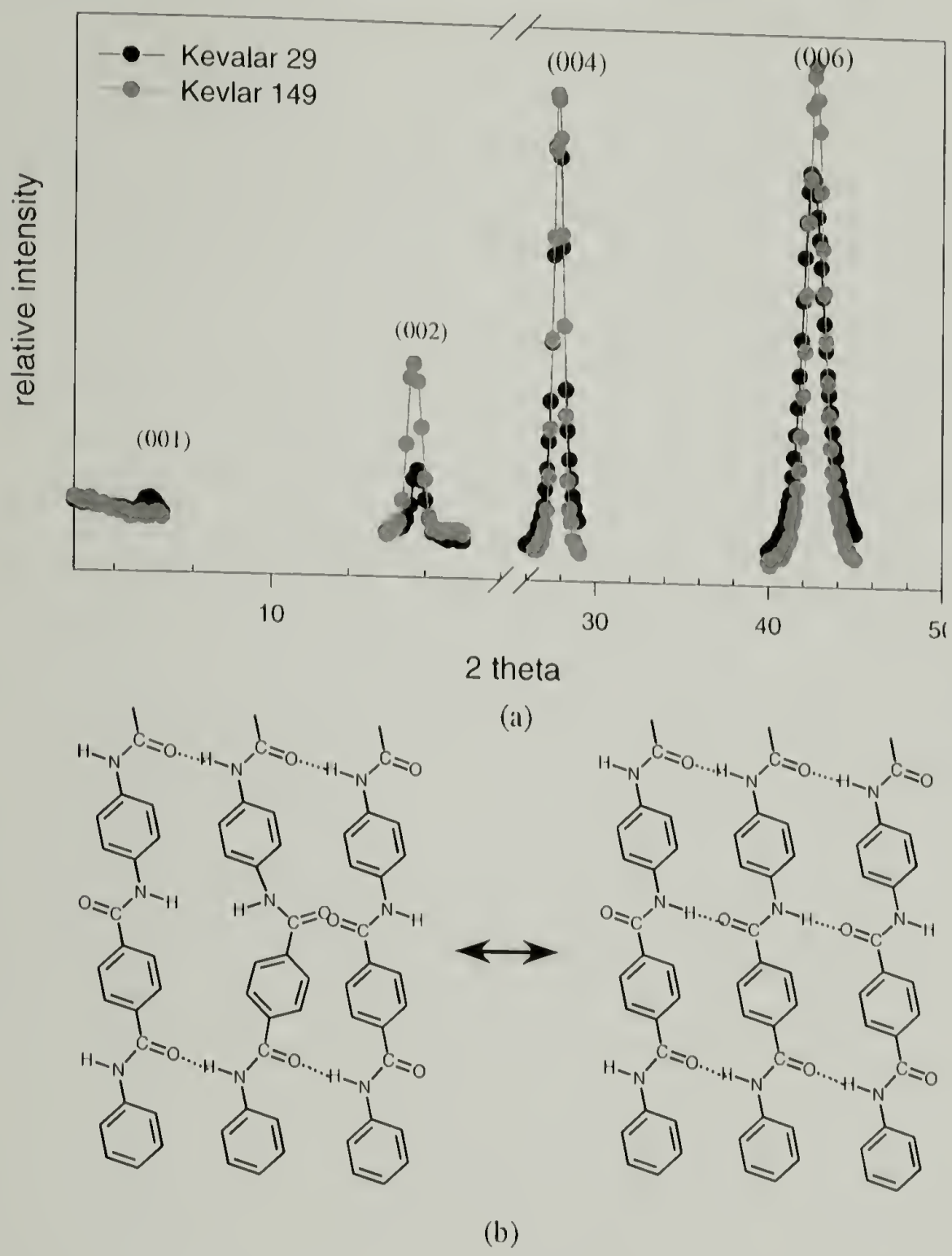

Figure 7.10 The difference in the structure measured by WAXD and the hypothesized chain conformation between Kevlar® 29 and Kevlar® 149. (a) meridional scans; (b) chain conformations.

existence of (001) diffraction in Kevlar® 119, Kevlar® 29 and Kevlar® 49 originates from the fact that the chain conformation in these fibers excludes the perfect 2_1 symmetry. Upon heat and tensioning, the existed *gauche*, or so-called *cis*, conformation in PPTA is transformed to a more

stretched *trans* conformation as shown in Equation 7.10(b). Then in Kevlar® 149, the structure has a more perfect 2_1 symmetry and the diffraction from (001) vanishes. This transformation also assists the formation of hydrogen bonds between chains. Therefore the number of hydrogen bonds increases and thus the *b*-dimension is shortened. Meanwhile, the *a*-dimension is enlarged due to steric reason. In addition, the change in chain conformation facilitates the crystal growth along the direction of hydrogen bonding, which is *b*-axis. Therefore, the crystal size of (110) is much larger than (200) in Kevlar® 149 compared to other types of Kevlar® fibers. This fine structure investigation also confirms the proposed chain deformation model as shown by Equation 7.6(a).

7.5 Conclusions

PPTA fibers with various properties were produced using a variety of post-treatment conditions including temperature, tension, hydrostatic pressure with an environment of inert gas and water or steam and starting from different types commercially available Kevlar® fibers. Mechanical properties and a number of structure parameters have been investigated for these fibers. The results show that several structure parameters change with the treatment condition and some of the changes account for the property changes. The *c*-dimension, g_{II} and I_{110}/I_{200} are proved interrelated and their change indicates the nonreversible chain deformation due to post-treatment. Our experimental results suggest that the fiber modulus is determined by the combination of the orientation of the crystallites and the paracrystalline parameter. The correlation between structure parameters and between the modulus and the structure parameters are confirmed by our morphological model, which indicates the significance of a local orientation and macro-orientation in determining the fiber properties.

The property and structure of different types of Kevlar® fibers, Kevlar® 119, Kevlar® 29, Kevlar® 49 and Kevlar® 149, were investigated. The obtained structure-property correlation

accurately explains the different properties of these fibers. Detailed diffraction studies also illustrate that the mechanism to obtain high modulus PPTA, such as Kevlar® 149, is to eliminate the "*cis*" conformation in the chain structure and thus form more ordered hydrogen-bonding sheets.

REFERENCES

1. Pennings, A. J.; Meihyizen, K. E. Polyethylene Fibers with Ultrahigh Modulus and Strength Produced by Flow Controlled Crystallization; Applied Science: London, 1979.

2. Kwolek, S. L., US Pat. 3671542; US Pat. 3,819,587, , 1972

3. Yang, H. H. Kevlar Aramid Fiber; Wiley-Intersience: New York, 1992.

4. Li, W. H.; Wu, Z. Q.; Zhang, A. Q.; Leland, M. E.; Park, J. Y.; Harris, F. W.; Cheng, S. Z. D., Journal of Macromolecular Science-Physics, **B36**(3), 315-333, 1997

5. Kim, Y. H.; Harris, F. W.; Cheng, S. Z. D., Thermochimica Acta, **283**, 411-423, 1996

6. Wu, Z.; Zhang, A.; Shen, D.; Leland, M.; Harris, F. W.; Cheng, S. Z. D., Journal of Thermal Analysis, 46, 719-731, 1996

7. Blades, H., US Pat. 3,767,756;US Pat. 3,869,429,, 1973

8. Southern, J. H.; Porter, R. S., Appl. Polym. Sci., 2305, 1970

9. Kunugi, T.; Suzuki, A.; Hashimoto, M., J. Appl. Polym. Sci., **26**, 213, 1981

10. Kunugi, T.; Suzuki, A.; Hashimoto, M., J. Appll. Polym. Sci., **26**, 1951, 1981

11. Capaccio, G.; Ward, I. M., Polym. Eng. Sci., **15**,, 1975

12. Luise, **US Pat. 4,183,895**,, 1980

13. Nakagawa, **US Pat. 5,045,257**,, 1991

14. Komatsu, T.; Enoki, S.; Aoshima, A., Polymer, **32**(11), 1983, 1991

15. Komatsu, T.; Enoki, S.; Aoshima, A., Polymer, **32**(11), 1988, 1991

16. Kunugi, T.; Suzuki, A., Journal of Applied Polymer Science, **62**, 713-719, 1996

17. Kunugi, T.; Chida, K.; Suzuki, A., Journal of Applied Polymer Science, **67**, 1993-2000, 1998

18. Fang, X.; Reneker, D. H., Journal of Macromolecular Science-Physics, **B36**(2), 169-173, 1997

19. Doshi, J.; Renker, D. H., Journal of Electrostatics, **35**(2-3), 151-160, 1995

20. Halldin, G. W.; Kamel, I. L., Polymer Engineering and Science, **17**(1), 21-26, 1977

21. Ogawa T, M. H., Osawa S, J Appl Polym Sci, **68**(9), 1431-1439, 1998

22. Hine, P. J.; Ward, I. M., Journal of Materials Science, **31**(2), 371-379, 1996

23. Sweeny, W., Journal of Polymer Science: Part A: Polymer Chemistry, **30**, 1111-1122, 1992

24. Jones, M. C. G.; Lara-curzio, E.; Kopper, A.; Martin, D. C., Journal of Materials Science, **32**, 2855-2871, 1997

25. Hearle, J. W. S.; Peters, R. H. Fiber Structure; Butterworth: London, 1963.

26. Spruiell, J. E.; White, J. L., Appl. Polym. Symp., **27**, 121, 1975

27. Ziabicki, A.; Kawai, H. High Speed Fiber Spinning; Wiley: New York, 1985.

28. Long, S. D.; Ward, I. M., J. Appl. Polym. Sci., **42**, 1911, 1991

29. Hindeleh, A. M.; Abdo, S. M., Polymer Communications, **30**(June), 184, 1989

30. Northolt, M. G.; Aartson, J. J. v., Journal of Polymer Science: Polymer Letters Edition, **11**, 333, 1973

31. Northolt, M. G., Euro. Polym. J., **10**, 799, 1974

32. Watt, W.; Perov, B. V. E. Strong fibres; North-Holland: New York, 1985.

33. Panar, M.; Avakian, P.; Blumem, R. C.; Gardner, K. H.; Fierke, T. D.; Yang, H. H., Journal of Polymer Science: Part B: Polymer Physics, **21**, 1955, 1983

34. Barton, R., Macromol. Sci. Phys., **B24**, 119, 1986

35. Wu, T.; Blackwell, J., Macromolecules, **29**, 5621, 1996

36. Hagege, R.; Jarrin, M.; Sotton, M. J., J. Microscopy, **113**, 65, 1979

37. Riekel, C.; Eddola, A.; Heidelbach, F.; Wagner, K., Macromolecules, **30**, 1033, 1997

38. Dobb, M. G.; Johnson, D. J.; Saville, B. P., Journal of Polymer Science: Polymer Physcis Edition, **15**, 2201, 1977

39. Krause, S. J.; Vezie, D. L.; Adams, W. W., Polymer Communications, **30**, 10, 1989

40. Konopasek, L.; Hearle, J. W. S., Journal of Applied Polymer Science, **21**, 2791, 1977

41. Northolt, M. B.; Aartsen, J. J. V., Journal of Polymer Science: Polymer Symposium, **58**, 283-296, 1977

42. Lee, K. D.; Barton, R.; Schultz, J. M., Journal of Polymer Science: Part B: Polymer Physics, **33**, 1, 1995

43. Dupont, **U.S. Patent 1,198,081**,, 1972

44. II, A.; Tashiro, K.; Kobayashi, M.; Tadokoro, H., Macromolecules, **19**, 1772, 1986

45. English, A. D., Journal of Polymer Science: Part B: Polymer Physics, **24**, 805, 1986

46. Jackson, C. L.; Schadt, R. J.; Gardner, K. H.; Chase, D. B.; Allen, S. R.; Gabara, V.; English, A. D., Polymer, **35**(6), 1123, 1994

47. Schadt, R. J.; Cain, E. J.; Gardner, K. H.; Gabara, V.; Allen, S. R.; English, A. D., Macromolecules, **26**; 6503, 1993

48. Schaefer, D. J.; Schadt, R. J.; Gardner, K. H.; Gabara, V.; Allen, S. R.; English, A. D., Macromolecules, **28**, 1152-1158, 1995

49. Schaefer, D. J.; English, A. D., Polymer, **36**(13), 2517, 1995

50. English, A. D., Korea Polymer Journal, **4**(2), 100-106, 1996

51. Penn, L., Journal of Applied Polymer Science, **23**, 59-73, 1979

52. Jaffe, M.; Jones, S. High Technology Fibers; Dekker: New York, 1985; Vol. 3.

53. Kunugi, T.; Watanabe, H.; Hashimoto, M., Journal of Applied Polymer Science, **24**, 1039-1051, 1979

54. Wu, Z.; Zhang, A.; Cheng, S. Z. D., Journal of Polymer Science: Part B: Polymer Physics, **28**, 2565-2583, 1990

55. Parimala, H. V.; Vijayan, K., Journal of Materials Science Letters, **12**, 99-101, 1993

56. Hindeleh, A. M.; Halim, N. A.; Zig, K. A., J. Macromol. Sci.-Phys., **B23**, 289, 1984

57. Knoff, W. F., Proceedings of the 21st Textile Research Symposium at Fuji Educational Training Center, 5, 1992

58. Fukuda, M.; Kawai, H.; Horii, F.; Kitamaru, R., Polym. Commun., **29**, 97, 1988

59. Fukuda, M.; Kawai, H., Journal of Polymer Science part B-Polymer physics, **35**(9), 1423-1432, 1997

60. Bunsell, A. R., Journal of Material Science, **10**, 1300, 1975

61. Cook, J. Fatigue and Creep of Composite Materials, 1982.

62. Ericksen, R. H., Polymer, **26**, 733, 1985

63. Lafitte, M. H., J. Mater. Sci., **17**, 2391, 1982

64. Guimaraes, G. B.; Burboyne, C. J., Journal of Materials Science, **27**, 2473-2489, 1992

65. Wortmann, F. J.; Schulz, K. V., Polymer, **36**(12), 2363-2369, 1995

66. Deteresa, S. J.; Farris, R. J.; Porter, R. S., Polym. Composites, **3**(2), 57, 1982

67. Dobb, M. G.; Johnson, D. J.; Saville, B. P., Polymer, **22**, 961, 1981

68. Bunsell, A. R., J. Mat. Sci., **9**, 1804, 1974

69. Wilfong, R. E.; Zimmerman, J., J. Appl. Polym. Sci., Appl. Polym. Symp., **31**, 1-21, 1977

70. Hobbs, R. E.; Burgoyne, C. J., International Journal of Fatigue, **13**(2), 174-180, 1991

71. Lacks, D. J., Journal of Materials Science, **31**, 5885-5889, 1996

72. Allen, S. R.; Farris, R. J., Mat. Res. Soc. Symp. Proc., **134**, 297, 1989

73. Allen, S. R.; Roche, E. J., Polymer, **30**, 996, 1989

74. Allen, S. R.; Roche, E. J.; Bennett, B.; Molaison, R., Polymer, **33**(9), 1849, 1992

75. Young, R. J., Journal of the Textile Institute, **86**(2), 360-381, 1995

76. Socci, E. P.; Thomas, D. A.; Eby, R. K.; Grubb, D. T.; Adams, W. W., Polymer, **37**(22), 5005-5009, 1996

77. Prasad, K.; Grubb, D. T., Journal of Applied Polymer Science, **41**(9), 2189-2198, 1990

78. Yeh, W. Y.; Young, R. J., Polymer, **40**(4), 857-870, 1989

79. Northolt, M. C., Polymer, **21**, 1199, 1980

80. Galiotis, C.; Robinson, J. M.; Young, R. J.; Smith, B. J. E.; Batchelder, D. N., Polymer Communicaitons, **26**, 354, 1985

81. Porto, S. P. S., Journal of the Optical Society of America, **56**(11), 1585, 1966

82. Prasad, K.; Grubb, D. T., Journal of Applied Polymer Science, **41**, 2189, 1990

83. Schadler, L. S.; Galiotis, C., Int. Mater. Rev., **40**(3), 116-134, 1995

84. Bunsell, A. R., J. Mater. Sci., **10**, 1300, 1975

85. Yoon, H. N.; Jaffe, M., Abstr. Pap., Am. Chem. soc. Natl. Meet., **185**,, 1983

86. Yang, D. K.; Krigbaum, W. R., J. Polym. Sci., Part B: Polym. Phys., **27**, 1837, 1989

87. Erdemir, A. B.; Johnson, D.; Karacan, I.; Tomka, J. G., Polymer, **29**, 597, 1988

88. Ozawa, S., Polymer Journal,Japan, **19**, 119, 1987

89. Tam, T. Y.; Boone, M. B.; Weedon, G. C., Polymer Engineering and Science, **28**(13), 871, 1988

90. Smith, P.; Lemstra, P. J., J. Mater. Sci., **15**, 505, 1980

91. Grubb, D. T., J. Polym. Sci., Poly. Phyys. Ed., **21**, 165, 1983

92. Smook, J.; Pennings, J., Colloid Polym. Sci., **262**, 712, 1984

93. Sakuda, M., unpublished result, ,

94. Rao, Y.; Farris, R. J., Korea Polymer Journal, **6**(1), 91-104, 1998

95. Ohta, Y.; Yasuda, H., Journal of Polymer Science: Part B: Polymer Physics, **32**, 2241-2249, 1994

96. Schmidtrohr, K.; Spiess, H. W., Macromolecules, **24**(19), 5288-5293, 1991

97. Ohta, Y.; Sugiyama, H.; Yasuda, H., Journal of Polymer Science: Part B: Polymer Physics, **32**, 261-269, 1994

98. Chen, M. J.,"Pressure-Volume-Temperature and Wave Propagation Studies of Polyimide Films," Polymer Science and Engineering Department,University of Massachusetts Amherst, Ph.D. Thesis, 1998

99. Bauer, C. L.; Farris, R. J., Polymer Engineering and Science, **29**(16), 1107, 1989

100. Peirce, F. T., J. Textile Inst., **17**, 355, 1926

101. Spencer-Smith, J. L., J. Text. Inst., **38**(P257),, 1947

102. Ohta, Y.; Yasuda, H., Journal of Polymer Science: Part B: Polymer Physics, **32**, 2241-2249, 1994

103. Lafitte, M. H.; Bunsell, A. R., Polymer Engineering and Science, **25**(3), 182, 1985

104. Wang, J. Z.; Dillard, D. A.; Ward, T. C., Journal of Polymer Science: Part B: Polymer Physics, **30**, 1391-1400, 1992

105. Ward, I. M., Journal of Material Science, **6**, 1397, 1971

106. Li, Y., J. Polym. Sci.: Pt B: Polym. Phys., **29**, 1309-1311, 1991

107. Griffith, A. A., Transactions, **221**,, 1920

108. Paris, P. C. Fatigue-- An Interdisciplinary Approach, Proceedings 10th Sagamore Conference; Syracuse University Press: Syracuse, N.Y., 1964.

109. Paris, P. C.; Erdogan, F., J. Basic Eng. Trans. ASTM, Series D, **85**(4), 528, 1963

110. Swanson, S. R.; Cicci, F.; Hoppe, W., ASTM STP, 415), 312, 1967

111. Hertzberg, R. W. Deformation and Fracture Mechanics of Engineering Materials; John Wiley and Sons:, 1976.

112. Hertzberg, R. W.; Manson, J. A.; Skibo, M. D., Polym. Eng. Sci., **15**(4), 252, 1975

113. Bunsell, A. R.; Hearle, J. W. S.; Hunter, R. D., J. Sci. Instrum., **4**, 860, 1971

114. Wagner, H. D.; Schwartz, P.; Phoenix, S. L., Journal of Materials Science, **21**(6), 1868-1878, 1986

115. Wu, H. F.; Phoenix, S. L.; Schwartz, P., Journal of Materials Science, **23**, 1851, 1988

116. Wilfong, R. E.; Zimmerman, J., J. Appl. Polym. Sci., Appl. Polym. Symp., **31**(1),, 1977

117. Coleman, B. D., J. Appl. Phys., **27**, 862, 1956

118. Ferreira, M.; Lam, T. M.; Labache, P.; Delvael, Y., Textile Research Journal, **69**(1), 30, 1999

119. Kpnopasek, L.; Hearle, J. W. S., Journal of Applied Polymer Science, **21**, 2791, 1977

120. Hertzberg, R. W.; Manson, J. A.; Skibo, M. D., Polymer Engineering Science, **15**(4), 252, 1975

121. Miner, M. A., Journal of Applied Mechanics, **A160**,, 1945

122. Landgraf, R. W., ASTM STP-467, 3, 1970

123. Krausz, A. S.; H., E. Deformation Kinetics; John Wiley & Sons: New York, 1975.

124. McMillan, J. C.; Hertzberg, R. W., ASTM STP, 600), 89, 1968

125. Pruneda, C. O.; Steele, W. J.; Kershaw, R. P.; Morgan, R. J., Polym. Propr., ACS Div. Polym. Chem., **22**, 216, 1981

126. Kuraray, "Vectran" Bulletin, ,

127. Smith, P.; Lemstra, P. J., U. S. Patents 4 344 908; 4 422 993; 4 430 383, ,

128. Kavesh, S.; Prevorsek, D. C., U. S. Patens 4 413 110;4 536 536;4 663 101, ,

129. Deteresa, S. J.; Allen, S. R.; Farris, R. J.; Porter, R. S., Journal of Material Science, **19**, 57, 1984

130. Tzou, D. L.; Schmidt-Rohr, K.; Spiess, H. W., Polymer, **35**, 4728, 1994

131. Allen, S. R.; Farris, R. J., Polymer, **31**(8), 1467-1472, 1990

132. Gegauff, C., Bull. Soc. Ind. Mulhouse, **77**, 153, 1907

133. Platt, M. M., Textile Research Journal, **20**, 665, 1950

134. Hearle, J. W. S., Journal of Textile Instititue, **49**, T389, 1958

135. Treloar, L. R. G.; Riding, G., Journal of Textile Institute, **54**, T156, 1963

136. Freeston, W. D.; Platt, M. M., J. Textile Inst., **63**, 239, 1972

137. White, J. L.; Cheng, C. C.; Spruiell, J. E., Applied Polymer Symposium, **27**, 275, 1975

138. Tsai, S. W.; Hahn, H. T. Introduction to Composite Materials; Tchnomic Publishing Co. Inc.:, 1980.

139. Zweben, C.; Hanh, H. T.; Chou, T. Mechanical Behavior and Properties of Composite Materials; Technomic PublishingCo., Inc.:, 1989; Vol. 1.

140. Agarwal, B. D.; Broutman, L. J. Analysis and Performance of Fiber Composites; John Wiley & Sons, Inc.:, 1990.

141. Hadley, D. W.; Pinnock, P. R.; Ward, I. M., Journal of Material Science, **4**, 152, 1969

142. Morton, V. E.; Hearle, J. W. S. Physical Properties of Textile Fibers; Heinemann: London, 1975.

143. Zorowski, C.; Murayama, T., Textile Research Journal, **37**, 852, 1967

144. Hearle, J. W. S.; El-Behery, H. M. A. E.; Thakur, V. M., J. Textile Inst., **50**, T83, 1959

145. Wilson, N., Nature, **198**, 474, 1963

146. Hearle, J. W. S.; El-Behery, H. M. A. E.; Thakur, V. M., J. Textile Inst., **52**, T197, 1961

147. Holdaway, H. W.; Robinson, M. S., J. Textile Inst., **56**, T168, 1965

148. Landstreet, C. B.; Ewald, P. R.; Simpson, J., Textile Res. J., **27**, 486, 1957

149. Kilby, W. F., J. Textile Inst., **55**, T589, 1964

150. Pan, N., J. Mater. Sci., **28**, 6107, 1993

151. Monego, C. J.; Backer, S., Textile Res. J., **38**, 762, 1968

152. Hearle, J. W. S.; Grosberg, P.; Backer, S. Structural Mechanics of Fibers, Yarns and Fabrics; Wiley-Interscience: New York, 1969; Vol. 1.

153. Rojstaczer, S.; Cohn, D.; Marom, G., J. Mat. Sci. Letters, **3**, 1028, 1984

154. Lide, D. R. Handbook of Chemistry and Physics; 73 ed.; CRC Press: Ann Arbor, 1993.

155. Stein, R. S.; Krimm, S.; Tobolsky, A. V., Text. Res. J., **19**, 325, 1949

156. Devries, K. L.; Farris, R. J., Int. Journ. of Fracture Mech., **6**, 411-420, 1970

157. Wang, D. X.; Lyon, R. E.; Farris, R. J., J. Macromolecular Science, , 1983

158. Buchanan, D. R.; Hardegree, C. L., Text. Res. J., **47**, 732, 1977

159. Pottick, L. A.,"The Infuence of Drying in the Structure and Mechanics of Poly(p-phenylene Benzobisthiazole) Fibers," Polymer Science and Engineering,University of Massachusetts Amherst, Ph.D. Thesis, 1986

160. Vogel, E. M.; Gallagher, P. K., Mater. Lett., **4**, 5, 1985

161. Weiner, J. H. Statistical Mechanics of Elasticity; John Wiley & Sons: New York, 1983.

162. Young, R. J.; Lovell, P. A. Introduction to Polymers; Chapman & Hall: London, 1991.

163. Turi, E. A. Thermal Characterization of Polymeric Materials; Academic Press, 1997.

164. Argon, A. S., Journal of Applied Physcis, **39**(9), 4080, 1968

165. Illers; Jenckel, Kolloid Z., **160**, 97, 1958

166. Hosemann, R.; Wilke, W., Faserforsch Textiledmik, **15**, 521, 1964

167. Eby, R. K.; M., S. K., Journal of Applied Physcis, **32**(9), 1765, 1961

168. Starkweather, H. W.; Jr., Macromolecules, **19**, 2541, 1986

169. Adams, G. W.,"The thermodynamics of deformation for thermoplastic polymers," Polymer Science and Engineering,University of Massachusetts Amherst, Ph.D. Thesis, 1987

170. Haraguchi, K.; Kajiyama, T.; Takayanagi, M., Journal of Applied Polymer Science, **23**, 903-914, 1979

171. Alexander, L. E. X-ray Diffraction Methods in Polymer Science; John Wiley & Sons, Inc.: New York, 1969.

172. Hosemann, R.; Wilke, W., Macromol. Chem., **118**, 230-249, 1968

173. Tashiro, K.; Kobayashi, M.; Tadokoro, H., Macromolecules, **10**, 413, 1977

174. Petch, N. J., JISI, **173**, 25, 1953

BIBLIOGRAPHY

Adams, G. W., "The thermodynamics of deformation for thermoplastic polymers," *Polymer Science and Engineering,* University of Massachusetts Amherst, Ph.D. Thesis, 1987

Agarwal, B. D. and L. J. Broutman, *Analysis and Performance of Fiber Composites*, John Wiley & Sons, Inc., 1990.

Alexander, L. E., *X-ray Diffraction Methods in Polymer Science*. New York, John Wiley & Sons, Inc., 1969.

Allen, S. R. and R. J. Farris, *Mat. Res. Soc. Symp. Proc.*, **134**, 297, 1989.

Allen, S. R. and R. J. Farris, *Polymer,* **31**(8), 1467-1472, 1990.

Allen, S. R. and E. J. Roche, *Polymer,* **30**, 996, 1989.

Allen, S. R., E. J. Roche, et al., *Polymer,* **33**(9), 1849, 1992.

Argon, A. S., *Journal of Applied Physcis,* **39**(9), 4080, 1968.

Barton, R., *Macromol. Sci. Phys.*, **B24**, 119, 1986.

Bauer, C. L. and R. J. Farris, *Polymer Engineering and Science,* **29**(16), 1107, 1989.

Blades, H., , US Pat. 3,767,756;US Pat. 3,869,429, , 1973.

Buchanan, D. R. and C. L. Hardegree, *Text. Res. J.*, **47**, 732, 1977.

Bunsell, A. R., *J. Mat. Sci.*, **9**, 1804, 1974.

Bunsell, A. R., *Journal of Material Science,* **10**, 1300, 1975.

Bunsell, A. R., *J. Mater. Sci.*, **10**, 1300, 1975.

Bunsell, A. R., J. W. S. Hearle, et al., *J. Sci. Instrum.*, **4**, 860, 1971.

Capaccio, G. and I. M. Ward, *Polym. Eng. Sci.*, **15**, , 1975.

Chen, M. J., "Pressure-Volume-Temperature and Wave Propagation Studies of Polyimide Films," *Polymer Science and Engineering Department,* University of Massachusetts Amherst, Ph.D. Thesis, 1998

Coleman, B. D., *J. Appl. Phys.*, **27**, 862, 1956.

Cook, J., Fatigue and Creep of Composite Materials, 1982.

Deteresa, S. J., S. R. Allen, et al., *Journal of Material Science,* **19**, 57, 1984.

Deteresa, S. J., R. J. Farris, et al., *Polym. Composites,* **3**(2), 57, 1982.

Devries, K. L. and R. J. Farris, *Int. Journ. of Fracture Mech.*, **6**, 411-420, 1970.

Dobb, M. G., D. J. Johnson, et al., *Journal of Polymer Science: Polymer Physcis Edition*, **15**, 2201, 1977.

Dobb, M. G., D. J. Johnson, et al., *Polymer*, **22**, 961, 1981.

Doshi, J. and D. H. Renker, *Journal of Electrostatics*, **35**(2-3), 151-160, 1995.

Dupont, , U.S. Patent 1,198,081, , 1972.

Eby, R. K. and S. K. M., *Journal of Applied Physcis*, **32**(9), 1765, 1961.

English, A. D., Journal of Polymer Science: Part B: Polymer Physics, **24**, 805, 1986.

English, A. D., *Korea Polymer Journal*, **4**(2), 100-106, 1996.

Erdemir, A. B., D. Johnson, et al., *Polymer*, **29**, 597, 1988.

Ericksen, R. H., *Polymer*, **26**, 733, 1985.

Fang, X. and D. H. Reneker, *Journal of Macromolecular Science-Physics*, **B36**(2), 169-173, 1997.

Ferreira, M., T. M. Lam, et al., *Textile Research Journal*, **69**(1), 30, 1999.

Freeston, W. D. and M. M. Platt, *J. Textile Inst.*, **63**, 239, 1972.

Fukuda, M. and H. Kawai, *Journal of Polymer Science part B-Polymer physics*, **35**(9), 1423-1432, 1997.

Fukuda, M., H. Kawai, et al., *Polym. Commun.*, **29**, 97, 1988.

Galiotis, C., J. M. Robinson, et al., *Polymer Communicaitons*, **26**, 354, 1985.

Gegauff, C., *Bull. Soc. Ind. Mulhouse*, **77**, 153, 1907.

Griffith, A. A., *Transactions*, **221**, , 1920.

Grubb, D. T., J. Polym. Sci., Poly. Phyys. Ed., **21**, 165, 1983.

Guimaraes, G. B. and C. J. Burboyne, *Journal of Materials Science*, **27**, 2473-2489, 1992.

Hadley, D. W., P. R. Pinnock, et al., *Journal of Material Science*, **4**, 152, 1969.

Hagege, R., M. Jarrin, et al., *J. Microscopy*, **113**, 65, 1979.

Halldin, G. W. and I. L. Kamel, *Polymer Engineering and Science*, **17**(1), 21-26, 1977.

Haraguchi, K., T. Kajiyama, et al., *Journal of Applied Polymer Science*, **23**, 903-914, 1979.

Hearle, J. W. S., *Journal of Textile Institue,* **49**, T389, 1958.

Hearle, J. W. S., H. M. A. E. El-Behery, et al., *J. Textile Inst.,* **50**, T83, 1959.

Hearle, J. W. S., H. M. A. E. El-Behery, et al., *J. Textile Inst.,* **52**, T197, 1961.

Hearle, J. W. S., P. Grosberg, et al., *Structural Mechanics of Fibers, Yarns and Fabrics*. New York, Wiley-Interscience, 1969.

Hearle, J. W. S. and R. H. Peters, Eds. *Fiber Structure*. London, Butterworth, 1963.

Hertzberg, R. W., Deformation and Fracture Mechanics of Engineering Materials, John Wiley and Sons, 1976.

Hertzberg, R. W., J. A. Manson, et al., *Polymer Engineering Science,* **15**(4), 252, 1975.

Hertzberg, R. W., J. A. Manson, et al., *Polym. Eng. Sci.,* **15**(4), 252, 1975.

Hindeleh, A. M. and S. M. Abdo, *Polymer Communications,* **30**(June), 184, 1989.

Hindeleh, A. M., N. A. Halim, et al., *J. Macromol. Sci.-Phys.,* **B23**, 289, 1984.

Hine, P. J. and I. M. Ward, *Journal of Materials Science,* **31**(2), 371-379, 1996.

Hobbs, R. E. and C. J. Burgoyne, *International Journal of Fatigue,* **13**(2), 174-180, 1991.

Holdaway, H. W. and M. S. Robinson, *J. Textile Inst.,* **56**, T168, 1965.

Hosemann, R. and W. Wilke, *Faserforsch Textiledmik,* **15**, 521, 1964.

Hosemann, R. and W. Wilke, *Macromol. Chem.,* **118**, 230-249, 1968.

II, A., K. Tashiro, et al., *Macromolecules,* **19**, 1772, 1986.

Illers and Jenckel, *Kolloid Z.,* **160**, 97, 1958.

Jackson, C. L., R. J. Schadt, et al., *Polymer,* **35**(6), 1123, 1994.

Jaffe, M. and S. Jones, *High Technology Fibers*. New York, Dekker, 1985.

Jones, M. C. G., E. Lara-curzio, et al., *Journal of Materials Science,* **32**, 2855-2871, 1997.

Kavesh, S. and D. C. Prevorsek, U. S. Patens 4 413 110;4 536 536;4 663 101, ,

Kilby, W. F., *J. Textile Inst.,* **55**, T589, 1964.

Kim, Y. H., F. W. Harris, et al., *Thermochimica Acta,* **283**, 411-423, 1996.

Knoff, W. F., Proceedings of the 21st Textile Research Symposium at Fuji Educational Training Center, 5, 1992.

Komatsu, T., S. Enoki, et al., *Polymer,* **32**(11), 1983, 1991.

Komatsu, T., S. Enoki, et al., *Polymer,* **32**(11), 1988, 1991.

Konopasek, L. and J. W. S. Hearle, *Journal of Applied Polymer Science,* **21**, 2791, 1977.

Kpnopasek, L. and J. W. S. Hearle, *Journal of Applied Polymer Science,* **21**, 2791, 1977.

Krause, S. J., D. L. Vezie, et al., *Polymer Communications,* **30**, 10, 1989.

Krausz, A. S. and E. H., *Deformation Kinetics*. New York, John Wiley & Sons, 1975.

Kunugi, T., K. Chida, et al., *Journal of Applied Polymer Science,* **67**, 1993-2000, 1998.

Kunugi, T. and A. Suzuki, *Journal of Applied Polymer Science,* **62**, 713-719, 1996.

Kunugi, T., A. Suzuki, et al., *J. Appll. Polym. Sci.,* **26**, 1951, 1981.

Kunugi, T., A. Suzuki, et al., *J. Appl. Polym. Sci.,* **26**, 213, 1981.

Kunugi, T., H. Watanabe, et al., *Journal of Applied Polymer Science,* **24**, 1039-1051, 1979.

Kuraray, "Vectran" Bulletin, ,

Kwolek, S. L., US Pat. 3671542; US Pat. 3,819,587, , 1972.

Lacks, D. J., *Journal of Materials Science,* **31**, 5885-5889, 1996.

Lafitte, M. H., *J. Mater. Sci.,* **17**, 2391, 1982.

Lafitte, M. H. and A. R. Bunsell, *Polymer Engineering and Science,* **25**(3), 182, 1985.

Landgraf, R. W., *ASTM STP-467*, 3, 1970.

Landstreet, C. B., P. R. Ewald, et al., *Textile Res. J.,* **27**, 486, 1957.

Lee, K. D., R. Barton, et al., Journal of Polymer Science: Part B: Polymer Physics, **33**, 1, 1995.

Li, W. H., Z. Q. Wu, et al., *Journal of Macromolecular Science-Physics,* **B36**(3), 315-333, 1997.

Li, Y., J. Polym. Sci.: Pt B: Polym. Phys., **29**, 1309-1311, 1991.

Lide, D. R., Ed. *Handbook of Chemistry and Physics*. Ann Arbor, CRC Press, 1993.

Long, S. D. and I. M. Ward, *J. Appl. Polym. Sci.,* **42**, 1911, 1991.

Luise, , **US Pat. 4,183,895**, , 1980.

McMillan, J. C. and R. W. Hertzberg, *ASTM STP*(600), 89, 1968.

Miner, M. A., Journal of Applied Mechanics, **A160**, , 1945.

Monego, C. J. and S. Backer, *Textile Res. J.*, **38**, 762, 1968.

Morton, V. E. and J. W. S. Hearle, *Physical Properties of Textile Fibers*. London, Heinemann, 1975.

Nakagawa, , **US Pat. 5,045,257**, , 1991.

Northolt, M. B. and J. J. V. Aartsen, *Journal of Polymer Science: Polymer Symposium*, **58**, 283-296, 1977.

Northolt, M. C., *Polymer*, **21**, 1199, 1980.

Northolt, M. G., *Euro. Polym. J.*, **10**, 799, 1974.

Northolt, M. G. and J. J. v. Aartson, *Journal of Polymer Science: Polymer Letters Edition*, **11**, 333, 1973.

Ogawa T, M. H., Osawa S, *J Appl Polym Sci*, **68**(9), 1431-1439, 1998.

Ohta, Y., H. Sugiyama, et al., Journal of Polymer Science: Part B: Polymer Physics, **32**, 261-269, 1994.

Ohta, Y. and H. Yasuda, Journal of Polymer Science: Part B: Polymer Physics, **32**, 2241-2249, 1994.

Ohta, Y. and H. Yasuda, Journal of Polymer Science: Part B: Polymer Physics, **32**, 2241-2249, 1994.

Ozawa, S., *Polymer Journal,Japan*, **19**, 119, 1987.

Pan, N., *J. Mater. Sci.*, **28**, 6107, 1993.

Panar, M., P. Avakian, et al., Journal of Polymer Science: Part B: Polymer Physics, **21**, 1955, 1983.

Parimala, H. V. and K. Vijayan, *Journal of Materials Science Letters*, **12**, 99-101, 1993.

Paris, P. C., Fatigue-- An Interdisciplinary Approach, Proceedings 10th Sagamore Conference. Syracuse, N.Y., Syracuse University Press, 1964.

Paris, P. C. and F. Erdogan, *J. Basic Eng. Trans. ASTM, Series D*, **85**(4), 528, 1963.

Peirce, F. T., *J. Textile Inst.*, **17**, 355, 1926.

Penn, L., Journal of Applied Polymer Science, **23**, 59-73, 1979.

Pennings, A. J. and K. E. Meihyizen, Polyethylene Fibers with Ultrahigh Modulus and Strength Produced by Flow Controlled Crystallization. London, Applied Science, 1979.

Petch, N. J., *JISI*, **173**, 25, 1953.

Platt, M. M., *Textile Research Journal,* **20**, 665, 1950.

Porto, S. P. S., Journal of the Optical Society of America, **56**(11), 1585, 1966.

Pottick, L. A., "The Infuence of Drying in the Structure and Mechanics of Poly(p-phenylene Benzobisthiazole) Fibers," *Polymer Science and Engineering,* University of Massachusetts Amherst, 1986

Prasad, K. and D. T. Grubb, *Journal of Applied Polymer Science,* **41**(9), 2189-2198, 1990.

Prasad, K. and D. T. Grubb, *Journal of Applied Polymer Science,* **41**, 2189, 1990.

Pruneda, C. O., W. J. Steele, et al., *Polym. Propr., ACS Div. Polym. Chem.,* **22**, 216, 1981.

Rao, Y. and R. J. Farris, *Korea Polymer Journal,* **6**(1), 91-104, 1998.

Riekel, C., A. Eddola, et al., *Macromolecules,* **30**, 1033, 1997.

Rojstaczer, S., D. Cohn, et al., *J. Mat. Sci. Letters,* **3**, 1028, 1984.

Sakuda, M., unpublished result, ,

Schadler, L. S. and C. Galiotis, *Int. Mater. Rev.,* **40**(3), 116-134, 1995.

Schadt, R. J., E. J. Cain, et al., *Macromolecules,* **26**, 6503, 1993.

Schaefer, D. J. and A. D. English, *Polymer,* **36**(13), 2517, 1995.

Schaefer, D. J., R. J. Schadt, et al., *Macromolecules,* **28**, 1152-1158, 1995.

Schmidtrohr, K. and H. W. Spiess, *Macromolecules,* **24**(19), 5288-5293, 1991.

Smith, P. and P. J. Lemstra, U. S. Patents 4 344 908; 4 422 993; 4 430 383, ,

Smith, P. and P. J. Lemstra, *J. Mater. Sci.,* **15**, 505, 1980.

Smook, J. and J. Pennings, *Colloid Polym. Sci.,* **262**, 712, 1984.

Socci, E. P., D. A. Thomas, et al., *Polymer,* **37**(22), 5005-5009, 1996.

Southern, J. H. and R. S. Porter, *Appl. Polym. Sci.,* 2305, 1970.

Spencer-Smith, J. L., *J. Text. Inst.,* **38**(P257), , 1947.

Spruiell, J. E. and J. L. White, *Appl. Polym. Symp.,* **27**, 121, 1975.

Starkweather, H. W. and Jr., *Macromolecules,* **19**, 2541, 1986.

Stein, R. S., S. Krimm, et al., *Text. Res. J.,* **19**, 325, 1949.

Swanson, S. R., F. Cicci, et al., *ASTM STP*(415), 312, 1967.

Sweeny, W., Journal of Polymer Science: Part A: Polymer Chemistry, **30**, 1111-1122, 1992.

Tam, T. Y., M. B. Boone, et al., *Polymer Engineering and Science,* **28**(13), 871, 1988.

Tashiro, K., M. Kobayashi, et al., *Macromolecules,* **10**, 413, 1977.

Treloar, L. R. G. and G. Riding, *Journal of Textile Institute,* **54**, T156, 1963.

Tsai, S. W. and H. T. Hahn, *Introduction to Composite Materials*, Tchnomic Publishing Co. Inc., 1980.

Turi, E. A., Ed. Thermal Characterization of Polymeric Materials, Academic Press, 1997.

Tzou, D. L., K. Schmidt-Rohr, et al., *Polymer,* **35**, 4728, 1994.

Vogel, E. M. and P. K. Gallagher, *Mater. Lett.,* **4**, 5, 1985.

Wagner, H. D., P. Schwartz, et al., *Journal of Materials Science,* **21**(6), 1868-1878, 1986.

Wang, D. X., R. E. Lyon, et al., *J. Macromolecular Science*, , 1983.

Wang, J. Z., D. A. Dillard, et al., *Journal of Polymer Science: Part B: Polymer Physics,* **30**, 1391-1400, 1992.

Ward, I. M., *Journal of Material Science,* **6**, 1397, 1971.

Watt, W. and B. V. E. Perov, *Strong fibres*. New York, North-Holland, 1985.

Weiner, J. H., *Statistical Mechanics of Elasticity*. New York, John Wiley & Sons, 1983.

White, J. L., C. C. Cheng, et al., *Applied Polymer Symposium,* **27**, 275, 1975.

Wilfong, R. E. and J. Zimmerman, *J. Appl. Polym. Sci., Appl. Polym. Symp.,* **31**(1), , 1977.

Wilfong, R. E. and J. Zimmerman, *J. Appl. Polym. Sci., Appl. Polym. Symp.,* **31**, 1-21, 1977.

Wilson, N., *Nature,* **198**, 474, 1963.

Wortmann, F. J. and K. V. Schulz, *Polymer,* **36**(12), 2363-2369, 1995.

Wu, H. F., S. L. Phoenix, et al., *Journal of Materials Science,* **23**, 1851, 1988.

Wu, T. and J. Blackwell, *Macromolecules,* **29**, 5621, 1996.

Wu, Z., A. Zhang, et al., Journal of Polymer Science: Part B: Polymer Physics, **28**, 2565-2583, 1990.

Wu, Z., A. Zhang, et al., *Journal of Thermal Analysis,* **46**, 719-731, 1996.

Yang, D. K. and W. R. Krigbaum, *J. Polym. Sci., Part B: Polym. Phys.,* **27**, 1837, 1989.

Yang, H. H., *Kevlar Aramid Fiber*. New York, Wiley-Intersience, 1992.

Yeh, W. Y. and R. J. Young, *Polymer*, **40**(4), 857-870, 1989.

Yoon, H. N. and M. Jaffe, Abstr. Pap., Am. Chem. soc. Natl. Meet., **185**, , 1983.

Young, R. J., *Journal of the Textile Institute*, **86**(2), 360-381, 1995.

Young, R. J. and P. A. Lovell, *Introduction to Polymers*. London, Chapman & Hall, 1991.

Ziabicki, A. and H. Kawai, *High Speed Fiber Spinning*. New York, Wiley, 1985.

Zorowski, C. and T. Murayama, *Textile Research Journal*, **37**, 852, 1967.

Zweben, C., H. T. Hanh, et al., *Mechanical Behavior and Properties of Composite Materials*, Technomic PublishingCo., Inc., 1989.